Fiber-Cavity Optomechanics with Hexagonal Boron Nitride Drum Resonators

INAUGURALDISSERTATION

zur
Erlangung der Würde eines Doktors der Philosophie

vorgelegt der
Philosophisch-Naturwissenschaftlichen Fakultät
der Universität Basel

von

David Jaeger

Basel, 2023

Genehmigt von der Philosophisch-Naturwissenschaftlichen Fakultät
auf Antrag von

Prof. Dr. Martino Poggio
Erstbetreuer/in

Prof. Dr. Richard Warburton
Zweitbetreuer/in

Prof. Dr. Eva Weig
Externe/r Experte/in

Basel, den 19.09.2023

Prof. Dr. Marcel Mayor
Dekanin/Dekan

UNIVERSITY OF BASEL

Abstract

Faculty of Science
Department of Physics

Doctor of Philosophy

Fiber-Cavity Optomechanics with Hexagonal Boron Nitride Drum Resonators

by David Jaeger

In an effort to overcome the limits imposed by the inherently weak radiation pressure interaction, the field of optomechanics aims to miniaturize both the mechanical elements and the mode volume of the optical cavities involved. Like this, the interaction can be boosted, and the quantum regime comes within reach. The possibility of introducing additional elements into the system, such as quantum emitters, offers alternative ways to move past current experimental limitations. This calls for versatile experimental platforms with a small footprint that allow for the integration and exploration of novel materials and experimental protocols.

Here we present a fiber based Fabry-Perot cavity that can be operated under atmospheric conditions, under vacuum, and at 4 K. We demonstrate our ability to stabilize the cavity length within the cavity linewidth while maintaining full tunability and a high finesse.

We fabricate mechanical drum resonators by suspending flakes of hexagonal boron-nitride over holes in a high-stress Si_3N_4 membrane. By imaging their motion and measuring their thermal displacement spectra, we characterize these drums and their hybridization with the underlying Si_3N_4 membrane. The observed mode shapes are consistent with theoretical models and finite-element simulations of an ideal drum, revealing that our fabrication procedure introduce little imperfections. The analysis of the thermal spectra reveals that hybridization with the Si_3N_4 membrane can shift the quality factor and effective mass of the drum modes by several orders of magnitude. This could be an important tool in the endeavor to improve the moderate mechanical quality factors of 2D material oscillators, and further enhance their sensitivity.

Combining our cavity with our hBN drum resonator yields an optomechanical platform with a single-photon coupling of up to $g_0 = 230\,\mathrm{kHz}$, several orders of magnitude higher than previous implementations employing mechanical resonators made of 2D materials. This high value is made possible by the small mode volume of our microscale cavity, as well as the low effective mass of our hBN drum resonator. Finally, the combination of the high stability of our system with this strong interaction allowed us to measure the optomechanically induced transparency effect, highlighting the potential of our experimental platform.

Contents

List of Figures

Chapter 1

Introduction

The radiation pressure force, experimentally demonstrated for the first time in 1901 [1, 2], allows to couple a mechanical oscillator to an electromagnetic field, creating an optomechanical system. Such a system is an intriguing platform for many experiments, including high precision sensing [3–7], cooling of the mechanical resonator [8–10], laser cooling and trapping of atoms or ions [11, 12], or preparation of non-classical states of motion and light [13–17]. However, the weak radiation pressure force puts these experiments in a challenging parameter space, especially when trying to reach the quantum regime [18]. To alleviate this issue, it is common to boost the interaction by employing optical resonators, often referred to as optical cavities. In the simple case of a Fabry-Perot cavity, this is achieved with two mirrors facing each other [19]. Another way to improve the optomechanical coupling is to employ mechanical oscillators that are highly sensitive, which is often achieved by pushing these devices to the nanoscale.

With this in mind, we set out to build and characterize a cavity optomechanics setup comprised of a sensitive hexagonal boron-nitride (hBN) drum resonator and a fiber based Fabry-Perot cavity (FFPC). We will employ the membrane-in-the-middle (MIM) configuration, in which the mechanical oscillator is placed in the middle of the cavity [186, 20]. This design is in contrast to systems where one of the mirrors of the Fabry-Perot cavity acts as the mechanical element [16, 21, 22], or systems based on other cavity designs, such as whispering-gallery mode resonators [23, 24] or photonic crystal cavities [25–28]. Making a good cavity mirror requires sufficient lateral dimensions and thickness, this makes it difficult to push these objects towards the nanoscale when using them as mechanical oscillators [22]. In a MIM system, where the mechanical and optical components are separated, each part of the system can be optimized independently. Whispering-gallery mode resonators or photonic crystal cavities can achieve small footprints and very high optomechanical coupling strengths [18], but the mechanical element is usually the cavity body itself. This limits the use of different mechanical elements with interesting properties, such as the hBN drums we will present here. Compared to these devices, the advantage of a MIM system employing an open Fabry-Perot cavity lies in its flexibility and tunability. In the case of whispering-gallery mode resonators, the optical losses in the medium of the device are an additional problem.

Beginning with the MIM aspect of our system, mechanical resonators have drawn much attention in recent years. Not only do they achieve record breaking force [29–31] and mass sensitivities [32, 33], but they can also be interfaced with a variety of different systems, making them a prominent choice for hybrid systems [34, 35, 187, 188]. They have been successfully brought into the quantum regime by cooling their motional state down to the quantum ground state [10, 36–38]. Considering their often macroscopic dimensions, this makes them an ideal platform to investigate the quantum to classical crossover [36, 39].

Mechanical resonators that are good sensors and the ones that lead to high optomechanical coupling strengths share many similarities [18, 40]. Since we in essence need a device that reacts strongly to radiation pressure forces in optomechanics, this is not surprising. For example, we can compare the force sensitivity S_F and the zero point motion x_{zpm} of a mechanical resonator, the latter being directly linked to the optomechanical coupling strength.

$$\sqrt{S_F} = \sqrt{4k_B T \Gamma m}, \qquad x_{zpm} = \sqrt{\frac{\hbar}{2\omega m}} \tag{1.1}$$

From these expression we can see that reducing the mass m is a key for both applications, while a low dissipation Γ additionally benefits the sensitivity and the optomechanical coupling further relies on a small resonance frequency ω. New fabrication techniques and the discovery of low-dimensional mechanical objects, such as 1D nanowires [41], carbon nanotubes [42], as well as 2D membranes made of graphene [43], hBN [44, 45] or other Van-der-Waals materials [46–48], have pushed the boundaries towards the nanoscale [48]. This not only results in a very low mass, but the extreme aspect ratios found in these lower dimensional objects can also help to reduce their resonance frequency, as is for example the case in nanowire resonators [31]. But also highly optimized and much larger silicon nitride (Si_3N_4) structures have achieved great success due to incredibly low dissipation and thus high mechanical quality factors [49, 50]. Si_3N_4 membranes in particular have been the standard device for MIM optomechanics in the past [51–57].

Efforts to integrate low-dimensional mechanical resonators with cavities have only just begun. Among the first successful implementations are carbon nanotubes [58], nanowires [59], as well as hBN [60] and graphene resonators [61–64]. Due to their extremely small size, integrating carbon nanotubes into optomechanical devices is a challenge, even the detection of their motion is not a simple task [58, 65]. In the case of larger nanowires, the extreme mechanical properties and aspect ratios could be utilized to achieve a strong optomechanical interaction, but the nature of the Mie-scattering interaction puts strict constraints on the system. In particular, it requires a rather modest cavity finesse due to strong scattering losses [59, 66, 197]. While a membranes, and thus 2D materials, do not share this issue, most Van-der-Waals materials tend to have significant optical absorption, leading to similar problems in optical cavities [67]. Among the vast variety of different 2D materials, hBN stands out as a large band-gap (6 eV [68]) insulator that is largely transparent and offers low absorption in the visibile to near infra-red (NIR) parts of the electromagnetic spectrum [69]. This makes hBN uniquely suitable for MIM optomechanics, especially when employing high finesse optical cavities. Indeed, a very recent implementation has demonstrated such a system, combining a hBN drum resonators with a very high finesse cavity (2×10^5) [70].

Aside from these advantages, there are further reasons that motivated us to employ hBN as our material of choice. 2D materials are known to have outstanding mechanical properties , and with a predicted Young's modulus of 780 GPa and a fracture strength of 12.5% [71, 72], hBN is even comparable to graphene [73]. Unlike graphene however, hBN is known to preserve these extreme properties even beyond the monolayer limit, where inter-layer interactions become important [71]. hBN is often employed to encapsulate other 2D materials or heterostructures [74–77], making hBN resonators a promising platform for functionalized 2D mechanical resonators. This can give access to the incredible variety of magnetic [78, 79], electronic [80–82] and optical [83, 84] features that 2D materials have to offer. Even hBN itself has been shown to host stable quantum emitters [85] that are strain coupled

to the host crystal lattice [86, 87]. This makes hBN a candidate for a hybrid system on its own, or, in conjunction with an optical cavity, it could even form a hybrid optomechanical system [88–92].

A big challenge regarding mechanical resonators made of 2D materials is the low Q factor across many different implementations, especially at room temperature [43, 45, 46, 93–95]. The reasons for this poor performance is still under investigation [47]. In addition, the modes of such resonators appear to react strongly to small imperfections in the resonator, leading to devices that are difficult to model [44, 96, 97]. Here we show our efforts to fabricate higher quality resonators that match simple theoretical models. We will also explore the hybridization between a hBN drum and a high stress Si_3N_4 membrane, showcasing a potential avenue to circumvent the low mechanical quality factors of 2D material resonators while still having access to the special properties of 2D materials.

The second constituent of our optomechanical system is the fiber based Fabry-Perot cavity. Such a FFPC is made by using the gap between the end facets of two cleaved optical fibers as cavity [98]. These end facets serve as mirrors of the cavity, and the quality and shape of these mirrors critically determine its performance. The desired concave shape is realized through laser ablation [99, 100], while the high reflectivity is achieved by employing a highly reflective dielectric coating. Fiber Fabry-Perot cavities can achieve high finesse and have the key advantage of a small footprint, leading to a small mode volume [101]. This property is critical to increase the coupling to nanoscale systems, making the FFPC a natural choice in cavity quantum electrodynamics experiments [102–113], but also when coupling to nano or microscale mechanical oscillators [58, 59, 114–118]. In the case of mechanical oscillators, the small mode volume not only increases the coupling but also helps to avoid clipping losses at the boundaries of the small devices. As such, the miniaturization of optical cavities naturally follows the push towards the nanoscale in the field of mechanics. The fiber based design also lends itself to integration in vacuum systems or cryostats [116, 119–123] since additional optical components to couple into the cavity [124, 125] can be avoided.

We will first discuss the hBN drum resonator and the FFPC separately; afterwards, we will combine the system and characterize the optomechanical interaction of the fully assembled MIM-FFPC system. An overview of the chapters that can be found in this manuscript is given in the following:

1.1 Thesis Outline

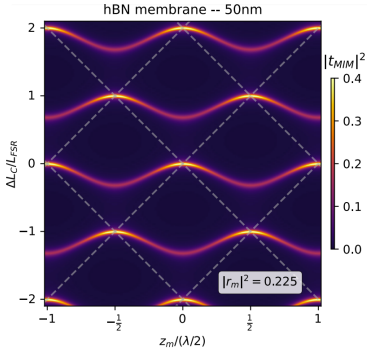

In **chapter 2**, we will discuss the necessary theoretical background. Regarding our mechanical system, we will develop models that allow us to characterize and identify our mechanical modes based on their thermal motion and spatial mode shape. For both the FFPC and the complete optomechanical system, we will employ the transfer matrix formalism to describe and understand the optically measured signals.

Chapter 3 will cover the experimental measurement and control setups. Aside from the probe that hosts the MIM-FFPC system, we will present a room temperature interferometer used to characterize the hBN drum resonators. In addition, we will give an overview of the involved optical setups and the cratered optical fibers making up the FFPC.

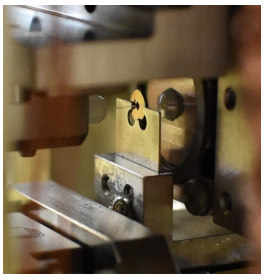

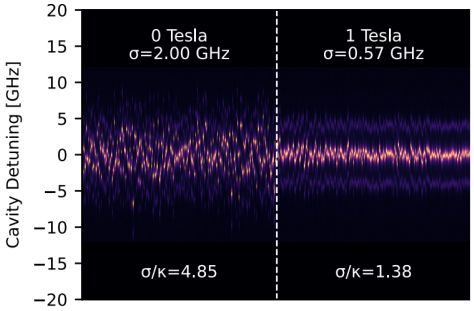

Chapter 4 is dedicated to the characterization of the FFPC. After establishing the fundamental properties of our cavity, we will discuss the passive and active stabilization of the cavity length. We will show that a stability better than the cavity linewidth can be maintained even for very low optical powers and at cryogenic temperatures.

In **chapter 5**, we will discuss the design and fabrication of our hBN drum resonators. After motivating the exact parameters of our devices, we will give a detailed explanation of the wet transfer technique we employ, including additional cleaning procedures. Finally, we will give a short overview of the hBN resonators fabricated like this.

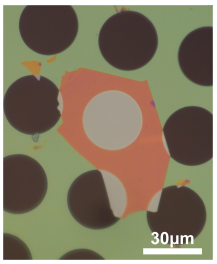

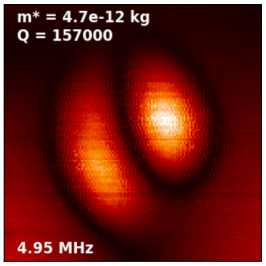

We will present the mechanical characterization of the drum resonators in **chapter 6**. Focusing mainly on one of the devices, we will characterize the properties of many different modes based on their thermal motion and spatial mode shape. We will further discuss the arising hybridization between higher order modes of the hBN drum and the Si_3N_4 substrate.

In **chapter 7**, the combined MIM-FFPC system is explored. We will establish the viability of hBN as a material for MIM operation under high finesse conditions by exploring static optomechanical interactions. As a final step, we will present a recent measurement of optomechanically induced transparency to showcase the dynamical optomechanical effects in our system.

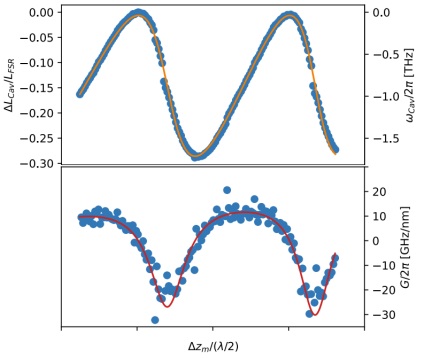

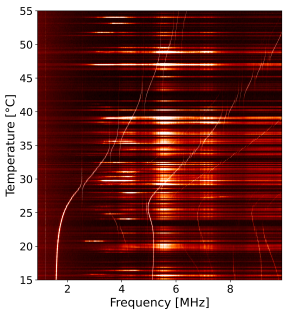

We will conclude in **chapter 8**, summarizing the main results of this thesis. In addition, a short outlook will be presented with currently ongoing measurements regarding this project and its potential future avenues.

Chapter 2

Theoretical Background

We will begin this thesis by introducing the theoretical models necessary for the discussion of the measurement results in the following chapters. After taking a look at the two constituents separately, namely the hBN drum resonators in section 2.1 and the FFPC in section 2.2, we will move on to a more complete description of the MIM-FFPC system in section 2.3.

2.1 Mechanics of a hBN Drum Resonator

To analyse the hBN drum resonators, we will use both thermal displacement spectra and spatial imaging maps of the drum's motion. For the former, we will employ a simple formalism based on a general harmonic oscillator. The latter will require a more detailed discussion tailored to drum resonators in particular.

2.1.1 Power spectral density

Here we follow [40, 126] and adopt a notation similar to [18] when possible. We begin with the equation of motion of a harmonic oscillator driven by a force $F(t)$

$$m^*\ddot{x}t + \gamma_m\dot{x}t + k_m x(t) = F(t) \tag{2.1}$$

where m^* is the effective mass, γ_m the damping coefficient and k_m the spring constant. It is convenient to convert to frequency space with angular frequency ω_m ($\omega_m = 2\pi f_m$, where f_m is the frequency) using the Fourier transform[1]:

$$-m^*\omega_m^2 x(\omega_m) - i\omega_m\gamma_m x(\omega_m) + kx(\omega_m) = F(\omega_m) \tag{2.2}$$

This algebraic equation can now simply be solved for $x(\omega)$.

$$x(\omega_m) = \frac{1}{m^*(\omega_{m,0}^2 - \omega_m^2 - i\omega_m\Gamma_m)}F(\omega_m) = \chi_m(\omega)F(\omega_m) \tag{2.3}$$

Here we used the definition $\omega_{m,0} = \sqrt{k_m/m^*}$ and also redefined $\gamma_m = \Gamma_m m^* = \frac{\omega_{m,0}}{Q}m^*$ to have a dissipation in units of Hz to be more in line with the definitions typically used in the field of optomechanics. Q denotes the Q-factor of the oscillator, *i.e.* the ratio between the stored energy and the energy loss per cycle. $\chi_m(\omega_m)$ is called the frequency response function or alternatively the mechanical susceptibility.

From this we can obtain the power spectral density (PSD) for the harmonic oscillator

$$S_x(\omega_m) = \lim_{\tau\to\infty}\frac{1}{\tau}|x(\omega_m)|^2 = |\chi_m(\omega_m)|^2 S_F(\omega_m) \tag{2.4}$$

[1] $x(\omega) = \int dt e^{i\omega t}x(t)$

The PSD of the driving force $F(\omega_m)$ is translated into the PSD of $x(\omega_m)$ accoring to the mechanical susceptibility $\chi_m(\omega_m)$. For thermal motion, we can use the fluctiation-dissipation theorem [127] to obtain

$$S_F(\omega_m) = \frac{2k_BT}{\omega_m} \operatorname{Im}\left[\frac{1}{\chi_m(\omega_m)}\right] = 2k_BTm^*\Gamma_m \tag{2.5}$$

This then results in the PSD for the thermal motion of our harmonic oscillator, for which we also show a general spectrum in Fig. 2.1.

$$S_x(\omega_m) = \frac{2\Gamma_m k_BT}{m^*((\omega_{m,0}^2 - \omega_m^2)^2 + \Gamma_m^2\omega_m^2)} \tag{2.6}$$

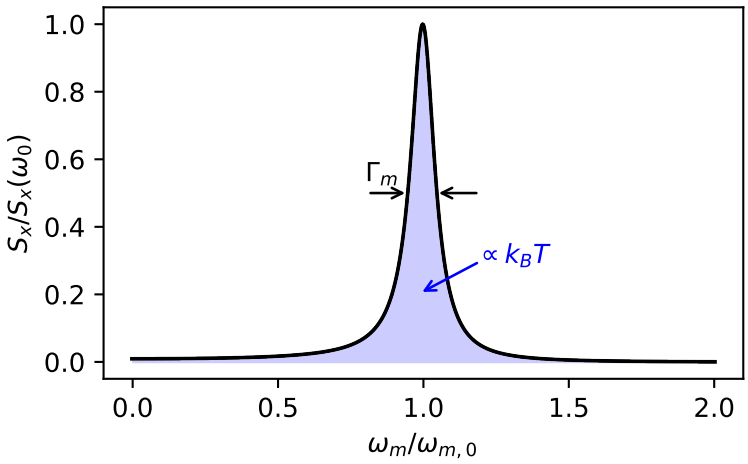

FIGURE 2.1: Normalized thermal displacement PSD of a harmonic oscillator, with Γ_m corresponding to the FWHM of the resonance peak. The area under the peak is highlighted in blue and is proportional to the temperature.

Thermal motion and zero point fluctuations

The PSD derived above can be used to fit a recorded thermal spectrum and extract the characteristic parameters of the mechanical resonator, such as Q, m^* and $\omega_{m,0}$, in particular when T is known. Meanwhile, it is useful to have an estimate of the expected amplitude of the thermal- and quantum fluctuations to have an idea of the required sensitivities for position detection, or expected optomechanical coupling strengths.

For the thermal fluctuations one simply needs to recall the equipartition theorem

$$\frac{1}{2}k_m\left\langle x^2\right\rangle = \frac{1}{2}k_BT \tag{2.7}$$

to arrive at the expression

$$x_{th} = \sqrt{\frac{k_BT}{\omega_{m,0}^2 m^*}} \tag{2.8}$$

The zero point fluctuations are given by the expectation value of the position operator of the quantum harmonic oscillator for the ground state $\langle 0|\hat{x}|0\rangle$, which gives

$$x_{zpm} = \sqrt{\frac{\hbar}{2\omega_{m,0}m^*}} \tag{2.9}$$

Micro and nanomechanical resonators are commonly used as sensors. In this case, one measures the effect of an added mass or an external force gradient on the resonance frequency. In this regard, thermal fluctuations set a lower limit, allowing us to define force and mass sensitivities as follows:

$$\sqrt{\bar{S}_F(\omega_m)} = \sqrt{4k_B T \Gamma_m m^*} \tag{2.10}$$

$$\sqrt{\bar{S}_m(\omega_m)} = \sqrt{2k_B T \Gamma_m m^*} \frac{2}{x\omega_{m,0}^2} \tag{2.11}$$

Here $\bar{S}_F(\omega) = 2S_F(\omega)$ is the single sided PSD for $\omega_m > 0$.

2.1.2 Circular drum resonators

It is now necessary to move from the general description of a harmonic oscillator to a formalism that captures the behavior of the mechanical resonators described in this thesis. For this, we consider a circular drum under tension as in [44, 128], additional information can be found in [129, 189]. In this model, both the bending rigidity and the tension of the plate are taken into account. Usually, for thick drums, the bending rigidity is the dominant term and the tension is neglected, resulting in the well known *plate* description. For very thin drums, it is the other way around and we enter the *membrane* regime. Our resonators tend to sit right between these two extremes, making it necessary to take both effects into account.

Mode frequencies of a circular membrane

The equation of motion for such a system is given by

$$D_p \Delta^2 z - T_p \Delta z + \rho \frac{\partial^2}{\partial t^2} z = 0 \tag{2.12}$$

where D_p is the bending stiffness, T_p is the tension, ρ is the density, z is the out of plane motion, Δ is the Laplace operator and Δ^2 the biharmonic operator. D_p depends on the plate thickness d_m and the material properties, namely the Poisson ratio ν and the Young's modulus E, as follows

$$D_p = \frac{E d_m^3}{12(1-\nu^2)} \tag{2.13}$$

The resonance frequencies for the different modes are then given by [128]

$$f_{mn} = \frac{1}{2\pi}(k_{mn}r)\sqrt{\frac{D_p}{\delta r^4}[(k_{mn}r)^2 + \frac{T_p r^2}{D_p}]} \tag{2.14}$$

Here r is the radius of the drum, $(k_{mn}r)^2$ is the numerically calculated eigenvalue for mode (m,n), where m,n denotes the lateral and circular mode number. The values for $(k_{mn}r)^2$ can be calculated using

$$(k_{mn}r)^2 = \alpha_{mn} + (\beta_{mn} - \alpha_{mn}) e^{-\eta_{mn}\, exp(\gamma_{mn} ln(\frac{T_p r^2}{D_p}))} \tag{2.15}$$

where $\alpha_{mn}, \beta_{mn}, \gamma_{mn}, \eta_{mn}$ are numerical values that are given for each mode and can be found in Appendix A.

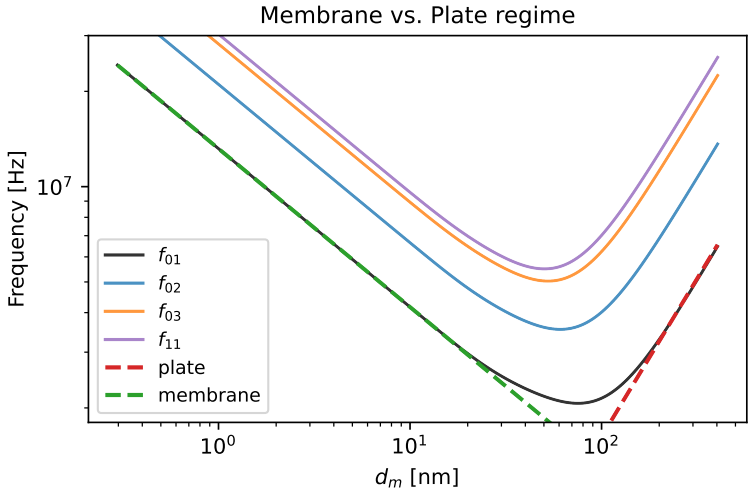

FIGURE 2.2: Resonance frequency of the first few modes of a hBN drum with r =10 µm. Shown are the curves obtained with Eq. 2.14 as well as the isolated plate model (red) and the isolated membrane model (green) for the fundamental mode.

The behavior of this model is captured in Fig. 2.2. For a drum of small d_m, the resonance frequency approaches that of the membrane model. One can retrieve the purely membrane-like expression from Eq. 2.14 by taking the limit $D_p \to 0$. For a larger d_m, the resonance frequency is dominated by the bending rigidity, i.e. by plate-like behavior, which is retrieved by neglecting the T_p term in Eq. 2.14. Both for very small and large thickness, the resonance frequency increases, with a minimum located between the purely plate- and membrane-like regimes.

Mode shapes of a circular membrane

The mode shapes of a circular membrane are most easily expressed in polar coordinates (θ, a). To label the different modes, we use indices (m, n) representing the amount of radial and circular nodal lines, respectively. Note that while the amount of radial nodal lines is equal to m, the circular nodal lines amount to $n-1$. In this case, the characteristic functions describing the out of plane motion of these modes, as defined in [190], are given by

$$\psi_{e,(m,n)}(\theta, a) = \cos(m\theta) J_m\left(\frac{\pi \beta_{m,n} a}{r}\right) \tag{2.16}$$

where J_m is the Bessel function of the first kind, r is the radius of the drum and $\beta_{m,n}$ is a value determined by the boundary condition $J_m = 0$ for $a = r$.

In addition to these solutions, there is another set of solutions for $m \geq 1$, *i.e.* for modes that are no longer radially symmetric. We call the solutions in Eq. 2.16 the even solutions and the ones in Eq. 2.17 the odd solutions:

$$\psi_{o(m,n)}(\theta, a) = \sin(m\theta) J_m\left(\frac{\pi \beta_{m,n} a}{r}\right) \tag{2.17}$$

These modes are simply rotated by $\pi/2m$ with respect to the ones in Eq. 2.16 and are otherwise degenerate. We plot $\psi_{m,n}$ for the first few modes according to Eq. 2.16 in Fig. 2.3.

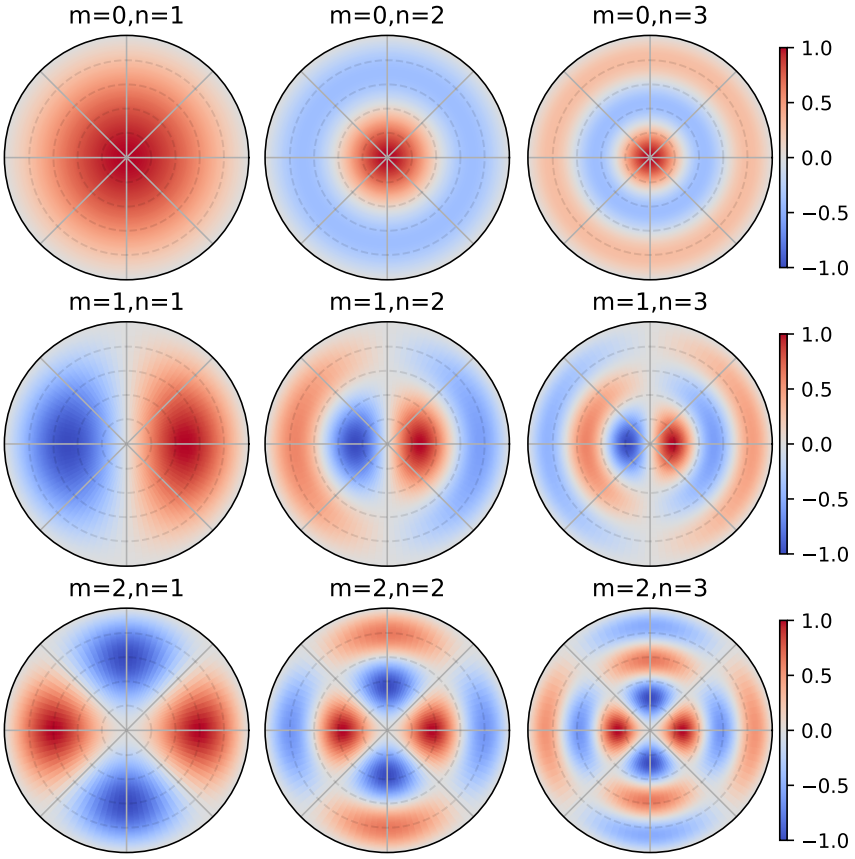

FIGURE 2.3: Out of plane motion $\psi_{m,n}$ for the first nine modes of a circular drum resonator, where we have omitted the additional solutions for $m \geq 1$ given by Eq. 2.17, which only differ in orientation.

Another important quantity is the effective mass m^*, which can be calculated once the mode shapes are known [191, 192]. For the fundamental mode of a circular drum, it is related to the geometrical mass m_g by $\frac{m^*}{m_g} \approx 0.27$ [130], giving

$$m^*_{th} = 0.27\pi r^2 d_m \tag{2.18}$$

as a theoretical prediction for m^* of the fundamental mode of our drums.

2.2 Fabry-Perot Cavity

We will now introduce the general description of a Fabry-Perot cavity that we will employ in the rest of the manuscript. Here we make use of the transfer matrix formalism, which is particularly useful when describing light that passes through a cascade of elements. We closely follow [66, 131, 203], more information can be found in [193–195].

When relating the ingoing and outgoing fields on one side of a system of elements to the ingoing and outgoing fields on the other side, one can obtain a single matrix M, describing the entire process simply by cascading the matrices describing the individual elements n in order $M = M_n \cdot M_{n-1} \cdot ... \cdot M_1$.

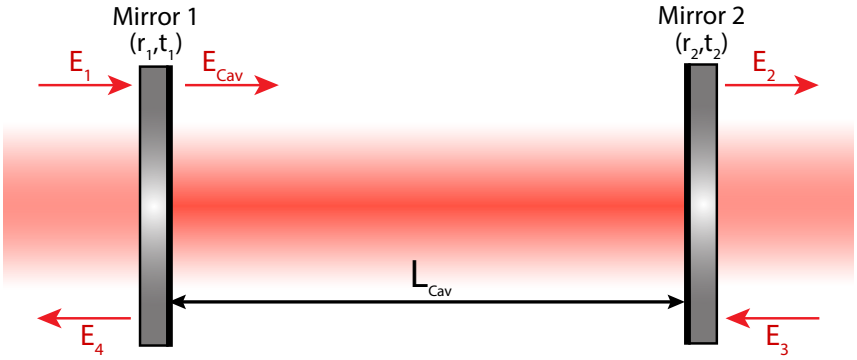

FIGURE 2.4: Simplified sketch of the Fabry-Perot cavity considered here. Two planar mirrors are separated by the cavity length L_{Cav}. They are characterized by their reflection and transmission coefficients r_i, t_i. Red arrows illustrate the relevant electric field components E_i.

We start with a simple Fabry-Perot Cavity of length L_{Cav} with two planar mirrors characterized by their reflection coefficients $R_{1,2} = r_{1,2}^2$ and their transmission coefficients $T_{1,2} = t_{1,2}^2$. Here R, T are the intensity coefficients and r, t the field coefficients. This system is sketched in Fig. 2.4.

For now, we assume a plane wave travelling along the optical axis z given by

$$\vec{E} = Ee^{i(kz-\omega t)} \tag{2.19}$$

We further assume no losses, *i.e.*, $R + T = 1$, and describe the light with its wave vector $\vec{k}$, with $|k| = k = 2\pi/\lambda = \omega/c$, where λ is the wavelength, ω the angular frequency and c the speed of light.

We can now derive a characteristic matrix, M_{Cav}, that relates the electric field components E_i, as defined in Fig. 2.4, as follows:

$$\begin{pmatrix} E_2 \\ E_3 \end{pmatrix} = M_{cav} \cdot \begin{pmatrix} E_1 \\ E_4 \end{pmatrix} \tag{2.20}$$

We assume that our cavity is only pumped from one side and ignore vacuum fluctuations, so we set $E_3 = 0$.

We require three constituent matrices to calculate M_{cav}, one for each mirror and one for the space of length L_{Cav} in between. The travel over L_{Cav} is described by the well known characteristic matrix for translation in a homogeneous medium. The ones describing the mirrors are given by the characteristic matrices for reflection/transmission at a flat interface.

$$M_{mir,i} = \frac{i}{t_i}\begin{pmatrix} -1 & r_i \\ -r_i & 1 \end{pmatrix}, \qquad M_{L_{Cav}} = \begin{pmatrix} e^{ikL_{Cav}} & 0 \\ 0 & e^{-ikL_{Cav}} \end{pmatrix} \tag{2.21}$$

Note that k in $M_{L_{Cav}}$ has to be adjusted for the refractive index n of the medium, but we assume an empty cavity here and hence $n = 1$.

The matrix describing the cavity is then given by the product of these matrices $M_{cav} = M_{mir,2} \cdot M_{L_{Cav}} \cdot M_{mir,1}$, resulting in

$$M_{cav} = -\frac{1}{t_1 t_2}\begin{pmatrix} e^{i\phi} - r_1 r_2 e^{-i\phi} & -r_2 e^{i\phi} + r_1 e^{-i\phi} \\ r_1 e^{i\phi} - r_2 e^{-i\phi} & -r_1 r_2 e^{i\phi} + e^{-i\phi} \end{pmatrix} \tag{2.22}$$

where we defined $\phi = kL_{Cav}$, the phase picked up when traversing the cavity.

With this characteristic matrix, we can now calculate the reflection and transmission coefficients of the cavity, given by the ratios $C_r = \frac{E_4}{E_1}$ and $C_t = \frac{E_2}{E_1}$ according to Eq. 2.20.

Since we are interested in the reflected/transmitted power, we evaluate $|E_i|^2$ to obtain the corresponding coefficients $C_{R,T}$ and express the results in terms of R, T rather than r, t.

$$C_R = \frac{(R_1 - R_2)^2 + 4\sqrt{R_1 R_2}\sin^2(\phi)}{(1 - R_1 R_2)^2 + 4\sqrt{R_1 R_2}\sin^2(\phi)} \tag{2.23}$$

$$C_T = \frac{T_1 T_2}{(1 - R_1 R_2)^2 + 4\sqrt{R_1 R_2}\sin^2(\phi)} \tag{2.24}$$

We can now plot these two coefficients as a function of ϕ, which corresponds to the very common procedure of scanning either the laser wavelength λ or the cavity length L_{Cav} to obtain the cavity spectrum in reflection/transmission, as shown in Fig. 2.5.

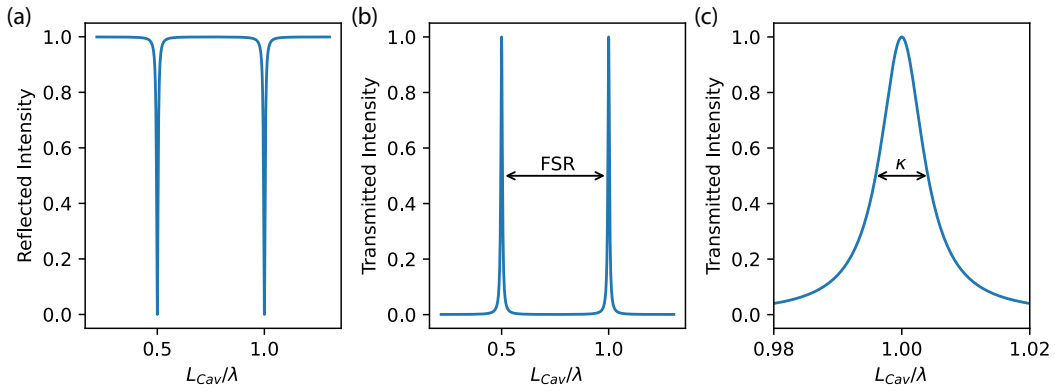

FIGURE 2.5: Normalized cavity spectrum in reflection (a) and transmission (b) when tuning the cavity length L_{Cav}. (c) shows a zoom of (b) to better visualize the line shape as well as the FWHM corresponding to κ. For these plots, we assume a critically coupled cavity with mirror reflectivities of $R_1 = R_2 = 0.95$.

We can also find a similar expression for the power circulating in the cavity, by comparing the field before and after the first mirror.

$$C_{cav} = \frac{T_1}{(1 - R_1 R_2)^2 + 4\sqrt{R_1 R_2}\sin^2(\phi)} \tag{2.25}$$

Note that here and in the following, we will assume a critically coupled cavity, *i.e.*, a cavity where the mirrors have the same reflectivity $R_1 = R_2$.

It is useful to introduce some quantities often employed to characterize optical cavities. The distance between the resonances in a cavity spectrum, as seen in Fig. 2.5 (b), is called the free spectral range and is given by

$$\omega_{FSR} = \frac{\pi c}{L_{Cav}} \tag{2.26}$$

The full width at half maximum (FWHM) of a cavity resonance can be extracted from the formulas above to give the cavity linewidth κ, as depicted in Fig. 2.5 (c),

$$\kappa = \frac{2c}{L_{Cav}} \sin^{-1}\left(\frac{1 - \sqrt{R_1 R_2}}{2\sqrt[4]{R_1 R_2}}\right) \tag{2.27}$$

And closely related to these quantities, the finesse of the cavity is defined as

$$\mathcal{F} = \frac{\omega_{FSR}}{\kappa} \tag{2.28}$$

$\mathcal{F}$ is a figure of merit often used since it is directly related to the losses of the optical resonator, the higher $\mathcal{F}$, the lower the losses.

Since we will work with high finesse cavities, implying high mirror reflectivities $R_1, R_2 \approx 1$ and thus $R_1, R_2 \gg T_1, T_2$, we can simplify these expressions as follows:

$$\kappa \approx \frac{c}{L_{Cav}}(1 - \sqrt{R_1 R_2}), \quad \mathcal{F} \approx \frac{\pi}{1 - \sqrt{R_1 R_2}} \tag{2.29}$$

This allows us to estimate $\mathcal{F}$ knowing nothing about the cavity but the mirror reflectivities.

If we further assume that we will be working only slightly detuned around a resonance of the cavity, we can simplify the intensity coefficients and express them in terms of $\Delta = \omega - \omega_{res} \ll \omega_{FSR}$, with ω_{res} being the frequency of said resonance:

$$C_T = \frac{1}{1 + \left(\frac{\Delta}{\kappa/2}\right)^2}, \quad C_R = 1 - \frac{1}{1 + \left(\frac{\Delta}{\kappa/2}\right)^2}, \quad C_{cav} = \frac{\mathcal{F}}{\pi} \frac{1}{1 + \left(\frac{\Delta}{\kappa/2}\right)^2} \tag{2.30}$$

Now the typical nature of a cavity spectrum becomes obvious when looking at the expressions above. A cavity resonance in transmission is simply a Lorentzian peak, while in reflection, it is a dip. The circulating power in the cavity is the same as the transmitted power, except for an additional amplification proportional to $\mathcal{F}$.

2.2.1 Transverse mode profile

So far, we have found a simple description of the cavity spectra and resonance behavior regarding its longitudinal modes. To arrive at a more realistic description of the cavity, we have to go beyond the simple plane wave model and consider the electromagnetic field in all three dimensions. A detailed discussion regarding this section and section 2.2.2 can be found in [131, 193].

We start with the general scalar wave equation

$$[\nabla^2 + k^2]E(x, y, z) = 0 \tag{2.31}$$

When describing laser beams or cavity modes, it is useful to work with the paraxial approximation of this equation. We again assume a beam that travels along z, this implies that we can factor out a term e^{ikz}, that describes the dominant (fast) sinusoidal evolution along z, resulting in

$$E(x, y, z) = u(x, y, z)e^{ikz} \tag{2.32}$$

We further assume that the remaining z-dependence in $u(x, y, z)$ is slow and $\frac{\partial^2}{\partial z^2}u(x, y, z)$ can be neglected. This then leads to the well known paraxial wave equation

$$[\nabla_\perp^2 - 2ik\frac{\partial}{\partial z}]u(x, y, z) = 0 \tag{2.33}$$

where $\nabla_\perp^2$ is the transverse Laplace operator.

One simple solution to this wave equation, which already brings us close to our final description, is a paraxial wave with spherical wavefronts originating from a point source:

$$u(x, y, z) = \frac{1}{R(z)} e^{-i\frac{k}{2R(z)}(\Delta x^2 + \Delta y^2)} \tag{2.34}$$

Here $\Delta x = x - x_0$, $\Delta y = y - y_0$ and $R(z) = z - z_0$ is the radius of curvature. From this point on we will choose our coordinate system so that $x_0, y_0, z_0 = 0$. The main problem with this solution is that the power does not fall off in the transverse direction, and thus it is not a realistic waveform.

All we need to do to convert this into a useful solution, that can be employed to model the fundamental mode of Fabry-Perot resonators and laser beams in general, is to assume an additional imaginary part for the Radius of curvature $R(z) \rightarrow q(z) = z + iz_R$. This will give us the typical Gaussian beam. Note that we renamed the radius of curvature here since it now represents the commonly used complex beam parameter $q(z)$. z_R is the Rayleigh range, signifying the length from the beam waist ω_0 after which the cross section of the beam has doubled, or the waist has grown to $\omega(z) = \sqrt{2}\omega_0$:

$$z_R = \frac{\pi\omega_0}{\lambda} \tag{2.35}$$

The complex beam parameter is often also given in the form

$$\frac{1}{q(z)} = \frac{1}{R(z)} - i\frac{\lambda}{\pi\omega(z)^2} \tag{2.36}$$

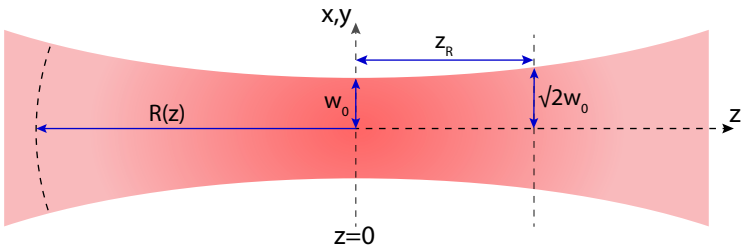

FIGURE 2.6: Gaussian beam expanding from its waist at $z = 0$, including the geometrical definitions necessary to determine the complex beam parameter $q(z)$.

The expression for a Gaussian beam, which can be completely characterize by its complex beam parameter $q(z)$, is then given by

$$u(x,y,z) = \frac{1}{q(z)} e^{-ik\frac{x^2+y^2}{2R(z)} - \frac{x^2+y^2}{\omega(z)}} \tag{2.37}$$

We can also express the radius of curvature and beam waist in terms of the Rayleigh range as follows:

$$R(z) = z\left(1 + \frac{z_R^2}{z^2}\right) \tag{2.38}$$

$$\omega(z) = \omega_0\sqrt{1 + \left(\frac{z^2}{z_R^2}\right)} \tag{2.39}$$

The radial ($r^2 = x^2 + y^2$) intensity profile of a Gaussian beam with power P is then given by

$$I(r,z) = \frac{2P}{\pi\omega(z)^2} e^{-\frac{2r^2}{\omega(z)^2}} \tag{2.40}$$

which is important when considering clipping losses, that can occur when the beam travels through an aperture of radius a

$$I_{apt}(a,z) = \frac{2P}{\pi\omega(z)^2}\int_0^a 2\pi r e^{-\frac{2r^2}{\omega(z)^2}} dr = P(1 - e^{-\frac{2a^2}{\omega(z)^2}}) \tag{2.41}$$

While the description above represents a good model for the fundamental mode of a cavity, which is most commonly employed in experiments, a more complete description needs to include higher order modes. Here we will focus on the Hermit-Gaussian modes, which form a complete set of orthogonal functions that can be used to expand any paraxial beam.

It is first useful to introduce a phase into our description by rewriting

$$\frac{i}{q(z)} = \frac{i}{R(z)} + \frac{\lambda}{\pi\omega(z)^2} = \frac{1}{|q(z)|}e^{\phi_G(z)} \tag{2.42}$$

where $\phi_G(z) = \tan^{-1}\left(\frac{z}{z_R}\right)$ is called the Guoy phase.

We then note that due to the symmetry in x and y, $u(x,z) \hat{=} u(y,z)$. It is thus sufficient to give an expression along one transverse dimension $u(x,z)$, the overall three dimensional expression is then retrieved by taking product of $u(x,z)$ and $u(y,z)$. The general expression for any Hermit-Gaussian mode is

$$u_n(x,z) = \left(\frac{2}{\pi}\right)^{1/4}\sqrt{\frac{1}{2^n n!\omega(z)}}H_n\left(\frac{\sqrt{2}x}{\omega(z)}\right)e^{-i\frac{kx^2}{2R(z)}-\frac{x^2}{\omega(z)^2}}e^{-i\phi_{G,n}(z)} \tag{2.43}$$

where $\phi_{G,n}(z) = (n+\frac{1}{2})\phi_G(z)$ is the Guoy phase for higher order modes and H_n are the Hermit polynomials. These Hermit-Gauss modes are not only useful because they can expand any paraxial wave, but also because the individual functions represent the transverse intensity profiles observed in typical real life Fabry-Perot cavities. Naturally, they contain the simple Gaussian beam introduced in Eq. 2.37 as the lowest order mode $u_{00}(x,y,z)$.

2.2.2 Gaussian beams in cavities and cavity stability

We can now combine the notions introduced in the two previous sections to describe a more realistic Fabry-Perot cavity. Since a Gaussian beam is characterized by its complex beam parameter $q(z)$, we can use the ABCD-law

$$q_2 = \frac{Aq_1 + B}{cq_1 + D} \tag{2.44}$$

to relate $q_1(z)$ before a system to $q_2(z)$ after that system. A, B, C and D are the entries of the ray transfer matrix (or ABCD-matrix) $\mathcal{M}$ of the system, not to be confused with the characteristic matrices M used before.

We are considering the round trip matrix of the cavity and assume that $q_1(z) = q_2(z) = q(z)$, since we are looking for the eigenmodes of the cavity, which are preserved after a roundtrip per definition. Some algebraic manipulation of Eq. 2.44, together with the fact that $det(\mathcal{M}) = 1$ for any ray transfer matrix where the refractive index n does not change between input and output, yields

$$\frac{1}{q} = \frac{1}{2B}\left[D - A \pm 2\sqrt{\left(\frac{A+D}{2}\right)^2 - 1}\right] \tag{2.45}$$

Remembering the definition given in Eq. 2.36, we notice that to have a corresponding imaginary part that represents a real value for ω_0, we require that

$$\left(\frac{A+D}{2}\right)^2 - 1 < 1 \tag{2.46}$$

The round trip matrix can be calculated by multiplying the ray transfer matrices $\mathcal{M}_{mir,i} = \left(\begin{smallmatrix} 1 & 0 \\ -2/R_{C,i} & 1 \end{smallmatrix}\right)$ for the two curved mirrors with radius of curvature $R_{C,i}$ and the one representing the travel over the cavity length $\mathcal{M}_{L_{Cav}} = \left(\begin{smallmatrix} 1 & L_{Cav} \\ 0 & 1 \end{smallmatrix}\right)$ twice, resulting in

$$\mathcal{M} = \begin{pmatrix} 1 - \frac{2L_{Cav}}{R_{C,2}} & -\frac{2}{R_{C,1}}\left(1 - \frac{L_{Cav}}{R_{C,2}}\right) \\ -\frac{2}{R_{C,1}} - \frac{2}{R_{C,2}} + \frac{4L_{Cav}}{R_{C,1}R_{C,2}} & 1 - \frac{4L_{Cav}}{R_{C,1}} - \frac{4L_{Cav}}{R_{C,2}} + \frac{4L_{Cav}^2}{R_{C,1}R_{C,2}} \end{pmatrix} \tag{2.47}$$

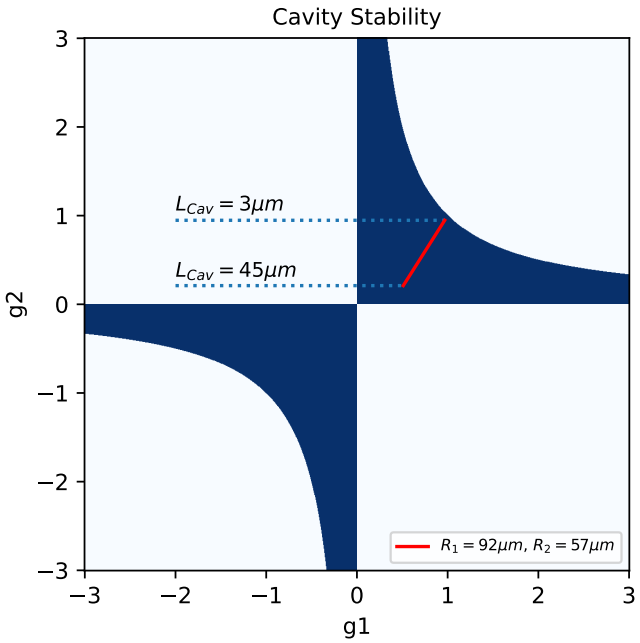

FIGURE 2.7: Stability diagram of an optical cavity. The dark blue areas are combinations of g-factors that lead to a stable cavity according to Eq. 2.49. The red line shows g_1g_2 as a function of L_{Cav} for the radii of curvature of the FFPC we will use in later chapters.

It is common to define the so called g-factors at this point, which represent the geometrical properties of the cavity

$$\frac{1}{2}\left(\frac{A+D}{2}+1\right) = \left(1 - \frac{L_{Cav}}{R_{C,1}}\right)\left(1 - \frac{L_{Cav}}{R_{C,2}}\right) = g_1g_2 = g \tag{2.48}$$

Combining this with Eq. 2.46, we can obtain the typical stability criterion for cavities, which only depends on the radii of curvature of the two mirrors and the cavity length

$$0 \leq g_1g_2 \leq 1 \tag{2.49}$$

These g-factors can also be used to express the size of the cavity waist, with only L_{Cav} and λ as additional parameters,

$$\omega_0^2 = \frac{L_{Cav}\lambda}{\pi}\sqrt{\frac{g_1g_2(1-g_1g_2)}{(g_1+g_2-2g_1g_2)^2}} \tag{2.50}$$

as well as the beam waist at the end of the cavity (*i.e.* at the mirror interfaces),

$$\omega_i^2 = \frac{L_{Cav}\lambda}{\pi}\sqrt{\frac{g_i}{g_j(1-g_1g_2)}} \tag{2.51}$$

where $i, j = 1, 2$ and $i \neq j$. This gives the necessary quantities to predict clipping losses together with Eq. 2.41.

In Fig. 2.7 we show the cavity stability as a function of the g-factors. For example, a cavity made of two planar mirrors, implying $R_{C,1}, R_{C,2} \to \infty$, would be situated in the origin of the graph. While this point is stable according to Eq. 2.49, in practice, such cavities on the edge of the blue stable region in Fig. 2.7 become unstable due to the smallest deviations in cavity parameters. It is easy to imagine that a small deviation from perfect parallel alignment of the two mirror surfaces in such a planar cavity would lead to a loss of confinement of the light in the cavity. The red line in Fig. 2.7 represents g-factors for the radii of curvature and cavity lengths corresponding to our experimental parameters, lying well within the stable region.

Finally, we have to take into consideration the phase that a beam picks up when travelling through the cavity. When combining the solutions for the Hermit-Gaussian modes into the three dimensional representation $u_{mn}(x, y, z) = u_m(x, z)u_n(y, z)$, we get a Guoy phase of $\phi_{mn} = (m + n + 1)\phi_G$, which can be expressed in terms of the g-factor as $\phi_G = 2\cos^{-1}(\sqrt{g})$ [131], resulting in a phase

$$\phi = kL_{Cav} - (m + n + 1)\phi_G \tag{2.52}$$

Because of the dependency on the mode order, this leads to a separation of higher order modes in the cavity spectrum.

2.2.3 Pound-Drever-Hall locking scheme

It is often necessary to lock the wavelength of a laser to a cavity resonance or vice versa, to maintain a stable signal for measurements. When locking on resonance, a drop in the cavity signal does not reveal in which direction the system needs to be corrected due to the symmetry of the cavity transmission/reflection. A solution is to use the derivative of the cavity signal instead, which is commonly achieved following the Pound-Drever-Hall technique [132, 133]. This procedure starts with a phase modulation of the input signal

$$\vec{E}_{in} = E_{in} e^{i(\omega t + \beta \sin(\omega_{mod} t))} \tag{2.53}$$

This phase modulation will result in sidebands spaced by the modulation frequency ω_{mod} from the main carrier at ω. We will assume that the power in the sidebands P_s is much weaker than the power in the main carrier P_c, with $P_{in} = P_c + 2P_s$. This means that we are using a small modulation amplitude β. With C_r as defined in section 2.2, the reflected power is then of the form

$$\begin{aligned} P_r(t) = P_{DC} + (\text{terms in } 2\omega_{mod}) + 2\sqrt{P_c P_s}[\\ \mathrm{Re}(C_r(\omega)C_r^*(\omega + \omega_{mod}) - C_r^*(\omega)C_r(\omega - \omega_{mod}))\cos(\omega_{mod} t) + \\ \mathrm{Im}(C_r(\omega)C_r^*(\omega + \omega_{mod}) - C_r^*(\omega)C_r(\omega - \omega_{mod}))\sin(\omega_{mod} t)] \end{aligned} \tag{2.54}$$

Here P_{DC} is the part of the signal independent of ω_{mod}. By mixing with a signal $\sin(\omega_{mod} t + \phi_{mod})$ and low-pass filtering, we retain only the sine and cosine terms as down-mixed DC components. Further defining $\chi(\omega) = C_r(\omega)C_r^*(\omega + \omega_{mod}) - C_r^*(\omega)C_r(\omega - \omega_{mod})$ we will be left with an error signal

$$\epsilon(\omega, \phi_{mod}) \propto \mathrm{Re}(\chi(\omega))\sin(\phi_{mod}) + \mathrm{Im}(\chi(\omega))\cos(\phi_{mod}) \tag{2.55}$$

With appropriate choice of ϕ_{mod}, we can measure each quadrature of $\chi(\omega)$. The common Pound-Drever-Hall error signal is retrieved for $\phi_{mod} = 0$.

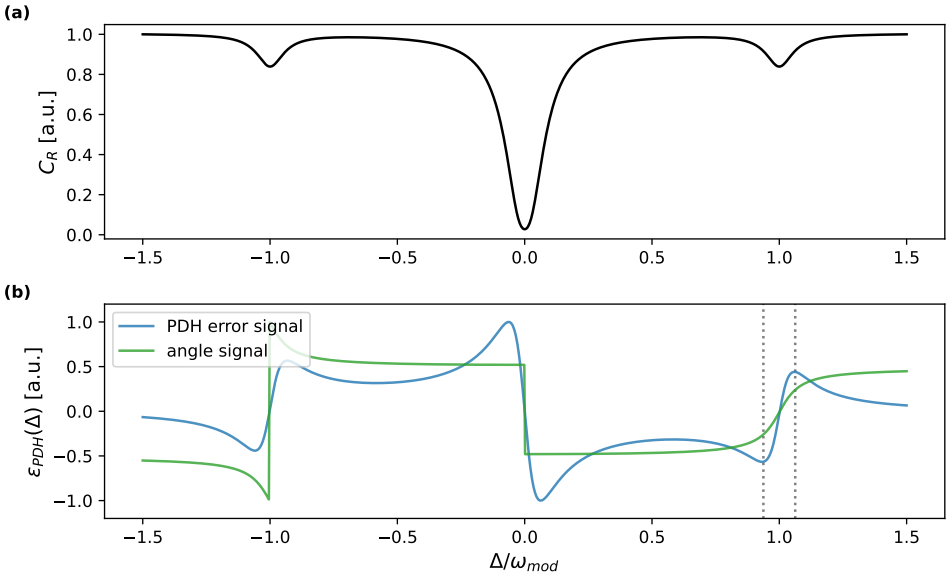

FIGURE 2.8: Reflected cavity signal including the sidebands at $\pm\omega_{mod}$ in (a). In (b) we show both the regular PDH error signal and the angle signal, which in this case can be used to lock at the upper sideband. The dotted lines show $\pm\kappa/2$ around the upper sideband, representing the limits of the lock range of the regular PDH error signal.

In Fig. 2.8 (a) we show the reflected cavity signal with sidebands at the modulation frequency as reference. In (b), we show the PDH error signal. In particular, the approximately linear regime around resonance ($\Delta = 0$) is used when locking the main carrier to the cavity. But the Pound-Drever-Hall error signal is also useful for locking around the areas corresponding to the sidebands at $\pm\omega_{mod}$. It is also worth noting that the entire error signal can be inverted by shifting ϕ_{mod} by π.

Instead of this PDH error signal, it is also possible to use the angle of the two quadratures X and Y measured by the LI-A as an error signal [198]

$$\epsilon_{PDH,\phi} = arg(X + iY)/\pi \tag{2.56}$$

For an appropriate choice of phase in the LI-A, this gives an error signal as shown in Fig. 2.8 (b) in green, which can be used to lock on the upper sideband. Due to the discontinuity around the main peak, it can only be used on the sidebands. A shift of the phase in the LI-A by π flips the signal and allows to lock on the lower sideband instead. There are two main advantages of this type of error signal over the regular PDH error signal. First, there are no turning points of the signal that limit the locking range. These turning points are the maxima of the regular PDH error signal that occur at $\kappa/2$, highlighted by the dotted lines in Fig. 2.8 (b). Second, this error signal does not scale with the laser power. This can be especially useful when varying experimental parameters since an adjustment of the lock settings can be avoided.

2.3 MIM Optomechanics

We now begin with the description of the combined MIM-FFPC system. To model what happens when we put a membrane in the middle of our cavity we use the same approach as with the empty cavity, we simply have to add a characteristic matrix M_m that describes the membrane, as in [66, 197, 203, 134, 135].

We assume that this membrane is positioned at z_m from the middle of the cavity and has a thickness of d_m, as sketched in Fig. 2.9. This results in two sub cavities, divided by the membrane, of lengths $L_{Cav,1} = \frac{L_{Cav}}{2} + z_m - \frac{d_m}{2}$ and $L_{Cav,2} = \frac{L_{Cav}}{2} - z_m - \frac{d_m}{2}$.

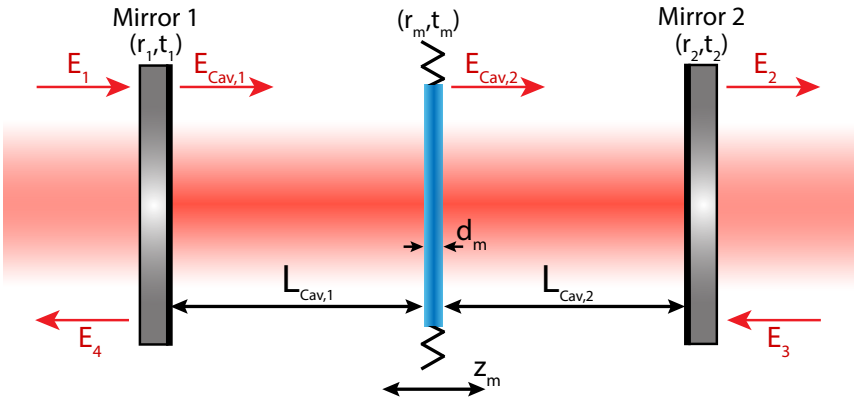

FIGURE 2.9: Extension of our previous model, shown in Fig. 2.4, to a MIM system. The cavity is now split into two sub cavities by a membrane placed at position z_m from the middle. Similarly to the mirrors, we characterize this membrane by its reflection and transmission coefficients (r_m, t_m) as well as its thickness d_m.

We can describe the membrane in terms of its reflection and transmission coefficients with a single characteristic matrix[2] in the form

$$M_m = \frac{1}{t_m}\begin{pmatrix} t_m^2 - r_m^2 & r_m \\ -r_m & 1 \end{pmatrix} \tag{2.57}$$

where we assumed that $t_m^2 + r_m^2 = 1$ [203]. The reflection and transmission coefficients of a lossless membrane with refractive index n_m are

$$r_m = \frac{(1-n_m)^2 \sin(\phi_m)}{2in_m \cos(\phi_m) + (1+n_m^2)\sin(\phi_m)} \tag{2.58}$$

$$t_m = \frac{2in_m}{2in_m \cos(\phi_m) + (1+n_m^2)\sin(\phi_m)} \tag{2.59}$$

where $\phi_m = n_m k d_m$ is the phase picked up when travelling through the membrane. The matrix describing the entire system is then given by

$$M_{MIM} = M_{mir,2} \cdot M_{L_{Cav,2}} \cdot M_m \cdot M_{L_{Cav,1}} \cdot M_{mir,1} \tag{2.60}$$

[2]This expression is equivalent to a product of matrices as in Eq. 2.21, to account for the two interfaces and the membrane medium. For the two interfaces $r_1 = r_2 = \frac{1-n_m}{1+n_m}$, $t_1 = \frac{2}{1+n_m}$ and $t_2 = \frac{2n_m}{1+n_m}$.

As before, we can find the overall reflection and transmission coefficients C_R, C_T of our MIM-cavity system with this matrix. The resulting spectra are plotted in Fig. 2.10 as a function of the cavity length and the position of the membrane.

The addition of the membrane shifts the resonance length (frequency) of the cavity compared to the empty cavity case $L_{res} \rightarrow L_{res} + \delta L$. For $\phi_m \in [0, \pi/2]$, and assuming the mirror reflectivities are $r = r_1 = r_2$, this perturbation can be expressed as [203, 134]

$$\delta L = \frac{\lambda}{2\pi}\left[\cos^{-1}\left((-1)^{N+1}\cos(2kz_m)\frac{1+r^2}{2r}|r_m|\right) - \phi_r\right] \tag{2.61}$$

where N is the longitudinal mode order of the cavity and ϕ_r is the phase associated with r_m:

$$\phi_r = \pi - tan^{-1}\left[\frac{2n_m\cos\phi_m}{(1+n_m^2)\sin\phi_m}\right] \tag{2.62}$$

The overall resonance condition in terms of length and frequency is then given by

$$L_{res,N} = \frac{N\lambda}{2} + \delta L, \qquad \omega_{res,N} = L_{res,N}\frac{2\omega_{FSR}}{\lambda} \tag{2.63}$$

Note that depending on the definition of the coordinate system the simulated cavity spectrum can show asymmetries. The spectrum shown in Fig. 2.10 (a) assumes that both $L_{Cav,1}$ and $L_{Cav,2}$ are changed by the same amount, leading to a symmetric increase of L_{Cav} around the central position where the membrane is located. This coordinate system is simple in theory but requires a more elaborate experimental setup, in which both cavity mirrors can be tuned in a synchronized way. A more realistic scenario for us is given in Fig. 2.10 (b), where only the left mirror is moved leading to a change of only $L_{Cav,1}$, while the membrane is detuned from its initial position by Δz_m, affecting both sub-cavities. Assuming that the first mirror is positioned at $z = 0$, the membrane at z_m and the second mirror at $z = L_{Cav}$, the two sub-cavity lengths are then given by

$$\begin{aligned} L_{Cav,1} &= z_m - \Delta L_{Cav,1} + \Delta z_m - d_m/2 \\ L_{Cav,2} &= L_{Cav} - z_m - \Delta z_m - d_m/2 \end{aligned}$$

Similar to Eq. 2.61, the perturbation of a thin membrane on the cavity resonance length in this reference frame can be approximated as follows [134]:

$$\delta L = \frac{\lambda}{2\pi}\tan^{-}1\left[\frac{\cos(\phi_r) + |r_m|\cos(2kz_m)}{\sin(\phi_r) - |r_m|\sin(2kz_m)}\right] \tag{2.65}$$

Both analytical expressions are also plotted in Fig. 2.10, matching the simulations.

It is common to quantify the effect of the membrane on ω_{res} with the frequency pull parameter, which is related to the single-photon optomechanical coupling strength g_0 through the zero point motion of the mechanical resonator

$$G = \frac{\partial}{\partial z_m}\omega_{res,N} = \frac{g_0}{x_{zpm}} \tag{2.66}$$

In addition, the effective optomechanical coupling strength, taking into account higher photon numbers n_p circulating in the cavity, is then

$$g = g_0\sqrt{n_p} \tag{2.67}$$

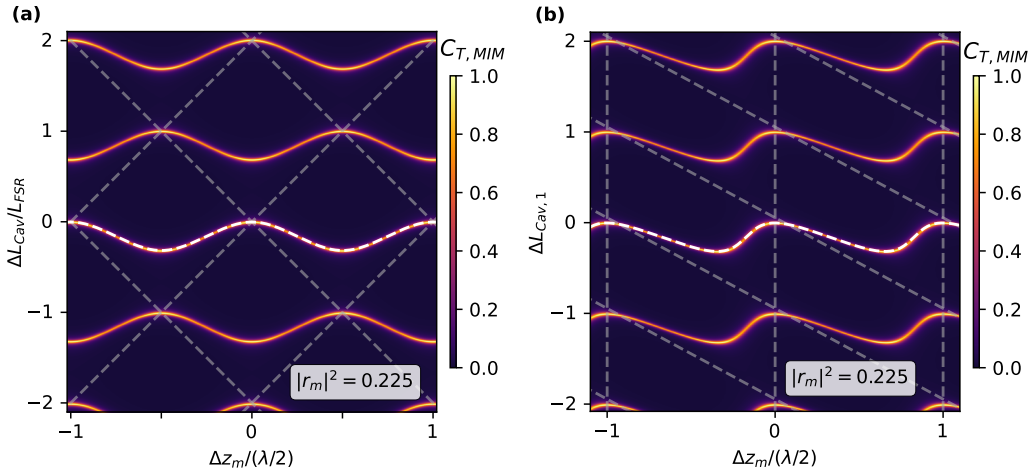

FIGURE 2.10: Transmission of a MIM system as a function of the detuning of the cavity length and the membrane position. Dashed grey lines show the case for unity r_m, resulting in two separated sub cavities. We used $R_1 = R_2 = 0.95$ and r_m, t_m are modelled for a 50 nm thick hBN membrane. White dashed lines show the analytical expressions defined in Eq. 2.61 and 2.65

2.3.1 Losses in a MIM-FFPC system

As a final step, we have to introduce losses to the description of our system. One immediate consequence of losses is that the R_i, T_i of our mirrors do not add up to unity anymore, instead we will now assume

$$R_i = 1 - T_i - L_i \tag{2.68}$$

where L_i contains contributions such as mirror absorption, but also the Gaussian clipping losses discussed in section 2.2.1. It is useful to rewrite Eq. 2.29 with this new definition, using the approximation $\sqrt{1+x} \approx 1 + x/2$ for $x \ll 1$ we get

$$\mathcal{F} \approx \frac{2\pi}{T_1 + T_2 + L_1 + L_2} \tag{2.69}$$

Resonance lineshape of a FFPC in reflection

We now want to discuss two less transparent consequences of imperfections in our system. First, we discuss a model for FFPC's that includes mode matching between the fiber modes and the modes of the cavity itself, taking into account coupling losses. In the case of a standard free-space cavity, mode matching can be adjusted with optics and mostly affects the contrast of the Lorentzian shaped cavity signal. In the case of an FFPC, the mode-matching is partially determined by the fibers and the mirror geometries, while also depending on the cavity alignment. Furthermore, the reflected beam in a FFPC has to be matched to the input fiber mode once again, leading to a modification of the reflected lineshape compared to standard cavities in addition to the changes in contrast.

The reflected power of a FFPC under these considerations can be described by a model including a dispersive term as described in [136],

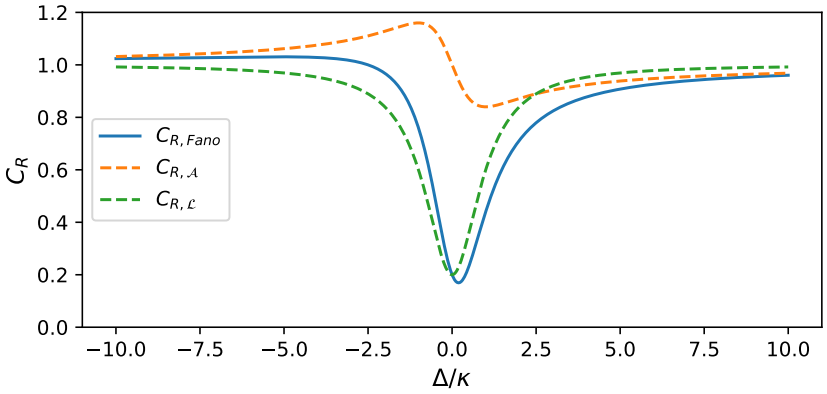

FIGURE 2.11: Reflected FFPC signal as a function of Δ according to Eq. 2.70, as well as the separated Lorentzian (green) and dispersive (orange) parts of the model.

$$C_{R,Fano} = \eta_r - \eta_{\mathcal{L}} \left(\frac{1}{1 + \left(\frac{2\Delta}{\kappa}\right)^2} - \mathcal{A} \frac{\frac{2\Delta}{\kappa}}{1 + \left(\frac{2\Delta}{\kappa}\right)^2} \right) \tag{2.70}$$

where η_r is an alignment independent reflected background, $\eta_{\mathcal{L}}$ is the amplitude of the Lorentzian dip and $\mathcal{A}$ is the amplitude of the dispersive part. C_T and C_{cav}, on the other hand, are not modified in lineshape by mode-matching or alignment, the signal is only affected in amplitude, which can be handled with a simple pre-factor.

The resulting line shape of $C_{R,Fano}$ is shown in Fig. 2.11 together with its contributions corresponding to the regular Lorentzian lineshape, matching C_R from before with reduced contrast ($\eta_{\mathcal{L}} < 1$), and the dispersive part which causes the Fano lineshape.

Scattering losses

Next, we consider losses due to the membrane. In the whole MIM system, the membrane is expected to lead to significant losses due to scattering channels out of the cavity mode. This can be caused by misalignment but also by surface roughness of the mechanical oscillator. As long as one does not care about additional implications, such as heating of the membrane, one can also model absorption this way, since it simply constitutes another loss channel out of the regular cavity mode.

We again employ the transfer matrix formalism to model this loss channel by introducing a beamsplitter term into our membrane, which models the part of the light that is deflected out of the cavity mode [203, 193]. We now have to consider additional input and output directions, which increases the dimensions of our matrices from (2×2) to (4×4).

We sketch the MIM system in Fig. 2.12, but this time with the additional channels corresponding to the two beamsplitters, one for each direction of propagation.

$$\begin{pmatrix} E_2 \\ 0 \\ E_{S1} \\ E_{S2} \end{pmatrix} = M_{(4\times4)} \begin{pmatrix} E_1 \\ E_4 \\ 0 \\ 0 \end{pmatrix} \tag{2.71}$$

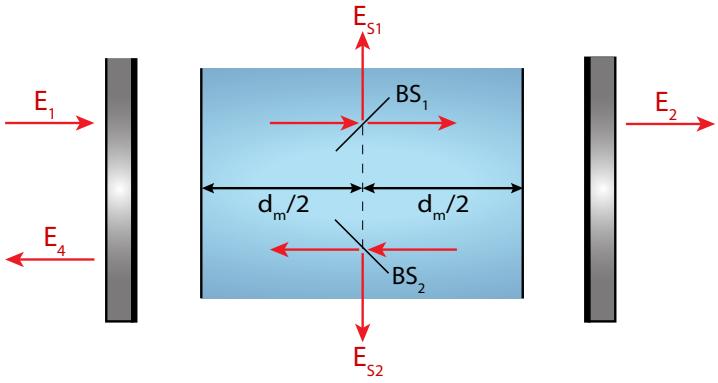

FIGURE 2.12: Membrane modelled as a beamsplitter to account for scattering losses. We only consider channels corresponding to output channels (*i.e.* losses) and no input channels due to the beamsplitters, leading to two new channels E_{S1} and E_{S2}.

We again assumed that the cavity is only pumped from one side and that the beamsplitters in the membrane only couple light from the cavity mode to the free space mode, and not the other way around. Any (2×2) matrix $M_{(2\times2)}$ in Eq. 2.60 that we defined before, which is not M_m, will be converted into a (4×4) matrix as follows:

$$M_{(4\times4)} = \begin{pmatrix} M_{(2\times2)} & \\ & \mathbb{I}_{(2\times2)} \end{pmatrix} \tag{2.72}$$

Here $\mathbb{I}$ is the identity-matrix, leading to no interaction with the free-space channels. This means that apart from M_m, the formalism discussed so far is still applicable. $M_{m,(4\times4)}$ will now include the characteristic matrix for a beamsplitter with transmission coefficient $T_{bs} = |t_{bs}|^2$ and reflection coefficient $R_{bs} = |r_{bs}|^2$

$$M_{bs,(4\times4)} = \begin{pmatrix} t_{bs} & 0 & -r_{bs} & 0 \\ 0 & 1/t_{bs} & 0 & r_{bs}/t_{bs} \\ r_{bs} & 0 & t_{bs} & 0 \\ 0 & r_{bs}/t_{bs} & 0 & 1/t_{bs} \end{pmatrix} \tag{2.73}$$

The membrane, as shown in Fig. 2.12, then is made of two flat interfaces, translation along two lengths of $d_m/2$, which are separated by a beamsplitter in the middle, leading to

$$M_{m,(4\times4)} = M_{2,(4\times4)} \cdot M_{d_m/2,(4\times4)} \cdot M_{bs,(4\times4)} \cdot M_{d_m/2,(4\times4)} \cdot M_{1,(4\times4)} \tag{2.74}$$

The matrices needed in addition to $M_{bs,(4\times4)}$ to calculate $M_{m,(4\times4)}$ are again converted as in Eq. 2.72, and we can reuse the definitions in Eq. 2.21 for the (2×2) matrices (see [2]).

We can now calculate a characteristic matrix including scattering losses $M_{MIM,sctr}$ for the entire system as in Eq. 2.60 and retrieve the transmission and reflection coefficients of the MIM system as before. We also define the scattering coefficient of the system, corresponding to the new loss channels, as

$$C_{s,MIM} = \frac{E_{S1}}{E_1} + \frac{E_{S2}}{E_1} = \frac{M_{31}M_{22} - M_{32}M_{21}}{M_{22}} + \frac{M_{41}M_{22} - M_{42}M_{21}}{M_{22}} \tag{2.75}$$

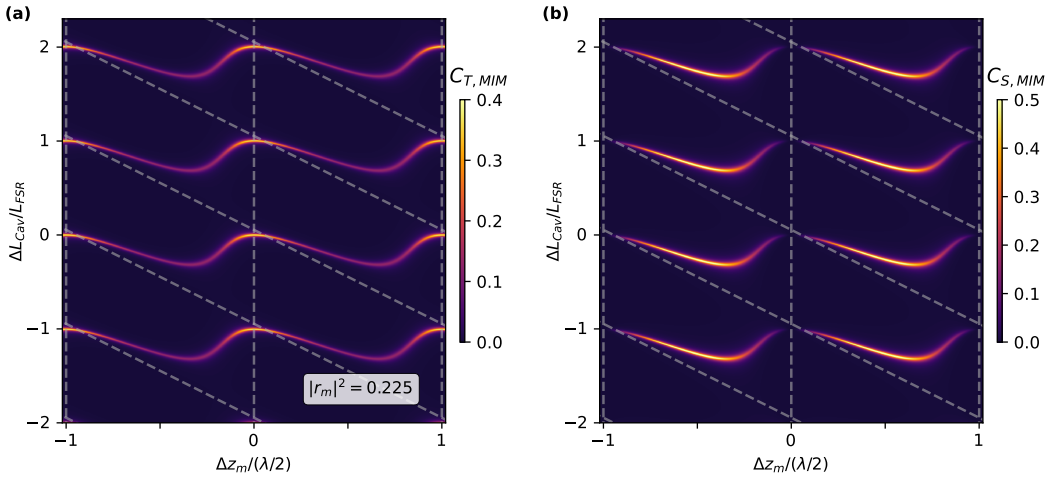

FIGURE 2.13: Cavity Transmission as a function of cavity length detuning and membrane position, including scattering losses in the membrane (a). Corresponding scattering parameter (b). We used $R_1 = R_2 = 0.95$ and $R_{bs} = 0.03$, (r_m, t_m) are modelled for a 50 nm hBN membrane.

where M_{mn} are the entries of $M_{MIM,sctr}$.

Fig. 2.13 (a) shows the same cavity spectrum as Fig. 2.10 (b), but with the additional losses. We see that the losses are particularly pronounced when the membrane is away from a node of the cavity field, where a higher field is present inside the membrane. The scattering parameter plotted in Fig. 2.13 (b) shows a distinct asymmetry in intensity when comparing the left and right side of the cavity (anti) node, but the transmission signal appears more symmetric in this regard. This is an asymmetry in addition to the aforementioned tilt of the signal due to the fact that we only scan one mirror of the cavity. This can be explained with the fact that the cavity is pumped from only the left side and thus the cavity field in the two sub cavities of the MIM system are not equal. In this configuration, the field in the right sub-cavity is constant and the transmission signal is symmetric as a function of membrane position z_m. However, the same is not true for the left sub-cavity, which affects the scattering parameter. When the membrane is positioned to the left of the node of the cavity field, the field in the left sub-cavity is higher than in the right and vice versa [197, 203]. This leads to the observed asymmetry in the scattering parameter.

Since in Fig. 2.13 we have chosen a rather moderate mirror reflectivity for visibility of the signal, this plot does not give a quantitative idea about the impact of losses in our system caused by the membrane. To this end, we have plotted the maximum transmission, reflection and scattering coefficient of the MIM system as a function of beamsplitter losses in Fig. 2.14. Here, the mirror reflectivities are chosen to result in a finesse of 15000 for an empty cavity, similar to the reflective coating used in our experiments. We keep the membrane position fixed and vary the cavity length, corresponding to a typical cavity scan in an experiment. To illustrate the impact of the membrane position, we show curves representing three different membrane positions. Each position is represented by a different color in Fig. 2.14, the transmitted (reflected) signal is shown by a solid (dashed) line, while the scattered intensity is shown as a dotted line. In all cases, the scattered intensity is maximal for a moderate amount of beamsplitter losses, since for higher losses no significant field can build up in the cavity, and most of the light is reflected. For $z_m = 0$, the membrane is positioned on a node of the cavity field and the losses are minimal, as already visible

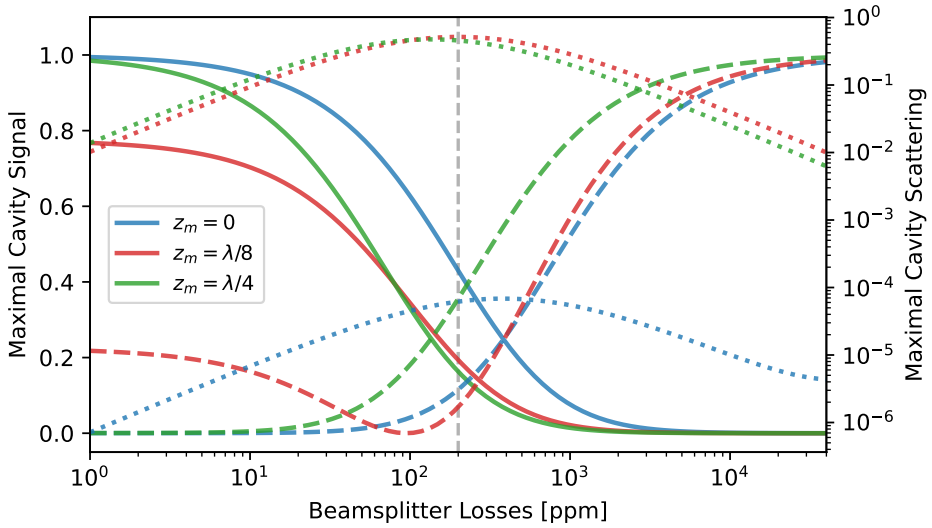

FIGURE 2.14: Impact of losses in a MIM system. The maximum cavity transmission is shown as a solid line, the reflected signal as a dashed line, and the scattering losses as a dotted line. $z_m = 0$ corresponds to the cavity node, while $z_m = \lambda/4$ corresponds to the anti-node. For these plots we used 200 ppm of mirror losses, to match the experimental parameters used in the measurements in this thesis, this level of losses is indicated by the vertical dashed line.

in Fig. 2.13. Further away from the node, for $z_m = \lambda/4$ and $z_m = \lambda/8$, the losses are significantly higher and the transmission signal is lost for smaller values of r_{bs}. Already for moderate losses, there is a clear impact on the observed cavity signal. But especially when overtaking the losses associated with the mirrors of 200 ppm, the signal quickly drops to zero, highlighting the importance of resonators made of low-loss materials in high finesse MIM systems.

2.3.2 Optomechanically induced transparency

In the resolved sideband regime of cavity optomechanics, where $\kappa \ll \omega_m$, the interaction between the cavity and the mechanical oscillator leads to observable sidebands spaced by ω_m. Due to the small dimensions of our FFPC, our system resides in the unresolved sideband regime, where $\kappa \gg \omega_m$. This means that the sidebands at ω_m are indistinguishable from the central cavity resonance peak, which is a prerequisite for many experimental protocols [18]. But even in this unresolved regime, where the cavity field reacts to the mechanical system quasi instantaneously, new experimental techniques are being developed [137–140] and strong interactions are observed [59]. One effect that allows us to observe the optomechanical interaction clearly in the cavity spectrum, and to characterize it even in the unresolved sideband regime, is optomechanically induced transparency (OMIT) [141, 142, 199, 143].

To develop a model for this dynamic optomechanical effect, we start with the general Hamiltonian of an optomechanical system [18]

$$\hat{\mathcal{H}}_{OM} = \hat{\mathcal{H}}_{Cav} + \hat{\mathcal{H}}_m + \hat{\mathcal{H}}_{int} + \hat{\mathcal{H}}_{in} \tag{2.76}$$

This Hamiltonian includes the contributions of the bare cavity and mechanical oscillator ($\hat{\mathcal{H}}_{Cav}$ and $\hat{\mathcal{H}}_m$), where $\hat{a}, \hat{a}^\dagger$ and $\hat{b}, \hat{b}^\dagger$ are the photonic and phononic ladder

operators respectively. We have also given $\hat{\mathcal{H}}_m$ in terms of the position and momentum operators $\hat{x}, \hat{p}$ as we will use this definition in the following derivation. $\hat{\mathcal{H}}_{int}$ accounts for the optomechanical coupling characterized by the single photon coupling strength g_0 as defined in the previous section. The classical input laser α_{in} is accounted for by the drive term $\hat{\mathcal{H}}_{in}$.

$$\begin{aligned}
\hat{\mathcal{H}}_{Cav} &= \hbar\omega_{cav}\hat{a}^\dagger\hat{a} \\
\hat{\mathcal{H}}_m &= \hbar\omega_{cav}\hat{b}^\dagger\hat{b} = \frac{1}{2m^*}\hat{p}^2 + \frac{1}{2}m^*\omega_m^2\hat{x}^2 \\
\hat{\mathcal{H}}_{int} &= -\hbar g_0\hat{a}^\dagger\hat{a}(\hat{b} + \hat{b}^\dagger) \\
\hat{\mathcal{H}}_{in} &= i\hbar\alpha_{in}(\hat{a} + \hat{a}^\dagger)
\end{aligned}$$

Moving forward, we consider the semi-classical limit in which we will assume that the involved quantities $(\hat{a}, \hat{p}, \hat{x})$ show small fluctuations around a steady state value. We now describe e.g. the cavity occupation by substituting the operators with $\alpha(t) = \overline{\alpha} + \delta\alpha(t)$, where $\overline{\alpha}$ is the steady-state value and $\delta\alpha$ is the smaller fluctuating term. This allows us to linearise the equations of motion as follows [18],

$$\begin{aligned}
\frac{\partial}{\partial t}\delta\alpha &= (i\Delta - \frac{\kappa}{2})\delta\alpha - iG\overline{\alpha} + \sqrt{\kappa_{in}}\delta\alpha_{in} \\
m^*\frac{\partial^2}{\partial t^2}\delta x &= -m^*(\Gamma_m\frac{\partial}{\partial t} + \omega_m^2)\delta x - \hbar G\overline{\alpha}(\delta\alpha - (\delta\alpha)^*)
\end{aligned}$$

where κ_{in} accounts for the input mirror losses and we re-define the detuning between the cavity and the laser to include the static offset caused by the optomechanical interaction $\Delta - G\overline{x} \to \Delta$.

We generate our probe tone via phase modulation at frequency Ω and thus consider an input drive of the form

$$\alpha_{in}(t) = \overline{\alpha}_{in} + \delta\alpha_{in}(t) = \overline{\alpha}_{in} + \delta\alpha_{in}^+ e^{-i\Omega t} + \delta\alpha_{in}^- e^{i\Omega t} \tag{2.79}$$

Following the derivation in [141], we use an Ansatz

$$\begin{aligned}
\delta\alpha &= \delta\alpha^+ e^{-i\Omega t} + \delta\alpha^- e^{i\Omega t} \\
\delta x &= \delta x^+ + e^{-i\Omega t} + \delta x^- e^{i\Omega t}
\end{aligned}$$

where we note that $(\delta x^+)^* = \delta x^-$. With this Ansatz we find coupled equations for $\delta x, \alpha^+$ and α^-

$$\begin{aligned}
\delta\alpha^+ &= \chi_{Cav}(\Omega + \Delta)(\sqrt{\kappa_{in}}\delta\alpha_{in}^+ - iG\overline{\alpha}\delta x^+) \\
\delta\alpha^- &= \chi_{Cav}(\Omega - \Delta)(\sqrt{\kappa_{in}}\delta\alpha_{in}^- - iG\overline{\alpha}\delta x^-) \\
2m^*\omega_m\chi_m^{-1}(\Omega)\delta x &= -i\hbar G\overline{\alpha}(\delta\alpha^+ + (\delta\alpha^-)^*)
\end{aligned}$$

Here we define the cavity and the mechanical susceptibility as

$$\begin{aligned}
\chi_{Cav}^{-1}(\Delta) &= \frac{\kappa}{2} - i\Delta \\
\chi_m^{-1}(\Omega) &= \frac{\Gamma_m}{2} - i(\Omega - \omega_m)
\end{aligned}$$

The cavity susceptibility is defined in analogy with the field reflection/transmission coefficients of the cavity $C_r = 1 - \kappa_{in}\chi_{cav}$. The mechanical susceptibility as defined

here is a deviation from the definition given in section 2.1.1, but as noted in [18], this definition matching χ_{Cav} is more convenient in this formalism.

With these equations, we can arrive at the following expression for our mechanics

$$2m^*\omega_m\chi_{m,eff}^{-1}(\Omega)\delta x = -i\hbar G\bar{\alpha}\sqrt{\kappa_{in}}(\chi_{Cav}(\Omega+\Delta)\delta\alpha_{in}^{+} - \chi_{Cav}(\Omega-\Delta)(\delta\alpha_{in}^{-})^*) \quad (2.83)$$

where we defined the effective mechanical susceptibility as

$$\chi_{m,eff}^{-1}(\Omega) = \chi_m^{-1}(\Omega) + g^2(\chi_{Cav}(\Omega+\Delta) - \chi_{Cav}(\Omega-\Delta)) \quad (2.84)$$

and used $g\sqrt{\hbar/2m^*\omega_m} = G\bar{\alpha}$. This $\chi_{m,eff}$ includes the optomechanical effects on the mechanics; in the limit of $\kappa > g$ these effects can be limited to the optomechanical damping and optomechanical frequency shift (or spring effect). In this regime we can rewrite $\chi_{m,eff}$ as [18]

$$\chi_{m,eff}^{-1}(\Omega) = \frac{\Gamma_m + \delta\Gamma_m}{2} - i(\Omega - (\omega_m - \delta\omega_m)) \quad (2.85)$$

Here $\delta\omega_m$ is the optomechanical spring effect given by

$$\delta\omega_m = g^2\left[\frac{\Delta-\omega_m}{(\frac{\kappa}{2})^2+(\Delta-\omega_m)^2} + \frac{\Delta+\omega_m}{(\frac{\kappa}{2})^2+(\Delta+\omega_m)^2}\right] \quad (2.86)$$

and $\delta\Gamma_m$ is the optomechanical damping defined as

$$\delta\Gamma_m = g^2\left[\frac{\kappa}{(\frac{\kappa}{2})^2+(\Delta+\omega_m)^2} - \frac{\kappa}{(\frac{\kappa}{2})^2+(\Delta-\omega_m)^2}\right] \quad (2.87)$$

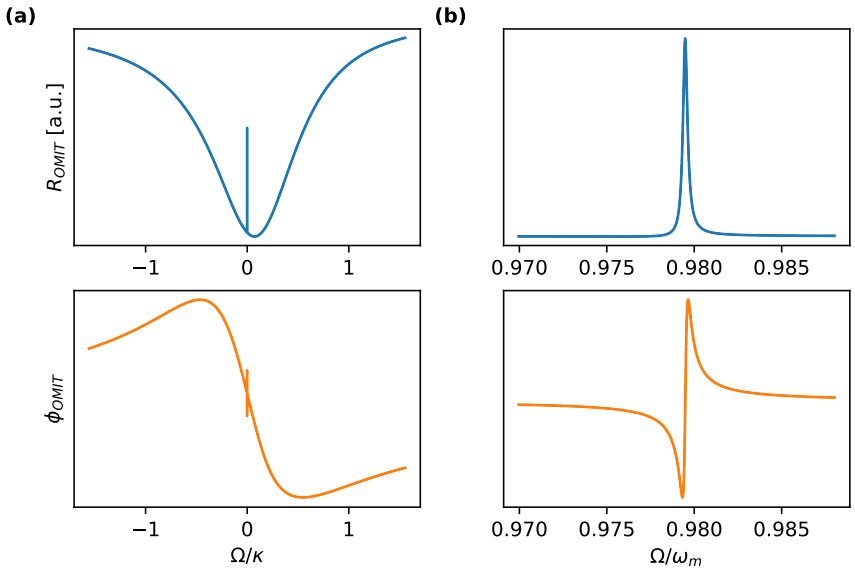

FIGURE 2.15: (a) Reflected signal based on R_{OMIT} for Ω on the order of κ, showing the overall cavity lineshape (top) and phase (bottom), with the narrow OMIT features. (b) Zoom in around ω_m. Values are typical for our system, with $\kappa/2\pi = 2\,\text{GHz}$, $\omega_m/2\pi = 2\,\text{MHz}$, $\Gamma_m/2\pi = 320\,\text{Hz}$, $m^* = 1\times10^{-14}\,\text{kg}$, $\Delta \sim -100\omega_m$ and a coupling given by $G/2\pi = 15\,\text{GHz}\cdot\text{nm}^{-1}$, with a photon number of $|\bar{\alpha}|^2 = 2000$.

We can finally derive solutions for $\delta\alpha^+$ and $\delta\alpha^+$ of the form

$$\delta\alpha^+ = \sqrt{\kappa_{in}}\delta\alpha^+_{in}\chi_{Cav}(\Omega+\Delta)K(\Omega)$$
$$\delta\alpha^- = \sqrt{\kappa_{in}}\delta\alpha^-_{in}\chi_{Cav}(\Omega-\Delta)(K(\Omega))^*$$

where $K = \chi_m^{-1}/\chi_{m,eff}^{-1}$ contains the omit signal.

We in the end measure $\alpha_{out,R} = \alpha_{in} - \sqrt{\kappa_{in}}\alpha$ in reflection, giving us an overall signal of

$$\begin{aligned}\alpha_{out,R}(t) = &\overline{\alpha_{in}} - \kappa_{in}\overline{\alpha_{in}}\chi_{Cav}(\Delta)\\ &+ (\delta\alpha^+_{in} - \kappa_{in}\overline{\alpha}_{in}\beta\chi_{Cav}(\Omega+\Delta)K(\Omega))e^{-i\Omega t}\\ &+ (\delta\alpha^-_{in} - \kappa_{in}\overline{\alpha}_{in}\beta\chi_{Cav}(\Omega-\Delta)(K(\Omega))^*)e^{i\Omega t}\end{aligned}$$

The first term is a constant signal offset, which we will ignore since we are interested in the signal at frequency Ω. Furthermore, the second and third line correspond to the contributions of the sidebands at $\pm\Omega$, but only the first will be resonant with our cavity and $\chi_{Cav}(\Omega-\Delta) \to 0$. The additional factor β accounts for the sideband amplitude compared to the main tone. We thus expect a reflected signal of the form

$$R_{OMIT} \sim |\delta\alpha^+_{in} - \kappa_{in}\overline{\alpha}_{in}\beta\chi_{Cav}(\Omega+\Delta)K(\Omega)|^2 \tag{2.90}$$

In the absence of optomechanical interaction (*i.e.* $g \to 0$), $\chi^{-1}_{m,eff} \to \chi^{-1}_m$ and thus $K(\Omega) \to 1$. In this case Eq. 2.90 simply contains the cavity lineshape described by $\chi_{Cav}(\Omega+\Delta)$. In the presence of optomechanical coupling, K adds the characteristic OMIT dip to the cavity signal, as shown in Fig. 2.15, caused by interference between the mechanical sidebands of the pump and the probe tone. Since this dip depends not only on the mechanical properties (Γ_m, ω_m), but also on the optomechanical coupling, such a measurement can be a useful tool to characterize an optomechanical system.

Chapter 3

Experimental Setups

In this chapter, we will introduce two experimental setups that were used to obtain the measurements presented in this thesis. The first is the membrane-in-the-middle fiber Fabry-Perot cavity (MIM-FFPC) setup, which was used to produce the measurements of the FFPC alone (see chapter 4) and the optomechanical measurements shown in chapter 7.

The second setup is a room-temperature Michelson interferometer used to characterize the hBN drum resonators, which was used to obtain most of the results presented in chapter 6.

3.1 MIM-FFPC Experimental Setup

Here we will begin by discussing the laser ablated fibers that make up the optical cavity. We will then show the low-temperature probe that hosts the MIM-FFPC system in the bath cryostat and the laser-based setup used to measure and control it.

3.1.1 Fiber based Fabry-Perot cavity

To build a FFPC, we require two optical fibers with cleaved end facets, which are facing each other, forming the optical cavity. Such cavities have been used with great success, especially in experiments that require a small footprint and vacuum or cryo-compatibility [98, 144, 145]. From the stability criterion in Eq. 2.49, we know that only for certain combinations of radii of curvature of the two mirrors, and for certain cavity lengths between them, can we expect a stable cavity. To this end, we need to appropriately shape the facets of the fibers. We do this by removing material from the cleaved surfaces with CO_2 laser-ablation, producing craters with well controlled profiles [99]. To improve the moderate reflectivity of cleaved optical fibers, amounting only to a few percent, we employ a highly reflective dielectric coating deposited by LaserOptik[1].

Specifically, we employed both single-mode[2] (SM) and multi-mode[3] (MM) fibers as constituents of our FFPC. The SM fibers are useful to supply a well defined input mode that can be matched to the mode of the FFPC by careful choice of the geometrical parameters of the cavity. The MM fiber, on the other hand, is a good choice for the transmission fiber, since it will provide a collection efficiency of almost unity.

The coating we use is intentionally capped to produce a moderate finesse of up to 15000. While it is possible to fabricate mirrors with much smaller transmission losses, resulting in finesse as high as 2×10^5 [118], this also results in more challenging experimental parameters. For example, relatively small scattering losses due to

[1] https://www.laseroptik.com/
[2] IVG fiber Cu800
[3] IVG fiber Cu50/125

the membrane would already have a detrimental effect on the cavity signal, see section 2.3.1. The requirements for the mechanical stability of the setup also scale with the finesse and are not easy to meet, as we will see in chapter 4.

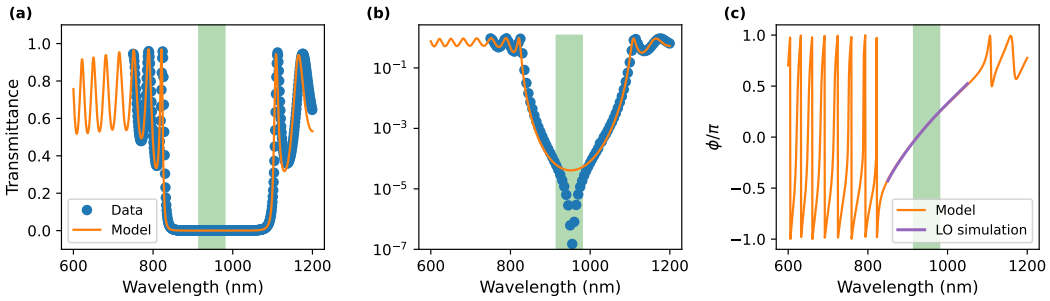

FIGURE 3.1: (a) Model (orange) and characterization data (blue) of the dielectric coating deposited onto our fibers. The green shaded area shows the tuning range of our NIR laser. (b) Same as in (a), but shown with a logarithmic scale to visualize the changes within the stop band of the coating. (c) The phase extracted from the model as well as a simulation within the highly reflected band, provided by LaserOptik.

The highly reflective Bragg window of our coating easily covers the entire tuning range of our near-infrared (NIR) laser of 915 to 980 nm. Fig. 3.1 (a) and (b) shows both the characterization data of the coating supplied by LaserOptik and a numerical model that can be extended beyond the characterized range. We will later use this model to gain insight into the behavior of our FFPC when operated at wavelengths below the highly reflective window. Note that the characterization data was not obtained from our cratered fibers, but from reference mirror blanks exposed to the same coating run. In (c), the corresponding phase is shown as obtained by our model, as well as a simulation provided by LaserOptik that is limited to within the highly reflective Bragg window. Within this range, our model agrees well with this simulation.

The coating is a 28 layer distributed Bragg reflector made of alternating layers of Nb_2O_5 and SiO_2. The layer thickness corresponds to $\lambda_n/4$, where $\lambda_n = \lambda_0/n$ with n the refractive index of the layer and the central wavelength $\lambda_0 = 944.6\,\text{nm}$. However, the thickness of the first two layers is adjusted to $1.825\lambda_n/4$ (Nb_2O_5) and $0.592\lambda_n/4$ (SiO_2). This is done to achieve a transmission of $100ppm$, matching our target finesse. The capping layer is a SiO_2 layer with a thickness of $0.933\lambda_n/4$, intended to shift the anti-node of the cavity field just outside the mirror surface.

Plugging all these specifications into a series of characteristic matrices, again using the definitions in Eq. 2.21, to characterize the alternating stacks of materials and their interfaces, we obtain the model shown in Fig. 3.1. The model appears to match the data well for lower wavelengths and along the stop band, but towards higher wavelengths as well as in the middle of the stop band, we observe some deviations. Some of these deviations could be caused by minor differences in the refractive index data we employ for these simulations. As will be discussed in section 3.1.3, we will be interested in the extension towards lower wavelengths that this model provides, for which the deviations are acceptable.

CO_2-ablated optical fibers

The ablation procedure is used to shape parabolic mirrors on the fiber facets [100]. Unlike the dielectric coating, this was performed in-house. We have built and characterized a CO_2-ablation setup and created a large array of fibers with different crater geometries, a detailed discussion can be found in [99, 200]. Here, we will limit ourselves to a short overview.

We use $\lambda = 10.6\,\mu m$ CO_2-laser pulses to ablate the craters. These pulses are created with an AOM and focused at the cleaved fiber facets with a 50 mm aspheric lens. An example of such a cratered fiber can be seen in Fig. 3.2 (a). The inset shows a fiber which features an especially large crater, due to the transparency of the fiber it is visible from the side. In Fig. 3.2 (b) we define the parameters used to characterize the fiber mirrors. Namely the crater depth t, the radius of curvature R, taken as the radius of the circular profile close to the center of the crater, and the spherical diameter D_s corresponding to this inner region. To produce craters with different geometries, we adjust the ablation parameters as described in [99]. Typical values used are around 1 W in laser power, pulse durations of 10-50 ms and a waist of approximately 40 µm, which is adjusted by moving the fiber facet away from focus.

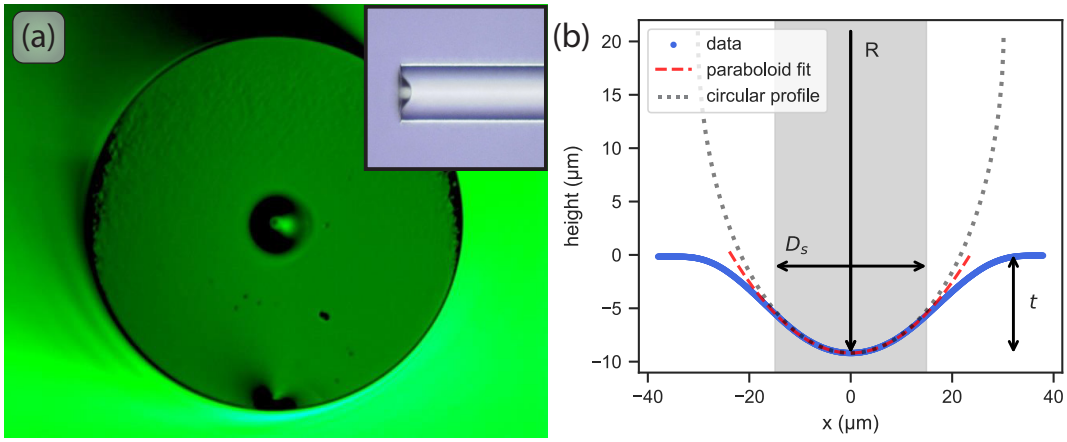

FIGURE 3.2: (a) Photograph of a crater on a fiber facet after ablation. Inset shows a side view of a much larger crater visible through the transparent fiber. (b) Definition of the different geometrical parameters used to characterize the crater. D_s is the spherical diameter, R the radius of curvature and t the crater depth. Data in blue is a linecut of a profilometer map of a cratered fiber. Note the difference in scale between the horizontal and vertical axis.

The data presented in this thesis was almost exclusively recorded with a FFPC made of a SM input fiber and a MM transmission fiber. The SM fiber has crater dimensions of $t_{SM} = 0.2\,\mu m$, $R_{SM} = 92\,\mu m$ and $D_{s,SM} = 14\,\mu m$. The MM fiber has crater dimensions of $t_{MM} = 1.1\,\mu m$, $R_{MM} = 57\,\mu m$ and $D_{s,MM} = 19\,\mu m$. D_s gives a close approximation for the effective mirror diameter, and with Eq. 2.41 allows us to estimate clipping losses for large beam diameters at the mirrors when increasing L_{Cav}. t_{SM} could pose a lower limit to a minimal L_{Cav}, but the craters used here are very shallow compared to our typical cavity lengths. Especially when inserting a membrane into the FFPC, several microns of safety distance are maintained.

3.1.2 Probe

The probe assembly has to hold the MIM-FFPC system and allow for its alignment, as well as connections for remote signal detection and control. The assembly needs to fit inside a vacuum can, which can be placed inside of our liquid-helium bath cryostat[4]. In addition, it must be possible to scan several parameters in order to perform different measurements, like the position of the mechanical oscillator in x, y, z, or the position of one of the fiber mirrors to change L_{Cav}. Since our cryostat also hosts a superconducting magnet, all materials used should be non-magnetic. Finally, the system should provide some shielding against mechanical noise and not undergo any drastic deformations when cooling down to cryogenic temperatures, so as to preserve the alignment of the system as much as possible.

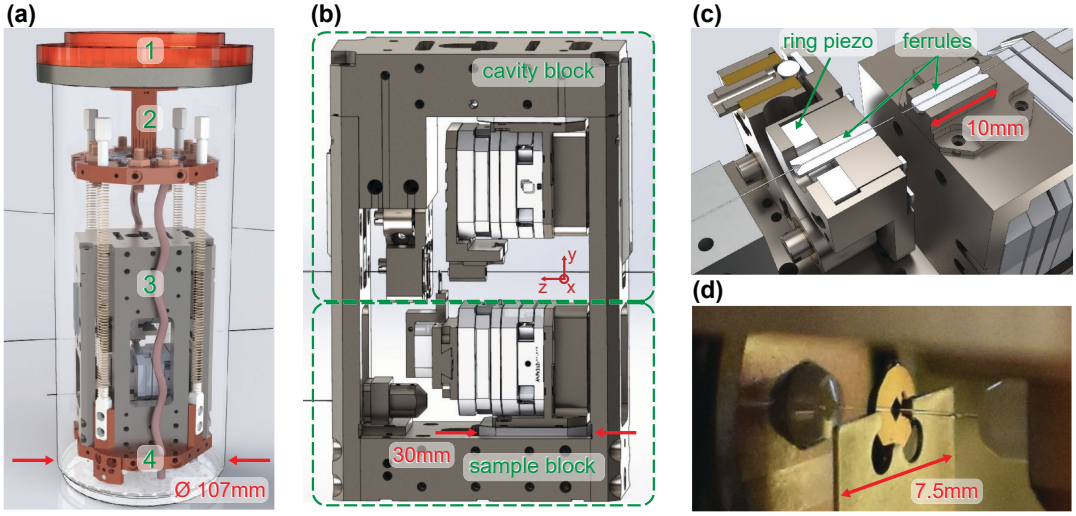

FIGURE 3.3: (a) Overview of the probe inside the vacuum can (transparent) with the copper plate (1), the top plate of the probe (2), the titanium cage hosting the MIM-FFPC system (3) and the bottom plate of the probe (4). (b) Detailed overview of the titanium cage including the cavity block hosting the FFPC and the sample block hosting the membrane. (c) Cut-out of the Cavity block showing the FFPC. (d) Photograph of the MIM-FFPC system, showing the sample chip in the middle of the two fibers.

With these goals in mind, we designed the probe depicted in Fig. 3.3 (a). The vacuum can (red arrows in (a)) containing the probe is closed against a copper plate (1) with an indium seal to ensure a low temperature compatible vacuum operation. A tube which is connected to the copper plate leads to the top of the cryostat. It contains all wires and optical fibers leading out of the cryostat, and is connected to a turbo-pump station[5] at the top. When the bath cryostat is filled, the stainless steel can and the copper plate (1) are in direct contact with the liquid helium and are thus thermalized to 4.2 K.

The top plate of the probe (2) is fixed to the copper plate (1). It is also made of copper which is gold plated to prevent oxidation and ensure good thermal contact to all attached components. It serves as a clamping point to thermalize all wires and fibers coming from the top and is connected to the bottom plate of the probe (4) by four long springs[6]. Apart from the springs, two additional soft copper braids

[4] Cryomagnetics liguid He bath cryostat with an 8 T superconducting magnet
[5] Agilent TPS
[6] 16 cm-long copper–beryllium springs with a spring constant of $0.023\,\mathrm{N}\cdot\mathrm{mm}^{-1}$

connect (2) and (4), ensuring sufficient cooling power to reach close to 4.2 K at the bottom of the probe. (4) is again made of gold plated copper and is the base for the FFPC-MIM assembly, thus the temperature of the probe is measured with a temperature sensor attached to this bottom plate.

The springs are meant to decouple the system from acoustic noise and are designed to be rather soft, resulting in low resonance frequencies. To deal with low-frequency seismic noise, the cryostat is additionally placed on a passive vibration isolation platform[7].

The frame holding the MIM-FFPC system (3) is mounted on top of the bottom plate (4). It needs to be stiff and maintain the alignment of the FFPC, which is why it is machined out of solid titanium blocks where possible. Titanium is a non-magnetic metal with a low thermal expansion coefficient and good mechanical properties, matching our design requirements. A more detailed view of (3) is shown in Fig. 3.3 (b). It is sub-divided into two blocks, as highlighted by the green boxes: one being the cavity block and the other the membrane block.

The cavity block holds both fibers of the FFPC, which are aligned horizontally in the probe. One fiber is mounted on a Attocube piezo xyz-positioner[8] (on the right in Fig. 3.3 (b)), while the other is mounted on a home-built tip-tilt stage (left). This tip-tilt stage is inspired by standard tip-tilt mirror mounts often employed in free space optical setups, but is made to be vacuum and low temperature compatible. A more detailed view of the cavity block is shown in Fig. 3.3(c), highlighting the FFPC. Each fiber is inserted and glued into a ceramic ferrule, which is then clamped into a titanium holder with screws pressing against the ferrule to secure it in place. The one on the right sits on an L-bracket connecting it to the Attocube positioners. The fiber on the left is fixed in a cylindrical holder, which is pressed against a ring piezo with a leaf spring. The fiber is inserted through the hole of that ring piezo, which can be used to tune the cavity length L_{Cav}.

While the x, y, z positioner can change L_{Cav} as well, the ring piezo has a higher bandwidth on the order of 100 kHz. This is important for fast scanning of the cavity length as well as for its active stabilization, but this piezo has a low range of $\approx$ 1 µm at RT and less than one FSR of the cavity at LT. The x, y, z positioner on the other hand can be moved over several mm in stepping mode, allowing for long range measurements, cavity alignment, and opening of the cavity to comfortably exchange a membrane chip. Aside from this stepping mode, a DC offset can be applied that gives reasonable scanning capabilities. Like this, several FSR can be scanned, although at a lower bandwidth compared to the ring piezo. While the ring piezo is used as feedback element on the cavity length, we still use the z-positioner to compensate larger offsets beyond the range of the ring piezo.

While all the piezos can be adjusted in-situ, the tip-tilt mount can only be adjusted by hand, making the angle alignment only available when the system is open. However, thanks to the monolithic and relatively symmetric titanium cage, we only expect negligible changes in the tip and tilt of the fibers when cooling the probe down. The biggest changes when going to low temperature are due to the contraction of the Attocube piezo stacks, which can be directly adjusted for.

The sample block is similar to the right half of the cavity block, employing the same Attocube xyz-positioner to place the membrane in between the FFPC. On top of this positioner is a dove-tail based sample holder, which also contains a x-y piezo

[7] Minus K 1000BM-1CMM
[8] Attocube ANPx312

scanner[9]. It also hosts a small disc piezo to drive vibrations in the membrane[10]. The dove-tail mechanism allows for relatively safe insertion of the sample holder due to its guiding features while also becoming a very rigid connection when clamped.

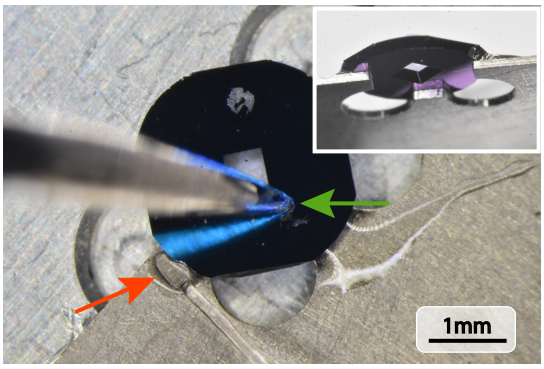

FIGURE 3.4: Glueing procedure for the membrane chip. The chip is pressed onto the metal holder with a needle (green arrow), while pre-cured UV glue is applied with a stripped optical fiber (red arrow) to the three contact points. The underside of the glued chip is shown in the inset, revealing the backside depression that one of the two fibers of the cavity can be inserted into.

As depicted in Fig. 3.3 (d), the membrane chip is glued to a thin metal holder which allows insertion between the two fibers. The gluing process of the chip on the sample holder is optimized to ensure that the sample is inserted into the cavity at normal incidence, while avoiding excessive contact between the sample chip and its holder. In addition, the sample holder has to keep the chip accessible from both sides for optical access. For similar Si_3N_4 chips, it has been observed that the Q of the devices benefited from as little clamping or gluing as possible [201]. Since our FFPC is horizontal, we need a way to fix our chip, but we limit the contact to three gluing points and employ a holder that has as little overlap with the chip as possible. We use glue that is cured under UV light[11] which is vacuum and low temperature compatible. We start the curing process with 30 sec of UV light illumination to increase the viscosity of the glue, making it easier to apply small quantities and preventing the glue from creeping underneath the chip. As shown in Fig. 3.4, we press on the chip with a metal needle mounted on a mechanical xyz micropositioner, to ensure that it is placed flat on the titanium holder. The titanium holder is polished before use to ensure that no burr might lead to uneven sample placement. The small drops of glue are applied with a stripped optical fiber to the side of the chip, and the glue is cured completly under UV light.

In addition to holding the mechanical oscillator in the MIM configuration inside the FFPC, the membrane block features an additional configuration shown in Fig. 3.5. When the dove-tail holder is inverted, the membrane block turns into a fiber-based confocal microscope. The microscope objective is a fiber-based objective that is built according to [146]. It uses a titanium tube in which the cleaved fiber is glued in front of two lenses, one for collimation and one for focusing on the sample[12]. The focusing lens has a focal length of 1.45 mm and an NA of 0.58. Due to

[9] Attocube ANSxy50
[10] PI ceramic piezp disc OD=3 mm, thickness=0.25 mm
[11] Norland Optical Adhesive NOA 65
[12] Collimation lens: Thorlabs 354430, focusing lens: Thorlabs 354140

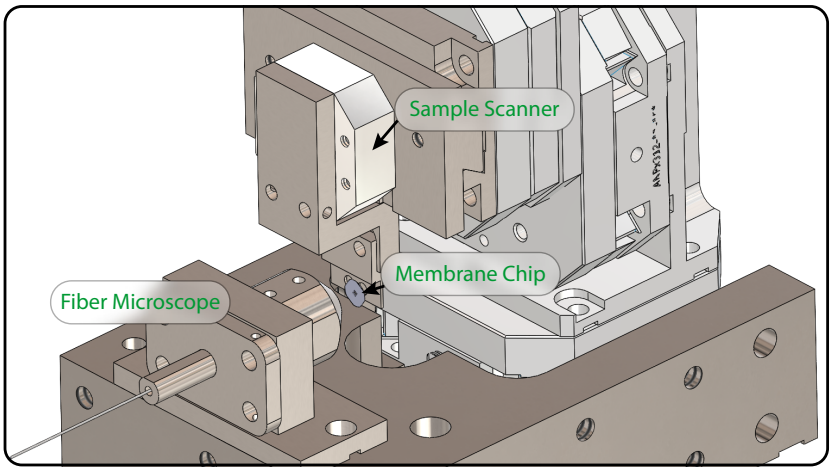

FIGURE 3.5: Membrane block of the titanium cage in the confocal microscope configuration, in which the dovetail hosting the sample scanner and the membrane chip is inverted compared to Fig. 3.3 to position the chip in front of the microscope objective.

the reflective surface of the cleaved fiber facet, a small interferometer is formed between the confocal objective and the surface of the mechanical oscillator. We use this setup to perform characterization of our mechanical samples at low temperature. At room temperature, we instead use the Michelson interferometer discussed later in section 3.2.

3.1.3 Optical setup and feedback lock-loop

The optical measurement and control setup we employ has to accomplish several tasks, some of them in parallel. It has to provide the main carrier at ω_{res}, with which the cavity is kept resonant. It has to record the reflected and transmitted signals of the FFPC. For more advanced measurements, it is often also necessary to generate an additional tone that can be detuned from ω_{res}, enabling us to perform pump-probe measurements. It has to stabilize the cavity length to the laser according to the PDH-technique, introduced in section 2.2.3. We also use a red laser, for which the reflectivity of the fiber mirrors is low, for coarse alignment of the setup. Finally, we employ white-light (WL) spectroscopy to measure the mirror-mirror and mirror-membrane distance in our FFPC-MIM system. This results in a rather elaborate setup that we will break up into several parts in our discussion.

Main optical setup

First, we will take a look at the main optical setup responsible for the standard FFPC operation at high finesse. Starting with the NIR laser[13] shown in the bottom-left corner in Fig. 3.6, the light passes a fiber-paddle polarization controller before entering the electro-optic modulator[14] (EOM), which we use to generate the modulation at ω_{mod} that is the basis of the PDH error signal, as discussed earlier in section 2.2.3. Afterwards, we transition into a free-space setup. A combination of a $\lambda/2$-plate and the first polarizing beamsplitter (PBS_1) allows us to split the beam into two paths with an adjustable ratio.

[13] Toptica CTL950
[14] iXblue NIR-MPX950-LN-10

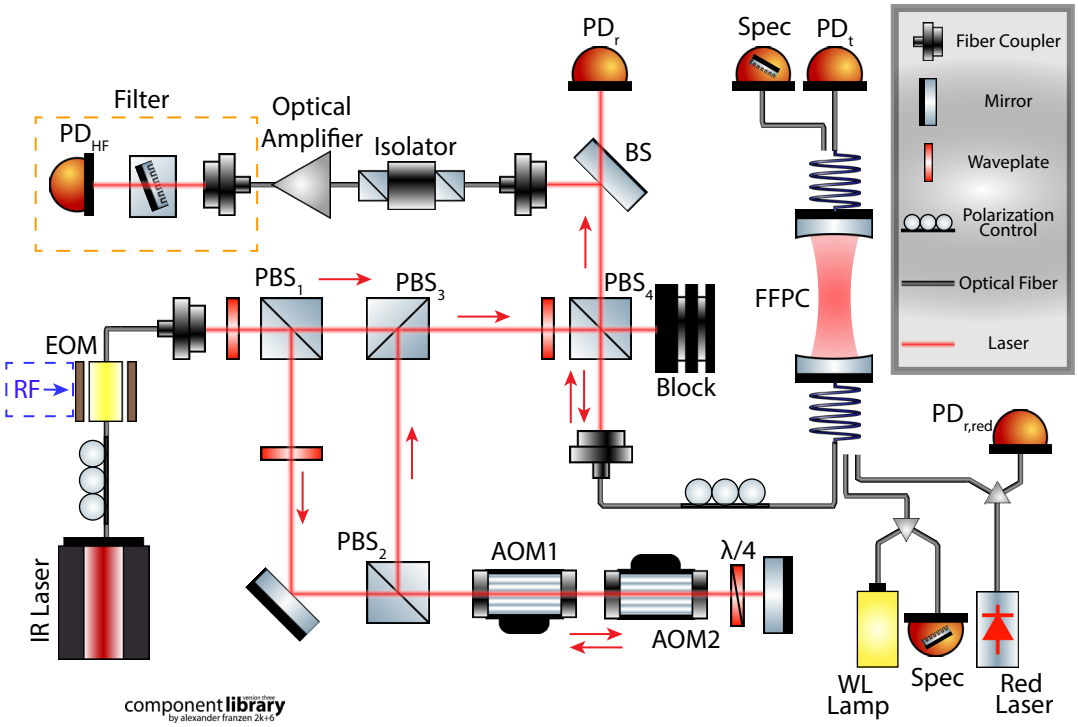

FIGURE 3.6: Sketch of the main optical setup[15], shown in the configuration for operation with the NIR laser. The filter setup (orange box) is shown in more detail in Fig. 3.7 and the involved microwave electronics that provide the RF input for the EOM (blue box) are discussed in section 3.1.3.

Following the path downwards, the polarization is turned by 90° and passes through PBS_2, entering two sequential acousto-optic modulators[16] (AOM) in double-pass configuration. Note that the AOM setup is heavily simplified in Fig. 3.6, refer to [147] for a more in depth discussion. These two AOMs are aligned in such a way, that one operates on the $n = +1$ diffraction order while the other operates on the $n = -1$ diffraction order. All other diffraction orders are not collected. An AOM will shift the frequency of the light in the first diffraction order by its operating frequency ω_{AOM}, in our case it can be tuned around its central value of 200 MHz by ±20 MHz. A single AOM would not be able to provide a detuning below 180 MHz, but the two AOMs effectively compensate each others offset of 200 MHz since they operate on opposite diffraction orders. This gives us a smaller tuning range which is centred around 0.

In addition to frequency detuning, an AOM also offers a good way to control the laser intensity. This is done by changing the amplitude of the RF tone applied to the AOM, which adjusts the amount of light diffracted into the first order. This can also be done in a dynamic way with a high bandwidth limited by the AOM rise time. This setup thus provides a convenient way to electronically control the laser power as well as modulate it with a bandwidth of up to around 30 MHz.

[15]The illustrations in Fig. 3.6,3.7,3.8,3.11 and 3.12 are in part made with the ComponentLibrary by Alexander Franzen, licensed under a CC BY-NC 3.0 license, see http://www.gwoptics.org/ComponentLibrary/

[16]G&H Aomo 3200-1117 with driver AODR 1200AF-AEF0-2.5

After passing the two AOMs twice, the polarisation has been turned by the quarter-waveplate in front of the end mirror in such a way that the back-travelling light will be reflected at PBS_2 and PBS_3. At this point, it is recombined with the fraction of the laser that was transmitted through PBS_1, which has not been altered.

By default, only the light that was reflected at PBS_3 would be reflected at PBS_4 towards the fiber coupler leading to our FFPC. Using the half-waveplate in front of PBS_4 allows to control the ratio of the two frequency components that we send towards the cavity. The beams transmitted through PBS_4 are discarded into a beam blocker.

The first way this setup can be used is to insert a beam blocker between PBS_1 and PBS_3 to collect only the laser beam that passed through the AOM setup, which can be amplitude controlled and modulated. The other way is to combine both paths to have two frequency components, one at the laser frequency and one at the frequency detuned by the AOM setup. Since we can also produce several sidebands to interact with the MIM-FFPC system using the EOM alone, we will use the setup in the former way in this thesis.

After being fed to the FFPC, the light is either reflected back or transmitted. The transmitted light is collected on a variable gain photodiode (PD_t)[17], while the reflected light passes a polarization controller (twice), which is adjusted so that the light is now transmitted by PBS_4 on its way back. This reflected beam is split by a $50:50$ beamsplitter (BS) after PBS_4. One half is collected on a second variable gain photodiode[18] (PD_r) for the reflected signal, the other half is sent to a fiber coupler that leads to the fast detection part of the setup.

This fast detection setup entails a high frequency (HF) detector[19] (PD_{HF}) that has a bandwidth of up to 10 GHz, intended to record the fast modulation necessary for the PDH stabilization. Since the sensitivity of this photodetector is more limited compared to our other detectors, we use a fiber-based amplifier[20] to boost the signal strength. Such an amplifier works similar to a laser diode, employing a gain medium to boost an incoming signal. The main difference is the lack of a laser resonator, transmitting the signal after a single pass, which is ensured by anti-reflection coatings. Similar to a laser diode, such an amplifier produces spontaneous emission proportional to the applied current, resulting in a broad background much higher in power than our signal of interest. This would lead to a reduction in the signal to noise ratio and defeat the purpose of the setup. The best way to recover the signal to noise ratio and achieve an effective gain in signal is spectral filtering of the light, a detailed discussion can be found in [198]. Furthermore, the spontaneous emission is emitted bidirectionally, making it necessary to employ an isolator to prevent feedback into the main optical setup.

Filter setup

The spectral filter is a home-built optical setup and is based on a reflective diffraction grating[21] with a groove density of $1200\,\mathrm{mm}^{-1}$ and a blaze wavelength of 1000 nm, employing a similar working principle as a spectrometer. To estimate the performance of our filter, we can start with the grating equation for the first diffraction

[17] FEMTO OE-300-01
[18] FEMTO OE-300-03
[19] Newport 818-BB-51A
[20] Thorlabs BOA930S
[21] Thorlabs GR25-1210

order [194]

$$\sin(\theta(\lambda)) - \sin(\theta_i) = -\frac{\lambda}{a} \tag{3.1}$$

where a is the grating period, θ_i the angle of the incoming light and θ the reflected angle of the first diffraction order. We can further define a spectral selectivity $\frac{d\lambda}{d\theta}$. This gives us a spectral width $\Delta\lambda$ depending on the angles $\Delta\theta$ that our detector captures,

$$\Delta\lambda = -a\cos(\theta)\Delta\theta \tag{3.2}$$

where θ is given by $\cos(\theta) = \sqrt{1 - (\frac{\lambda}{a} - \sin(\theta_i))^2}$.

For our typical wavelength of 920-980 nm and an a of 833 nm, this results in $\Delta\lambda$ on the order of 1 nm if we collect 0.1° with our detector.

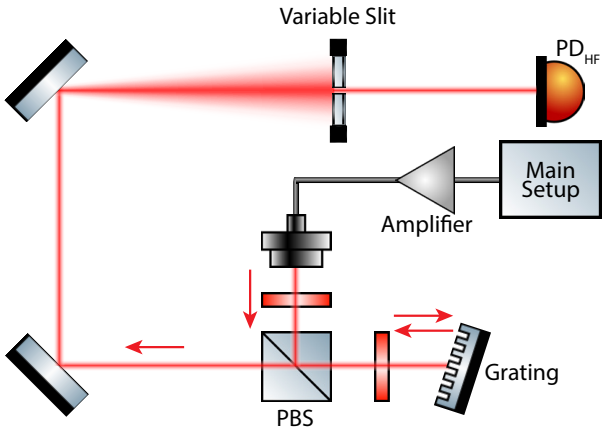

FIGURE 3.7: Detailed overview of the filter setup in front of the high frequency detector in Fig. 3.6.

In principle, one also has to take into consideration that the beam expands while it travels according to Gaussian beam theory, as well as the beam diameter to begin with. To optimize $\Delta\lambda$ one might think that a smaller beam diameter would be useful, but from section 2.2.1 we know that this leads to a small z_R and thus to a quickly expanding diameter $\omega(z)$ of the beam. In the end, the easiest way to optimize the filter performance in practice is to use a grating with a small a, a moderate beam diameter (1 mm in our case), leading to a relatively slowly diverging $\omega(z)$, and a long distance between the grating and the detector (2 m) in order to capture a small $\Delta\theta$.

In Fig. 3.7 the filter setup is sketched. After the fiber amplifier, the beam is reflected towards the grating with a combination of a half-waveplate and a PBS. The grating is operated in the Littrow-configuration, in which $\theta_i = \theta(\lambda_c)$ [194]. Here λ_c is our central wavelength of interest around which we want to filter. Due to a quarter-waveplate positioned between the PBS and the grating, the diffracted light will be transmitted through the PBS, slowly dispersing. After some distance, a variable slit filters the now spatially separated spectral intervals other than some narrow range $\Delta\lambda$ around λ_c. By adjusting the slit size, it is possible to set $\Delta\theta$ and thus the sharpness of the filter. Furthermore, since we operate in the Littrow-configuration, simply changing the grating angle allows to tune λ_c without realigning any other component in the setup. Finally, the filtered signal is detected by the HF detector.

Pound-Drever-Hall setup

The PDH stabilization requires the reflected cavity signal to be recorded on the HF detector, including the modulation provided by the EOM, with the setup introduced above. It further involves a microwave electronics setup introduced here to perform the up and down mixing of the signal.

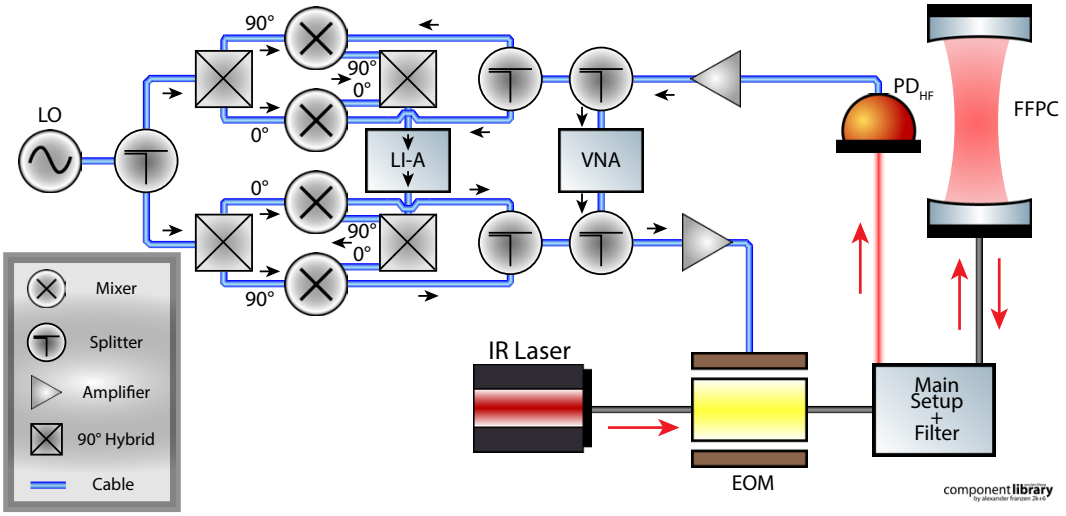

FIGURE 3.8: Microwave electronics setup for our PDH stabilization scheme used to lock the FFPC length to the IR laser.

A radio frequency (RF) source[22] provides the local oscillator (LO), which is split into two paths, shown to the left of Fig. 3.8. The first of these two signals (lower path) is mixed with the output of the lock-in amplifier[23] (LI-A) to obtain a a frequency $\omega_{mode} = \omega_{LO} - \omega_{LI-A}$. Instead of a simple mixer, we use a image rejection mixing scheme, to suppress one of the two sidebands generated in frequency mixing. This is achieved by using two 90° hybrid couplers in conjunction with two mixers. Both the signal from the LI-A and the LO are split into a non phase shifted and a 90° phase shifted part, the signals with the same phase shift are then mixed together. After recombining, this leads to a cancellation of one of the two sidebands [204].

The signal we then obtain is amplified before being applied to the EOM as an input. The EOM then generates a phase modulation of the light at the same frequency, creating the foundation for the PDH error signal as in Eq. 2.53. After passing the parts of the optical setup introduced before, and being reflected by the cavity, the signal is detected by the HF detector.

Now, following the upper path in Fig. 3.8, the detected signal is amplified[24] before being mixed with the LO and fed to the lock-in amplifier. A similar image rejection mixing scheme is used as before. The LI-A is then used to demodulate the signal and record both of its quadratures, corresponding to a signal as in Eq. 2.55, providing the PDH error signal. For the PDH stabilization itself, the vector network-analyser[25] (VNA) is not necessary. Its output is coupled into the setup between the EOM amplifier and the up-conversion electronics, while the input of the VNA is picked up between the amplified HF detector signal and the down-conversion electronics. Like this, it is a useful addition for pump-probe measurements. Such measurements are

[22] Rohde & Schwarz SGS100A
[23] Zurich Instruments HF2LI
[24] Pasternack PE15A1010
[25] Rohde & Schwarz ZNB4

often employed in optomechanics experiments, and we will make use of this aspect of the setup in chapter 7.

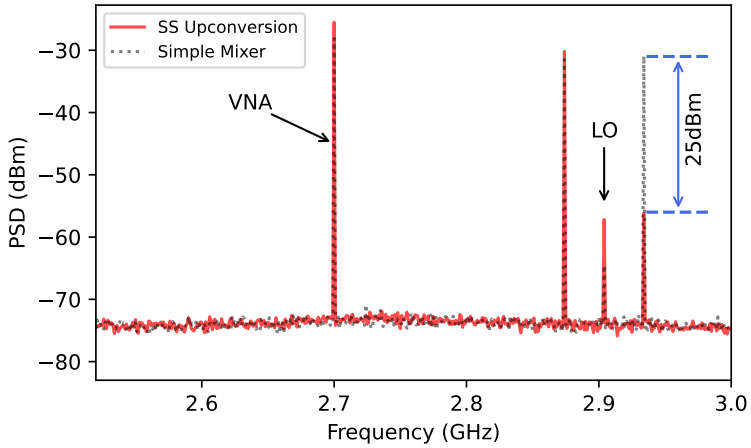

FIGURE 3.9: Spectrum of the RF signal supplied to the EOM amplifier, generated with a simple mixer (dotted line) and a single side mixing scheme (red line), to suppress one of the sidebands around the LO.

To make sure that the setup produces a clean output spectrum with the intended tones present, we record a spectrum just before the signal is sent to the EOM, shown in Fig. 3.9. We compare the performance of the single side mixing scheme and a simple mixer, showing that the unwanted sideband is suppressed by roughly 25 dBm by the former. While there are small contributions left from the LO and the suppressed sideband, the setup succeeds in predominantly supplying the EOM with the modulation tone for the PDH stabilization scheme and an additional variable tone generated by the VNA, which can be turned on and off at will.

After obtaining the PDH error signal, we use a red pitaya running the PyRPL software package[26] to generate a PID signal that is fed to the ring piezo of the cavity, to act on the cavity length. We also use the infinite impulse response (IIR) module of PyRPL to digitally filter our error signal in order to smooth out the response and maximize the gain of our feedback loop, as will be discussed in more detail in chapter 4.

Low reflectivity operation

Fig. 3.6 shows the main configuration where we use the NIR laser to operate the cavity in a high finesse regime. To the bottom right of the figure, we show a white-light (WL) lamp[27] and a 633 nm laser[28] that we use to characterize the MIM-FFPC system.

The red laser is used to operate outside of the highly reflective coating window (see Fig. 3.1) of the FFPC. This makes the system much easier to work with, since instead of sharp cavity resonances, one observes a simple sine wave behavior, and the cavity alignment is much more forgiving in terms of signal drops. We circumvent most of the optical setup in Fig. 3.6 in this configuration and use a fiber beamsplitter that is directly connected to the FFPC input fiber, while the other arm of this splitter

[26] https://pyrpl.readthedocs.io/
[27] Thorlabs SLS201L/M
[28] Q-Photonics QFBGLD-633-30

is connected to another detector[29] ($PD_{r,red}$) for the reflected signal. For the transmitted signal, we use the same detector as before, which still performs reasonably well around 633 nm.

Apart from the alignment of the FFPC, we also use the red laser to image the sample using the sample scanner, producing images that are detailed enough to navigate the sample, especially when the input fiber of the cavity is in close proximity to the membrane, see for example Fig 7.1.

White-light spectroscopy

To be able to bring the system in close enough proximity so that we can start the fine alignment with the red and NIR lasers, we use a WL spectroscopy technique to estimate L_{Cav} [148]. In this third configuration of the setup, we connect the WL lamp directly to the FFPC, again with a fiber-based beamsplitter. We use a fiber coupled spectrometer[30] to record the response of the cavity to this broadband source, giving us a cavity spectrum in a single-shot measurement. Due to the limited resolution of the spectrometer, we perform these measurements outside of the highly reflective window of the coating, where the spectral features are not as sharp.

The main purpose of these measurements is to estimate the distances between the fibers and the sample, which is particularly useful when the system is enclosed in the vacuum can or cooled down inside the cryostat. The spectrometer can be connected in transmission and in reflection. In transmission, it replaces PD_t, while in reflection, we use the fiber beamsplitter as we did with the red laser. Even though the WL setup uses MM fibers, APC connectors are essential to remove back reflections onto the spectrometer, leading to a strong reduction in the background level of around three orders of magnitude in reflection. The measurements in transmission are performed without the membrane in the signal path, achieved by using holes that are present in the membrane chip (see chapter 5). Like this, we can gain information about the fiber to fiber distance, *i.e.*, L_{cav}. In reflection, we move the membrane in front of the input fiber, giving us the length of the first sub-cavity $L_{cav,1}$ instead. The measurement of $L_{cav,1}$ is best done when the second fiber is far removed to not disturb the measurement by adding an additional reflecting surface. Thus, we usually begin by adjusting $L_{cav,1}$. This provides us with all the necessary distances to position the constituents of the system along the cavity axis.

We usually not only record the cavity spectrum as a function of the wavelength, but also repeat this measurement for varying cavity lengths or sample-fiber distances, to produce a more robust measurement; such a measurement will be presented in chapter 4.

3.2 Room Temperature Interferometer

To characterize the mechanical oscillators developed in this thesis before they are integrated into the FFPC-MIM setup, we have built a simple room-temperature (RT) test setup. It is comprised of a polarization based Michelson interferometer with balanced detection. The sample is placed in a vacuum chamber with a microscope head on top, which leads to the interferometer. The system is designed for ease of use and quick sample exchange times. A camera that makes use of the same microscope head as the interferometer allows one to observe the sample in the vacuum chamber. The

[29] Thorlabs APD130A/M
[30] Ocean Optics QEPro

sample can be excited with a piezo shaker, and an additional amplitude modulated green laser can be used as an optical drive.

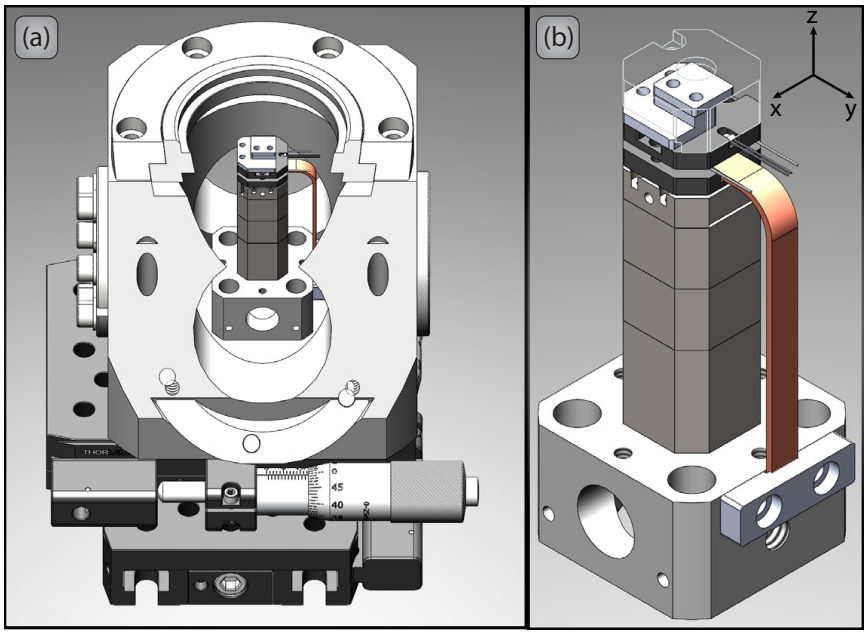

FIGURE 3.10: (a) Vacuum chamber on top of a x-y translation stage with a cutout to show the sample holder inside. Optical access is achieved through the window in the top of the chamber. (b) Isolated sample tower. The sample holder is mounted on a temperature control stage on top of a stack of piezo positioners and a x-y piezo scanner. A copper braid is used for thermal contact to the base block of the tower, which is used as a thermal sink for the Peltier element.

An overview of the vacuum chamber can be seen in Fig. 3.10 (a). It is a small home-built aluminium cube with a vacuum window in the top for optical access, as well as several electrical connectors and a valve leading to a turbo pump station[31] on its sides. This cube is mounted on two linear translation stages[32] for coarse translation of the sample under the microscope in x and y, where z is the optical axis. Looking at the internal structure in Fig. 3.10 (b), the mechanical oscillator is placed on the top plate of this sample tower. Below this topmost plate, there is a temperature control stage and a x, y piezo scanner[33], used for fine position control and scanning of the sample.

The temperature control stage[34] can be used to stabilize the temperature or perform sweeps in a range of 10 °C to 70 °C. It uses the lower part of the sample tower as heatsink. To bridge the poor thermal conductivity of the Attocube tower, we use the copper link shown in Fig. 3.10 (b) for thermal contact. For additional shielding from thermal radiation, a metal shroud (transparent part in Fig. 3.10 (b)) is put on top of the sample with a small aperture for optical access. This temperature control was added only recently and was not available for all measurements presented in this thesis.

[31] Pfeiffer-Vacuum HiCube
[32] Thorlabs XR25/M
[33] Attocube ANSxy50
[34] Peltier element: CUI Devices CP2088-258P; TEC controller: meerstetter TEC-1091 and Pt1000 temperature sensors

As depicted in Fig. 3.11 (a), the 50x microscope objective[35] is mounted outside the chamber above the vacuum window. This objective is designed for use with a 3.5 mm thick glass window and has a long working distance of 13.89 mm, giving us enough space to position the sample in focus. We use a z-translation stage[36] to move the objective with respect to the chamber, allowing us to adjust the focus of the microscope. A cage-based periscope with several mirrors then aligns this microscope head with the rest of the interferometer setup.

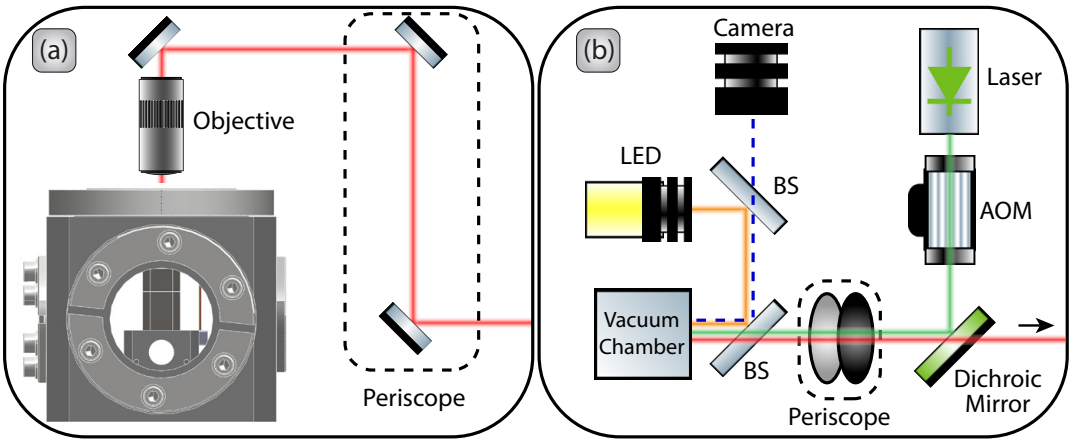

FIGURE 3.11: (a) Microscope objective head above the vacuum chamber (side view). (b) Overview of the additional camera and green laser excitation arms (top view). The dashed box in both images highlights the position of the periscope used to bridge the height difference between the microscope head and the interferometer setup (towards the black arrow in (b), shown in Fig. 3.12)

Apart from interfacing the microscope head with the interferometer, we also use the cage system of the microscope head to couple to the camera setup with two beamsplitters (BS), as shown in Fig. 3.11 (b). The BS shown at the bottom combines the camera setup with the main optical path, while the upper BS couples in an LED to illuminate the sample. Furthermore, just before the interferometer, we use a dichroic beamsplitter to combine the red laser used for detection with the green laser[37] used for optical excitation. This green laser is intensity modulated with a single pass AOM setup[38], allowing for frequency modulation up to 30 MHz.

3.2.1 Optical interferometer setup

The interferometer follows to the right of Fig. 3.11 (b) (black arrow). In Fig. 3.12, we have omitted the parts introduced above except for the sample itself for simplicity, and the black arrow matches the one in Fig. 3.11 (b). A short discussion of the theoretical operation principles has been included in Appendix B since polarization based interferometers with balanced detection are not exceedingly common.

Starting at the input (E_{in}), the incoming light is split at the left PBS in Fig. 3.12 by a ratio that is determined by the polarization of the incoming light, which can be adjusted with a polarization controller. The two signal components are then reflected back by either the sample (left) or the end mirror in the reference arm (top). In

[35] Mitutoyo G Plan Apo 50x
[36] Thorlabs CT1A/M
[37] Q-Photonics QFLD-520-10S
[38] G&H 3350-199 with 1350AF-AEFO-01

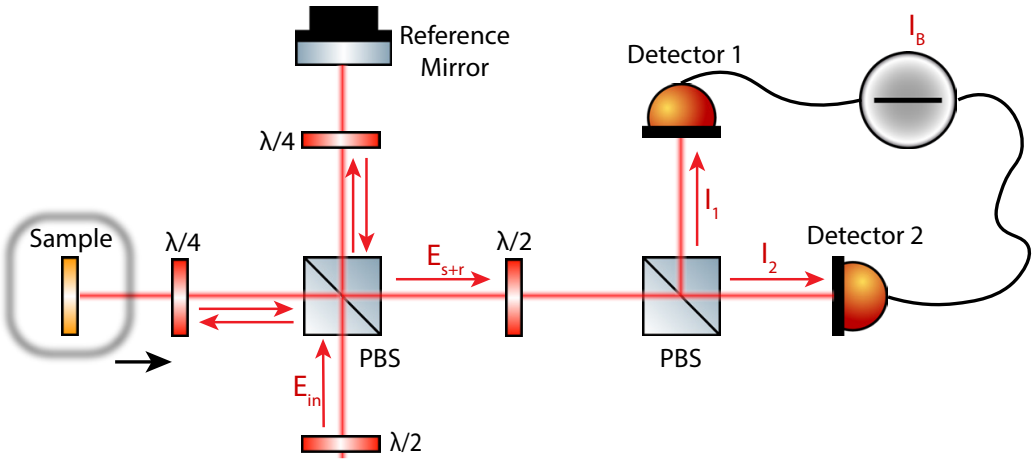

FIGURE 3.12: Sketch of the polarization based Michelson interferometer with balanced detection. The design of this setup roughly follows [149].

both cases, passing a $\lambda/4$ plate twice. This effectively results in a $\pi/2$ shift in the polarization, meaning that light that was reflected before at the PBS will now be transmitted, and vice versa. Like this, the two signals from both arms are collected and directed towards the right in Fig. 3.12, towards the second PBS.

On the way towards the second polarising beamsplitter, the polarisation state has to be adjusted once more. Otherwise, the two contributions would simply be separated again, and we would not obtain an interference signal on the detectors. This is done with a $\lambda/2$ plate, which can be rotated to obtain the optimal working point, where the two signals are equally mixed in both output directions of the second PBS. This naturally also leads to a scenario where both I_1 and I_2 are equal in amplitude. Subtracting the two intensities then gives us our balanced signal, removing signal offsets due to incomplete interference contrast and common amplitude noise.

Such a polarization based setup has a few advantages. First, it allows us to collect all light reflected from the sample and the reference mirror, as well as preventing back reflection of light into the laser diode. Such back reflections can lead to instability of the laser and would have to be avoided with optical isolators in such a setup. Second, a standard Michelson interferometer without balanced detection typically employs a single non-polarising beamsplitter and makes use of all four of its sides. To use two outputs of the cube for balanced detection and the two remaining sides for the reference arm and the sample arm, one needs to find other means to couple in the laser source. But in the case of a polarization based setup as presented here, we have additional paths to use and can avoid this issue. Finally, the setup becomes adjustable with regards to the splitting ratios of the polarizing beamsplitters, allowing us to perfectly balance the signal as well as to control the power incident on the sample, independently of the overall laser power.

After taking the difference of the two detected signals from the balanced detector[39], we are left with the following signal (see Appendix B),

$$I_B = \frac{1}{4} I_{in} \eta r \sin(\delta\phi) \tag{3.3}$$

where $\delta\phi$ contains the signal of interest as phase fluctuations, η is the interference contrast and r the sample reflectivity. In Fig. 3.13 (a), we show the expected balanced

[39] Thorlabs PDB230A

interference signal I_B, which is centered around zero. η can be optimized by ensuring that the beams originating from the sample and the reference mirror are spatially well overlapped. To this end, it is beneficial to ensure similar lengths in both arms to account for changes in the beam waist. Any additional constant phase offset ψ between the reference arm and the sample arm would lead to an overall phase $\delta\phi + \psi$ in Eq. 3.3. This constant phase can be adjusted with a piezo mounted under the reference mirror, allowing us to choose the region of the interference fringe with the highest sensitivity, *i.e.*, the region with maximum slope, where $\psi = 0$.

In practice, we not only adjust the sensitivity of the interferometer with the piezo[40] controlled reference mirror, but we also use it to stabilize the balanced signal with a PID feedback loop. Since we can scan more than one period of the expected signal in Eq. 3.3 with this piezo, and the wavelength of the laser is known, we can also use this to calibrate a conversion factor between the detected voltages and the actual displacement of the sample. Such a measurement is shown in Fig. 3.13 (b), matching the predicted signal shape in (a). Assuming an amplitude V_p of the calibration sine wave, and a measured voltage δV corresponding to $\delta\phi$, the displacement is then [149]:

$$\delta x \approx \frac{\lambda \delta V}{4\pi V_p} \tag{3.4}$$

Here it is assumed that $\delta V \ll V_p$.

In addition, assuming that the interferometer is at its optimal point of sensitivity, the lower limit for the displacement spectral density to be measured is given by [149, 150, 196],

$$\sqrt{S_x} = \frac{\lambda}{2\pi}\left(\frac{\eta_d I_{in}}{\hbar\omega}\right)^{-1/2} \tag{3.5}$$

where λ and ω are the wavelength and frequency of the laser and η_d is the overall detection efficiency of the setup. This detection efficiency also includes contributions such as the interference contrast η from before.

We show the estimated sensitivity we can achieve in Fig. 3.13 (c). Due to the difficulty in predicting all contributions that might affect η_d, we plot a large range of possible values. The white dashed line represents the expected peak signal for our hBN drums, calculated using Eq. 2.6. For a characterization of the properties of these resonators see chapter 6. Here, we assumed $m^* = 1 \times 10^{-14}$ kg, $\omega_{m,0}/2\pi = 2$ MHz and $\Gamma_m/2\pi = 300$ Hz. The region to the top right of this line represents the parameter space for which a signal should be observable.

In Fig. 3.13 (d), we show a displacement spectral density of one of our hBN drums. This spectrum was obtained by measuring the thermal motion at room temperature. Considering the input power of around 80 µW, this measurement is in good agreement with Fig. 3.13 (c) and shows that we can comfortably observe the thermal motion of our devices. We will return to this measurement in section 6.1 for further analysis.

Finally, to control and read out the interferometer, we again use a Red Pitaya in conjunction with the PyRPL software package, which we already used for the digital filtering of the PDH error signal of the cavity. However, here we do not use this digital filtering feature, but the many useful instruments provided, such as the network- and spectrum-analyser. We also use the lock-box feature provided by this software package. The lock-box allows us to implement the PID feedback loop of

[40] Thorlabs PA44M3KW

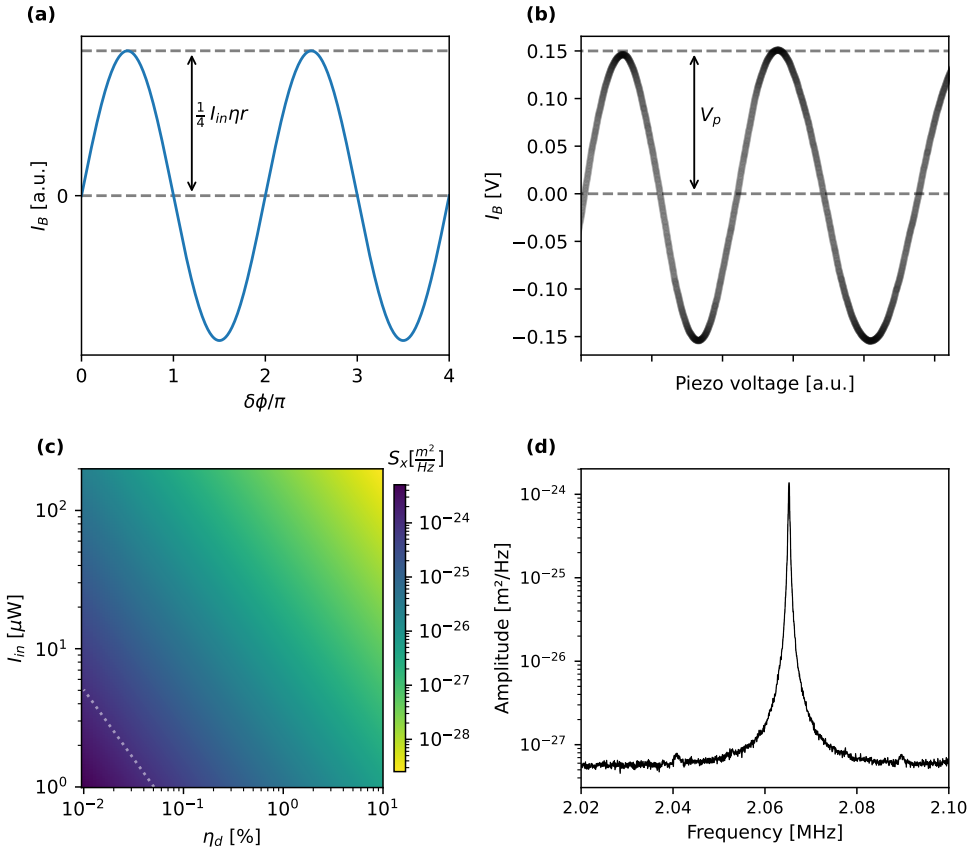

FIGURE 3.13: (a) Interference signal for large detunings of $\delta\phi$ according to Eq 3.3. (b) Measured calibration signal, obtained by detuning the reference mirror over several interference fringes. (c) Expected sensitivity range for our interferometer. The dashed line represents the expected peak signal for our hBN devices. (d) Shows a measured thermal spectrum of the fundamental mode of one of our hBN drums at room temperature (see chapter 6 for further discussion). The input power in this measurement was ∼80 µW.

the interferometer as well as a re-locking scheme. It re-engages the lock on a neighboring fringe of the interferometer when the setup drifts beyond the travel range of the piezo under the reference mirror, keeping the interferometer operational indefinitely. Of course, the built in instruments often lack the necessary performance for more sophisticated measurements, and when using the setup beyond simple characterization (as, for example, in chapter 6), the instruments will be substituted. We will note when this is the case and which instrument was used in the following chapters.

Chapter 4

Fiber Fabry-Perot Cavity

We will begin the discussion of the results with the characterization of the empty FFPC. Following the models developed in chapter 2, we will first investigate the cavity signals both in transmission and reflection, and extract figures of merit such as the finesse of the cavity. Afterwards, we will demonstrate our ability to operate this system in a stable and well controlled fashion. To this end, we will discuss our WL spectroscopy technique to measure the length of the cavity as well as the stabilization of the cavity with the PDH technique. The latter aspect was published in [151]. A more detailed discussion of the characterization of our FFPCs and the involved measurement techniques can be found in [200].

4.1 Characterization of the FFPC

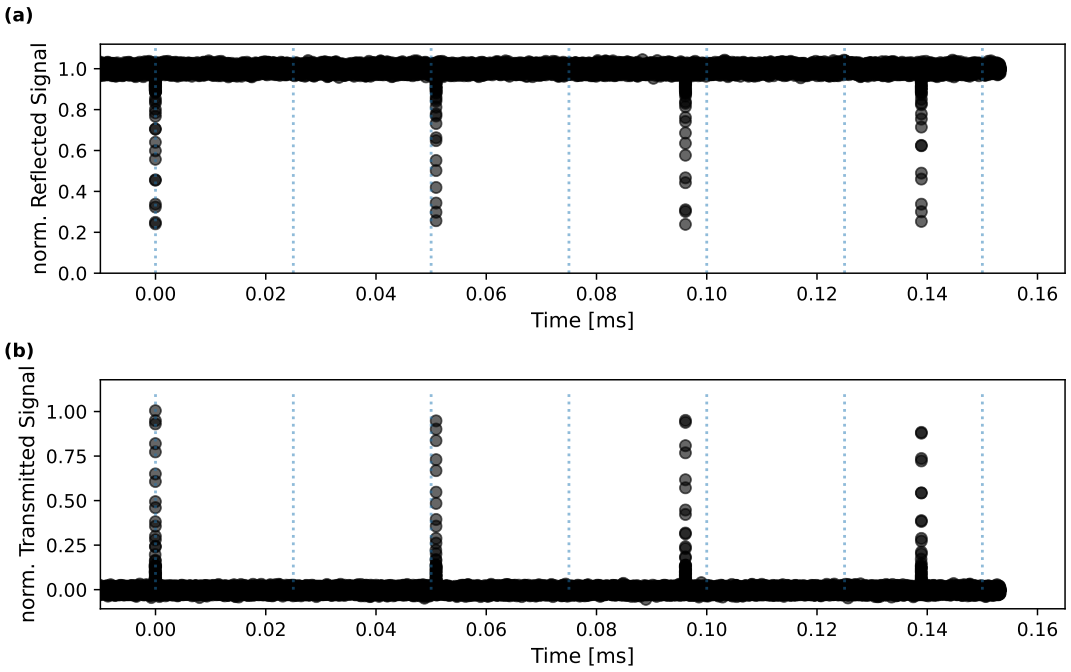

FIGURE 4.1: Long range scan of the cavity length, spanning several times the FSR: reflected cavity signal in (a) and transmitted cavity signal in (b). The vertical dashed lines serve as a guide for the eye to see the changing splitting between the resonances in this measurement due to the piezo's non-linear behavior. These measurements were taken with the z-positioner of the cavity.

We begin with a long range scan of the cavity length, covering several times the FSR of the cavity. At this point, we have not established the cavity length, but usually our FFPC is operated around $L_{Cav} = 20 - 40\,\mu m$. Similar to Fig. 2.5, we would expect repeating resonances spaced by an interval corresponding to the FSR of the cavity.

When looking at Fig. 4.1, we do see repeating cavity resonances, with the expected dip in the reflected signal and a peak in the transmitted signal on resonance. But the spacing between the resonances changes when comparing subsequent pairs. This is due to the fact that the cavity piezo tends to not respond linearly to the applied voltage. Even if we were able to convert this scan to units of frequency, this would make it difficult to establish the FSR and, subsequently, the cavity length L_{Cav}. This highlights the need to calibrate the cavity length by other means, as we will discuss in the next section.

We use the positioner for this task due to the limited range of the ring piezo. While this positioner is intended to operate as a slip-stick stepper, an offset voltage can be applied to generate a length scan that covers a much larger range than the ring piezo. To avoid acoustic noise and drifts that interfere with the recorded cavity scans, these measurements have to be recorded rapidly. In order to keep the positioner from taking steps during such fast scans, as intended by its design, we employ an S-shaped voltage ramp. This voltage ramp has an acceleration and a deacceleration phase limited to a fixed value, avoiding abrupt changes in velocity. The data is recorded between those (de-)acceleration phases.

Another important observation is the absence of higher order modes in the spectrum. As discussed in section 2.2.2, such higher order modes have a shift in resonance frequency compared to the fundamental cavity resonance. During the alignment process, such higher order modes are often visible, but once properly aligned, this particular cavity shows no visible higher order modes in such a scan. In fact, we even use the presence of such higher order modes to gauge our alignment. We have taken similar scans employing different fibers where higher order modes could not be suppressed to this extent [200].

To characterize the lineshape of the resonances and extract some characteristic values of our FFPC, we take a more detailed look at a fundamental resonance of such a cavity in Fig. 4.2.

In (a), we show the recorded signal of one of our FFPCs in reflection, revealing an obvious Fano lineshape. This matches our discussion in section 2.3.1 well and is due to mode matching between the fiber mode and the cavity mode. As expected, this feature is only present in the reflected signal of the FFPC and the transmitted signal shown in (b) follows a simple Lorentzian lineshape. This measurement was taken with an earlier FFPC that illustrated the asymmetric lineshapes particularly well, this indicates that the mode matching of the fiber mode to the FFPC was not ideal. All other measurements presented in this thesis were taken with a single combination of fibers, whose properties we discussed in section 3.1.1.

In order to extract the cavity linewidth, we require a frequency calibration of the x-axis of these scans. While it would be possible to estimate the displacement based on the known characteristics of the piezos involved, which could be converted to frequency when using an estimate for L_{Cav}, this would only be a rough approximation. Especially since the piezo's performance under load is not well calibrated.

We can instead use sidebands that we add to the signal by phase modulation with the EOM. These sidebands, in conjunction with the setup presented in section 3.1.3, not only produce the desired PDH error signal but also constitute a reference due to the fact that the sideband splitting is determined by the well known

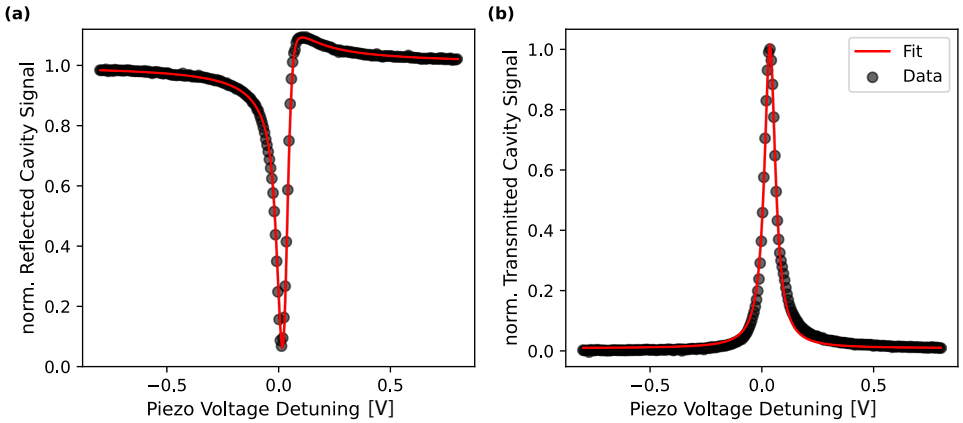

FIGURE 4.2: Zoomed in scan of a fundamental cavity resonance, the reflected signal is shown in (a) and the transmitted signal in (b). The signal in reflection is fitted with the expected fano lineshape as discussed in section 2.3.1, while the signal in transmission is fitted with a Lorentzian lineshape. These scans were taken with the ring piezo of the cavity.

value of our modulation tone. This tone was set to $\frac{\omega_{mod}}{2\pi} = 9.03\,\text{GHz}$ in the measurements shown here.

Fig. 4.3 (a) again shows the expected cavity signal in reflection, with a more moderate Fano lineshape, indicating better mode matching for this FFPC. In addition, the now present sidebands are included in the fit and serve as a calibration to give the spectrum as a function of frequency.

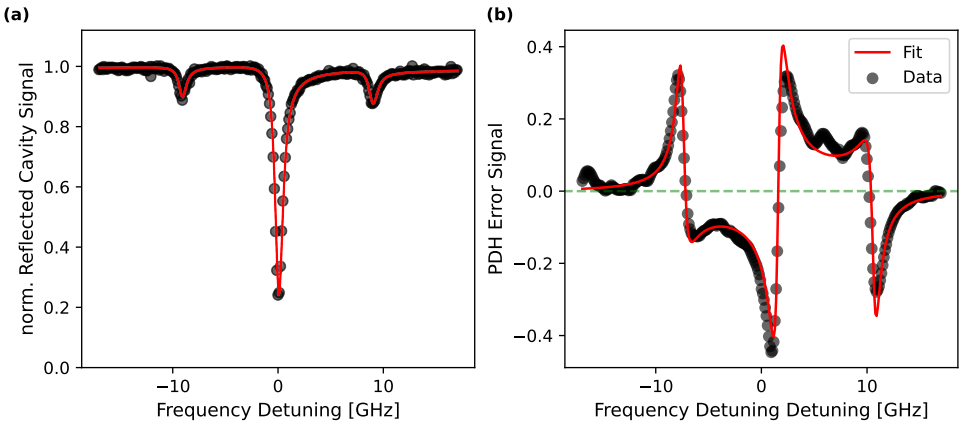

FIGURE 4.3: (a) Reflected signal as in Fig 4.2 (a), but now including sidebands at $\pm\omega_{mod}$ that serve as calibration for the frequency detuning. The sidebands are split by 9.03 GHz in this scan. (b) PDH error signal.

In Fig. 4.3 (b), we show the resulting PDH error signal and fit it with the model derived in section 2.2.3. It should reveal a linear region around zero detuning, which could be used to lock the FFPC, but the graph is slightly shifted to the right. This shift is due to an electronic delay in the acquisition, and we find that it has no impact on the locking itself, as we will see later. The PDH signal also shows additional linear regions detuned by $\frac{\omega_{mod}}{2\pi}$, these regions can be used to lock to the sidebands instead of the central laser frequency. We will make use of this in chapter 7, where we will lock to one of the sidebands using the angle signal, as discussed in section 2.2.3.

From the now calibrated spectrum in (a), we can extract the linewidth of the cavity from the fit in units of frequency, resulting in a value of $\kappa/2\pi = 0.88\,\mathrm{GHz}$. This measurement also reveals why we opt to perform our cavity scans by varying the length of the cavity and not the frequency of the laser source. While modern tunable lasers can comfortably span a few GHz, covering the cavity resonance in a short time, scanning an entire FSR would be more difficult. The frequency detuning necessary to cover several times the FSR would be well in the THz range for cavity lengths around 10-50 µm (see Eq. 2.26). This is difficult to achieve with a tunable laser, but the corresponding length detuning only amounts to values around 1 µm, which is well within the range of our piezo positioner.

4.1.1 White-light spectroscopy

As previously mentioned, precise knowledge of L_{cav} is essential in order to determine the other parameters of the FFPC. To estimate the cavity length, which will give us the FSR as well as the finesse of the cavity, we will now discuss the WL spectroscopy measurements. We use the setup described in section 3.1.3 to produce a spectrum outside the highly reflective coating of our cavity. Even outside the coating window, there will be a number of cavity resonances at wavelengths that depend on L_{cav}. This spectrum is then repeated for an array of cavity lengths, to produce a robust statistical measurement. While there are alternatives to this technique, as discussed in [200], WL spectroscopy is fast and does not require intrusive changes to the FFPC, making it our standard measurement of the cavity length.

In a naive approach, one could extract several estimates for L_{Cav} by extracting the distances of neighbouring pairs of resonances in the cavity spectrum, according to

$$L_{Cav} = \frac{\lambda_n \lambda_{n+1}}{2(\lambda_n - \lambda_{n+1})} \tag{4.1}$$

where n is the mode index of the resonance.

However, as pointed out in [152], one has to take a phase penetration depth $L_\phi = \phi_r/2k$ into account, where ϕ_r is the reflection phase obtained from the mirror coating simulation, which was shown in Fig. 3.1. The additional phase penetration depth is particularly important in the case of short micro-cavities. This leads to a modified expression

$$L_{Cav} = \frac{\lambda_n \lambda_{n+1}(\pi + \phi_n + \phi_{n+1})}{2\pi(\lambda_n - \lambda_{n+1})} \tag{4.2}$$

In Fig. 4.4, we compare a very simple model for the cavity transmission with the one featuring the simulated reflectivities for our mirror coating and the correction for ϕ_r.

To fit this data and extract an estimate for L_{Cav}, we go through several steps. First, we use a peak finder to identify the resonance positions in the spectrum. Real world data can contain some false positives, resulting in an overestimation of L_{Cav} or miss a peak, resulting in the opposite scenario. Because of this, we start with some estimation for possible values of L_{Cav} and hence the mode order n, to exclude such data points. We perform a fit using Eq. 4.2 for each pair of resonances and then take the average over each spectrum.

We then use these first results as an initial guess for a more involved procedure, where we fit all neighboring pairs of resonances in a spectrum simultaneously. This fit enforces a common mode number n in each spectrum. Like this, we explore an array of possible integer values of n, and finally pick the one that minimizes the error of the fit and use it to determine L_{Cav}. This procedure might seem elaborate, but in

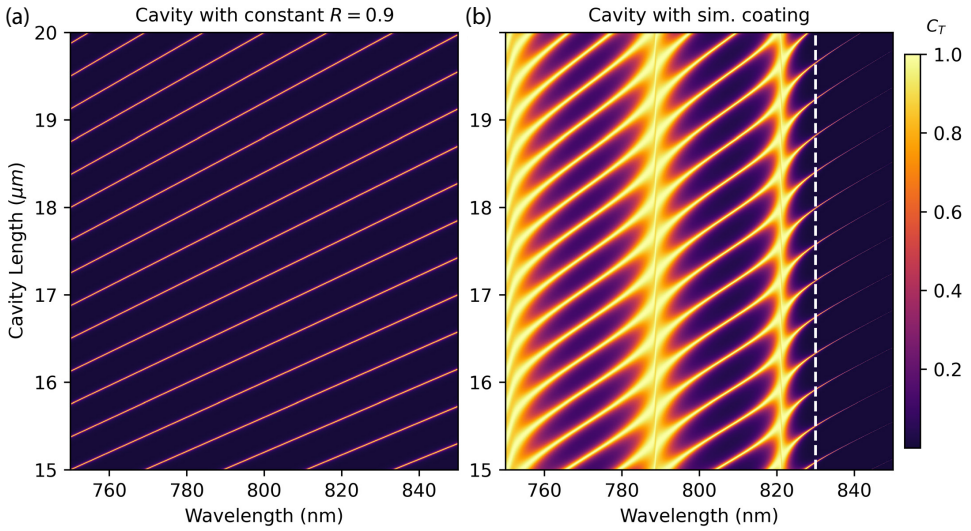

FIGURE 4.4: Simulated cavity transmission as a function of cavity length and wavelength for a constant mirror reflectivity (a) and with the mirror coating modelled according to our simulation, including adjustments of the resonance condition due to L_ϕ (b). The white dashed line indicates the onset of the highly reflective band of our coating.

practice, the measurement noise can easily lead to deviations on the order of a few µm when evaluating the data carelessly. Especially when operating at short L_{Cav} in the MIM configuration, such deviations can lead to collisions in the system when scanning the sample position, as the lateral dimensions of both the membrane and the fibers are much larger than L_{Cav} and not necessarily perfectly parallel in motion.

We show a WL measurement in Fig. 4.5 (a). To obtain this spectrum, we subtract the average of all lines from each spectrum, to remove background independent of the cavity length.

The result of the initial fit is shown in Fig. 4.5 (b), together with the estimated longitudinal cavity mode number in (c). This fit already appears quite reasonable and shows the expected increase in cavity length with piezo detuning. But the estimated error bars shown in red, and the somewhat inconsistent jumps in mode number in (c), reveal that it is not yet a very precise measure of our cavity length, as mentioned before.

The final fit, shown in (d), is now much more stable, and the statistical fit error is too small to be visible. The corresponding mode numbers are shown in (e) and do not show the same inconsistencies as (c). We attribute the non-linearity in (d) to a non-linear response of the piezo. The cavity length is given by the value at zero piezo detuning; in this case, $L_{cav} = 38.2\,\mu m$ has been estimated. Note that this measurement changes drastically depending on the cavity length. For short lengths, the measurement might be limited to 10 pairs of resonances in a spectrum, and the precise knowledge of the phase penetration depth has a larger impact. For very long cavities, on the other hand, the number of observed pairs can approach 100, giving stronger statistics. In this regime, the resolution of our spectrometer becomes a limiting factor. For our setup, we find that between 20 and 100 µm the technique works reliably.

We note that the fit error alone is not a very good figure of merit for the precision of this measurement, since it includes no systematic errors. To ensure that this measurement technique is reliable, we have compared the cavity lengths extracted from

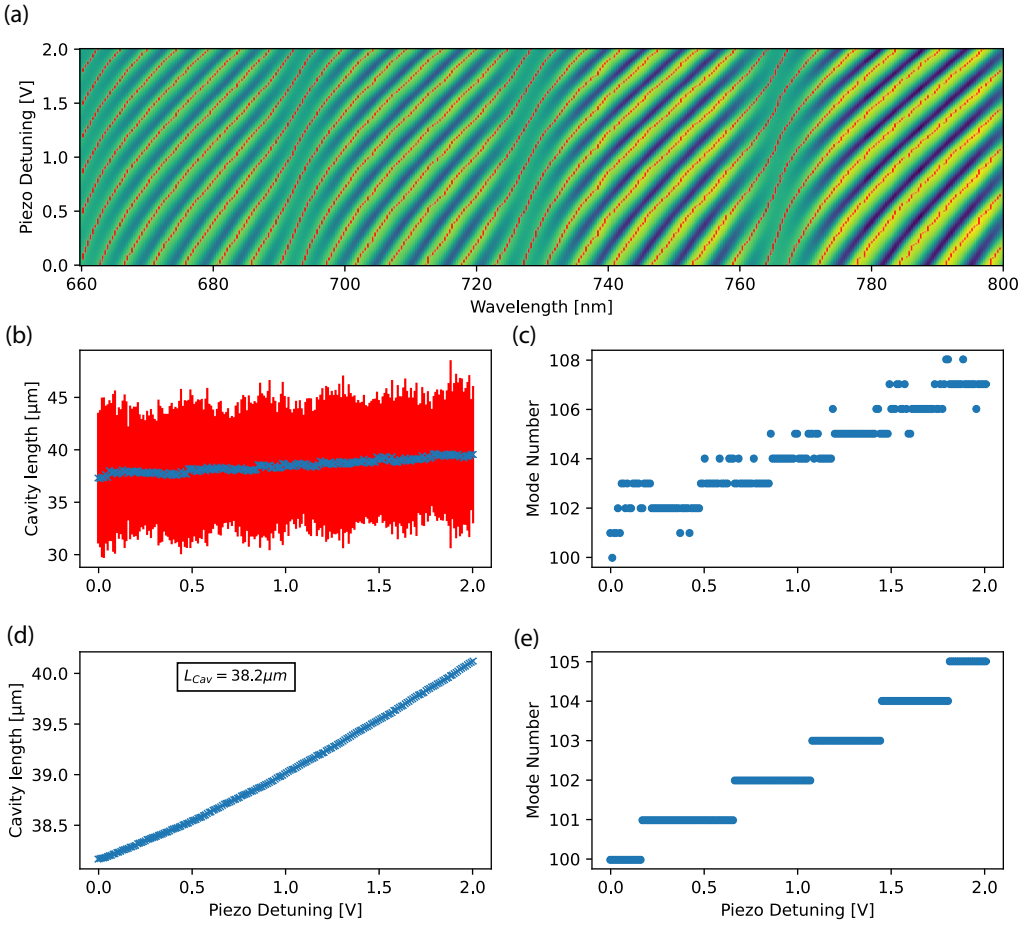

FIGURE 4.5: (a) White light spectrum in a wavelength range below the highly reflective window of the FFPC. The identified peak positions are shown in red. (b) The cavity length estimated with the initial fit in blue, error bars in red, (c) shows the corresponding longitudinal mode number. (d) and (e) show the same as (b) and (c), but for the final fit. Best estimate of the cavity length is shown in (d).

the fit to the ones measured with direct microscope imaging of the FFPC.

We imaged the FFPC with a digital microscope and used the known diameter of the optical fibers of 125 µm as a reference to estimate the cavity length, as shown in two examples in Fig. 4.6 (a) and (b). We then performed WL spectroscopy measurements to compare the two measurements, Fig. 4.5 shows one of the measurements in this series. Our WL measurements generally take into account the (phase) penetration depth in such a way that the obtained result corresponds to the physical separation of the mirrors. The crater depths in our FFPC only amount to a little over 1 µm, which we assume to be well below the precision of the estimation of L_{Cav} using the microscope images, and are thus unimportant.

Apart from the two examples in (a) and (b), we repeated these measurements until the fibers were almost in contact, staring at a length of over 400 µm. We show the absolute discrepancy as well as the relative discrepancy of the two measurements in Fig. 4.6 (c). Generally, the values are in good agreement, the large absolute discrepancy towards the longest cavity configurations amounts to an acceptable relative discrepancy. This is especially true considering that 400 µm is well beyond the maximal operational L_{Cav} for the NIR laser, as we will discuss later. Only the large

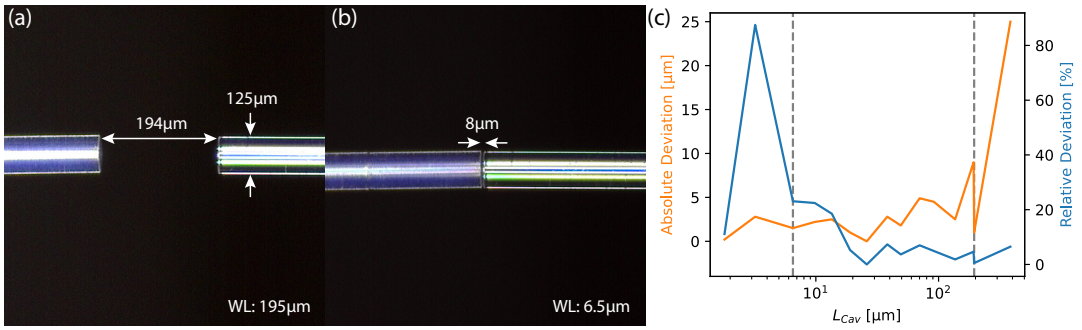

FIGURE 4.6: (a) and (b) show microscope images of the open FFPC, where we used the diameter of the fiber as reference to visually estimate the fiber separation. For comparison, the resulting L_{Cav} as estimated by WL measurements are given at the bottom of the images. In (c) we show the absolute (orange) and relative (blue) deviation between such visual estimations and WL measurements for a large range of cavity lengths. The dashed lines corresponds to the measurements in (a) and (b).

relative errors towards the shorter lengths appear problematic, but as shown in (b), estimating these lengths with the camera images is very difficult, and the error might simply be the result of this visual inaccuracy and not the spectroscopy technique itself. These extremely short values will hardly be relevant in our experiments as well, since we need space to introduce the mechanical resonator in between the fibers. We will typically work with a L_{cav} corresponding to the middle region in (c), where the WL spectroscopy measurements appear to be sufficiently reliable to align the system otherwise 'blind'.

We will revisit these WL measurements in chapter 7, where we use such spectroscopy in reflection to determine the distance between the input fiber and the membrane. There we will also discuss the alignment procedure of the complete system, including the FFPC and the membrane.

4.1.2 Finesse and clipping losses

Now that we have obtained a measure for the cavity length, we can estimate the finesse of our cavity. We do not only want to do this for a fixed L_{cav}, but over a large range covering the entire stable region of our cavity, as indicated in Fig. 2.7. To this end, we again start with the fibers almost in contact. We take a spectrum of the cavity to extract the linewidth as before (see Fig. 4.3), and also perform an initial WL measurement to calibrate our starting cavity length. We then take a step with the positioner to increase L_{Cav}, limiting the voltage of this step to be small enough to move less than one FSR of the cavity. This allows us to keep track of the longitudinal mode order across the stepping process and thus keep track of L_{Cav}. A detailed description of this measurement technique, and alternative estimations based on fitting of higher order modes, can be found in [200]. With this procedure, we keep increasing the cavity length, covering the range shown in Fig. 4.7. At the end of this measurement, we perform another WL measurement to make sure that we kept track of L_{Cav} correctly.

Having obtained spectra of the cavity signal for each length, we can now estimate the finesse using Eq. 2.28, shown as the black line in Fig. 4.7. While we can take WL measurements at much longer L_{Cav} than 60 µm, the losses have increased to the point where a measurement with the NIR laser is no longer possible.

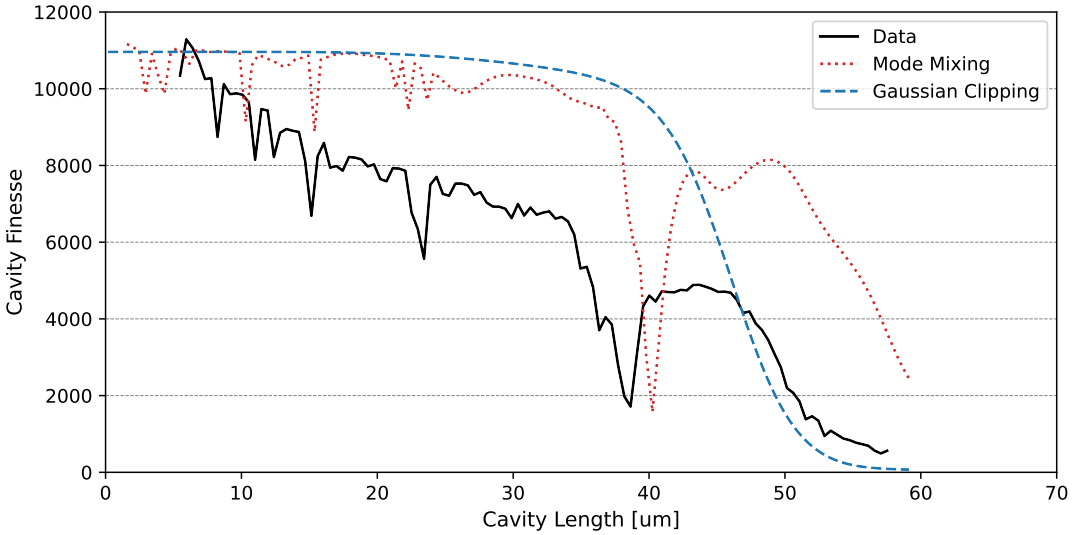

FIGURE 4.7: Cavity finesse recorded over a long range of cavity lengths. The finesse drop off is modeled using Gaussian clipping losses in blue, and a model based on mode mixing simulations in red. The Models have been normalized to the measured Finesse at the start of the measurement.

We compare the measured finesse with two theoretical models, both of which have been renormalized to match the measured finesse for very short cavity lengths. The first is a simple Gaussian clipping model based on Eq. 2.41. It captures the drop off between 40 and 60 µm of the finesse, corresponding to the cavity length where the waist of the fundamental mode of the cavity at the mirrors becomes comparable to the spherical diameter of the craters.

The second model is a mode mixing simulation based on the measured crater profiles of our fibers. These simulations are again discussed in detail in [200], further information can be found in [153]. Apart from the fact that these simulations take the real physical shape of our mirrors into consideration, they also take coupling between different transverse modes into account. These transverse mode couplings present themselves as dips in both the simulation and our measured data, corresponding to cavity lengths where the fundamental mode becomes resonant with a higher order mode, leading to an increase in losses and thus a drop in finesse.

Both of these models fail to capture the gradual drop off we observe in the measured finesse already before 40 µm. We believe that this drop off is due to an increased misalignment of the setup since the cavity axis does not perfectly coincide with the axis of motion of the piezo positioner. A realignment of the system after each step would have been an unreasonable time investment, but we are generally able to align the system to a better finesse for a given L_{Cav} than this measurement would indicate. Typically, a finesse of at least 8×10^3 can be achieved for cavity lengths below 40 µm, except for the regions where we couple to higher order modes.

4.2 Cavity Stability

As mentioned before, we generally have to perform these cavity scans in a quick fashion (10 to 100 Hz) to avoid the detrimental effects of mechanical and acoustic noise on the stability of the optical cavity. But for most measurements, this is not enough, especially when we need to stay at resonance, or at a precise detuning from

it. While a cavity such as ours tends to have a very large linewidth (and FSR) in terms of laser frequency, the corresponding changes in cavity length are exceedingly small, on the order of 100 pm. This means that we have to stabilize L_{Cav} to such a level so that we do not lose the cavity signal in a locking scheme, and to an even better level if we want to stay on resonance or maintain a precise detuning. In most similar systems [109, 116, 118–123, 154] sacrifices are made in terms of either finesse, tunability, or cryo-compatibility, where our goal is to maintain a high degree of all these parameters. We will naturally employ our PDH stabilization scheme to this end, but first we will discuss the passive stability of our system.

4.2.1 Passive cavity stability

Since the useful linear region of the PDH error signal is only present around a cavity resonance, we need to obtain a passive stability already close to the cavity linewidth to be able to employ our active stabilization. We also want to use our setup both at room temperature and under cryogenic conditions, each configuration having slightly different challenges, as we will see below.

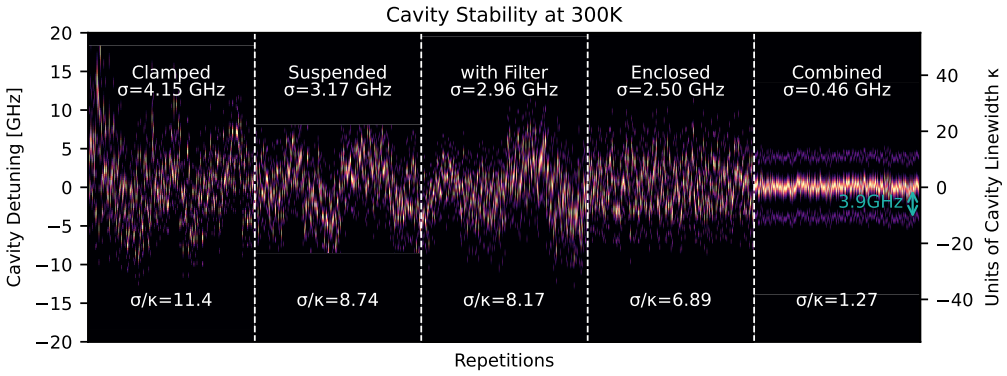

FIGURE 4.8: Repeated measurements of the light transmitted through the cavity while scanning its length around a cavity resonance, showing the impact of different system configurations on the stability of the FFPC. Scans were performed with the DC offset of the cavity positioner.

Most of the measures used to achieve high passive stability have already been discussed in chapter 3, and they can be summarized as follows: We rely on springs and a passive vibration isolation platform under our cryostat to shield the FFPC from mechanical noise. In addition, we design our probe as rigidly as possible.

In order to get a rough estimate of the cavity's stability, we perform repeated scans of the cavity transmission around a fundamental resonance. For this purpose, we again use the offset voltage of our positioner since the ring piezo is too limited in range. In our experience, the repeatability of these scans is good enough so that shifts in the cavity resonance position between scans should be dominated by mechanical noise, and not by the piezo's behavior. Thus, such a measurement allows us to measure the passive stability of our cavity length. Fig. 4.8 shows a selected set of these measurements that were carried out at room temperature. Each vertical line represents a cavity scan. We again employ sidebands produced by EOM modulation of the input signal, this time corresponding to a splitting of 3.9 GHz, to calibrate the spectra. These sidebands are present in all measurements but are easier to observe in the last part of Fig. 4.8 labeled "Combined".

A measure of the displacement noise is provided by the standard deviation of the main peak position, both in units of frequency and in terms of the cavity linewidth to better illustrate at what point our goal of stability on the order of κ is achieved. The cavity linewidth is estimated to be 0.36 GHz. This estimation was obtained by fitting each spectrum in Fig. 4.8 with a Lorentzian and taking the average linewidth, as well as taking the average of the observed sideband splitting. We chose such a statistical approach since the quality of the spectra in this measurement was rather limited compared to the ones shown in section 4.1. This is due to the slower scan speed of the piezo positioner compared to the ring piezo, making the measurements more susceptible to noise.

We again use WL spectroscopy to determine a cavity length of $L_c = 25\,\mu m$. The measurements shown were affected by thermal drifts, leading to a slope in the data which was removed. Such thermal drifts are easy to compensate for when employing active stabilization and are minimized mostly by the conditions in the room and the choice of materials of the probe.

A number of different experimental conditions were studied to shed light on what is required to best passively isolate the system from external noise. These conditions are combinations of employing the spring suspension in the probe, covering the probe with the vacuum can, putting it under vacuum, and putting it into the cryostat (without cryogenic liquids) on top of the passive vibration isolation stage. In addition, we have found that electronic low-pass filtering is useful to remove noise that acts on the cavity length through the piezo elements in the system. The specified output noise of the amplifiers[1] is less than 5 mV (RMS), which corresponds to a change in cavity length by 5 times the cavity linewidth at room temperature. The filter used is a third-order low-pass filter at 10 Hz. It is important to note that not only the piezos acting directly along the cavity axis play a role since, due to the shapes of the mirrors, even perpendicular motion can affect L_{Cav}. These piezos could also induce additional vibrations in the system. In general, piezo elements that are not needed for a certain measurement are grounded and disconnected to avoid ground loops.

As a baseline, we clamp the top and bottom plates (see Fig. 3.3 (a)) with a metal bridge to circumvent the springs in the system. The probe is not covered by the vacuum can, is outside of the cryostat, and no electrical filters are used. The resulting stability of this configuration is shown in the first section of Fig. 4.8, labeled "Clamped", with noise levels several times larger than κ.

The second configuration, labeled "Suspended", differs from the first only in that the titanium frame is suspended using springs, resulting in a slight improvement.

The third configuration, labeled "with Filter", differs from the first only in that the electronic filters are activated to reduce the noise of the voltage driving the piezoelectric positioners.

The fourth configuration, labeled "Enclosed", differs from the first by including both the suspension of the titanium frame via springs and its enclosure inside the vacuum can. The effect of the enclosure could not be tested without the spring suspension since the metal bridge used for clamping does not fit inside the vacuum can. Comparing this configuration to the one with only the suspension, it appears that the slower modulation of the cavity length is suppressed. This indicates that these modulations are likely caused by air currents or thermal fluctuations in the air. Whether or not the system is under vacuum does not notably affect the mechanical noise.

[1] Attocube ANC300

Finally, the fifth configuration, labeled "Combined", includes the spring suspension, the electronic filters, and the enclosure in the vacuum can. The combination of these measures results in passive stability close to the cavity linewidth, thus bringing the system into a regime where active PDH stabilization can be employed. The clear improvement in this final configuration compared to all the others indicates that all the measures play a significant role in the stability of the system and are necessary to reach the desired effect.

We have analysed other configurations not shown here, such as the "Enclosed" configuration under vacuum, but there was no observable difference. While some measures might have small effects, they are generally overshadowed by the difference caused by the electronic filtering and the spring suspension, which appear to be the key elements in this system. We have thus omitted the configurations that did not result in further insight into the system's behavior.

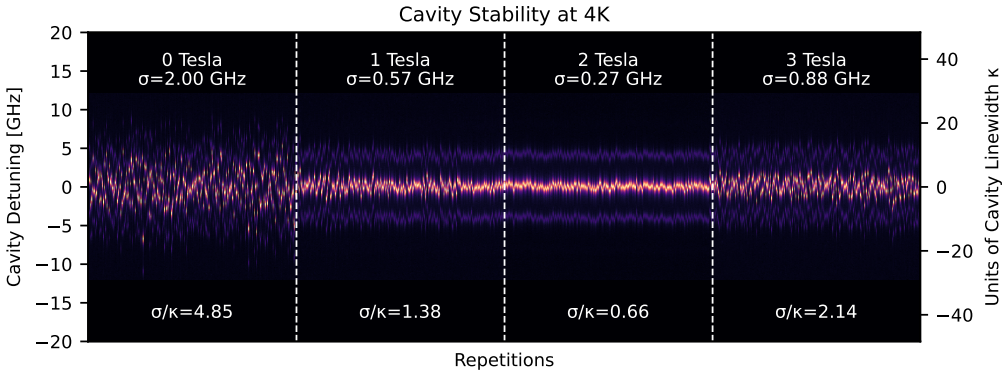

FIGURE 4.9: Same measurement procedure as in Fig. 4.8, but this time the impact of damping due to a vertical magnetic field is studied at 4 K.

We now turn to measurements at 4 K, where the probe is inserted into the cryostat in liquid helium. Naturally, we have no choice but to keep the system suspended and under vacuum at low temperature, making the same measurement series as in Fig. 4.8 impossible. The electronic filters do not have a noticeable effect under these conditions, most likely because of the 10-fold reduction in the piezoelectric coefficient of the positioners from room temperature to 4 K.

In Fig. 4.9 instead, we study the impact of the application of a vertical magnetic field with the superconducting magnet in our cryostat. Such a magnetic field dampens vibrational noise via eddy-currents induced in the suspended conducting frame of the probe, leading to additional passive stabilization of the system.

We again start with a baseline configuration in which no magnetic field is applied. Interestingly, the system shows degraded stability compared to the comparable configuration, labeled "Combined", at room temperature. This deterioration may be caused by bubbling of the liquid helium that surrounds the probe or bubbling of the liquid nitrogen in the outer jacket of the cryostat. A temperature-dependent change in the mechanical properties of the probe materials could also lead to differences in mechanical stability.

We then apply a magnetic field of 1 T, where the damping due to the magnetic field brings the stability to better than a cavity linewidth and thus into a regime in which the cavity can be actively stabilized. At 2 T of applied field, the stability is even further increased due to an increase in the damping effect. However, a subsequent increase to 3 T leads to an increase in vibrational noise. We believe that this

may be the result of residual magnetization in some part of the suspended system, causing it to deflect and come into contact with the vacuum can. Once the lower parts of the probe are in contact with the vacuum can, mechanical noise can bypass the spring suspension and affect the cavity more directly.

In summary, we have found configurations both at low temperature and at room temperature where the passive stability could be improved to below the cavity linewidth κ, putting the system into a state where we should be able to employ active feedback stabilization. Operating the system at liquid nitrogen temperatures is challenging since the deleterious effects of the boiling liquid are already present, but we cannot employ the superconducting magnet for damping, leaving us in a configuration similar to the first one in Fig. 4.9.

4.2.2 Active stabilization

While the system is kept in one of the stable configurations outlined above, the cavity length is locked with respect to the fixed laser wavelength via active feedback. The feedback signal is generated using the PDH setup introduced in section 3.1.3 and applied to the piezoelectric ring, which modulates the cavity length at a sufficiently high bandwidth.

When simply using the PDH error signal in conjunction with a PID feedback loop, the cavity can in principle be locked, but this lock is limited due to mechanical resonances in the system. These resonances can be observed when recording the transfer function of the system by using a network analyser to record the systems response to mechanical modulation applied with the ring piezo, as can be seen in Fig. 4.10. These resonances are not only frequencies at which the feedback applied to the ring piezo drives the system particularly well, but also anti-resonances that respond poorly compared to the average level. This means that when increasing the gain of the PID feedback signal, the system will become unstable and start ringing at the strongest resonance, while at the anti-resonances, the feedback would require a much higher gain for effective stabilization.

Using a digital IIR filter, we can then smooth out the response, increasing the maximal stable gain and bandwidth of the lock. The digital nature of this filter has the additional advantage that it can be adjusted to accommodate changes in the transfer function due to temperature drifts, changes in alignment, or in the probe itself. All measurements, as well as the filtering, are done with the PyRPL software package running on a Red Pitaya FPGA.

In Fig. 4.10 (a) and (b), we use the network analyser module to drive the ring piezo at a frequency that is ramped between 100 Hz and 30 kHz. This measurement is first performed with the system in a quasi open-loop configuration, *i.e.*, the feedback signal sent to the ring piezo is low-pass filtered at only 10 Hz. This is so as to only cancel low-frequency drifts of the cavity resonance, such as thermal effects, to maintain the cavity signal while having no effect on the mechanical noise at higher frequencies.

The result is shown in blue and reveals several regions with clear peaks or dips in the response. In (c) and (d), we zoom in around the most prominent resonances in the transfer function. This group of resonances, between 800 Hz and 2 kHz, is likely caused by resonances of the piezo positioners, roughly matching the manufacturer's specifications. They are an expected downside of our system, which favors tunability to a large degree. Changes in alignment, via displacement of the positioners, alters their amplitude and slightly changes their frequency, making these resonances particularly tricky to deal with.

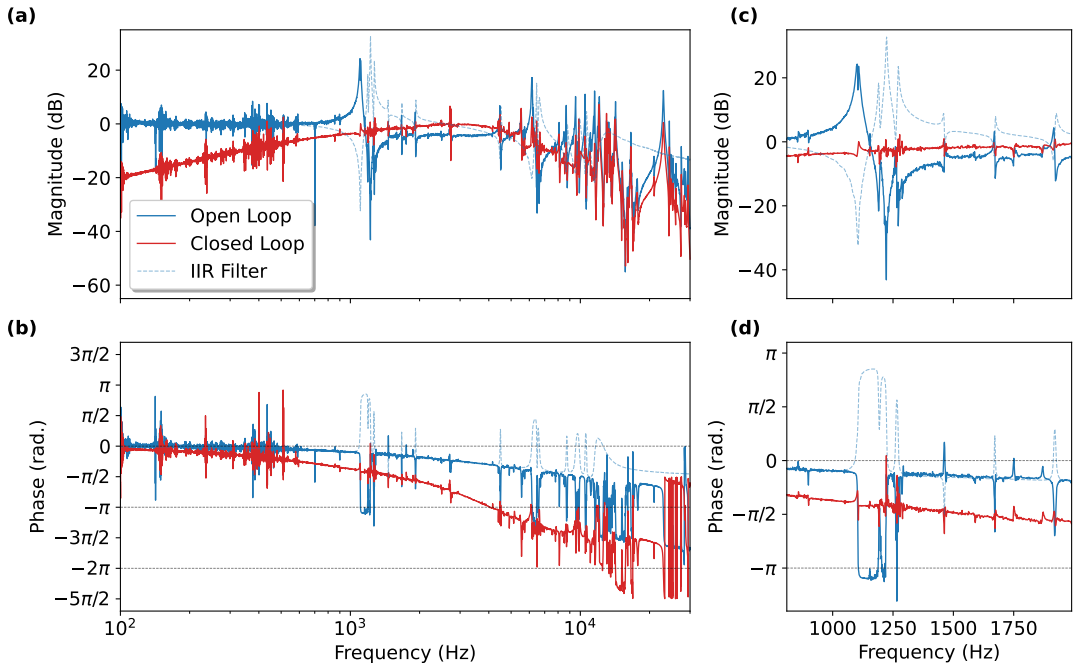

FIGURE 4.10: Feedback loop transfer function (amplitude (a) and phase (b)) of the cavity lock: In blue, the system's response in the quasi-open loop configuration. It is possible to identify many resonances in the system, mostly due to the piezo positioners and the cantilever modes of the fiber mirror. The dotted line shows the IIR filter designed to suppress most of the system's resonances below 20 kHz (limited by the computational power of the FPGA itself). The red line is the system response when the IIR filter is enabled. (c) and (d) are a zoom in around the most problematic region around 1 kHz.

The next prominent resonances appear above 6 kHz, and we believe these are at least in part caused by the cantilever modes of the overhanging fiber mirrors. Their frequencies match the expected resonance frequencies for fibers protruding by about 4 mm from their support ferrules. This significant overhang is the result of some of the material deposited for the highly reflective coating attaching itself to the side of the fiber. When retracting the fiber into the ferrule, which has a very low tolerance of only 1 µm for the central bore, this results in the fiber becoming wedged with a overhang of several mm.

Finally, an overall low-pass filter behavior can be observed. This is simply the result of the limited bandwidth of the ring piezo, leading to a decrease in response.

The IIR filter is designed in the IIR module of the PyRPL GUI by manually placing zeros and poles, in order to obtain a filter that is as close to the inverse of the system transfer function as possible. The result is shown as the dotted blue line in Fig. 4.10. We focused on the most prominent resonances in the transfer function, in particular, the region shown in (c) and (d), while neglecting many of the numerous smaller features. A maximum of 13 pairs of zeros and poles can be used, limited only by the computational power of the Red Pitaya, together with an additional real pole that acts as a low-pass filter to stabilize the filter response.

To gauge the effectiveness of the filter, we again perform a response measurement, but this time in closed-loop configuration, *i.e.*, with the feedback signal being sent to the piezoelectric ring after the application of the IIR filter. The closed-loop response, shown in red in Fig. 4.10, now shows a strong reduction in the system's

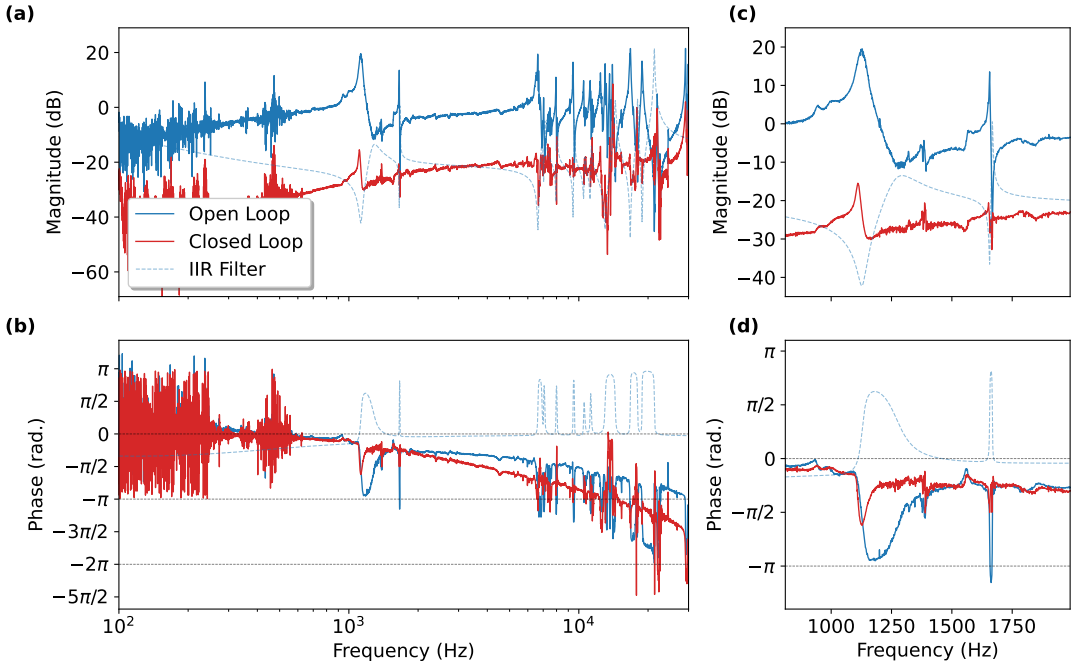

FIGURE 4.11: Same measurement as in Fig. 4.10 performed at 4 K. The transfer function has changed significantly after cooling the probe down and a new IIR filter has to be designed. The most problematic region is still between 1 and 2 kHz.

mechanical resonances. This allows us to increase the gain of the feedback much further without causing the system to ring. The stabilization loop now has a bandwidth of 4 to 6 kHz at room temperature (corresponding to the frequency at which the phase crosses $-\pi$ [133, 155]).

At low temperature, the transfer function of the system shows several differences, making it necessary to re-design the filter. The same procedure is again employed and the resulting filter, as well as the open- and closed-loop measurements, are shown in Fig. 4.11. Like this, we achieve a feedback loop with a bandwidth of 10 kHz at 4 K.

Long term stability

The stability achieved by the system is demonstrated by recording the FFPC's transmission signal over an extended period of time, as shown in Fig. 4.12. The plot in (a) shows the transmission signal with the cavity locked over a period of 3 h. Such stability can be sustained for much longer periods without the need for a re-locking system. The slow decrease in signal is the result of drifts in the input laser power, which is not stabilized in this measurement. A plot of a 10 s segment of the locked transmission signal, shown in (b), reveals that the transmission is capped by a maximum value with the cavity on resonance, as expected. The cavity detuning stays within a few percent of this maximum. Given the cavity linewidth of around 50 pm, this corresponds to better stability than a few pm. The seemingly narrower line in (a) is the result of a lower resolution in time binning, effectively averaging the signal. Unfortunately, the data volume would not have been manageable over this long period, employing the same settings as in (b).

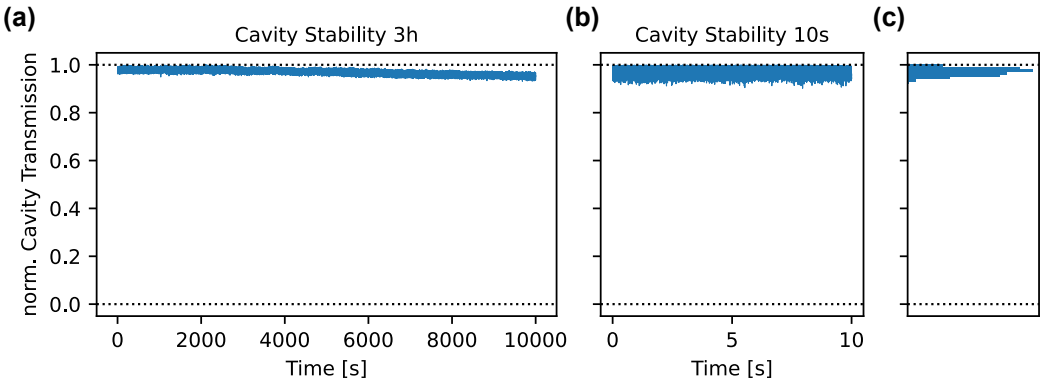

FIGURE 4.12: Long term stability of the cavity transmission signal while the cavity is locked. (a) shows a stability measurement over 3 hours, the dashed line at 1.0 showing the maximum cavity transmission; we attribute the drift towards lower values of the cavity transmission signal to power instability of the optical measurement setup, not to an instability of the cavity itself. (b) shows a shorter term version of the same measurement, revealing a clearly visible maximum value when the cavity is on resonance, again shown by a dashed line at 1.0. (c) shows a histogram of the measurement points taken in (b).

Fig. 4.12 (c) shows a histogram of the data shown in (b), revealing that the cavity transmission predominately stays very close to its maximal value, while only occasionally dropping to the lower boundary of the signal visible in (b).

4.2.3 Low power operation

Even though high frequency detectors, such as the one used for our active stabilization scheme, are generally not as sensitive as their lower bandwidth counterparts, we can operate our system at remarkably low intra-cavity powers. This is mostly achieved by amplifying the signal with an optical amplifier in conjunction with the filter setup presented in section 3.1.3. This is of particular interest in an optomechanical system involving nanomechanical resonators, where a strong optical power quickly leads to unwanted effects such as heating of the mechanical resonator, auto oscillations, or non-linear effects [47, 58, 156]. To demonstrate the performance of our setup, we perform active stabilization as before while reducing the optical power coupled into the cavity.

In Fig. 4.13 (a), we show long term measurements of the recorded cavity transmission as in Fig. 4.12, while decreasing the injected laser power. We estimate the number of photons present $|\overline{\alpha}|^2$ based on the input power P [18],

$$|\overline{\alpha}|^2 = \frac{\kappa_{ex}}{\Delta^2 + \frac{\kappa^2}{4}} \frac{P}{\hbar\omega_L} \tag{4.3}$$

where κ_{ex} are the coupling losses. We estimate the injected laser power by measuring these losses in our setup where possible, but also by comparing our reflected signal with the one in transmission. Since we use a multimode fiber in transmission, we can reasonably assume a coupling close to unity, which is then directly connected to a detector, giving us a good estimation of the intra-cavity power. Comparing the estimated intra-cavity power based on our reflected signal agrees well with the one estimated based on the transmitted power, indicating that we have a good understanding of the coupling losses in our system.

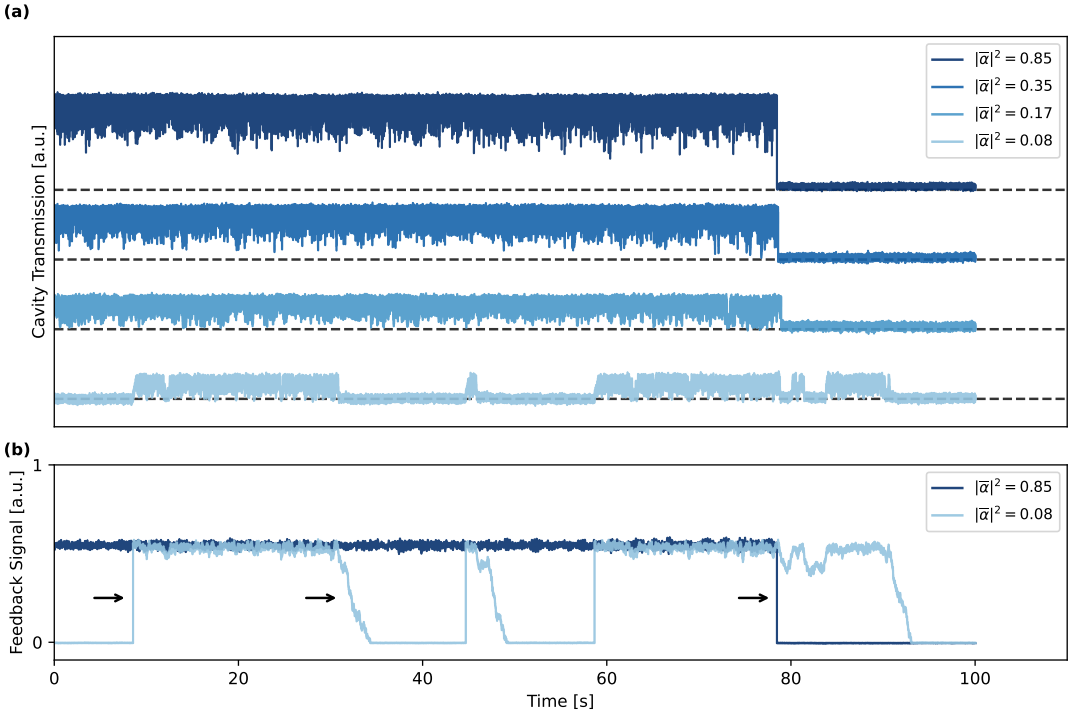

FIGURE 4.13: Cavity lock at low optical powers. (a) shows long term measurements of the cavity transmission, for clarity the lock was deactivated towards the end of the measurement to show the baseline signal. Each measurement has been vertically offset for clarity, the dashed lines indicate the noise floor. The estimate intra-cavity photon number is shown in the legend. In (b) the feedback signal is shown for two of the measurements in (a). For $N_\gamma = 0.08$ the lock failed sever times and had to be re-engaged. The arrows show the abrupt changes when the lock is intentionally turned on or off, and the less abrupt decline (second arrow) when the lock fails.

The feedback signal, which is applied to the ring piezo of the FFPC, is shown in (b) for the measurement at the highest and lowest power. To illustrate the change in signal quality, we turn the active stabilization off at around 80 s into the measurement for all but the lowest power setting, for which a stable lock could not be maintained for the measurement duration. This turn-off point is indicated by the third arrow in (b) and the corresponding signal drop in (a). The first arrow indicates the activation of the active stabilization in the measurement at $|\overline{\alpha}|^2 = 0.08$ while the second arrow shows the less abrupt failure of the lock.

These measurements show that we can comfortably operate our system at powers corresponding to well below a single photon in the cavity and maintain a stable lock indefinitely, highlighting the effectiveness of our stabilization as well as the efficiency of our detection scheme. The main limiting factor in these measurements is the lack of sensitivity of the high bandwidth photodiode: Surprisingly, for these low power levels, a PDH error signal is no longer visible when performing a scan, as in Fig. 4.3, yet the lock remains effective.

Chapter 5

Fabrication of hBN Drum Resonators

Having discussed the cavity, we will now introduce the mechanical element of our FFPC-MIM system, the hBN drum resonators. In this chapter, the focus is on the design and fabrication of these devices, while in chapter 6, we will go over a thorough mechanical characterization. Since low optical absorption is a key requirement for MIM-optomechanics devices, we will also discuss different cleaning procedures and their impact on organic residue deposited during the fabrication process. Finally, we will give an overview of a few devices that have been successfully fabricated and were used in the measurements shown in the subsequent chapters.

5.1 Device Design

Our goal was to fabricate hBN microdrum resonators that could be combined with our FFPC to form a MIM system. A first choice to be made is the one between mechanically exfoliated flakes or CVD grown sheets of hBN. Mechanical exfoliation is generally viewed as a convenient way to produce very high quality flakes of 2D materials at the cost of thickness control and yield [157]. CVD grown films, on the other hand, can be well controlled and cover a large area, making them a good choice when scalability becomes an issue. But their quality is still considered inferior by many, even though progress is continuously being made [158] and the concept of quality depends on the exact material and application [159].

In the case of hBN in particular, finding a mono-layer flake by exfoliation is known to be a difficult endeavor [160], while it is easy to obtain multi layer flakes of around 50 nm ($\approx$ 150 layers [77]) by exfoliation. The situation is different for CVD grown hBN. While mono and few layer films of many 2D materials are commercially available, thicker layers are more difficult to find. This makes CVD grown hBN a natural choice when aiming for very thin devices, as in [45]. However, since we are interested in MIM optomechanics, we aim for significant reflectivity, yielding a stronger optomechanical coupling. This requires relatively thick hBN flakes as shown in Fig. 5.1, making exfoliation a natural choice for our application.

Another important question is the nature of the frame that supports the microdrum. The typical approach of directly exfoliating [43, 93] or stamping [161] 2D flakes on top of a thick substrate with trenches or cavities is unsuitable for our application. On one hand, such a substrate does not have optical access from both sides. On the other, it is too thick for the short cavity lengths of our FFPC. We thus have to choose a thinner frame to support our drums, with holes all the way through, to enable optical access.

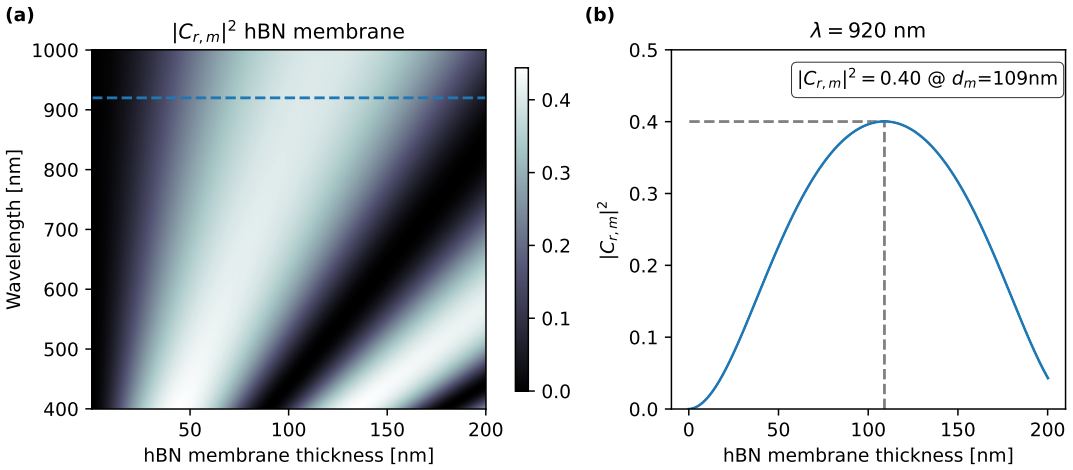

FIGURE 5.1: (a) Reflectivity of a hBN membrane as a function of wavelength and flake thickness. (b) Linecut along the blue dashed line in (a), representing 920 nm, the wavelength we typically work with in our FFPC.

The size of these holes determines many of the mechanical properties of the drums, such as their resonance frequency and effective mass. Since it is difficult to find flakes of much larger lateral dimensions than 50 µm while maintaining good flake quality, (*i.e.*, no steps, folds, cracks, or other imperfections) this poses an upper limit. Some room for error has to be included for the deposition precision of our transfer process, as well as some area for the flake to adhere to the frame, so the hole diameter should be considerably smaller than this upper limit. A lower limit is posed by the waist of the cavity mode and the associated clipping losses, discussed in section 2.2.1 and section 2.2.2. The drum diameter also has a significant impact on the resonance frequency of the devices (see Eq. 2.14).

In practice, we find holes with a diameter of 20-30 µm a good choice. Fortunately, such substrates are commercially available as Si_3N_4 membranes with hole grids by Norcada, a sketch of such a chip is shown in Fig. 5.2.

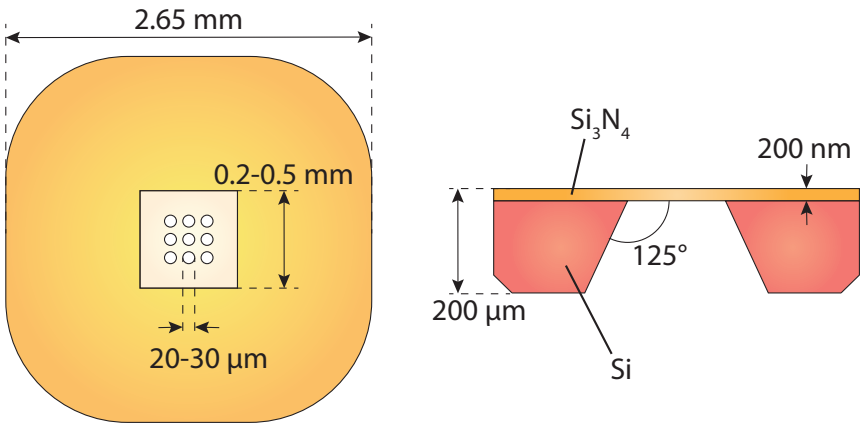

FIGURE 5.2: Dimensions of a typical Norcada chip. The diameters of the window and the holes are given in ranges since we used three different window sizes (0.2, 0.3, and 0.5 mm) and three different hole diameters (20, 25, 30 µm).

These devices are based on a 200 µm thick Si-chip with a 200 nm Si_3N_4 film on top. A backside etch creates a cavity and leaves a suspended square Si_3N_4 membrane supported by a Si frame. This backside cavity is large enough to insert one of the fibers of our FFPC, allowing for short cavity lengths. The hole grid is etched into the Si_3N_4 membrane, over which a hBN flake can be suspended, forming drum resonators. The hole grids are designed in such a way that there is a central hole which coincides with the center of the square membrane.

While chips with a low stress Si_3N_4 film and specifications within the ranges outlined in Fig. 5.2 are available as standard devices, we have opted for an array of custom made devices, which includes chips with high stress stoichiometric ($\sim$ 1 GPa) Si_3N_4 films and a wider selection of geometrical parameters. The reason for this choice concerns the mechanical properties of the Si_3N_4 membranes and will be discussed in the following section.

5.1.1 Estimation of device properties

The expected resonance frequencies for the hBN drums can be estimated using Eq. 2.14. In Fig. 5.3 (a), we show the resonance frequency of the fundamental mode of the hBN drum for a span of dimensions that could be reasonably fabricated. While the Young's modulus of suspended hBN flakes has been measured [44, 45], the results showed a high variance and did not match theoretical predictions [72]. As a starting point, we will use the average value of 392 GPa reported in [44], since the devices fabricated there were rather similar to the ones presented in this thesis.

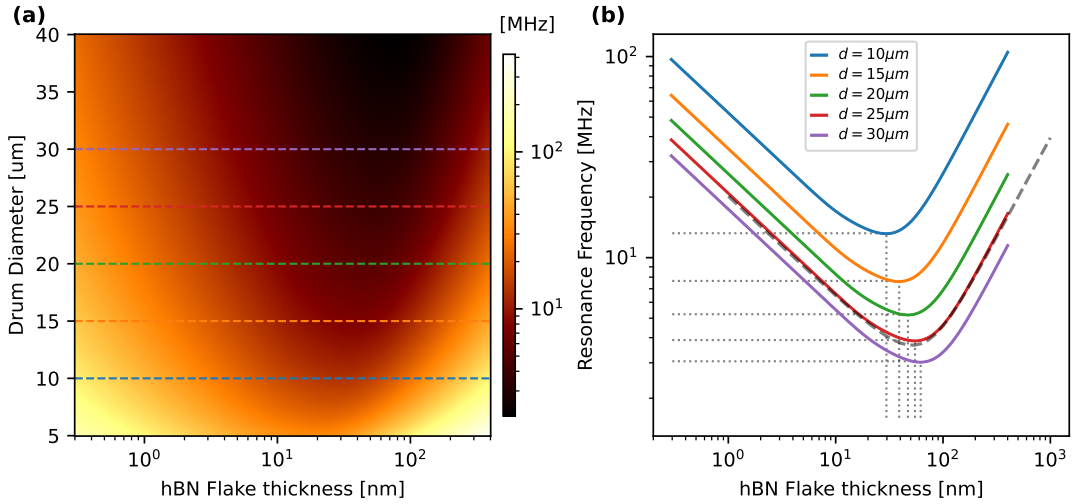

FIGURE 5.3: (a) Resonance frequency of the fundamental mode of the hBN drum as a function of drum diameter and membrane thickness. (b) Linecuts of (a) with the minima of each curve highlighted with dotted lines. We also compare the analytical solution plotted here with a Comsol simulation (dashed line) for a diameter of 25 µm, finding excellent agreement.

As already shown in Fig. 2.2, there is a transition from the membrane to the plate regime, explaining the lower frequencies for moderate thicknesses. We have plotted the expected frequencies for a few typical drum diameters in Fig. 5.3 (b) to make the exact values more obvious. It becomes apparent that one needs to make rather large drum resonators that are thick enough to be situated in the transition regime

between a membrane and a plate when aiming for low resonance frequencies. Resonance frequencies can instead be maximized by making small drums with either very thin or very thick flakes.

Since the thin Si_3N_4 membrane has to be treated as a mechanical oscillator on its own, which might couple to the hBN drum resonators we want to investigate, we simulated the expected resonance frequencies of these devices using Comsol multiphysics in Fig. 5.4.

The size of the backside cavity in the chip determines the size of the Si_3N_4 membrane. It is limited by our ability to insert a fiber when aligning the system, meaning that it should be significantly larger than the outer fiber diameter of 125 µm. Since we wanted our devices to not be too fragile for our transfer process, we kept the Si_3N_4 film at a thickness of 200 nm.

Looking at Fig. 5.4, we expect the resonances of the Si_3N_4 membrane to start at a few hundred kHz for a low-stress film (250 MPa) and at around 1 MHz for a high-stress film (900 MPa). These resonances quickly become denser when going to higher frequencies.

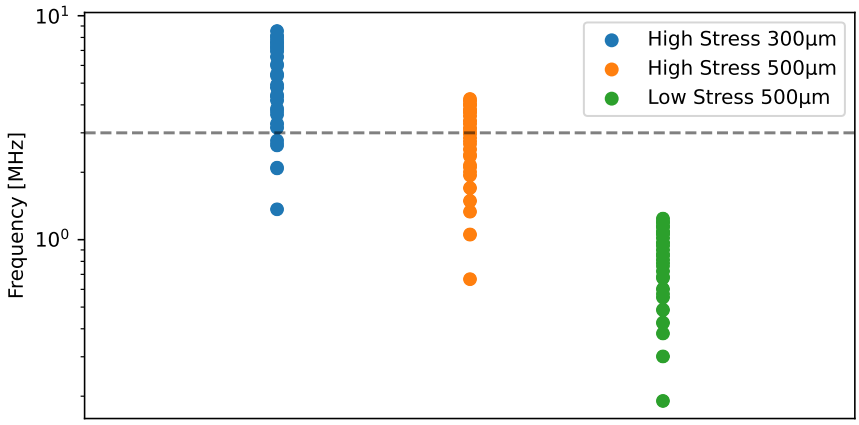

FIGURE 5.4: The first 60 modes of Si_3N_4 membranes with different sizes and stress configurations. The dashed line is set to 3 MHz and visualizes the lowest expected resonance frequency for our hBN drum.

Since we not only need to separate the resonance frequencies of the two resonators involved, but also have to consider limitations in the bandwidth of our excitation piezos and detectors, we would like to keep the resonance frequency of the hBN drum as low as possible, while pushing the ones of the Si_3N_4 membranes as high as possible. As an estimate for the lowest possible hBN resonance frequency, we chose 3 MHz (dashed line in Fig. 5.4), which corresponds to the lowest value in Fig. 5.3. It is also worth mentioning that the zero point motion is inversely proportional to the square root of the resonance frequency (see Eq 2.9), which directly affect the optomechanical coupling strength (see Eq 2.66). Note that the frequency estimates of the hBN drum heavily depend on the tension T_p in Eq. 2.14, which is difficult to predict. We chose a value of $1\,\mathrm{N}\cdot\mathrm{m}^{-1}$ in line with reported values of similar devices [44].

To at least avoid an overlap with the denser parts of the mode spectrum of the supporting membrane, we have to work with high-stress Si_3N_4 membranes. In addition, they should ideally feature a relatively small membrane size of 200-300 µm. Since we are interested in optomechanics, we also have to pay attention to the optical properties of the hBN flake. Fortunately, the thickness at which the frequency

minima are expected also happen to produce reasonable reflectivities, as can be seen when comparing Fig. 5.1 and Fig. 5.3. From this, we can conclude that we have found a parameter space that should fulfill most of our needs.

5.2 Device Fabrication

Having motivated the structure and properties of the desired devices, we will now discuss the fabrication procedure. While stamping techniques, as in [161], have become the standard for deterministic placement of 2D materials, we employ a wet transfer as is more commonly used with CVD grown materials. Such a transfer involves more steps and the use of additional chemicals, which in the case of CVD grown materials cannot be avoided since the underlying metal foil has to be removed in an etching step. But it is also a more gentle approach, which is advantageous to protect the rather fragile high-stress Si_3N_4 membrane. As will be discussed in chapter 6, it could also help to keep the pre-tension T_p of the membrane on the lower end, reducing the resonance frequencies of our drum resonators.

For clarity, a short overview of the entire procedure will be given, after which we will go into more detail for each step. Following Fig. 5.5 (a), we first exfoliate hBN

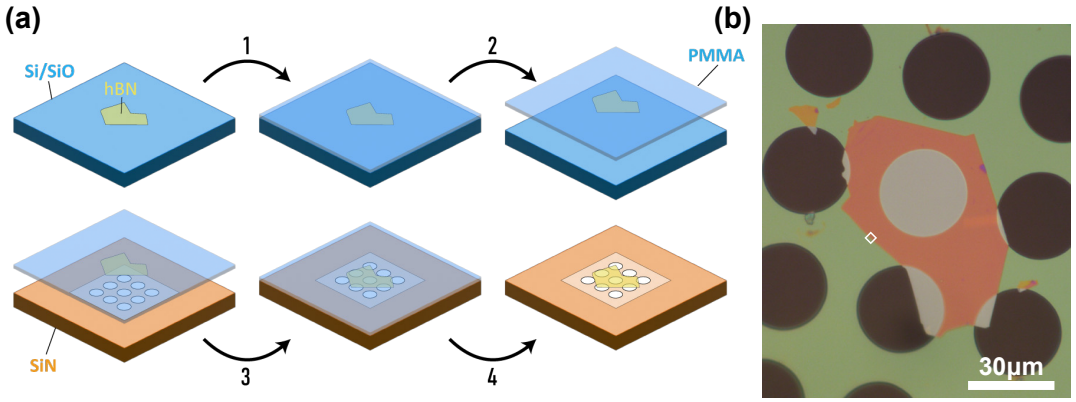

FIGURE 5.5: (a) Fabrication procedure. hBN flakes on a Si/SiO_2 substrate are spin-coated with PMMA (1). The PMMA membrane is removed in an etching step (2) and then placed on the Norcada membrane using a wet transfer (3). Finally, the PMMA is removed (4). (b) Microscope image of a finished hBN drum resonator. An AFM measurement in the area highlighted by the small white box is shown in Fig. 5.8.

flakes onto Si substrates with a SiO_2 layer (step 1). We then spin coat the chip with Poly(methyl methacrylate) (PMMA) and etch away the underlying oxide, releasing the PMMA membrane with the attached hBN flakes (step 2). This membrane is then transferred onto the Norcada chip using a micromanipulator setup in a wet transfer process (step 3). The final step is to remove the PMMA with a solvent cleaning procedure (step 4), resulting in a device as shown in Fig. 5.5(b).

Exfoliation of hBN flakes

As source material, we use commercially available crystals of hBN[1]. We start by thinning out such a crystal over a larger adhesive master-tape[2] ($\approx$10 cm$\times$10 cm) by

[1] HQ-Graphene
[2] Nitto ELP BT-150P-LC

repeated folding. From this master tape, we then collect flakes with smaller pieces of the same kind of adhesive tape, and transfer them onto 1 cm^2 Si chips with a 290 nm SiO_2 layer (see Fig. 5.7 (a)). This layer is not only the sacrificial layer for the later etching process, but it also increases the visibility of the hBN flakes on the substrate. The substrates are cleaned before use by sonication in acetone for 5 min, followed by isopropyl alcohol (IPA) for the same duration. After this step, the substrates are cleaned in a UV-ozone cleaner for 10 min. It is important to only use substrates with cleaved edges and not the edge of the original wafer, since at the edge of the wafer the oxide layer disappears and the PMMA membrane would not detach during the later etching process.

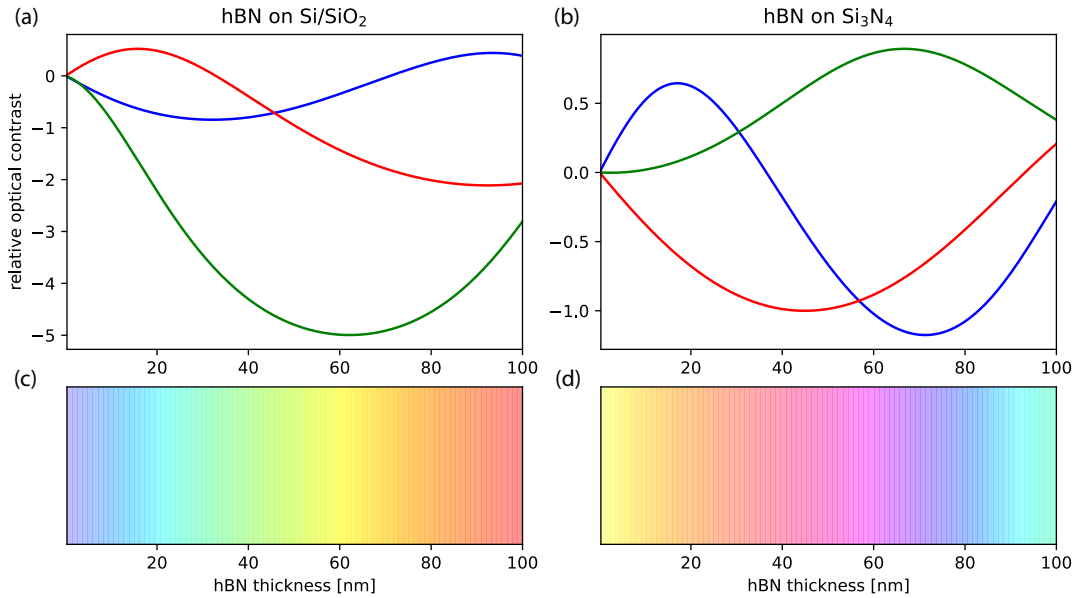

FIGURE 5.6: Relative contrast of the different color channels for hBN on a SiO_2 substrate in (a) and on top of a 200 nm Si_3N_4 membrane in (b). (c) and (d) show the corresponding simulated apparent colors we use to estimate the thickness of the hBN flakes under an optical microscope.

To estimate the thickness of the hBN flakes optically, we use their apparent color as a result of white light illumination under an optical microscope. While such an estimate is not as accurate as, *e.g.*, an AFM measurement, it is much quicker. Given that one has to sort through a large quantity of flakes at this stage of the fabrication procedure, such a quick evaluation is strongly preferred.

We simulate the color as a function of flake thickness using the procedure introduced in [162]. This procedure uses intensity reflection coefficients to integrate the intensity over three color bands, 435-520 nm for blue, 520-590 nm for green, and 590-720 nm for red. These three color channels can then be used to produce an RGB color image. Comparing the flakes apparent color under an optical microscope to the resulting color chart, as shown in Fig. 5.6, then gives an estimate of the thickness. Apart from the thickness, we also try to avoid any flakes that show imperfections, which typically present themselves as lines or changes in color across the flake.

Before proceeding further, we again clean the chip for 10 min in the UV-ozone cleaner to remove residue left by the adhesive tape.

Spin coating and etching of SiO_2 layer

We spin-coat the chips with PMMA with a molecular weight of 950, 000 dissolved in anisole (4 % solids) [3]. We spin at 4000 rpm for 40 sec, resulting in a PMMA thickness of 200 nm. After spin-coating, the chip is baked at 180 °C for 5 min on a hot plate.

For etching of the SiO_2 , we use a 2 mol solution of NaOH. The chip is placed at the bottom of an empty beaker, which is then carefully filled with the etching solution so as to keep the chip floating on top of the liquid. The NaOH will then underetch the PMMA, removing the oxide layer, resulting in a floating PMMA membrane with embedded hBN flakes.

We perform this step at room temperature, resulting in a slow etching process over night. In our experience, this results in a cleaner membrane with fewer gas bubbles trapped underneath, which can interfere with the wet transfer procedure. After the membrane has detached, we replace the NaOH solution with DI water in several rinsing steps.

Wet transfer

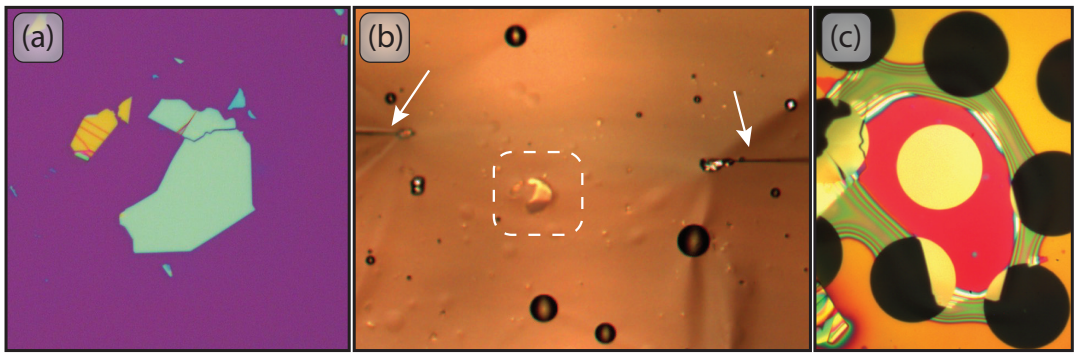

FIGURE 5.7: Microscope images of the fabrication process. (a) hBN flake on a Si/SiO_2 substrate. (b) PMMA membrane with the same hBN flake (white dashed rectangle) held by two glass needles (see arrows), while floating on water above the Norcada chip. (c) hBN flake in contact with Norcada chip.

The wet transfer is performed using a Narashige micro-manipulator setup with an optical microscope. We employ the two pneumatic micro-manipulator arms of this setup to control two pulled glass needles to position the PMMA membrane during the procedure, as shown in Fig. 5.7 (b).

As preparation, the Norcada chip is glued above a hole in a metal plate using Crystalbond. This is done to secure the small chip in place and make it easier to handle. Crystalbond is a glue that can be repeatedly melted at a temperature above 70 °C, making it convenient to apply. It can also be removed in a simple solvent cleaning procedure since it dissolves in acetone. The hole in the metal plate allows for drainage of water while the chip is covered by the PMMA membrane. This metal holder is then submerged in DI water, before the PMMA membrane is transferred into the same dish, floating above the chip.

The pre-selected flake is held in position above the central hole of the Si_3N_4 membrane with the micro-manipulator setup. This alignment is continuously monitored by adjusting the focus between the chip and the flake, overlapping the two with a

[3] MicroChem 950PMMA A4

crosshair in the eyepiece of the microscope. For this task, two needles are necessary in order to avoid movement and rotation of the PMMA membrane.

The water in the dish is then slowly removed with a pipette while continuously lowering the two glass needles to stay in contact with the PMMA membrane. Just before the flake comes into contact with the Si_3N_4 , usually indicated by the appearance of interference fringes, the flake position can be fine-tuned.

If the positioning fails, the PMMA membrane can be carefully re-floated by adding DI water, and the procedure can be repeated. Once the placement of the flake is successful (Fig. 5.7 (c)), the remaining water is removed, and the device is left to dry over night.

Removal of PMMA layer

The dried device, still fixed to the metal holder, is cleaned using solvents. This removes both the PMMA as well as the Crystalbond, detaching the chip from the metal holder.

The first step of this cleaning procedure is to submerge the chip in acetone, heated to 50 °C for a duration of 1 h. This step is followed by IPA at the same temperature for the same duration. The sample is then once again cleaned in a UV-ozone cleaner for 15 min.

5.3 Device Cleaning and Characterization of Organic Residue

During several steps of our fabrication procedure, the hBN flake comes into contact with organic contaminations, *e.g.*, residue of the adhesive tape used for exfoliation, the solvents, or the PMMA. Such residue can lead to excessive losses in a MIM system due to an increase in surface roughness and thus scattering losses, but also due to optical absorption. Most of this contamination can be removed by the cleaning steps outlined above, but a residue of the fabrication process can still be identified in an AFM measurement as clearly visible surface roughness, as is for example visible in Fig. 5.8.

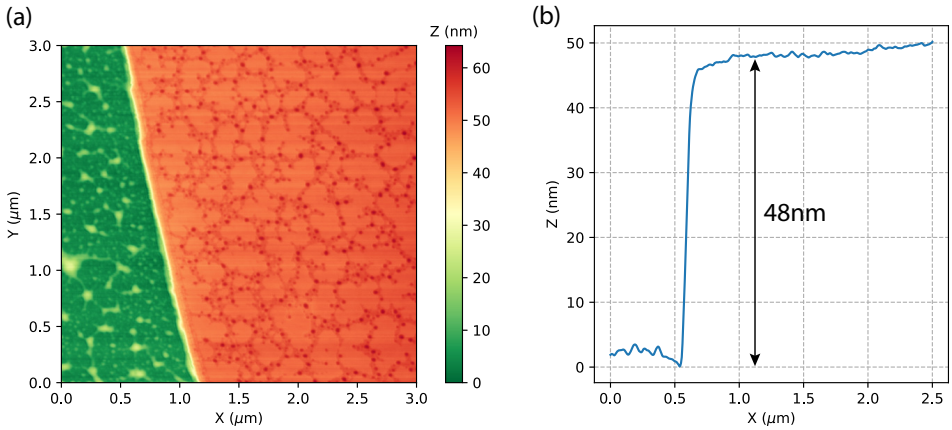

FIGURE 5.8: AFM measurement in the region highlighted by the white box in Fig. 5.5. 2D map in (a), and the averaged horizontal linecut showing the flake height in (b).

The AFM measurement shows residue on both the hBN flake and the Si_3N_4 surface. Especially in the 2D map in (a), features as high as 10 nm can be identified.

These measurements were taken after treating the sample with solvent and UV-ozone cleaning, as outlined above.

We can not only use AFM measurements to characterize organic contamination of the flake and the surrounding substrate but also Raman spectroscopy. The contamination can be identified as spectral features and as broad background beyond the Raman signatures associated with hBN and the underlying substrate, especially after the sample has been exposed to high temperature annealing in an inert gas like argon. As we will see later, such annealing appears to make the contamination optically active and easily visible in optical spectra. Like this, we can gain some insight into the necessity and success of the cleaning procedures we employ.

We begin by examining the flakes after exfoliation. In Fig. 5.9 (a), we show Raman spectra taken on both the Si/SiO_2 substrate and on an exfoliated hBN flake. The first two spectra were taken after high temperature annealing in argon gas, both showing a broad background across the entire spectrum. After a cleaning step in a UV-ozone cleaner for 5 min, the background is eliminated and only the expected Raman peaks of Si, SiO_2 and hBN remain. Note that the latter two spectra appear identical to the spectra one would obtain before the annealing step in argon, showing no broad background and only the expected Raman peaks. The high temperature annealing is performed for 30 min at 850 °C in a vacuum quartz tube furnace under continuous argon gas flow, resulting in a pressure of 1.3 mbar.

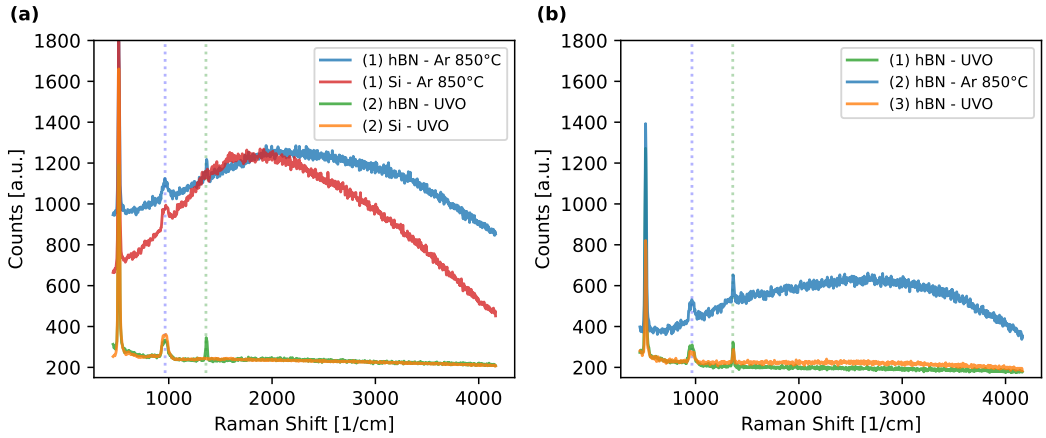

FIGURE 5.9: (a) Raman spectra on hBN and the surrounding Si substrate showing strong background counts after annealing in Argon (1) at 850 °C. The background is removed after 5 min in a UVO cleaner (2). (b) Raman spectra on hBN after an initial UVO cleaning step (1), after argon annealing (2) and after a subsequent UV-ozone cleaning step (3). The Raman peaks of SiO_2 and hBN are shown as a green and a blue dotted line, respectively. The strong leftmost peak in the spectra is the Raman peak of Si.

To make sure that the contamination is indeed present before the annealing, we perform UVO cleaning first and then the argon annealing step afterwards. This results in a reduced background, as shown in Fig. 5.9 (b), compared to the one in (a), indicating that the cleaning step still had an effect. An additional UVO cleaning step again removes this remaining background. These tests have been repeated with several samples, and the results were comparable, indicating that the differences between (a) and (b) were not a coincidence. This shows that a significant fraction of the observed contamination is already present before the annealing in argon, but

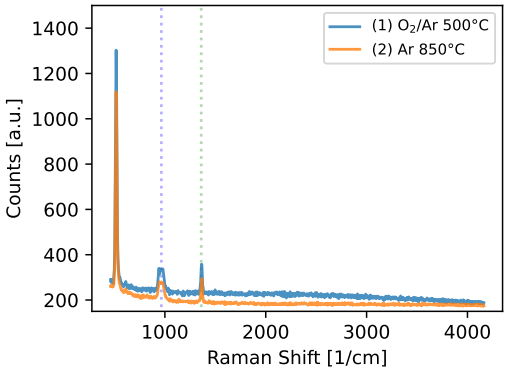

FIGURE 5.10: Raman spectrum taken on an hBN flake after annealing in an O_2/Ar mixture (1) and after subsequent annealing in a pure Ar atmosphere (2).

that some contamination might be added during the annealing as well. Another possibility is that the contamination is easier to remove once it has been annealed and that no additional residue is added during the annealing step.

A careful reader might have noticed that our annealing procedure is identical to the recipe used to create single-photon emitters in hBN, as outlined in [85]. While one can indeed create such emitters with this recipe, here we will focus solely on the effects on the Raman spectra and the organic contamination, where it mostly serves to make such contamination visible.

Apart from UV-ozone treatment, another method to clean such organic contamination is to perform annealing at an elevated temperature in an oxidizing gas environment. Such annealing procedures have been used to not only clean contamination visible in optical spectra on hBN [163], but also to bake off PMMA layers in a liquid free process during similar device fabrication [164]. High temperature annealing has also been shown to positively affect the mechanical properties of suspended hBN [45] and graphene devices [80, 165]. To this end, we again use our vacuum quartz tube furnace, but now we use a gas mixture of 20% oxygen and 80% argon. The temperature is lowered to 500 °C, and the pressure is increased to 0.1 bar. The pressure is kept at this value solely to protect the outer parts of the annealing oven from overheating. To our knowledge, this annealing step would work under atmospheric pressure as well. The annealing is performed for several hours, depending on the degree of contamination of the sample.

We again perform a measurement series as in Fig. 5.9 (b), but instead of cleaning the sample with a UV-ozone treatment, we perform the oxygen annealing procedure. As shown in Fig. 5.10, the results appear to be more promising. After the initial oxygen annealing step, there is no visible background in contrast to annealing in a pure argon environment. Furthermore, after a subsequent argon annealing step meant to reveal remaining contamination, the background remains low. This confirms that the background visible after the argon annealing in Fig. 5.9 was likely due to contamination already present, which was converted to a fluorescent background in the high temperature environment. It also shows that annealing in oxygen could completely remove this background as opposed to UV-ozone treatment. We still perform several UV-ozone cleaning steps throughout our fabrication procedure to minimize the contamination, since it still shows good results considering its ease of use.

Moving on from exfoliated flakes on SiO_2 substrates to our hBN-Si_3N_4 devices, we might encounter contamination not only from the adhesive tape but also from

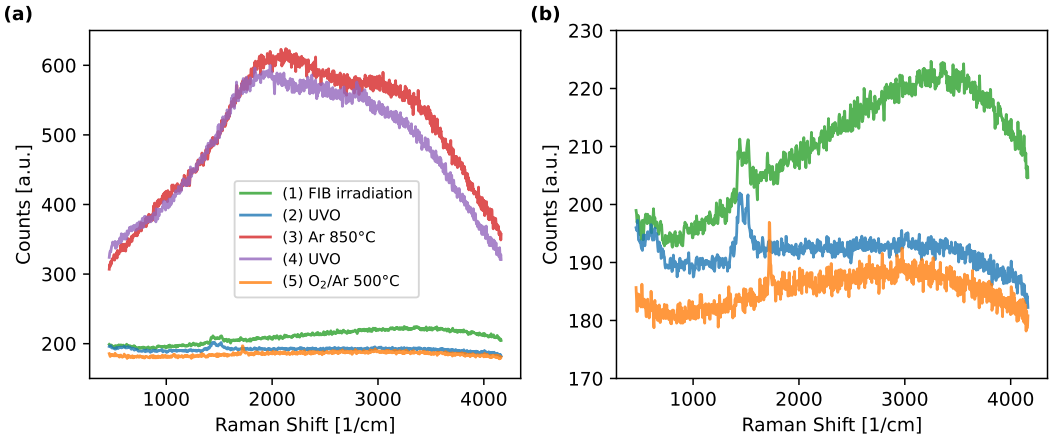

FIGURE 5.11: Raman spectra on a suspended hBN flake, capturing the impact of a series of treatments. In order, the sample was irradiated in a FIB microscope, cleaned in a UVO cleaner, annealed in an Ar atmosphere, again cleaned in a UVO cleaner, and finally annealed in a O_2/Ar mixture. (a) shows the spectra taken after each step, while (b) shows the three spectra lowest in counts for clarity.

the PMMA assisted transfer process. In addition to this, both for imaging and further processing, one might expose such devices to irradiation in a scanning electron microscope (SEM) or a focused ion beam (FIB) microscope [166, 167]. The contamination caused by SEM and FIB irradiation is known to present itself as a double peak around 1350 cm^{-1} and 1600 cm^{-1} corresponding to the D and G bands associated with graphite [166, 168, 169].

The measurements shown in Fig. 5.11 were performed on a suspended drum after exposure to FIB irradiation. In this device, all aforementioned contaminants should be present. Note that since the sample is suspended and there is no underlying substrate, the Raman signal is much lower. Apart from the absence of the Raman peaks associated with the substrate, the initial spectrum (green in Fig. 5.11) shows a moderate background and a clearly visible D and G band, expected from the FIB irradiation. This is especially visible in Fig. 5.11 (b), where we focus on the spectra with lower intensity. After a UV-ozone cleaning step, some of the broad background is removed, but the double peak structure remains unchanged (blue spectrum). This is in line with our assumption that this device has several different kinds of contamination, some of which can be removed as before in Fig. 5.9. An argon annealing step again reveals a strong contamination shown in Fig. 5.11 (a), which is not affected by a subsequent UV-ozone treatment. However, a long term (12 h) annealing in an oxygen/argon mixture, as outlined before, not only manages to remove the broad background but also the D and G band peaks associated with surface graphitization caused by FIB irradiation, as visible in the final orange spectrum.

Finally, we return to AFM measurements to confirm the effectiveness of this cleaning procedure in another way, especially since the surface quality of the membrane is of high importance in MIM optomechanics. We performed AFM measurements before and after annealing in an O_2/Ar mixture for 4 h. This test was performed on a new suspended hBN drum with a flake thickness of 22 nm (see Fig. 5.13 (b) for further details). As visible in (a), the initial contamination of this device appears to be less severe compared to the one shown in Fig. 5.8. Nevertheless, a clear surface roughness on the flake and some larger contamination on the substrate can

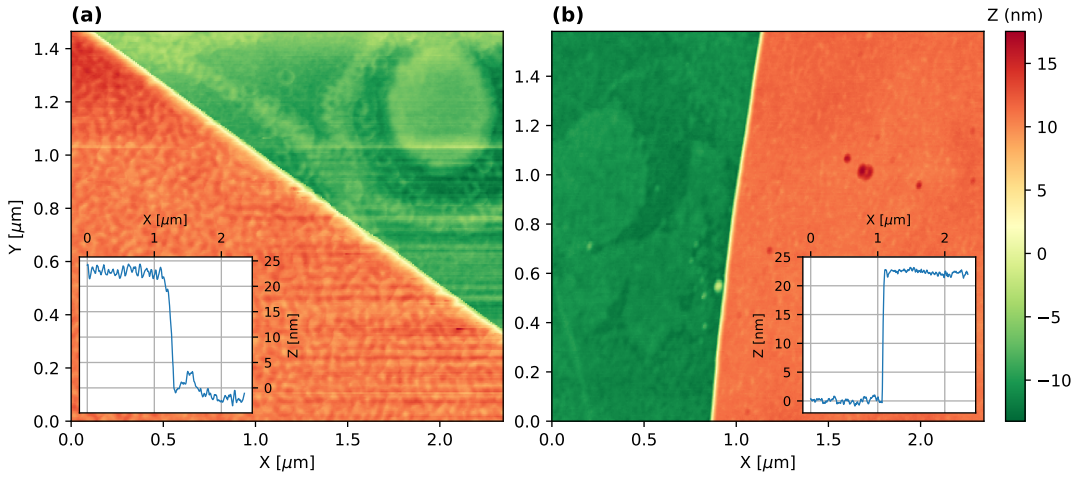

FIGURE 5.12: AFM measurements around the flake edge before (a) and after (b) annealing in an O_2/Ar mixture. The insets show line cuts that give a better impression of the surface roughness. In addition, the thickness of the hBN flake in this device is confirmed to be 22 nm.

be observed. After the annealing step (b), the surface roughness is reduced, and the spotty surface appears much more homogeneous.

From these AFM and Raman measurements, we can conclude that high temperature annealing in an O_2/Ar mixture is a gentle and effective approach to remove residue caused by different steps in the fabrication procedure. It even proved effective in removing contamination caused by FIB irradiation. No damage to the sample and no observable change to, *e.g.*, the flake thickness could be observed. In addition, UV-ozone treatment is a less effective but more convenient alternative, that shows good results when treating contamination introduced during the exfoliation procedure.

5.4 Sample Overview

We have fabricated a variety of samples with varying drum thicknesses between 5 nm and 50 nm. While thicker samples should result in a higher reflectivity and thus in a stronger interaction with the cavity, thinner samples present a lower effective mass. This leads to advantages in sensitivity (see Eq. 2.10) when using such a resonator as sensor, but due to the impact on x_{zpm} (Eq. 2.9) it also has implications for the optomechanical coupling according to Eq. 2.66, as we will explore later in chapter 7 (Fig. 7.8). The mechanical characterization of these samples will be discussed in chapter 6.

The samples shown in Fig. 5.13 are all fabricated on high-stress Si_3N_4 membranes with lateral dimensions of 300 µm. The hole sizes are 30 µm for the samples shown in (a),(d) and (e), while in (b) and (c) the holes have a diameter of 20 µm. This is mostly due to the fact that finding flakes with a thickness of only a few nm is difficult with the lateral dimensions necessary for our larger holes.

The dark-field images shown in the lower half are well suited for the identification of imperfections in the flake. While in Fig. 5.13 (a) and (b), the dark-field image reveals no obvious imperfections in the drum, the one shown in (c) shows several lines. We believe that these lines represent folds rather than cracks or steps since no steps were visible in the flake before transfer and, under close inspection, no gap in

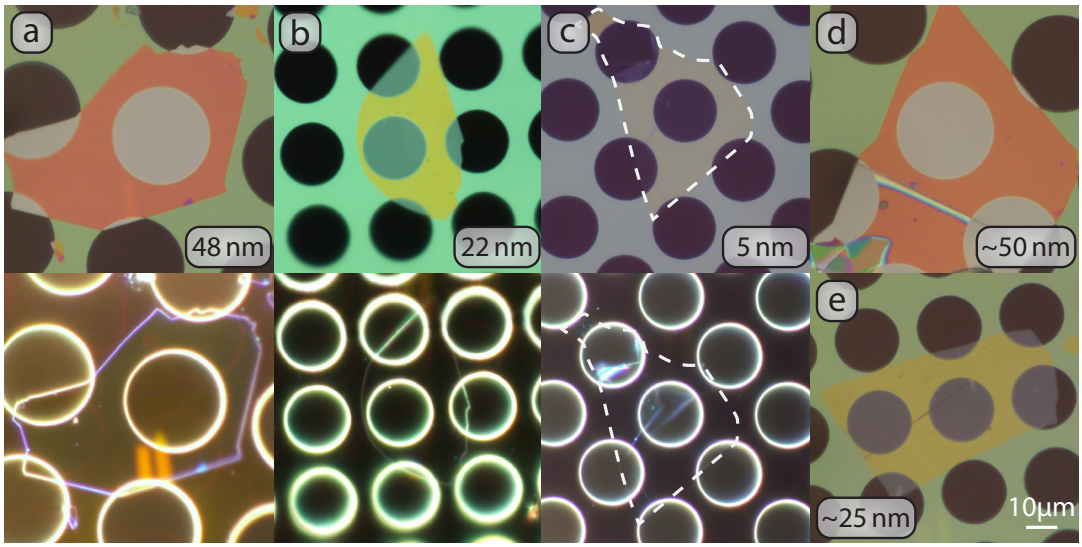

FIGURE 5.13: Overview of samples for which measurements will be presented in this thesis. (a) Is the sample used for most results shown in chapter 6 and [170]. For (a)-(c) a regular photograph (top) and a dark-field image (bottom) are shown. The thickness for (a)-(c) was measured via AFM and is indicated in the bottom right of each photograph. For (d) and (e), only a regular photograph is available, and the thickness was estimated based on the color instead.

the material could be seen. We further believe that it is much more difficult to avoid folding of such thin flakes since they are deep in the membrane limit and thus do not hold their own shape as a plate would. This is also consistent with thin hBN samples based on CVD grown material shown in other publications [45]. In contrast, the lines visible in Fig. 5.13 (e) show a clear gap in the material due to damage caused during the flake transfer.

Chapter 6

Mechanical Characterization of hBN Drum Resonators

Here we discuss the mechanical properties of the hBN samples presented in Fig. 5.13, in particular the sample shown in Fig. 5.13 (a), but also those of the Si_3N_4 membranes and their hybridization with our microdrums. These results have been published in [170]. Similar hybridization between 2D material resonators and underlying Si_3N_4 membranes has been observed before [171, 172], but here we focus on the impact on the quality factor (Q) and effective mass (m^*). In our case, the underlying Si_3N_4 membrane has a much higher Q than the hBN drum. The resulting hybridized system, where the Si_3N_4 membrane lends its mechanical properties to the modes of the hBN drum, could be useful for sensing applications [171, 173, 174], and the engineering of functionalized mechanical systems.

The measurements at room temperature were performed with the interferometer setup introduced in section 3.2, while the ones at low temperature were performed using the confocal microscope configuration of our FFPC-MIM probe introduced in section 3.1.2.

6.1 Mechanical Properties of the hBN Drum

We start by focusing the laser of the interferometer onto the center of the hBN drum, where the fundamental drum mode ($m = 0, n = 1$ in Fig. 2.3) should have its peak motional amplitude. We then record a thermal spectrum with the built-in spectrum analyser of the RedPitaya to obtain an overview of the resonances present. We expect to observe several resonances belonging to both the hBN drum and the Si_3N_4 membrane, as is the case in Fig. 6.1 (a). Since the simulations of the Si_3N_4 membrane should be rather precise due to its well characterized properties, we can expect a good agreement between simulation and measurement. It is thus reasonable to assume that the peak at 1.2 MHz is its fundamental mode, matching the lowest value in Fig. 5.4 for a 300 µm membrane dimension.

In Fig. 6.1 (b) and (c), we show higher resolution spectra of the two modes highlighted in Fig. 6.1 (a). These more detailed spectra were taken with our LI-A instead of the Red Pitaya. While (b) shows the fundamental Si_3N_4 mode, we suspect (c) to show the fundamental mode of the hBN resonator.

To further investigate which resonances in the overview spectrum belong to the hBN drum, one could move the focus of the microscope to a region just outside the drum and see which resonances remain or disappear in the overview spectrum. However, a more sophisticated approach is to scan the laser spot across the drum and some of the surrounding Si_3N_4 membrane while recording the peak intensity

of a specific resonance by demodulating the signal with the LI-A around the corresponding frequency. While such a measurement can image the thermal motion as well, here we drive the resonance in question with the disc piezo mounted on the sample block (see section 3.1.2) to ensure a high SNR. This procedure effectively generates an image of the motional amplitude and thus the mode shape for the resonance in question. The measurements shown here correspond to the absolute value of the mode shapes shown in Fig. 2.3, which is sufficient to identify most modes. If necessary, the LI-A gives access to the phase as well as the individual quadratures, making it possible to perform measurements matching Fig. 2.3.

In Fig. 6.2 (a), we show such mode images for both the fundamental Si_3N_4 mode at 1.2 MHz and the potential fundamental hBN drum mode at around 2 MHz. While both modes show strong motion in the drum, the one at 2 MHz is much more confined and matches the expected mode shape of a fundamental drum mode well. The one at 1.2 MHz that we assigned to the Si_3N_4 membrane shows clear motion outside of the drum and appears to be much broader in shape. Unfortunately, the scanning range of our setup is not large enough to image the entire Si_3N_4 membrane.

Apart from identifying the mode a resonance in a spectrum corresponds to, mode imaging is also useful in gaining insight into the imperfections of the membrane and their effects on the mode shapes. As pointed out in [44], mode shapes are, for example, sensitive to asymmetric tension in the flake and bulging effects. Our mode images in Fig. 6.2, especially in the case of the fundamental Si_3N_4 mode, reveal a diagonal line, highlighted by the arrows in Fig. 6.2. This line is not visible in the microscope image in Fig. 5.13, but it was present in AFM measurements shown in Fig. 6.2 (b). The AFM measurement was performed outside of the suspended drum, but the line extends into the drum, matching the feature observed in the mode

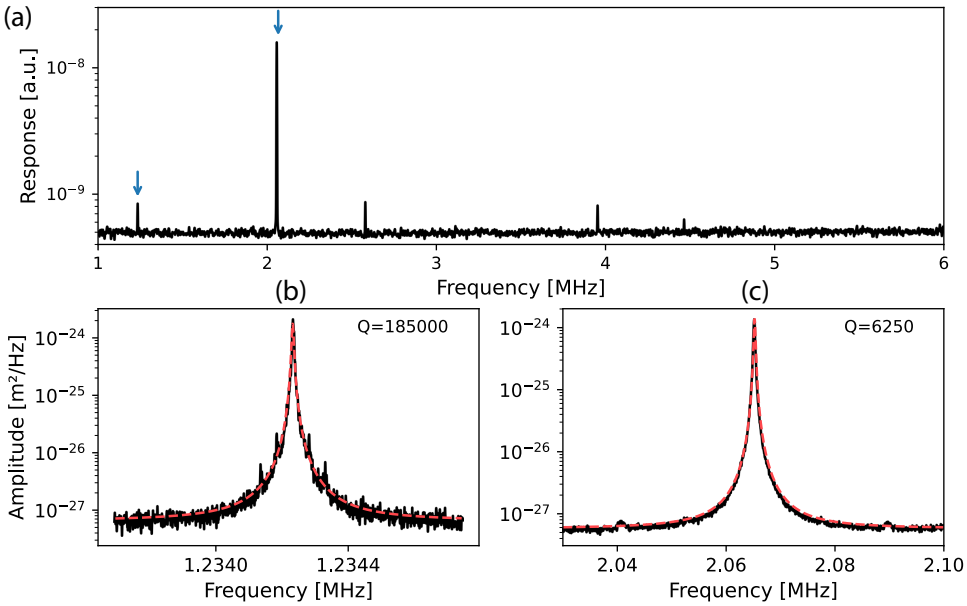

FIGURE 6.1: (a) Overview spectrum of the thermal response taken in the middle of the hBN drum. (b) Detailed spectrum of the first peak highlighted with a blue arrow in (a), which we attribute to the fundamental mode of the Si_3N_4 membrane. (c) Second highlighted peak in (a), which we attribute to the fundamental mode of the hBN drum. Fit in (b) and (c) is shown in red and is used to extract the Q-factors shown in the top right of the two graphs.

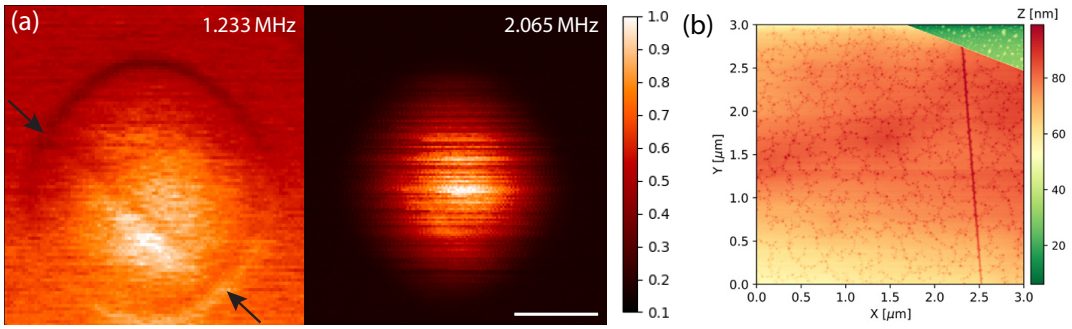

FIGURE 6.2: (a) Mode images recorded by demodulating the response around the frequencies of the fundamental SiN mode (Fig. 6.1 (b)) on the left and of the fundamental hBN mode (Fig. 6.1 (c)) on the right. Both responses have been normalized to unity. The scale bar corresponds to 10 µm. Especially the mode image of the Si_3N_4 mode reveals a linear feature highlighted by arrows; this line is found as a feature of approximately 10 nm in the AFM measurement shown in (b).

image. This line appears to be a feature of around 10 nm in height. Since the flake height is equal on both sides of this line, we assume that it is caused by a fold rather than by a step in the flake. While this feature is observable in some of the mode images, it does not appear to disturb the expected mode shapes of the hBN drum, as we will see in the following measurements.

Now that the fundamental mode of the drum has been identified, we further investigate the properties of our mechanical resonator by fitting the thermal spectrum with Eq. 2.6, as shown in red in Fig. 6.1. From this fit, we can extract the linewidth and hence the Q-factor of our resonators.

If we know the temperature of the sample and measure the peak amplitude of the mode in question, we can extract the effective mass as a fit parameter as well. To ensure that we are not heating the sample with our laser, we increase its power until we see a shift in the resonance frequency, a clear sign that heating has occurred. Then we lower the optical power well below that point, where no thermal effects due to the laser can be observed. This usually results in an optical power below 100 µW. In this configuration, we can be reasonably confident that the sample temperature is thermalized with the surrounding bath at room temperature.

With these assumptions, we extract a value of $m^* = 1.71 \times 10^{-14}$ kg for our hBN drum. We can also calculate the expected effective mass for our hBN drum according to Eq. 2.18, giving us a theoretical value of $m^*_{th} = 1.89 \times 10^{-14}$ kg, in good agreement with our measurement. Here we assumed a density of hBN of $\rho_{hBN} = 2100\,\mathrm{kg \cdot m^{-3}}$. This further shows that this mode is unlikely to be associated with the much heavier Si_3N_4 membrane and that it is indeed confined to the hBN drum.

We have done similar investigations regarding the fundamental modes of the other samples shown in Fig. 5.13; the observed fundamental modes are shown in Fig. 6.3.

Fortunately, we were successful in separating the fundamental hBN modes from the ones of the Si_3N_4 membrane for most devices. This is evident by the effective masses shown in Fig. 6.3, but it also becomes obvious when looking at the overview spectrum in Fig. 6.1, where the resonances are clearly separated. Only the thermal spectrum in (c) reveals a higher effective mass and also a higher resonance frequency. This spectrum belongs to the hBN drum with a crack, shown in Fig. 5.13 (e). We note that the frequencies of resonances associated with the Si_3N_4 membranes are very

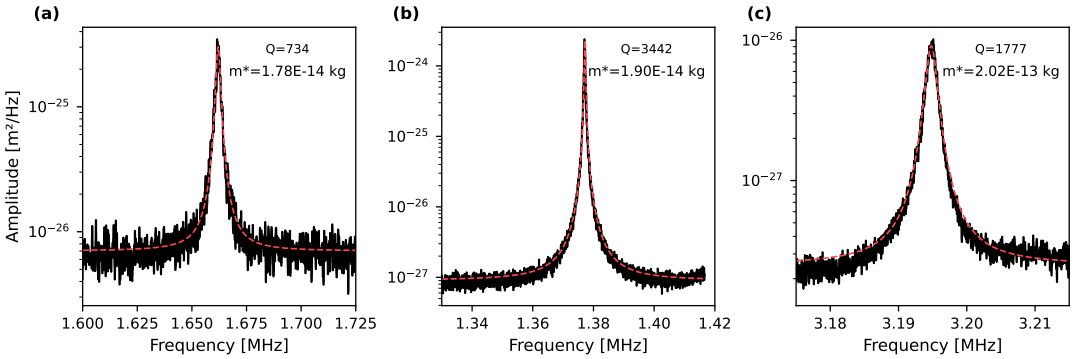

FIGURE 6.3: Spectra of the fundamental modes of the remaining devices shown in Fig. 5.13 (b), (d), and (e) in order. So far, no spectrum of the sample shown in Fig. 5.13 (c) could be recorded.

consistent across different devices, usually presenting a gap in the spectrum similar to Fig. 6.1.

In Fig. 6.4, we show the resonance frequencies of the Si_3N_4 membrane and the ones of the hBN drum, simulated with Comsol. The simulation for the Si_3N_4 membrane is the same we already used in Fig. 5.4. The parameters match the device measured here (Fig. 5.13 (a)). While there are visible modes of the Si_3N_4 membrane at around 2.5 MHz, there is still a low enough density of Si_3N_4 resonances for the hBN drum modes to be well separated in this interval. In principle, there are additional modes associated with the Si_3N_4 membrane at around 1.8 MHz. But those are the ones exhibiting a node in the middle of the membrane, making them not observable in our spectra (see Fig. 6.1), which should also result in a low interaction with the hBN drum.

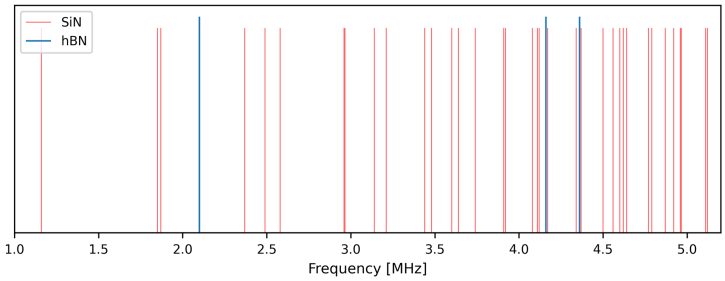

FIGURE 6.4: Simulated mechanical spectrum of the Si_3N_4 membrane (red) and a hBN drum (blue). Device parameters match the one shown in Fig. 5.13 (a).

6.2 Mode Imaging of Higher Order Modes

Having characterized the fundamental mode of our hBN resonator, we now turn to the higher order modes. At the higher frequencies where these modes are expected, the density of the modes associated with the Si_3N_4 membrane will drastically increase, as seen in Fig. 6.4. In such a scenario, mode imaging becomes an indispensable tool to identify the hBN drum modes.

Aside from the identification of the drum modes, one should pay attention to two different aspects when investigating how close to an ideal system the resonator performs. The first is how well the mode shapes match between simulation and

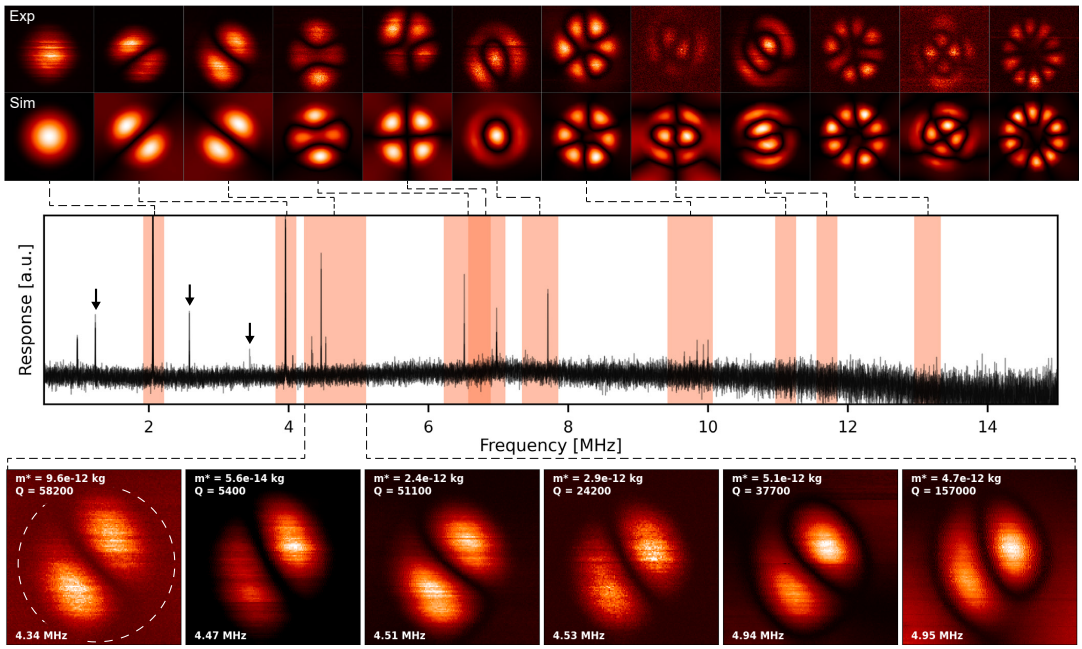

FIGURE 6.5: Mode images and spectrum obtained for the sample shown in Fig. 5.13 (a). The top row shows the measured mode images while the second row shows mode images simulated with COMSOL. Since often more than one mode could be found with matching mode shapes, the modes are represented with a shaded area rather than with a specific peak in the thermal spectrum shown in the middle. The last two mode images are beyond the frequency range of the thermal spectrum shown, therefore, no shaded area is indicated. Arrows highlight modes of the Si_3N_4 membrane that did not hybridize with any hBN drum modes, starting with the fundamental Si_3N_4 mode. The last row shows an example of a series of apparently identical modes in one of the shaded areas. m^*, Q and f_m are displayed on each of the six graphs. The dashed circle shows the drum outline with a diameter of 30 µm.

measurement. In general, mode images of mechanical resonators based on 2D materials tend to show mode shapes that deviate significantly from theory [44, 96, 97]. We have thus compared all modes we could identify in the thermal overview spectrum (middle of Fig. 6.5) with the expected mode shapes simulated with Comsol. The results are shown in the top two rows of images in Fig. 6.5. In our measurements, there is very good agreement in this regard, showing that this sample exhibits mode shapes in agreement with a geometrically ideal membrane. This remains to be the case up to high order modes, only limited by our ability to find these modes in a thermal spectrum. While the observed mode shapes of the drum are also in good agreement with the analytical ones shown in Fig. 2.3, the simulation takes into account additional interactions with the Si_3N_4 membrane, as we will discuss below in section 6.2.1.

To show that the sample fabrication procedure outlined in chapter 5 can reliably produce samples with such well defined mode shapes, we show another series of mode images in Fig. 6.6. This series of measurements was performed with the sample shown in Fig. 5.13 (d). The thermal spectrum of the fundamental mode of this device (Fig. 6.3 (b)) revealed a surprisingly low resonance frequency around 1.38 MHz, hinting at a low tension in the hBN flake, and a relatively high Q of 3400. Naturally,

samples with obvious defects, as in Fig. 5.13 (e), do not show such predictable mode shapes.

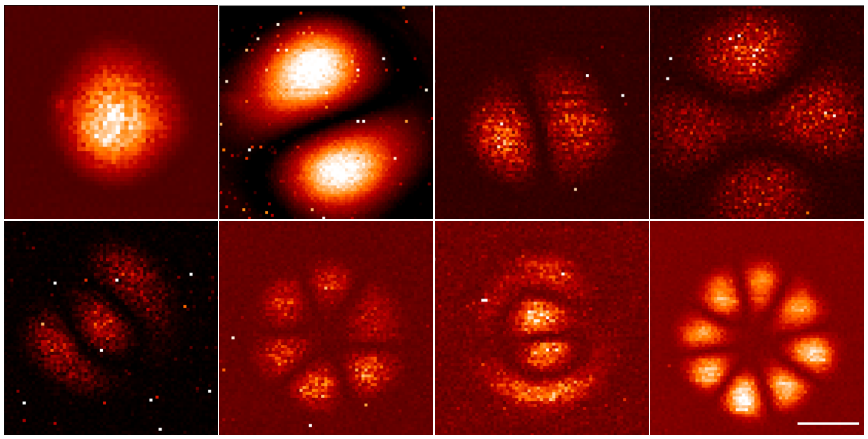

FIGURE 6.6: Mode images similar to the ones shown in the top row of Fig. 6.5, but performed on the sample shown in Fig. 5.13 (d). Scale bars correspond to 10 µm.

The second aspect is whether the mode spacings in frequency match well between experiment and simulation. Unfortunately, this question is difficult to answer in our case, as we observe a multitude of copies for a single expected mode shape of our drum resonator over a relatively large frequency interval. Such a series of modes is shown at the bottom of Fig. 6.5. We have highlighted the intervals in which modes of the same mode family can be found in the thermal overview spectrum in Fig. 6.5 as red shaded areas. These shaded areas also include some uncertainty due to temperature drifts in our setup, leading to shifts in resonance frequencies between measurements.

6.2.1 Comsol simulation of a hybrid hBN-Si_3N_4 device

To gain more insight into our measurements, we will now take a closer look at the Comsol simulations mentioned before, where we simulate the combined hBN-Si_3N_4 device. Regarding the geometry of the simulation shown in Fig. 6.7 (a), we simply approximate the hBN flake as a rectangle covering the central hole of the Si_3N_4 membrane, while the Si_3N_4 membrane itself could be accurately reproduced due to its well-defined dimensions. The shape of the rectangle was chosen instead of a square to break the symmetry, which should be more in line with the real shape of the hBN flake. Here we again focus on the sample shown in Fig. 5.13 (a) and use the thickness extracted from the AFM measurements shown in Fig. 5.8 of 48 nm.

The combined system is simulated as a union, and the mode shapes are evaluated as a shell model instead of a membrane model to take bending stiffness into account. We introduce asymmetry into the system with a 1% distortion of the shape of the Si_3N_4 membrane. This asymmetry leads to a better match with our measurements and is well within the fabrication tolerances of our Si_3N_4 devices.

We match the simulated frequency of the fundamental mode of the hBN drum to the one we observe experimentally using the pre-tension of the flake. As noted in chapter 5, the reported values for the Young's modulus of hBN vary greatly, and we tentatively chose the average value of 392 GPa reported in Ref. [44]. With this value, we have to set the pre-tension to 0.36 N/m.

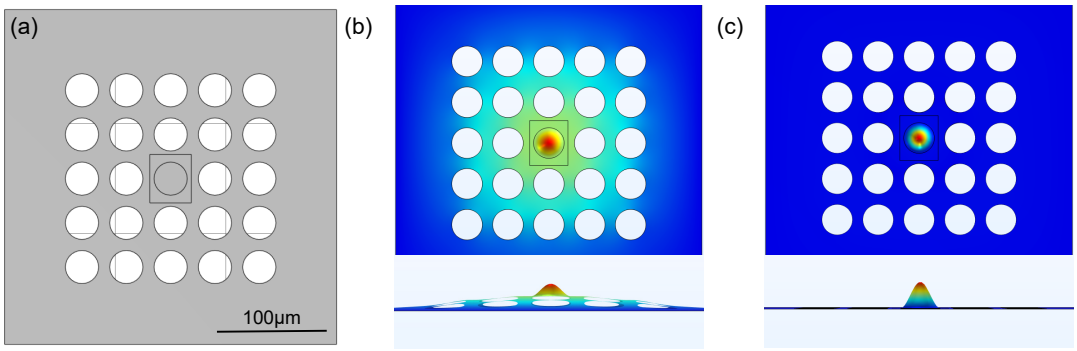

FIGURE 6.7: (a) Simplified geometry used for our simulations. (b), (c) Top and side view of the two fundamental modes of the Si_3N_4 membrane and the hBN drum, respectively. The simulations match the experimentally measured mode images in Fig. 6.2 well.

However, for a Young's modulus of 700 GPa, which is still within the range of reported values and closer to theoretical predictions [72], we have to use a pre-tension of only 0.15 N/m. With this set of values, the simulation matches the measured higher order modes much better. However, it is difficult to match the simulations perfectly to our measurements due to the aforementioned interval over which drum modes repeat themselves and our inability to image the involved Si_3N_4 membrane modes. We have nevertheless switched to the latter combination of parameters.

Simulated mode shapes for the fundamental mode of Si_3N_4 and the one of the hBN drum are shown in Fig. 6.7 (b) and (c), and they match the experimental data in Fig. 6.2 well. Interestingly, it is expected that even for the Si_3N_4 mode, there is a clear motional peak in the hBN drum. Such an effect is not entirely unexpected due to the difference in mechanical properties between the two materials. This effectively serves as an amplification of the motional amplitude of the Si_3N_4 membrane and can also be observed as a bright spot in the middle of the drum in Fig. 6.2 (a). The same conclusion has also been drawn in [174], where the motion of a Si_3N_4 membrane was amplified with a thin graphene drum.

The hBN mode is expected to be entirely confined to the drum, and its profile appears to be more focused compared to the mode shape within the drum simulated for the fundamental Si_3N_4 mode. This also matches our previous measurements, especially the value of m^*, which is in agreement with the calculated value for the isolated drum, implies no additional motion in the Si_3N_4 membrane.

Regarding higher order modes, the simulations predict a vast number of such modes, much larger in quantity than the ones we can observe in our thermal spectrum. In addition, they are spread over even larger frequency intervals than we observe in our spectra.

6.3 Mechanical Mode Hybridization in a hBN-Si_3N_4 Device

We will now turn to discuss the copies of hBN drum modes within one mode family observed before. We attribute the presence of these copies to hybridization between an hBN drum mode and several modes of the Si_3N_4 membrane that are close in frequency. When taking a closer look at the bottom row in Fig. 6.5, it becomes apparent that some of the mode images show motion surrounding the typical double maxima of the drum mode, hinting at hybridization with the surrounding Si_3N_4 membrane.

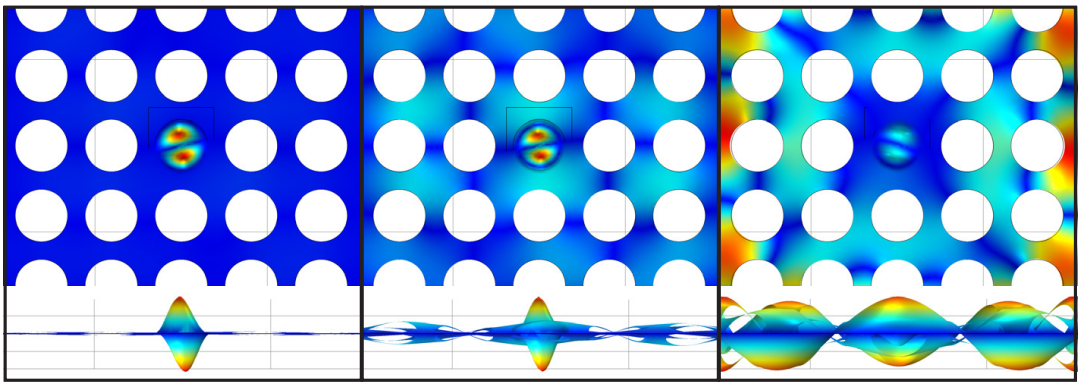

FIGURE 6.8: Top and side views of three examples of the $(m{=}1, n{=}1)$ drum modes present in our simulation at different frequencies. The modes show differences in the surrounding Si_3N_4 membrane, implying different degrees of hybridization but also different Si_3N_4 modes.

Comparing this to our simulation, we observe that each of the simulated modes show differences mostly in the surrounding Si_3N_4 membrane, consistent with our assumption that a hBN mode hybridizes with many Si_3N_4 modes, as can be seen when comparing, *e.g.*, the first two mode images in Fig.6.8. The drum modes shown here match the ones at the bottom of Fig. 6.5.

The last mode image shows a case with especially strong hybridization. The drum mode is additionally rotated with respect to the other modes, but not enough for it to be clearly attributed to the second $(m = 1, n = 1)$ drum mode rotated by 90° predicted by theory (see section 2.1.2). So the hybridization not only results in a much larger number of modes compared to a bare hBN drum, but it can also affect the rotational orientation of the hBN drum modes, explaining why some of the orientations of the modes in Fig. 6.5 differ from an ideal isolated drum.

Modes where the motion is confined to the hBN drum alone, *i.e.*, those that are not hybridized with the Si_3N_4 membrane, were almost not present in the simulation towards higher frequencies. Most likely, the density of Si_3N_4 modes is simply too large for an hBN mode to be isolated, underlining the importance of our choice to employ high stress Si_3N_4 membranes with higher resonance frequencies.

We can again use the measured thermal spectra to characterize the mechanical properties of the modes in question, in particular their m^* and Q. The values obtained like this are displayed for each mode at the bottom of Fig. 6.5, showing a large range of different values. As expected, the mode with the lowest Q-factor (second image) shows no motion in the surrounding Si_3N_4 membrane, while the one with the highest Q-factor (last image) shows strong motion that even merges with the mode shape of the hBN drum across its edge.

To further investigate this hybridization, we extract m^* and Q for all the modes observed in the thermal spectrum in Fig. 6.5. In Fig. 6.9 (a), we show Q as a function of the resonance frequency. A first observation is that there is a large spread of different values of Q, which tend to be lowered towards higher frequencies. The large spread can be understood as an effect of hybridization. Knowing that the hBN drum has a much lower Q (6×10^3 for the fundamental mode) than the Si_3N_4 membrane (1.8×10^5 for the fundamental mode), it is expected that any value within this interval can be observed depending on the degree of hybridization. This is confirmed by the fact that among the modes shown in the bottom row of Fig. 6.5, we have found Q-factors in excess of 1×10^5, almost reaching the value of the Si_3N_4 membrane's fundamental mode.

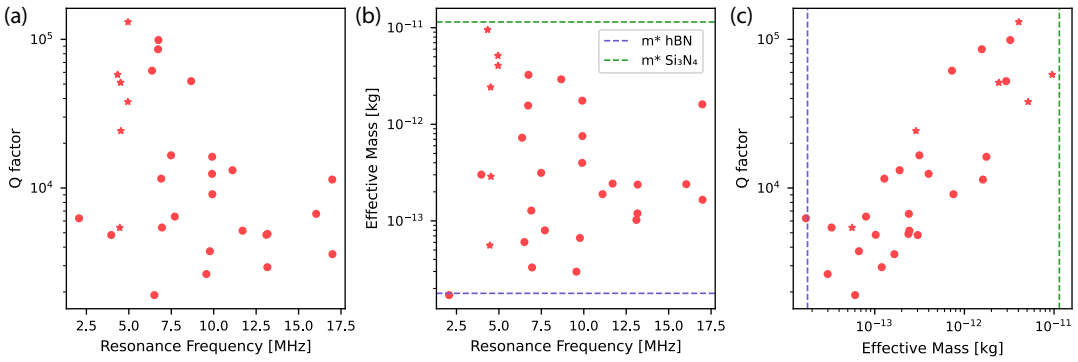

FIGURE 6.9: (a), (b): Q and m^* as a function of the resonance frequency for all observed modes at room temperature. The six modes shown at the bottom of Fig. 6.5 are represented by star shaped markers. (c) Q vs. m^*, revealing an apparent correlation between both quantities. The dashed lines in (b) and (c) indicate m^*_{th} for the fundamental modes of the hBN drum and Si_3N_4 membrane.

Of course, the higher order modes of the two resonators do not need to have the same Q as the fundamental modes but might tend towards lower values, which matches our observations regarding empty Si_3N_4 membranes. The maximum in Q for the observed modes can be found at around 4 MHz, since below this value only the fundamental hBN mode can be found, which is not yet hybridized with the Si_3N_4 membrane as pointed out before. And at higher frequencies, the Q starts to diminish, leading to a tapering off of the observed values.

Finally, for a small frequency interval, there are often many modes at different Q's that almost appear in a vertical line, representing groups of modes such as the one shown at the bottom of Fig. 6.5. This is again a sign of the hybridized modes clumping around a hBN drum mode that is hybridized with many nearby Si_3N_4 modes.

For m^*, we expect a similar dependency on the degree of hybridization as with Q. Similar to the theoretical value for the effetive mass of the hBN drum's fundamental mode that we estimated before ($m^*_{th} = 1.89 \times 10^{-14}$ kg), we can estimate a value for the Si_3N_4 membrane of $m^*_{th} = 1.14 \times 10^{-11}$ kg, giving us the upper and lower bounds in Fig. 6.9. As can be seen in Fig. 6.9 (b), we find that the measured values fall into this interval. Note that these values for m^*_{th} are only estimates, especially when evaluating higher order modes for the circular hBN drum. The effective mass of a circular drum changes depending on the mode in question [130], and can differ significantly from the value of the fundamental mode. Unsurprisingly, the fundamental mode of the hBN drum has the lowest effective mass of all observed modes since it is the only one not expected to hybridize with the Si_3N_4 membrane.

Since both m^* and Q should depend on the degree of hybridization, we would expect a correlation between the two quantities. We plot the observed Q vs. m^* in Fig. 6.9 (c), where we indeed find that the modes with higher Q tend to have a higher m^*. From this observation, we can conclude that, via hybridization, the Si_3N_4 membrane can lend its high Q-factor to the hBN at the cost of a higher effective mass.

6.4 Characterization at Cryogenic Temperatures

We now investigate the behavior of this device at low temperatures. To this end, we mount the sample in our probe using the confocal microscope configuration (see

section 3.1.2) and cool it down in our bath cryostat. We will perform similar characterizations as before, both in liquid nitrogen (77 K) and liquid helium (4 K).

Upon cooling down, we immediately observe drastic changes in the behavior of our resonator. Bulk hBN is known to have a negative thermal expansion coefficient [175], so, as in graphene, it is reasonable to expect that this property is preserved or even enhanced in the 2D limit [176]. Therefore, we expect a bulging of the membranes at low temperatures.

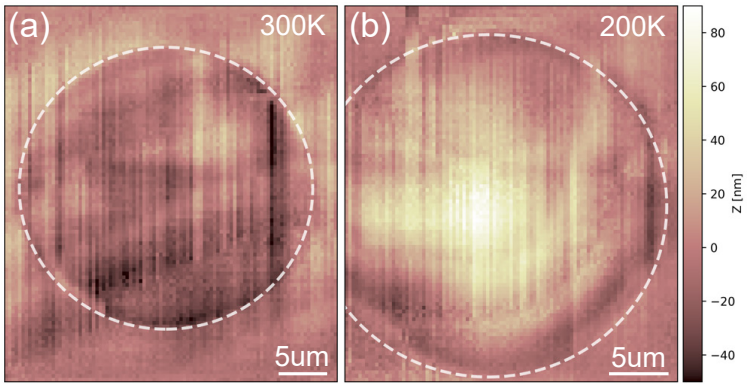

FIGURE 6.10: Reflected intensity maps that show the topography of the drum due to the interferometric nature of the measurement setup. The data was tilt corrected, leading to visible artefacts, this was necessary due to deviations in the scanner movements. The room temperature map in (a) shows no obvious features, while the one at lower temperatures in (b) has a clearly bulged shape.

In Fig. 6.10, we plot reflected intensity maps of the drum resonator. These maps reveal the topography due to static interference between the fiber facet of the confocal microscope and the sample and can be used to test our hypothesis. When comparing the room temperature map in (a) with the one at 200 K shown in (b), it becomes apparent that bulging of the drum has taken place. While no such effect was observed for monolayer hBN [45], the sample presented here is not thin enough to be clearly in the membrane regime, where the drum would be expected to stay under tension by adhering to the side walls of the underlying substrate [44].

In the raw scanned data, we observe an additional interference pattern corresponding to a tilt in the scan. This tilt is not caused by an actual tilt of the membrane but by deviations in the motion of the membrane scanner. After correcting for this tilt, the observable vertical artefacts are left in Fig. 6.10.

Mode imaging reveals that the modes we observed at room temperature are replaced with entirely different mode shapes. All the modes we could observe now show motion mostly in one of three small circular regions of the drum.

In Fig. 6.11 (b), a mode is shown that exhibits motion in all three mentioned regions (see green arrows), serving as an overview. Most other modes can be imagined as a subset of the regions shown in this image. An example is shown in Fig. 6.11 (c). As can be seen when comparing these regions to the fundamental mode at room temperature (Fig. 6.11 (a)), the area of motion appears to be significantly reduced at low temperature. Most of the deformation happens early on in the cooldown, consistent with the expected thermal expansion coefficient of hBN [175], which has a relatively constant value at higher temperatures but approaches zero between liquid nitrogen and liquid helium temperatures.

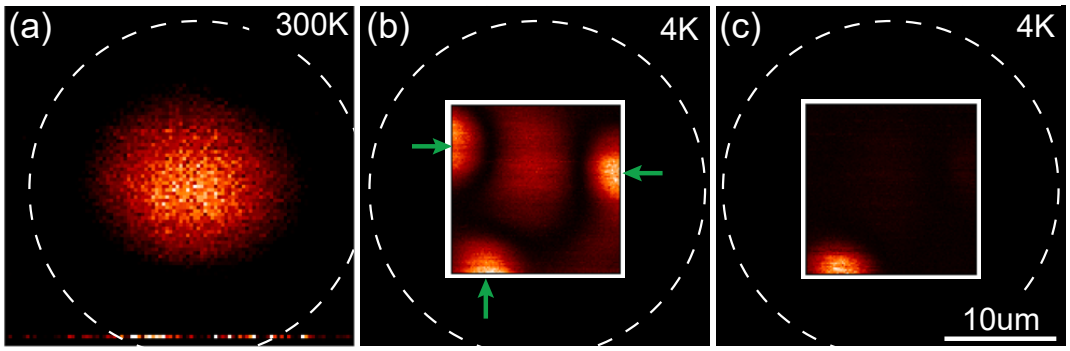

FIGURE 6.11: (a) Fundamental hBN mode at room temperature as a comparison. Two different modes of the bulged drum at 4 K (b) and (c). The image in (b) shows a complex mode that spans a large area, for which thermal motion could not be observed. The image on the right is a more typical mode, representing the ones that we were able to characterize (see Fig. 6.12). Most modes show motion in only one of the three circular regions in (b), highlighted by the green arrows. Dashed circles show the drum edge while the white squares in the last two images indicate the limited scan window at 4 K.

The frequencies of the Si_3N_4 modes did not change significantly when cooling down, while the modes of this hBN drum tend to react strongly to temperature changes, even before the mode shapes are lost.

Despite these changes, we can again investigate the Q and m^* of the observed resonances. We plot these values together with the ones obtained before for room temperature as comparison in Fig. 6.12.

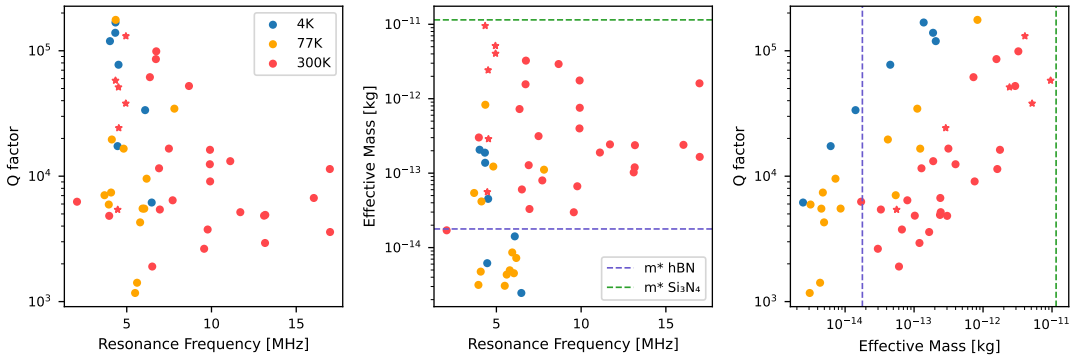

FIGURE 6.12: Measurements as presented in Fig. 6.9, but with the additional data taken at 77 K (yellow) and at 4 K (blue).

At lower temperatures, there is no mode low enough in frequency that we can expect it to not show hybridization. The only mode at such a low frequency is still the fundamental mode at room temperature, shown by the leftmost red dot in Fig. 6.12 (a).

In general, cooling down such 2D material resonators should result in an increase in Q. While we do observe an increase in our highest observable Q at low temperatures, the effect is not as big as in other published work [45, 80, 164, 177]. It would naturally be beneficial to follow a certain mode and measure how its Q changes with temperature, but due to the change in mode shapes, this is difficult in our case. For example, we can not observe the evolution of the Q-factor of the fundamental drum mode since no corresponding mode exists after buckling of the resonator occurs.

Looking at Fig. 6.12 (b), m^* tends towards lower values for lower temperatures. It even falls well below the expected value for the fundamental mode of hBN, which we used as a lower bound at room temperature. As mentioned before, this is expected from our mode images, which show a much smaller area of motion at low temperatures, especially considering that most modes that exhibited observable thermal motion were similar to the one shown in Fig. 6.11 (c) rather than the one in (b).

Unlike at room temperature, we do not observe m^* reaching the upper limit given by the motional mass of the Si_3N_4 membrane. We believe that this is due to our inability to observe thermal motion for such modes. When looking at Eq. 2.6, one notices that the thermal motion scales with T and inversely with m^*, ω_m and Γ_m. As already visible in Fig. 6.1 (a), the thermal peak of the fundamental mode of hBN is much higher in amplitude than the one of Si_3N_4 . This is due to the fact that the difference in Q (and thus Γ_m) is not nearly as large as the several orders of magnitude difference in m^* between the two resonators. Because of this, strongly hybridized modes are more difficult to observe for this device. With the additional reduction in signal due to the lower temperature, this lowers the cutoff of observable thermal motion, leading to the disappearance of modes at higher frequencies but also at high degrees of hybridization (*i.e.* high Q and m^*).

Finally, when plotting Q vs. m^* in Fig. 6.12 (c), we again find a similar correlation due to hybridization. The main difference is the shift towards lower m^* and higher Q, especially when comparing the Q for a similar effective mass.

6.5 Force and Mass Sensitivities

As a last step in characterizing these mechanical resonators, we will estimate their force and mass sensitivities. In particular, we would like to investigate how these sensitivities depend on the degree of hybridization. The force and mass sensitivities in units of $[N/\sqrt{Hz}]$ and $[kg/\sqrt{Hz}]$ are given by Eq. 2.10 and 2.11.

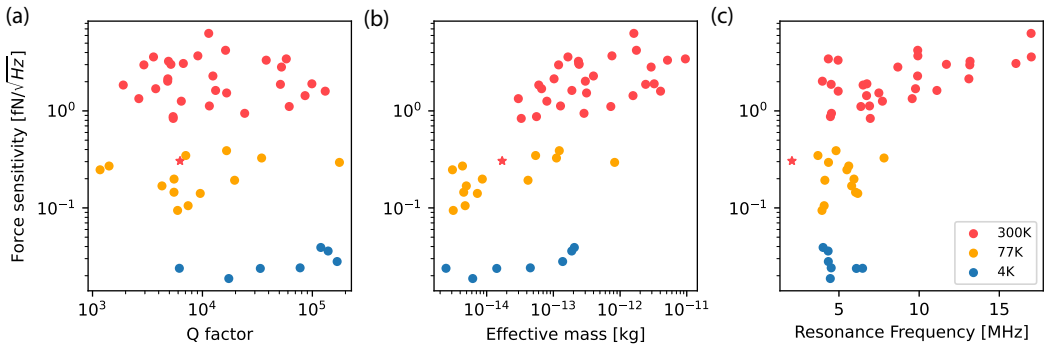

FIGURE 6.13: Force sensitivity as a function of Q, m^* and f_m. The star shaped marker corresponds to the fundamental mode of the hBN drum at room temperature.

In Fig. 6.13, the resulting force sensitivities for the mechanical modes characterized in Fig. 6.12 are shown as a function of Q, m^* and their resonance frequency f_m. We have highlighted the fundamental mode of the drum with a star shaped marker. Since no such mode exists at low temperatures, this only applies to the room temperature dataset in red.

In Fig. 6.13 (a), no clear correlation can be observed between Q and $\sqrt{S_F}$. The only point that stands out at room temperature is the fundamental mode, which

appears to show a much better force sensitivity than the other modes. Since $S_F \propto T$, it is not surprising that a decrease in temperature leads to a better sensitivity, independently of the mechanical properties. This explains, in part, the difference in sensitivity between the three datasets, not only in (a), but in all graphs in Fig. 6.13. But we also observed an overall increase in Q (and thus a decrease in Γ_m) and a decrease in m^* in this device when cooling down. And since $S_F \propto \Gamma_m, m^*$, we expect this effect to also play a role in the improved sensitivities at lower temperature.

This is illustrated by the trends seen in Fig. 6.13 (b), where we observed an improvement for modes with the same m^* at lower temperature but also an improvement for lower m^* within each dataset. This shows that we can observe an effect of the mechanical properties and not just the temperature. The fact that we do not clearly observe such a dependency for Q might be caused by the fact that the change in m^* spans several orders of magnitude while the difference in Q is more moderate.

Looking at Fig. 6.13 (c), the room temperature data shows some correlation with f_m. While a similar trend appears to be visible for the datasets at low temperatures, due to the lack of data points, it is difficult to be certain. This trend might be due to the fact that at higher frequencies, while m^* remains high, Q tends to decrease, thus affecting the sensitivity. The good sensitivity of the fundamental mode can be explained by the fact that it offers a reasonable Q at the lowest m^*. This indicates that for our system, the gain in Q does not outweigh the increase in m^* when hybridization occurs. The fundamental mode of hBN has the lowest effective mass at room temperature, *i.e.*, it is the only mode that is clearly not hybridized.

This is also in line with our discussion in the previous section about thermal motion, in which the fundamental mode had the highest amplitude of all observed modes. Since thermal motion and these sensitivities are inherently connected, as discussed in section 2.1.1, one would expect a similar trade off.

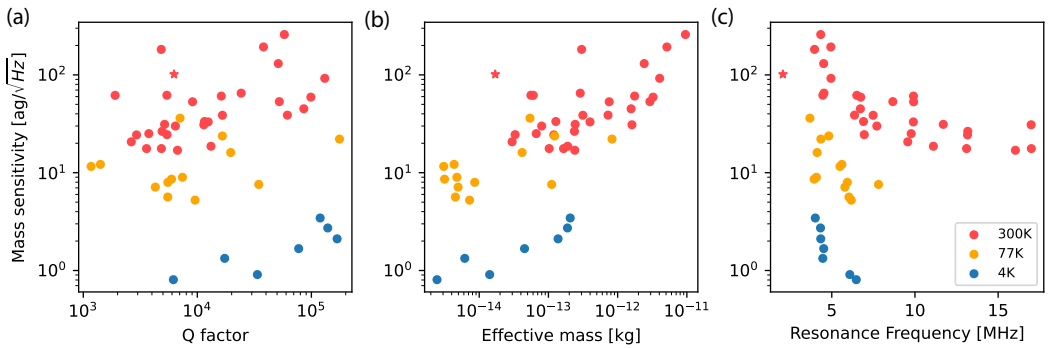

FIGURE 6.14: Mass sensitivity as a function of Q, m^* and f_m. The star shaped marker corresponds to the fundamental mode of the hBN drum at room temperature.

In Fig. 6.14, we show the mass sensitivity. It has an additional term $\frac{2}{x_0\omega_0^2}$ compared to the force sensitivity (see Eq. 2.10 and 2.11), giving it a strong dependency on frequency, as clearly visible by the trends shown in (c). This also explains why the fundamental mode does not perform as well compared to the force sensitivity estimations. Still, no increase in mass sensitivity can be observed for the strongly hybridized modes with high values of Q and m^*. On the contrary, when looking at Fig. 6.14 (b), we observe that the modes with lower m^* still tend to perform best. The temperature dependency naturally follows the same trend as before.

While hybridization did not have a positive effect on the sensitivities of this device, this trade off depends on the properties of the two involved resonators. Better Si_3N_4 resonators, as for example demonstrated in [49, 178], could improve the sensitivity of such 2D resonators through hybridization. It was furthermore demonstrated in a graphene-Si_3N_4 device that such hybridization can improve the signal to noise ratio in a force measurement, especially for high Q Si_3N_4 resonators (see SI of [171]). However, this requires precise control of the relative frequencies of the hybridized modes.

Chapter 7

Optomechanics with hBN Drum Resonators

Having characterized the constituents of our FFPC-MIM system and developed the necessary tools to control and measure them, we are now ready to explore the complete system. First, we will discuss more practical aspects of aligning the system using WL spectroscopy as well as red laser scans of the sample. We will then explore the viability of the hBN drum as a MIM system in our FFPC under high finesse conditions and measure the static optomechanical interaction. Finally, we will take a look at the dynamic interaction by measuring the OMIT effect.

7.1 Low Reflectivity Measurements

As a starting point, the sample is inserted into the cavity while the fibers are at a distance of several mm. Before closing the system, we bring the fibers into closer proximity around the sample. At this point, L_{Cav} is at several hundred µm, well beyond the range where a signal with the NIR laser could be observed (see Fig. 4.7). This is necessary to protect the system when inserting the probe into the cryostat. Especially due to the spring suspension, the probe can swing freely inside the vacuum can (see Fig. 3.3), leading to mechanical shocks that could destroy the system when the constituents are in close proximity.

Without visual access to the system, we first perform a scan of the sample. We use the x-y piezo scanner in the sample block to produce a map similar to the one shown in Fig. 7.1. Here we use the red laser, bypassing the highly reflective window of the coating, which still gives a signal at much greater distances compared to the NIR laser. The purpose of this scan is mainly to navigate the sample.

The maps shown in (a) and (b) were measured when the system was already closer, but these red light measurements still show a clear enough image at long distances. The main difference is a reduction in resolution and a drop in intensity in transmission, but identifying the hBN drum or an empty hole is still easily possible. We then move the sample using the membrane positioners until the hBN drum can be accessed within the scanning window of the membrane scanner. We usually position the membrane in such a way that we also have access to an empty hole to perform measurements without the interference of the membrane. For example, we can measure L_{Cav} using WL spectroscopy through this hole, as in chapter 4.

Fig. 7.1 (c) shows the corresponding sample region as a microscope image for reference. Comparing this image to the scans in (a) and (b), we notice that we can differentiate the empty hole from the one covered with the hBN flake as a difference in, *e.g.*, the transmitted intensity. We further observe lines where the flake boundary and the edges of the holes are situated.

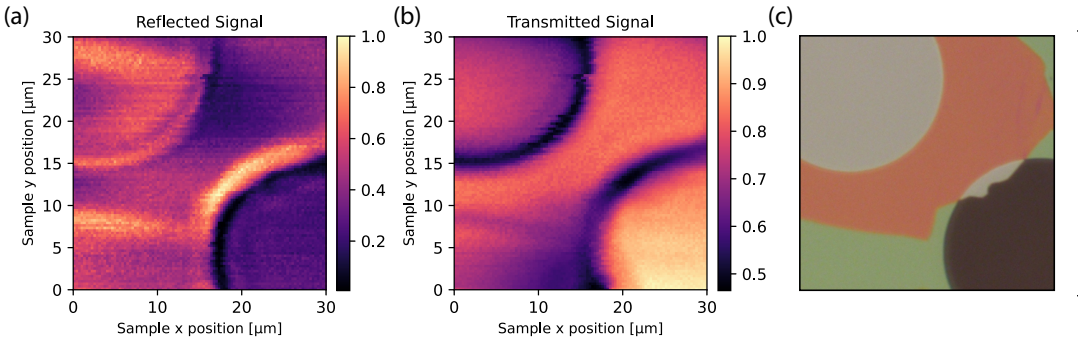

FIGURE 7.1: Sample scanned in the orthogonal plane to the cavity axis using the red laser, reflected signal in (a) and transmitted signal in (b). (c) shows a microscope image of the scanned region for reference.

Having aligned the sample in the orthogonal plane with respect to the cavity axis, we can now use WL spectroscopy to bring the constituents of the MIM-FFPC system into close proximity.

We begin by moving the sample close to the fixed input fiber. To this end, we position the sample in such a way that either the hBN drum or the Si_3N_4 membrane is in front of the input fiber. The transmission fiber is at a far enough distance to not contribute significantly to the reflected WL spectrum, typically around 100 µm.

The WL spectra in reflection usually have higher levels of noise due to additional reflections from, *e.g.*, the fiber couplers. But as shown in Fig. 7.2 (a), we can still find the peak positions in the spectrum reasonably well. However, this is only true for some intervals of the spectrum, which is why the one shown only covers 610 to 680 nm, a much smaller range compared to Fig. 4.5. At this length, this subset of the measured spectrum still features more than enough resonances to perform the fit. The measurement is again evaluated as described in chapter 4, the results of the fits are shown in Fig. 7.2 (b)-(e). Due to the higher levels of noise in these measurements, the evaluation of the mode number is not consistent across all lines, resulting in jumps of $\lambda/2$. This results in the three lines visible in Fig. 7.2 (d).

We have again performed a comparison with microscope images while the system was open to test the reliability of this technique. An example of such a microscope image is shown in Fig. 7.3 (a), where the transmission fiber is also visible to the right (red arrow). Since the dark surface of the sample is almost invisible and the distance would be difficult to estimate given the orientation, we use the reflection of the input fiber on the sample instead (white arrows). This gives a measurement of twice the distance between the sample and the input fiber.

While the spectra suffer from higher levels of noise, surprisingly, the deviations between image based estimations of the length and WL spectroscopy shown in (b) are very small. This could imply that the larger discrepancies shown in Fig. 4.6 (b) are due to a less reliable image based estimation of L_{Cav}, and that the WL measurement is as reliable for measurement of the fiber-fiber distance as for the fiber-sample distance.

After bringing the sample in close proximity, usually about 10-15 µm so as to position the sample close to $L_{Cav}/2$ for our typical cavity lengths, we move the sample to position the empty hole in front of the input fiber. We then perform WL measurements as in chapter 4 and incrementally reduce L_{Cav} to about 20-30 µm.

At these distances, a signal under high finesse conditions with the NIR laser should be observable, but often the transmission fiber is not well enough aligned

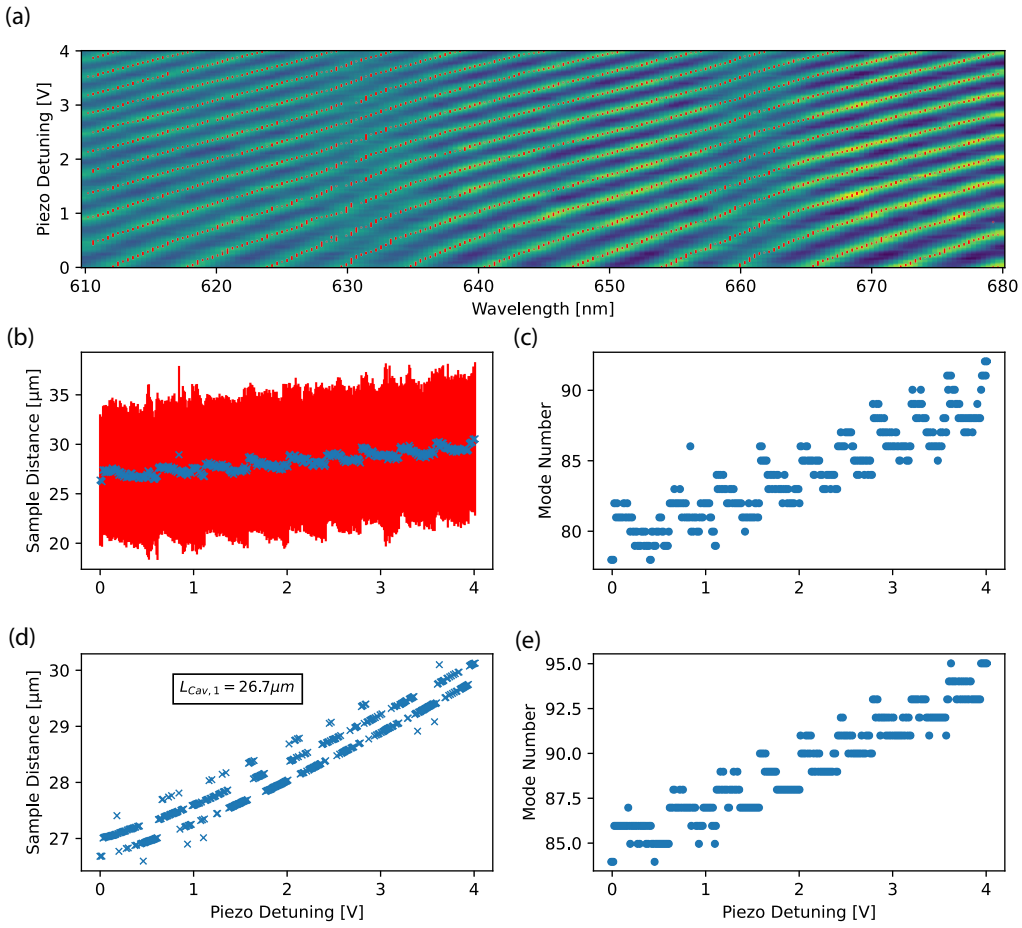

FIGURE 7.2: Whitelight measurement as in Fig. 4.5, but this time performed in reflection with the sample in front of the input fiber. The transmission fiber is kept at a long distance for these measurements. (a) Spectrum with peak positions in red. (b) and (c) show the initial fit and the corresponding mode number, (d) and (e) show the final fit and the corresponding mode number. The extracted length between the fiber and the sample ($L_{Cav,1}$) is displayed in (d).

with the input fiber in x-y. We have found that maximizing the contrast of the cavity signal in transmission with the red laser is a good first step to align the FFPC. At such low reflectivities, the cavity signal approaches a simple sine wave that is easy to observe on an oscilloscope while continuously scanning the cavity length with the piezo positioner. Typically, this sine wave is combined with a relatively large constant offset. One might think that maximizing the overall signal intensity in transmission would be a good choice, but this point of optimal fiber coupling does not coincide with a good alignment of the FFPC for us. We instead have more success when aligning for maximal contrast of the sine wave, ignoring the overall signal strength. This might be due to a small error in crater centering with respect to the fiber core or other geometrical imperfections. After these steps, we can usually observe a signal using the NIR laser through the hole in the sample, which can then be used to optimize the alignment and operate the cavity as in chapter 4.

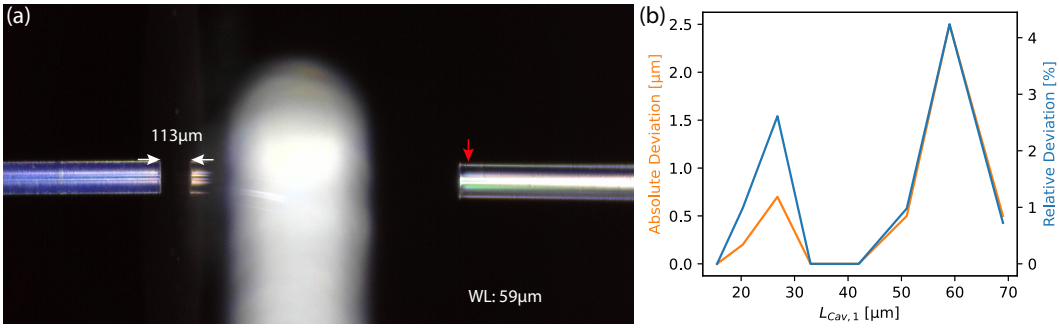

FIGURE 7.3: (a) Microscope photograph of the FFPC with the inserted sample. The length (white arrows) between input fiber and sample is measured by looking at the fiber's reflection on the sample surface, not to be mistaken for the transmission fiber (red arrow). The measured distance is thus roughly twice the distance of the WL measurement (displayed bottom right). (b) Relative (blue) and absolute (orange) deviation between the visually and spectroscopically measured values.

7.2 High Finesse Operation and Static Optomechanical Interaction

Having aligned the system, we are now interested in the viability of our sample for high finesse optomechanics. As pointed out in section 2.3.1, even moderate levels of scattering losses and absorption in the membrane have a big impact in such a system and quickly lead to a complete loss of the cavity signal. While hBN is predicted to show low levels of absorption [69] and has recently been placed inside a high finesse cavity [70], cleanliness and surface quality of the sample can still play a major role. We again perform scans of the sample in the x-y plane while also scanning the cavity length. The simultaneous scanning of the cavity length is performed over more than one FSR to record a long range cavity spectrum as in Fig. 4.1. For these measurements, the membrane is positioned close to a node in the cavity field, where the losses should be minimal. We then plot the minimal signal in reflection and the maximal signal in transmission in Fig. 7.4 (a) and (b), which corresponds to the highest observable cavity signal in both cases.

While not useful in reflection, due to the constant maximal signal, we can adjust the gain of the transmission detector to boost the signal when it drops to lower levels. This adjustment is done automatically throughout the scan, the order of magnitude of this gain is shown in (c). Note that due to this gain adjustment, (b) is plotted using a logarithmic scale while (a) is shown on a linear scale.

The empty hole on the bottom right of each scan serves as a reference for the undisturbed cavity signal; ideally, we would hope to reach a similar signal through the hBN drum, signifying minimal losses. The broad bright (dark) regions in the reflected (transmitted) signal show areas where the cavity signal is largely lost. Here, scattering losses are high due to edges in the sample topography. While these regions are centred around thin features such as flake boundaries or hole edges, they are broadened due to the waist size of the cavity field. We see a rather sharp contrast, implying that even if the edge is only present in the outer parts of the Gaussian mode profile, the cavity signal is lost. Even though the gain is adjusted to the highest possible value, as indicated by the bright regions in (c), no signal is present in transmission in these regions.

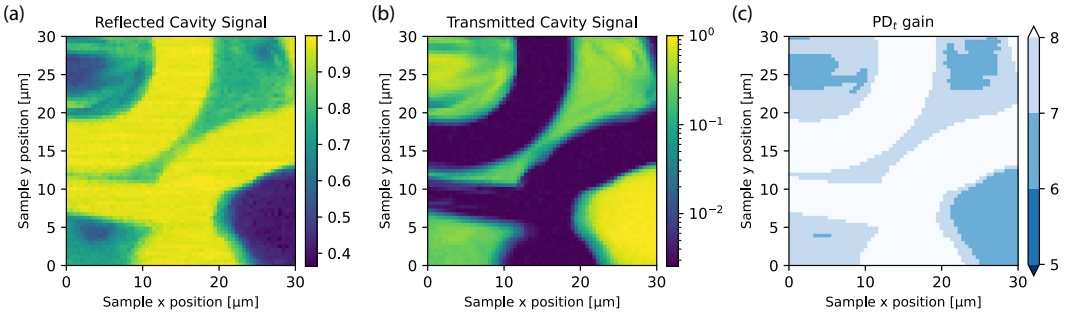

FIGURE 7.4: Sample scan covering the same region of the sample as in Fig. 7.1, but with the NIR laser (*i.e.*, high finesse operation). Shown is the peak cavity signal in a scan of the cavity length over more than one FSR. Since the cavity signal is a dip in reflection (a) and a peak in transmission (b), the color is inverted between the two maps. The gain setting of the transmission diode is automatically adjusted throughout the measurement the order of magnitude of the gain is shown in (c).

While we generally observe a reduction in signal outside of the empty hole and away from boundaries, there are areas on both the Si_3N_4 membrane and the hBN drum that reveal high signal levels. Notably, the gain is lowered to the same value as for the empty hole in the middle of the hBN drum. This shows that the loss in signal does not exceed one order of magnitude, a manageable change in signal. We also observe a high signal in the area to the top right, where we measure through Si_3N_4 and hBN, and on the bottom left of the scan, where we measure through only Si_3N_4. This indicates that the hBN drum does not appear to cause larger losses compared to the Si_3N_4 membrane. This is a good sign considering Si_3N_4 is a well established material in the optomechanics community, not only due to its mechanical properties but also because it causes low optical losses [51, 201].

We can now perform cavity scans covering a length corresponding to several FSR for different sample positions along the cavity axis z. Like this, we can experimentally reproduce maps as shown in Fig. 2.10 and fig. 2.12, mapping the static effect of the membrane on the cavity's resonance length. The result is shown in Fig. 7.5.

We perform these measurements through the empty hole, through the Si_3N_4 membrane, and through the hBN drum, where we observed high levels of signal before. In these measurements, the cavity length is kept at 20 to 25 µm. We only show the transmitted cavity signal since the reflected signal is complementary and reveals no additional insights, but has higher levels of background noise. We expect different levels of interaction for each of these measurements due to the different reflectivities of the materials (or lack thereof). The measurement through the hole mostly serves as a check that the system behaves as intended; naturally, the sample position along z should not have any effect on the cavity spectrum in this case. We observe the expected horizontal lines corresponding to the fundamental modes of the cavity spaced by the FSR, highlighted by the white arrows in Fig. 7.5. We also observe a slight non-linearity at the edge of the scan, which we attribute to non linear piezo motion. We will exclude this interval of the data in our following analysis. We can also see some fainter features that correspond to higher order modes of the cavity, highlighted by green arrows in Fig. 7.5 (a).

The measurement performed through the Si_3N_4 membrane (b) and the one through the hBN drum (c) share similar qualities. The main difference is the smaller modulation in the case of the Si_3N_4 membrane, which is expected due to a difference

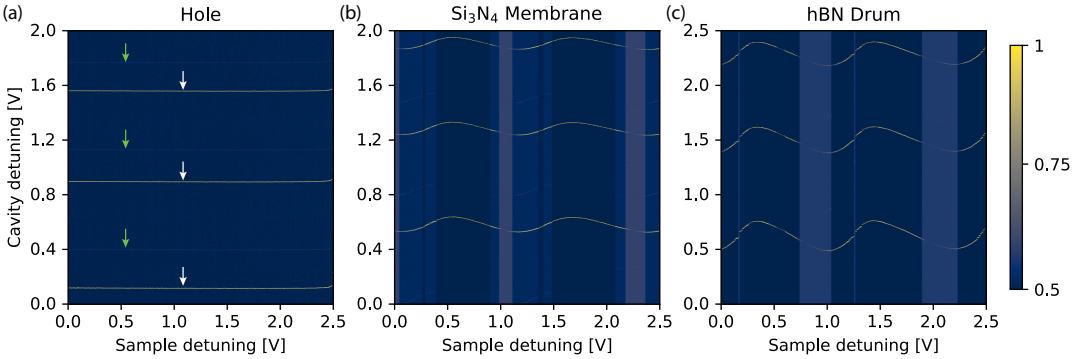

FIGURE 7.5: Cavity scans covering several FSR for different sample positions, only the cleaner transmission signal is shown. The fundamental cavity resonances reveal themselves as narrow lines (white arrows) while some higher order modes also appear to be visible (green arrows). The measurement is performed through the hole (a), the Si_3N_4 membrane (b) and the hBN drum (c), revealing different levels of interaction between membrane and FFPC. The bright vertical stripes are due to an increase in the gain setting of the photodiode and indicate regions with a lower cavity signal.

in reflectivity. While the hBN drum has an estimated reflectivity of $|r_m|^2 = 0.225$ at $\lambda = 920\,\text{nm}$ according to Eq. 2.58, the Si_3N_4 membrane only has a value of $|r_m|^2 = 0.08$. From our data, we not only see the periodic modulation of the cavity resonance length as a function of the sample position, but we also notice the asymmetric shape of the two slopes as predicted in Fig. 2.10 (b), due to the fact that we only move one cavity mirror.

We further observe changes in signal strength as a function of the sample position. These changes are difficult to observe in the graphs due to the narrow linewidth of the cavity, but the gain of the transmission photodiode gives a clear indication. The brighter shaded vertical stripes in Fig. 7.5 (b) and (c) correspond to higher levels of background, which is a result of the higher gain setting, and thus correspond to a lower cavity signal in transmission. These areas match the regions that are predicted to show high levels of scattering losses according to the beamsplitter model introduced in section 2.3.1 (Fig. 2.12), being the regions where a higher field is present within the membrane.

From these measurements, we can also extract both the frequency pull parameter G as well as the dissipative interaction of the system. The latter becomes accessible when fitting each cavity spectrum, *i.e.*, each vertical line in Fig. 7.5, and fitting the cavity lineshape to extract the linewidth, as we did in chapter 4. An increase in linewidth corresponds to a higher dissipation in the system. Similar to the frequency pull parameter G, we can quantify this effect with a parameter G_κ in units of $\text{GHz} \cdot \text{nm}^{-1}$ as well.

In Fig. 7.6, we show the extracted values for the measurement through the hBN drum. For each vertical line, we use a peak finder to extract the peak positions of the fundamental resonances; the resulting positions are plotted in (a) for one of the three observable fundamental cavity modes in Fig. 7.5. Since the scan covers several FSR, we can easily obtain the normalized cavity detuning $\Delta L_{Cav}/L_{FSR}$ or $\Delta\omega_{Cav}/\omega_{FSR}$. We fit this data with a model corresponding to Eq. 2.65, shown in orange in Fig. 7.6 (a). However, we replace the sample position z_m with a function $f(z_m)$ that includes a scaling factor z_V and an exponent ν_{NL}.

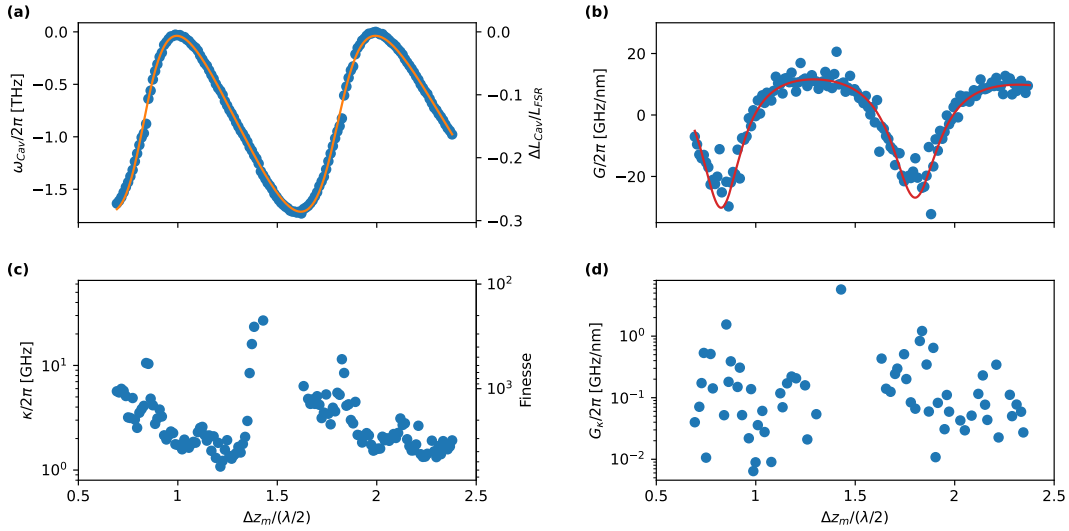

FIGURE 7.6: Values extracted from the measurement shown in Fig. 7.5 through the hBN drum. (a) Modulation of the cavity resonance length due to the sample position, normalized by L_{FSR}. Fit according to Eq. 2.61 in orange. (b) Extracted frequency pull parameter (Eq. 2.66) by taking the derivative of (a), note that the red line is the derivative of the fit in (a) and not a fit itself. (c) Linewidth (finesse) of the cavity as a function of sample detuning. (d) Dissipative coupling obtained by taking the derivative of (c).

$$f(z_m) = z_V (z_m)^{\nu_{NL}} \tag{7.1}$$

The purpose of the scaling factor is to convert from the voltage detuning to units of length normalized by $\lambda/2$, as used in Fig. 7.6. The exponent ν_{NL} is necessary to account for the non-linear motion of the piezo, a problem already observed *e.g.* in Fig. 4.1. This ν_{NL} is left as a free parameter and is adjusted by the fit to a value of ~ 1.25.

In Fig. 7.6 (b), we show the derivative of the data points in (a) as well as the derivative of the fit function itself in red. From this, we can estimate a maximal frequency pull parameter $|G|/2\pi$ of 30 GHz. It is important to note that since we perform this measurement by detuning one of the cavity mirrors, the observed frequency pull parameter shares the asymmetry of the signal in (a). This asymmetry affects the slopes of the signal and thus the magnitude of G, effectively leading to an increase in the $|G|$ on one side and a decrease on the other side of the signal. A measurement based, *e.g.*, on the laser frequency would not show such an effect and would result in a different maximal value of G.

The extracted linewidth and finesse are shown in Fig. 7.6 (c). We have removed outliers where the identification and fitting of the cavity resonance failed. This leads to a gap in the middle of the graph corresponding to the area with the lowest signal in Fig. 7.5. As the trend surrounding this gap indicates, the linewidth appears to increase towards this gap, as expected in an area with higher losses. Apart from this area, we can maintain a linewidth of around 2 GHz.

In Fig. 7.6 (d), we extract a dissipative coupling parameter G_κ by taking the derivative of the data in (c). Due to the difficulty of evaluating the interval where the broadening of the cavity linewidth is the strongest and the noise in the data in (c), a clear trend is hard to observe.

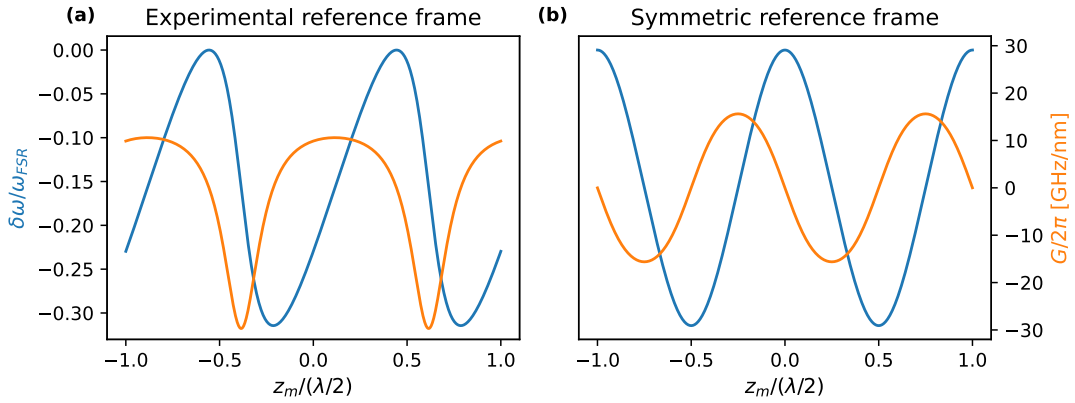

FIGURE 7.7: We compare the frequency shift (blue) and the frequency pull parameter G (orange) in the experimental reference frame (a) where only one cavity mirror is moved, and in the symmetric reference frame (b), where both are moved around the central membrane position. The graphs are based on the analytic expressions given in section 2.3 using parameters in line with our experiment ($\lambda = 920\,\text{nm}$, $|r_m|^2 = 0.225$ and $L_{Cav} = 20\,\mu\text{m}$). We see that the maximal value of G is around a factor of 2 lower in the symmetric case.

To estimate the value of G in the symmetric case, which is more in line with commonly cited values in literature, we compare the two analytical expressions for the different scenarios given in section 2.3. In Fig. 7.7 (a), we plot the resonance shift of our MIM-FFPC system according to Eq. 2.65, where only one cavity mirror is displaced. This model is equivalent to the fit in Fig. 7.6 (a), except for the aforementioned non-linearities of the piezo. In (b), we plot Eq. 2.61, corresponding to the symmetric case, using the same parameters as in (a). In both cases, we take the derivative to extract a value of G, shown in orange. In the symmetric case, we find a maximal value of $|G|/2\pi = 15\,\text{GHz}\cdot\text{nm}^{-1}$, which is approximately a reduction by a factor of 2 compared to the asymmetric case.

Since we have characterized our mechanical resonator in depth in chapter 6, we are well equipped to estimate the resulting optomechanical single photon coupling strength g_0 as defined in Eq. 2.66. For the fundamental mode of this hBN resonator, we can estimate an upper limit for the coupling strength of $g_0/2\pi = 460\,\text{kHz}$, based on the highest value for G in the asymmetric measurement. For the symmetric case, we can expect a value of $g_0/2\pi = 230\,\text{kHz}$, according to the conversion shown in Fig. 7.7.

To estimate not only the values achievable with this hBN drum device but for other similar devices, we explore the optomechanical coupling strength as a function of drum diameter and thickness in Fig. 7.8. In (a), we first plot the zero point fluctuations of the drums estimated using Eq. 2.9, where we compute the resonance frequency for the fundamental mode according to Eq. 2.14 and the effective mass with Eq. 2.18. The value of G given in (b) was obtained as in Fig. 7.7, assuming the symmetric case. Combining these two values then gives the single photon coupling strength in (c).

We see that the zero point motion is maximized for small and thin devices. While such small devices might not have the lowest resonance frequency, the reduction in effective mass appears to be the key property. The frequency pull parameter G, on the other hand, requires high reflectivity and thus favors a much larger drum thickness. For even thicker drums, the reflectivity is then again reduced, leading

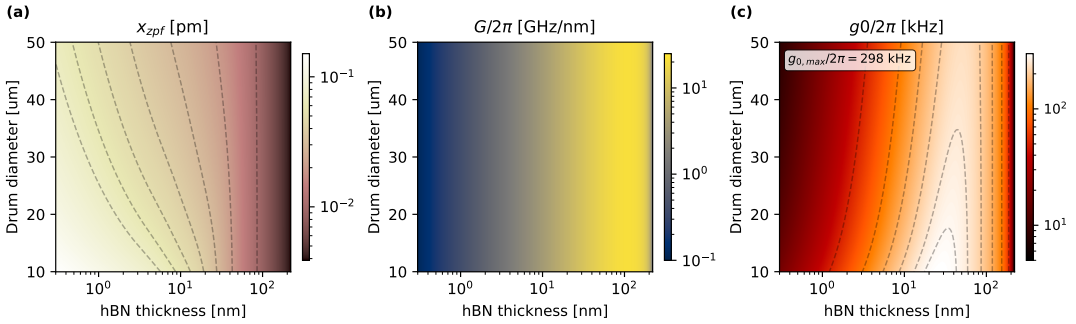

FIGURE 7.8: Shown are the zero point fluctuations (a), the maximal frequency pull parameter G (b) and the resulting single photon coupling strength g_0 (c) for different drum diameters and thicknesses. The estimations are based on the symmetric reference frame for G. The maximal value of g_0 is displayed in (c) and is achieved for a drum diameter of 10 µm and a hBN thickness of 27 nm.

to the darker region at the right edge of the graph. This, in conjunction with the opposing trend seen in the magnitude of zero point fluctuations, leads to a maximal g_0 between a drum thickness of 20 and 60 nm, depending on the drum diameter, as seen in (c). While smaller drum diameters appear to be advantageous, the effect is rather modest compared to the thickness. We can also observe that for large drum diameters, the highest coupling g_0 tends towards slightly thicker drums, which is especially obvious when following the contours.

We can deduce that the parameters of the device presented here are already close to optimal, especially considering that much smaller drums than the lower limit of 10 µm assumed in Fig. 7.8 (c) would lead to clipping losses and degrade the cavity signal. The maximal coupling within the displayed parameter space is $g_{0,max}/2\pi = 298$ kHz, and would be achieved with a drum diameter of 10 µm and a thickness of 27 nm. For a drum diameter of 30 µm, as the hBN drum used for the measurements shown here, the highest value would be $g_{0,max}/2\pi = 257$ kHz with a drum thickness of 42 nm, close to the 48 nm of our device.

7.3 Dynamical Measurements and Optomechanically Induced Transparency

We now move on to measurements where we do not look at a static offset caused by the position of the membrane but instead at the dynamic interaction of the FFPC and the motion of the hBN drum. We first lock the cavity on resonance with the hBN drum in the middle of the cavity, employing the PDH feedback scheme used in section 4.2. We can then observe the fundamental mode of the hBN drum resonator with the LI-A, similar to the measurements with the RT interferometer in chapter 6 (*e.g.*, Fig. 6.1), but using our cavity instead of the interferometer. Such a measurement is shown in Fig. 7.9.

Locking the cavity like this is much more challenging compared to the empty FFPC due to the additional noise and losses introduced by the membrane. While the lock quality in this state is not as good as in chapter 4, it is sufficient to perform more complex measurements.

To observe OMIT, we require several input tones to perform a pump-probe measurement, as outlined in section 2.3.2. We generate these tones by applying a phase

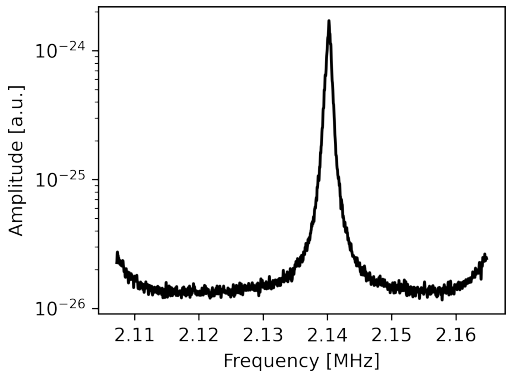

FIGURE 7.9: Thermal motion of the fundamental mode of the hBN drum measured using the FFPC. The signal is recorded using the LIA while the cavity is locked.

modulation with our EOM (see section 3.1.3), using a similar measurement procedure as in [198, 202]. An overview of the involved resulting frequency components is shown in Fig. 7.10.

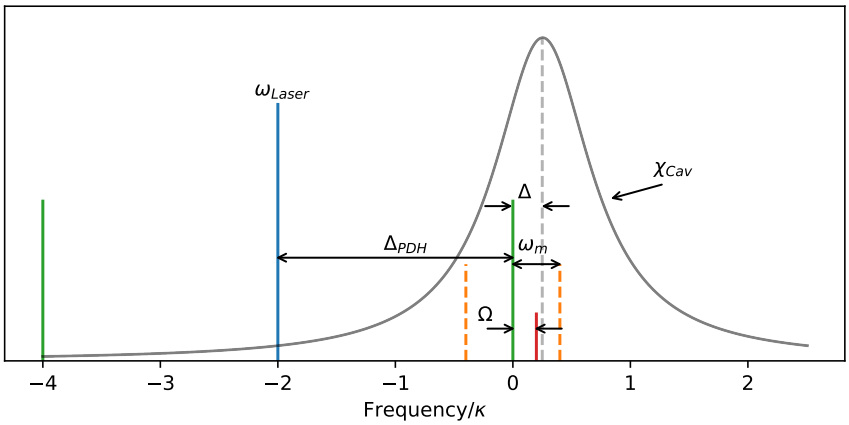

FIGURE 7.10: Overview of the different frequencies that are involved in the OMIT measurement. The central laser is shown in blue, and the two sidebands for the PDH locking scheme are shown in green. One of the sidebands is locked to the cavity, representing our pump tone, with mechanical sidebands shown in orange. The probe tone shown in red is an additional sideband obtained by phase modulation from the main laser tone, but we define its frequency detuning Ω with respect to the pump.

As a starting point, we always employ our main laser tone (shown in blue) with sidebands (green) spaced by Δ_{PDH} for our PDH locking scheme. These sidebands are spaced by several GHz to separate them from the main cavity peak. Unlike before, we now lock one of the sidebands of the cavity instead of the central peak. We furthermore use the angle error signal instead of the regular PDH error signal, as shown in Fig. 2.8. As discussed in section. 2.2.3, this is only an option when locking on a sideband and is preferable due to the larger usable interval of the error signal and the robustness against changes in laser power.

Regarding the different tones shown in Fig. 7.10, we use the sideband as our pump, while the main laser tone and the other sideband are off resonance with respect to the cavity. This allows us to scan a second probe tone (red in Fig. 7.10),

which is also obtained via phase modulation from the central laser, over the entire cavity resonance (χ_{Cav}). The pump can be detuned from the cavity by changing the setpoint of the lock; this detuning is shown as Δ in Fig. 7.10. Such a measurement setup is in contrast to a measurement procedure where the probe is produced by modulating the pump tone directly (*e.g.*, as in [141]), potentially leading to two sidebands within the cavity envelope.

The stronger pump tone produces sidebands through its interaction with the mechanics at $\pm\omega_m$, shown in orange. The OMIT signal is obtained when the probe is scanned around this region and interacts with a mechanical sideband, leading to a transparency window superimposed on the cavity response given by χ_{Cav}. The shape of this transparency window is determined by the mechanical susceptibility χ_m modified by the optomechanical interaction. As such, a fit with the model presented in section 2.3.2 should be able to characterize many of the parameters of the system, many of which we have already characterized by other means and can use for comparison.

It is important to note that in our case, $\kappa \gg \omega_m$, and while we are able to keep Δ reasonably stable compared to the cavity linewidth κ, we cannot stably set the cavity detuning with respect to ω_m as in [141], where OMIT was also measured in the unresolved regime. However, the frequencies of all the tones shown in Fig. 7.10 are stable with respect to each other, given that they are derived from the same source. This still allows us to observe their interaction around ω_m and thus the OMIT feature. We use the VNA to produce the probe tone and record the signal, and we define the probe tone frequency Ω with respect to the pump tone (*i.e.*, we subtract the offset from the main peak Δ_{PDH}). In this configuration, the noise in Δ affects the measurement by its influence on the optomechanical spring and damping effect, as well as by modulating the overall signal since our probe tone measures $\chi_{Cav}(\Omega + \Delta)$.

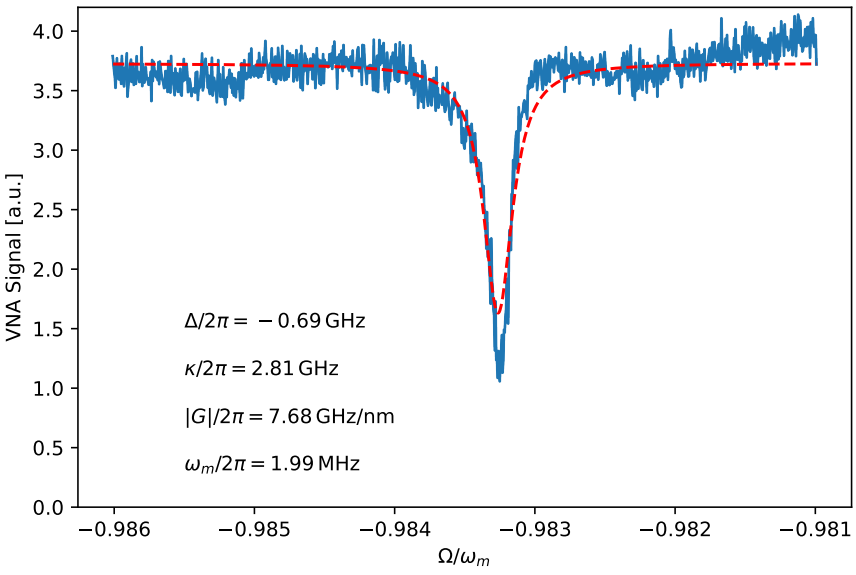

FIGURE 7.11: OMIT measured as a response using the VNA. The dip caused by the interaction with the mechanical resonator is visible close to ω_m, the cavity lineshape is much too broad to be observed on this scale. The free parameters of the fit are listed and are in good agreement with the system parameters established in chapter 4 and chapter 6. The measurement was taken with the sample close to a node of the cavity field and an input power of 20 µW.

A measurement revealing a clear OMIT feature is shown in Fig. 7.11, where the much broader cavity response only appears as a constant background signal. Since the effect of the thermal motion of the drum on the cavity resonance frequency (given by the product of x_{th} and G) approaches the value of κ for our maximal $|G|/2\pi = 15\,\mathrm{GHz}\cdot\mathrm{nm}^{-1}$, it is not trivial to keep the cavity lock stable. We tend to avoid this issue by positioning the hBN drum closer to the node of the cavity field, where the system experiences a more moderate coupling strength.

Because the coupling efficiency of the optical input is on the order of a few percent, the photon number in the cavity is only around $|\overline{\alpha}|^2 = 650$. The number of photons is estimated from the input power in a similar way as in section 4.2.3, but since we are locking using the PDH sideband, the number of photons is further reduced by the ratio between the main peak and the sidebands. This shows that we can observe the OMIT effect at very low power.

The fit shown in Fig. 7.11 is performed according to the model developed in section 2.3.2, but since we measure the signal with the VNA, it appears as a peak with the OMIT feature as a dip. This is because the modulation of the VNA is applied as a phase modulation to the laser, which in turn is transduced into an intensity modulation by the cavity that can be measured by the detector. When off-resonant with the cavity, the phase modulation is not transduced into an intensity modulation, and the typical constant signal when measuring a cavity in reflection is absent [198].

We further include a scaling factor to match the signal level outside of the OMIT dip to the model, given by the regular cavity response χ_{Cav}. Aside from this additional parameter, we use the cavity detuning Δ, the linewidth of the cavity κ, the frequency pull parameter G, as well as the mechanical resonance frequency ω_m as fit parameters. Other parameters, such as the effective mass m^* and the mechanical linewidth Γ_m are kept fixed, and we use the values characterized in earlier chapters. We in particular keep G and Δ and κ as free parameters since they are critical for the shape of the OMIT signal, and we do not have a good calibration for these quantities since they are either unstable (Δ) or rely heavily on the exact sample position (G and κ). The mechanical frequency, on the other hand, is detuned by the optomechanical spring effect and heavily affected by temperature, making it difficult to give a precise estimation. This prompted us to leave it as a free fit parameter as well. On the other hand, the mechanical linewidth Γ_m and the effective mass of the fundamental mode m^* were carefully measured in chapter 6 and should not significantly change.

The resulting values shown in Fig. 7.11 are in agreement with the system parameters we observed before. We set the lock setpoint to $\frac{1}{4}$ of the maximal angle error signal. According to Fig. 2.8, this should result in a detuning of about $\kappa/4$, in close agreement with the observed value. The linewidth is within the range shown in Fig. 7.6 (c), even though a precise comparison is difficult due to the large spread in values. The lower G is in line with our intention of measuring closer to the node of the cavity field, where the system is more stable. Finally, the mechanical resonance frequency only slightly deviates from the values measured in chapter 6, and is within the deviations due to temperature that we observed before.

A notable difference between the fit and the data in Fig. 7.11 can be observed regarding the depth of the OMIT feature. We are currently uncertain about the origin of this discrepancy. It is possible that the model used here is incomplete and does not include some effects, as, for example, pointed out in [179, 180], where an increased depth of the OMIT dip in the deep unresolved sideband regime is predicted. At the same time, further measurements are necessary to rule out improper calibration. In particular, the measurement chain involving the VNA and the microwave electronics is difficult to characterize since a calibration in our current setup requires the

cavity as a transducer. Like this, it is difficult to differentiate the broad cavity signal from background noise originating from other sources.

In Fig. 7.12, we repeat the measurement for different input powers (a) and membrane positions (b). Both parameters affect the effective optomechanical coupling strength since G depends on the sample position and the coupling strength g is scaled by $|\overline{\alpha}|$ compared to g_0. This results in similar behavior for both measurement series, where the OMIT feature becomes more pronounced.

The detuning Δ is kept at around $-\kappa/4$, as in Fig. 7.11. In (a), the sample is detuned by 30 mV from the cavity node (see Fig. 7.5), while in (b), the input power is kept at around 20 µW. Since the measurement shown in Fig. 7.11 is the same as the one shown in Fig. 7.12 (a) for 20 µW, we can assume similar values as shown in the fit. However, for Fig. 7.12 (b), the sample position will have a large effect on both G and κ.

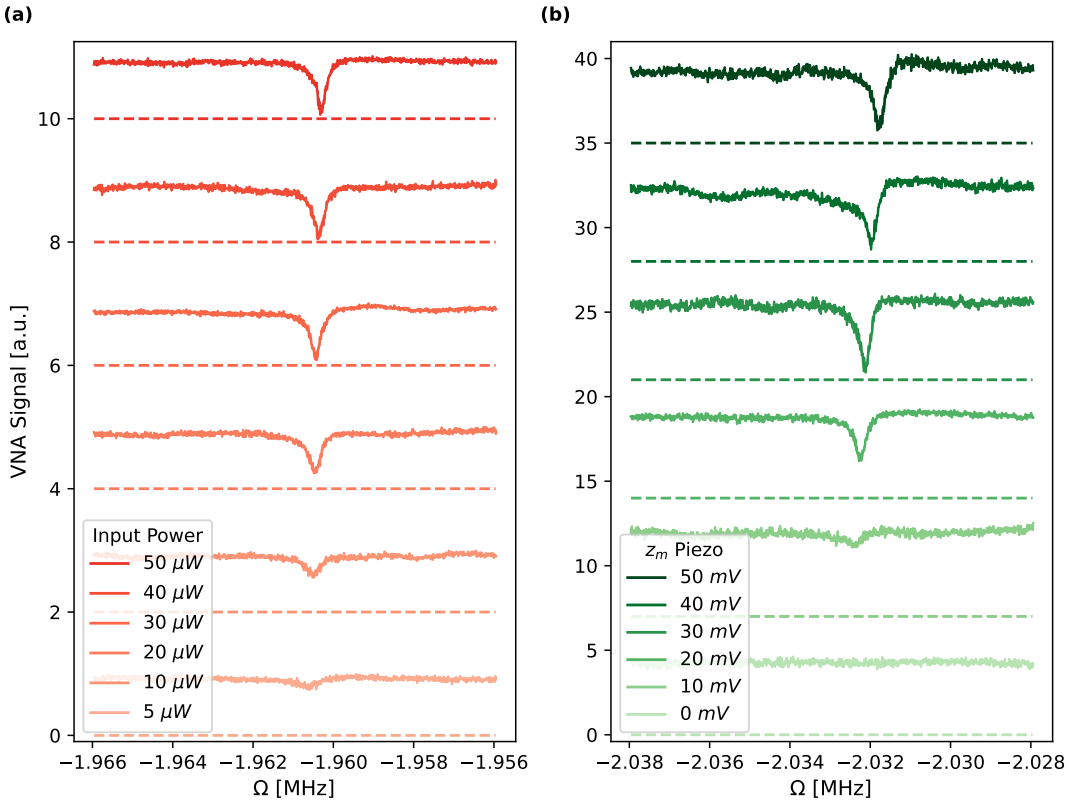

FIGURE 7.12: (a) OMIT measurement as a function of input power. The data sets are offset for clarity, the dashed lines indicate the zero level of each measurement. (b) OMIT measurement as a function of sample position along the cavity axis. At 0 mV, the sample is positioned at the node of the cavity field, corresponding to no optomechanical coupling. With higher voltages applied to the piezo, the sample is moved towards the antinode. However, even at 50 mV, the sample is still relatively close to the node, and we expect a moderate coupling.

In (a), the OMIT feature is barely observable at low optical input powers. When the power is increased, a clear dip manifests with increasing contrast. A slight shift in frequency towards lower $|\omega_m|$ can also be observed with an increase in input power. The contrast of the dip appears to approach 100%, resulting in an even more

drastic deviation from the model used to fit Fig. 7.11 and motivating further investigation in the future. When detuning the sample position in (b), we begin at the node of the cavity field (0 mV) where there is essentially no coupling ($G = 0$) and no dip can be observed. Moving away from the node of the cavity field, a clear OMIT feature can once again be observed. Here a more drastic shift towards lower $|\omega_m|$ appears to take place.

Both the spring effect $\delta\omega_m$ and the damping effect $\delta\Gamma_m$ are proportional to the coupling strength g^2, and as such a shift in resonance frequency is expected. Unfortunately, we do not currently have access to temperature stabilization in the cavity probe at room temperature, and the resonance frequency ω_m of our hBN drums is very sensitive to temperature changes. It is difficult to disentangle drifts due to the temperature from the optomechanical interaction. To give the reader an idea of the expected frequency shift due to $\delta\omega_m$, we plot Eq. 2.86 as a function of the photon number $|\overline{\alpha}|^2$ and G in Fig. 7.13. We also plot Eq. 2.87, the optomechanical damping effect, for completeness.

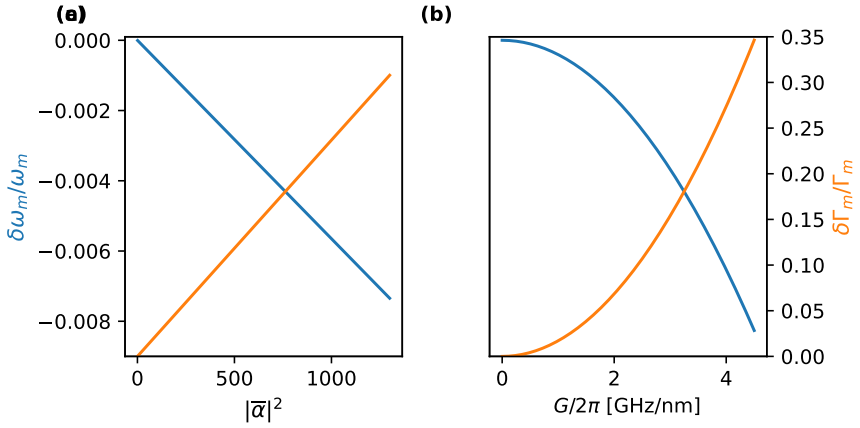

FIGURE 7.13: Optomechanical spring effect (blue) and optomechanical damping (orange) as a function of photon number $|\overline{\alpha}|^2$ (a) and as a function of frequency pull parameter G (b).

The graphs in Fig. 7.13 assume similar parameters as the ones we established in Fig. 7.11. In general, we expect deviations on the order of a few kHz which amounts to changes below 1% of ω_m, this can explain some of the frequency shifts in Fig. 7.12. However, when attempting to fit the different datasets, we cannot assume a consistent ω_m across the different measurements, indicating that the temperature drift cannot be ignored. This is especially obvious when comparing the average frequency between Fig. 7.12 (a) and (b), which are drastically different even for measurements where the optomechanical coupling would be rather low.

This measurement nonetheless illustrates our ability to perform dynamical optomechanical measurements with our MIM-FFPC system and showcases the viability of hBN as a material for cavity optomechanics. We achieve very high coupling strengths due to the miniaturization of both the cavity and the mechanical resonator. OMIT in particular can be the foundation for further exotic phenomena [143], as for example the generation of slow light [141]. It also allows us to determine many parameters of the system that would be difficult to access without moving the sample, such as Δ or G. It further provides an alternative way to characterize the mechanical properties with our cavity setup instead of the interferometric measurements shown in chapter 6.

Chapter 8

Conclusion and Outlook

In this thesis, we have presented and characterized an optomechanical membrane-in-the-middle system based on a fiber-based cavity and a hBN drum resonator. Regarding the optical cavity, we have demonstrated a fiber-based design that combines high finesse, stability, tunability, and cryo-compatibility. We have employed and introduced different techniques to utilize this system, some of which are notable improvements over existing protocols. First, a precise white light spectroscopy procedure that allows us to characterize not only the cavity length but also the position of a membrane in the middle of the cavity. This is especially important when pushing cavities to the micro scale, and when integrating them into cryostats, where visual access is often limited. Second, measures to improve the passive mechanical stability and active PDH stabilization allowed us to lock the cavity length to a reference laser. This resulted in a stability much better than the cavity linewidth κ, corresponding to only 3 pm at room temperature and 5 pm at 4 K, while maintaining the tunability of the system. The FFPC can also maintain a finesse as high as 10^4 over a large range of cavity lengths.

The hBN drum devices presented show excellent mechanical properties when compared to other similar devices and exhibit mode shapes that are consistent with theory up to high mode orders. We believe that the most important reason for this good performance is a combination of the fabrication procedure and the high stress Si_3N_4 substrates. The wet transfer technique allows the flakes to gently settle onto the substrate, avoiding inhomogeneous stress in the drum and maintaining its ideal mode shape. The high stress Si_3N_4 membrane avoids hybridization with the fundamental hBN drum mode, and if hybridization takes place, the high quality of the Si_3N_4 membrane does not cause a detrimental effect on the mechanical properties. While the thickness does not appear to have an effect on the Q of similar devices [43, 44, 46, 60, 93], there may be a positive effect due to the large drum diameter of our drums [181]. Another factor that is known to influence Q is the tension [164], which we estimate in our samples to not be any higher compared to similar published work [44, 45, 80]. This analysis is supported by recent measurements, where we tune the temperature of the devices, as shown in Fig. 8.1. This not only allows us to tuned the hybridization between the two resonators as in [171, 172], but also lets us affect the stress of the hBN membrane. Like this, we were able to lower the stress until the observed mode shape distorted and the mechanical properties deteriorated. We were also able to significantly increase the stress, recovering the ideal mode shapes. This increase in tension also leads to a large increase in resonance frequency, but only a moderate increase in Q.

When characterizing the full MIM-FFPC system, we have demonstrated a large dispersive coupling of up to $|G|/2\pi = 15\,\mathrm{GHz}\cdot\mathrm{nm}^{-1}$, resulting in $g_0 = 230\,\mathrm{kHz}$ for the fundamental mode of our hBN drum resonator. For hBN, a value of $G/2\pi = 0.4\,\mathrm{MHz}\cdot\mathrm{nm}^{-1}$ was reported in [60], while a value of $G/2\pi = 2.5\,\mathrm{GHz}\cdot\mathrm{nm}^{-1}$ and

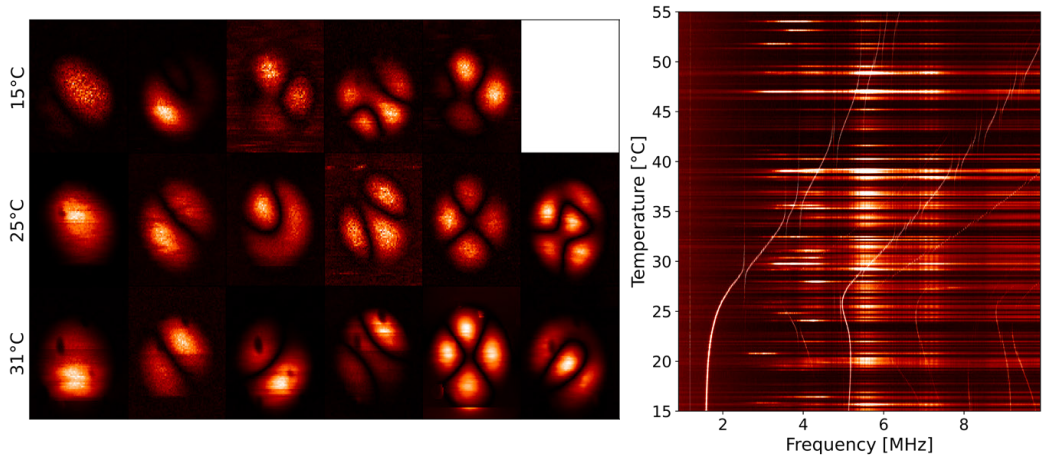

FIGURE 8.1: Temperature tuning experiments of the hBN device shown in Fig. 5.13 (b). hBN has a negative thermal expansion coefficient, causing an increase in tension at higher temperatures. In (a), each column shows one mode, and each row is a mode image taken at a different temperature. Only at slightly elevated temperatures do the mode shapes match those of a standard circular membrane. (b) Evolution of the resonance frequency of several hBN modes. The Si_3N_4 modes experience little modification as a function of temperature and appear as faint vertical lines. Several anti-crossings between the hBN and the Si_3N_4 modes can be observed. A minima in resonance frequency appears since the membrane-to-plate transition also depends on the tension.

$g_0/2\pi = 1.2\,\mathrm{kHz}$ has been demonstrated in [70]. In systems based on graphene resonators, reported values are $g = 70\,\mathrm{Hz}$ in [61] and $g_0/2\pi = 0.83\,\mathrm{Hz}$ ($g/2\pi = 14\,\mathrm{kHz}$) in [62]. This comparison shows that the coupling achieved in our system stands out among 2D material based implementations. To further demonstrate the potential of hBN as a MIM material, we performed OMIT with this system. While we had to lower the coupling strength in these measurements, the observed value of $|G|/2\pi = 7.68\,\mathrm{GHz}\cdot\mathrm{nm}^{-1}$ still results in a remarkably high single photon coupling strength of $g_0/2\pi = 120\,\mathrm{kHz}$. We plan to further investigate the observed deviations between our theoretical model and the OMIT measurements.

Moving forward, there are several ways to improve our system. The finesse of the FFPC is currently limited by the fiber mirror coating, which is designed for a finesse of 1.5×10^4. The fabrication of new fiber mirrors with an ultra-low-loss coating should lead to a reduction in the linewidth of the empty cavity from $\kappa/(2\pi)\approx 500$ to 50 MHz and, consequently, to an increase of the finesse by an order of magnitude. The bandwidth of the active stabilization is partially limited by the low-frequency cantilever mode of the overhanging fiber mirrors. By slightly modifying the design of the fiber supports, this overhang can be drastically reduced, leading to improved active stabilization. Given the current performance of the stabilization, we expect to be able to reliably lock a cavity with a finesse of around 10^5, while maintaining all other advantages of the system.

While the gain in Q does not outweigh the increase in m^* when estimating the sensitivity of our hBN devices, Si_3N_4 membranes with higher Q or lower m^* have been demonstrated and could make this trade-off more favorable [49, 178]. In particular, since the placement of hBN on our membranes resulted in only a modest

drop in Q of the fundamental Si_3N_4 mode, we are optimistic that hybrid modes with much higher Qs are feasible. It was demonstrated theoretically and experimentally that hybridization can increase thermally limited sensitivity in a similar system [171], which, together with the temperature control showcased in Fig. 8.1, would improve the estimated sensitivity of the devices further.

The ongoing miniaturization of mechanical systems in an effort to increase their sensitivity and approach the quantum regime causes cavities to follow suit, to increase coupling strength, and exhibit a sufficiently small mode volume. The system presented here is one such example that shows remarkable performance. We have achieved a strong optomechanical interaction reaching values observed in whispering-gallery mode resonators [24, 182] or photonic crystal cavities [27, 28, 183], while maintaining the open and flexible design of a Fabry-Perot cavity. The unresolved sideband regime often becomes unavoidable in these endeavors, and many new measurement protocols have been developed with this in mind. Among other examples, sensing of the mechanics approaching the quantum limit [3], cooling the mechanics close to the quantum ground state [137], even from room temperature [184], or achieving exotic phenomena such as slow light with OMIT [141] has been demonstrated experimentally. Further new measurement protocols for improved sensing and cooling schemes in the unresolved sideband limit are continuously proposed [138–140], some of which could be explored with our system.

Hybridization of a Si_3N_4 resonator with a 2D membrane can also boost its motional amplitude, allowing for larger optomechanical coupling in a cavity or giving access to non-linear mechanical effects such as signal amplification and noise squeezing [47, 172, 174]. This highlights the potential of the presented hybrid device to further increase the performance of Si_3N_4 based MIM optomechanics.

We see the presented hBN devices not only as interesting mechanical systems by themselves but as a platform for further experiments. The fact that other 2D materials can be combined with our hBN drum resonators, using the hBN as a mechanical element and for encapsulation, opens up countless avenues. In addition, hBN itself can host defects that serve as single photon emitters [167]. The ability to study high-Q mechanical modes in a variety of 2D materials opens possibilities for studying their mechanical properties, for strain coupling to embedded quantum emitters, or even for measuring the magnetic properties of 2D materials via the magnetic torques and forces acting on 2D magnets encapsulated in suspended hBN drum resonators.

Because of its high sensitivity and versatility, the FFPC platform introduced here is also suitable for studying a broad range of other nanomechanical resonators, including silicon carbide nanowires [59], nanowires with embedded emitters [104], carbon nanotubes [58], or functionalized membranes [185].

Appendix A

Constants for eigenvalues of the circular plate under tension

Here we give the constants $\alpha_{mn}, \beta_{mn}, \eta_{mn}$ and γ_{mn} used in Eq. 2.15 to calculate the eigenvalues of the drum modes. The values are taken from [128] and are for the first 15 modes, assuming a clamped circular plate under tension. Note that we have kept the naming scheme of the mode number consistent with [190], as in Fig. 2.3, where $n > 0$.

(m,n)	α	β	η	γ
(0,1)	5.7832	10.215	0.1148	0.4868
(0,2)	14.682	21.260	0.0613	0.5273
(0,3)	26.375	34.877	0.0444	0.5334
(1,1)	30.471	39.771	0.0428	0.5315
(0,4)	40.707	51.030	0.0360	0.5307
(1,2)	49.219	60.829	0.0341	0.5282
(0,5)	57.583	69.666	0.0303	0.5284
(1,3)	70.850	84.583	0.0283	0.5265
(2,1)	74.887	89.104	0.0278	0.5260
(0,6)	76.939	90.739	0.0258	0.5278
(1,4)	95.278	111.02	0.0239	0.5271
(0,7)	98.726	114.21	0.0223	0.5290
(2,2)	103.50	120.08	0.0232	0.5268
(1,5)	122.43	140.11	0.0204	0.5296
(0,8)	122.91	140.06	0.0193	0.5316

Appendix B

Michelson interferometer with balanced detection

Here we will discuss the working principle of a polarization based balanced Michelson interferometer. We assume a plane wave $\vec{E_{in}} = E_{in}e^{kz-\omega t}\vec{P}$ as in our earlier treatment of the simple Fabry-Perot cavity in section 2.2, but now we will also include a vector for the polarization state $\vec{P} = a\vec{P}_v + b\vec{P}_h$, written in linear polarization basis.

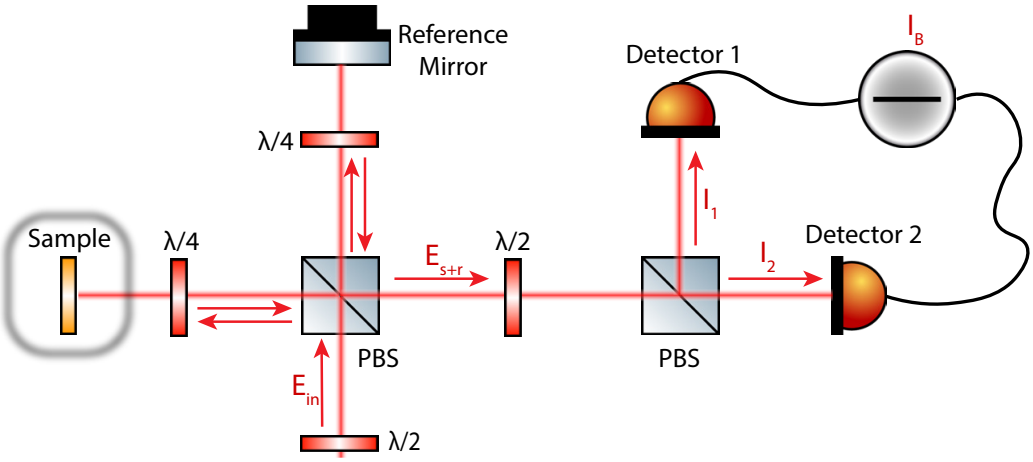

FIGURE B.1: Sketch of the polarization based Michelson interferometer with balanced detection.

Following the sketch given in Fig. B.1, we start at the input ($\vec{E_{in}}$). This input is split by the first PBS by a ratio ϵ_1, which is determined by the polarization state $\vec{P}$. The two split signals travel through the sample arm and the reference arm, respectively, and are then reflected back. We assume the reflectivity of the reference mirror to be unity, while the sample has a reflectivity of r. The two components will also acquire phases ϕ and ψ from the sample arm and the reference arm, respectively. We place a $\lambda/4$ plate in each of the two arms to rotate the phase by $\pi/2$, so that the light that was transmitted by the PBS at first is now reflected and vice versa.

After recombining at the PBS, we now have two contributions from the two arms of the interferometer.

$$\vec{E}_{s+r} = E_0 e^{kz-\omega t}[r(1-\epsilon_1)e^{i\phi}\vec{P}_h + \epsilon_1 e^{i\psi}\vec{P}_v] \tag{B.1}$$

Before reaching the second beamsplitter, the two contributions, which are still in two orthogonal polarization states, need to be mixed. This is done by a $\lambda/2$ plate rotated by an angle θ with respect to the horizontal axis, which can be described by the following Jones matrix:

$$J(\theta) = e^{-i\pi/2} \begin{pmatrix} \cos(2\theta) & \sin(2\theta) \\ \sin(2\theta) & -\cos(2\theta) \end{pmatrix} \tag{B.2}$$

Since our goal is a balanced detection scheme in which both detectors see an equal contribution from the sample arm and the reference arm, we choose θ so that

$$J(\theta)\vec{P}_h = \frac{1}{\sqrt{2}} \begin{pmatrix} e^{-i\pi/2} \\ e^{-i\pi/2} \end{pmatrix}, \quad J(\theta)\vec{P}_v = \frac{1}{\sqrt{2}} \begin{pmatrix} e^{-i\pi/2} \\ e^{+i\pi/2} \end{pmatrix} \tag{B.3}$$

This shows that the $\lambda/2$ plate not only mixes the signals from the sample arm and the reference arm, but that it also introduces a phase shift of π in one of the four terms that contribute to the final signal. This is the reason that the balanced signal does not average to zero but retains the interference signal. The π shift here replaces the one in a simple Michelson interferometer due to the beamsplitter, or, to put it in other terms, we replace the single regular beamsplitter of a Michelson interferometer with two PBS cubes and a $\lambda/2$ plate.

After adjustment of the polarization state, the second PBS splits the signal according to $\epsilon_2(\vec{P})$ and we detect a power $I = \int \vec{E}\vec{E}^* dt$ on each photodiode of our balanced detector. We also introduce a factor η characterizing the degree of spatial overlap between the interfering beams on the detectors, which we can adjust by overlapping the two arms of the interferometer by aligning the reference mirror, as well as ensuring that the two beam paths are of equal lengths, resulting in equal beam waists.

The two intensities are thus given by

$$\begin{aligned} I_1 &= I_{in}(1-\epsilon_2)^2\eta[r^2(1-\epsilon_1)^2 + \epsilon_1^2 + 2r(1-\epsilon_1)\epsilon_1\cos(\psi-\phi)] \\ I_2 &= I_{in}\epsilon_2^2\eta[r^2(1-\epsilon_1)^2 + \epsilon_1^2 - 2r(1-\epsilon_1)\epsilon_1\cos(\psi-\phi)] \end{aligned}$$

Subtracting the two detected signals to obtain the difference signal and assuming balanced detection ($\epsilon_2 = 0.5$), we get

$$I_B = I_{in}\eta r(\epsilon_1 - \epsilon_1^2)\cos(\psi-\phi) \tag{B.5}$$

The phase ψ, originating from the exact distance of the reference mirror, can be adjusted so that a good contrast can be achieved. To this end, the reference mirror is mounted on a disc piezo for fine length adjustment, allowing us to span well over $\lambda/2$ in displacement. Assuming that the phase originating from the sample is in the form of small fluctuations around a constant offset $\phi = \phi_{const} + \delta\phi$, the condition for optimal sensitivity is $\psi - \phi_{cont} = \frac{\pi}{2}$.

It is also noteworthy that there is an optimum for $\epsilon_1 = 0.5$, independent of the sample reflectivity r, assuming that I_{in} remains constant and is not increased to compensate for the power lost at the sample. This is a reasonable assumption in our measurements since we want to avoid any heating of the sample and thus have to limit the power. The samples presented in this work are also intended for optomechanics measurements and are designed to have a relatively high reflectivity.

Finally, we arrive at the following expression for our detected signal:

$$I_B = \frac{1}{4} I_{in}\eta r \sin(\delta\phi) \tag{B.6}$$

where $\delta\phi$ contains the signal of interest.

Bibliography

[1] Peter Lebedew. "Untersuchungen Über Die Druckkräfte Des Lichtes". In: *Annalen der Physik* 311.11 (1901), pp. 433–458. DOI: 10.1002/andp.19013111102 (cit. on p. 1).

[2] E. F. Nichols and G. F. Hull. "A Preliminary Communication on the Pressure of Heat and Light Radiation". In: *Physical Review (Series I)* 13.5 (Nov. 1901), pp. 307–320. DOI: 10.1103/PhysRevSeriesI.13.307 (cit. on p. 1).

[3] A. Schliesser, G. Anetsberger, R. Rivière, O. Arcizet, and T. J. Kippenberg. "High-Sensitivity Monitoring of Micromechanical Vibration Using Optical Whispering Gallery Mode Resonators". In: *New Journal of Physics* 10.9 (Sept. 2008), p. 095015. DOI: 10.1088/1367-2630/10/9/095015 (cit. on pp. 1, 107).

[4] E. Gavartin, P. Verlot, and T. J. Kippenberg. "A Hybrid On-Chip Optomechanical Transducer for Ultrasensitive Force Measurements". In: *Nature Nanotechnology* 7.8 (Aug. 2012), pp. 509–514. DOI: 10.1038/nnano.2012.97 (cit. on p. 1).

[5] Marc Sansa et al. "Optomechanical Mass Spectrometry". In: *Nature Communications* 11.1 (July 2020), p. 3781. DOI: 10.1038/s41467-020-17592-9 (cit. on p. 1).

[6] G. Anetsberger, O. Arcizet, Q. P. Unterreithmeier, R. Rivière, A. Schliesser, E. M. Weig, J. P. Kotthaus, and T. J. Kippenberg. "Near-Field Cavity Optomechanics with Nanomechanical Oscillators". In: *Nature Physics* 5.12 (Dec. 2009), pp. 909–914. DOI: 10.1038/nphys1425 (cit. on p. 1).

[7] A. Schliesser, O. Arcizet, R. Rivière, G. Anetsberger, and T. J. Kippenberg. "Resolved-Sideband Cooling and Position Measurement of a Micromechanical Oscillator Close to the Heisenberg Uncertainty Limit". In: *Nature Physics* 5.7 (July 2009), pp. 509–514. DOI: 10.1038/nphys1304 (cit. on p. 1).

[8] P. F. Cohadon, A. Heidmann, and M. Pinard. "Cooling of a Mirror by Radiation Pressure". In: *Physical Review Letters* 83.16 (Oct. 1999), pp. 3174–3177. DOI: 10.1103/PhysRevLett.83.3174 (cit. on p. 1).

[9] M. Poggio, C. L. Degen, H. J. Mamin, and D. Rugar. "Feedback Cooling of a Cantilever's Fundamental Mode below 5 mK". In: *Physical Review Letters* 99.1 (July 2007), p. 017201. DOI: 10.1103/PhysRevLett.99.017201 (cit. on p. 1).

[10] Jasper Chan, T. P. Mayer Alegre, Amir H. Safavi-Naeini, Jeff T. Hill, Alex Krause, Simon Gröblacher, Markus Aspelmeyer, and Oskar Painter. "Laser Cooling of a Nanomechanical Oscillator into Its Quantum Ground State". In: *Nature* 478.7367 (Oct. 2011), pp. 89–92. DOI: 10.1038/nature10461 (cit. on p. 1).

[11] A. Ashkin. "Trapping of Atoms by Resonance Radiation Pressure". In: *Physical Review Letters* 40.12 (Mar. 1978), pp. 729–732. DOI: 10.1103/PhysRevLett.40.729 (cit. on p. 1).

[12] Stig Stenholm. "The Semiclassical Theory of Laser Cooling". In: *Reviews of Modern Physics* 58.3 (July 1986), pp. 699–739. DOI: 10.1103/RevModPhys.58.699 (cit. on p. 1).

[13] S. Bose, K. Jacobs, and P. L. Knight. "Preparation of Nonclassical States in Cavities with a Moving Mirror". In: *Physical Review A* 56.5 (Nov. 1997), pp. 4175–4186. DOI: 10.1103/PhysRevA.56.4175 (cit. on p. 1).

[14] A. Szorkovszky, A. C. Doherty, G. I. Harris, and W. P. Bowen. "Mechanical Squeezing via Parametric Amplification and Weak Measurement". In: *Physical Review Letters* 107.21 (Nov. 2011), p. 213603. DOI: 10.1103/PhysRevLett.107.213603 (cit. on p. 1).

[15] E. E. Wollman, C. U. Lei, A. J. Weinstein, J. Suh, A. Kronwald, F. Marquardt, A. A. Clerk, and K. C. Schwab. "Quantum Squeezing of Motion in a Mechanical Resonator". In: *Science* 349.6251 (Aug. 2015), pp. 952–955. DOI: 10.1126/science.aac5138 (cit. on p. 1).

[16] Amir H. Safavi-Naeini, Simon Gröblacher, Jeff T. Hill, Jasper Chan, Markus Aspelmeyer, and Oskar Painter. "Squeezed Light from a Silicon Micromechanical Resonator". In: *Nature* 500.7461 (Aug. 2013), pp. 185–189. DOI: 10.1038/nature12307 (cit. on p. 1).

[17] T. P. Purdy, P.-L. Yu, R. W. Peterson, N. S. Kampel, and C. A. Regal. "Strong Optomechanical Squeezing of Light". In: *Physical Review X* 3.3 (Sept. 2013), p. 031012. DOI: 10.1103/PhysRevX.3.031012 (cit. on p. 1).

[18] Markus Aspelmeyer, Tobias J. Kippenberg, and Florian Marquardt. "Cavity Optomechanics". In: *Reviews of Modern Physics* 86.4 (Dec. 2014), pp. 1391–1452. DOI: 10.1103/RevModPhys.86.1391 (cit. on pp. 1, 2, 5, 24–26, 61).

[19] A. Perot and Charles Fabry. "On the Application of Interference Phenomena to the Solution of Various Problems of Spectroscopy and Metrology". In: *The Astrophysical Journal* 9 (Feb. 1899), p. 87. DOI: 10.1086/140557 (cit. on p. 1).

[20] J. D. Thompson, B. M. Zwickl, A. M. Jayich, Florian Marquardt, S. M. Girvin, and J. G. E. Harris. "Strong Dispersive Coupling of a High-Finesse Cavity to a Micromechanical Membrane". In: *Nature* 452.7183 (Mar. 2008), pp. 72–75. DOI: 10.1038/nature06715 (cit. on p. 1).

[21] Benjamin S. Sheard, Malcolm B. Gray, Conor M. Mow-Lowry, David E. McClelland, and Stanley E. Whitcomb. "Observation and Characterization of an Optical Spring". In: *Physical Review A* 69.5 (May 2004), p. 051801. DOI: 10.1103/PhysRevA.69.051801 (cit. on p. 1).

[22] Thomas Corbitt, Yanbei Chen, Edith Innerhofer, Helge Müller-Ebhardt, David Ottaway, Henning Rehbein, Daniel Sigg, Stanley Whitcomb, Christopher Wipf, and Nergis Mavalvala. "An All-Optical Trap for a Gram-Scale Mirror". In: *Physical Review Letters* 98.15 (Apr. 2007), p. 150802. DOI: 10.1103/PhysRevLett.98.150802 (cit. on p. 1).

[23] Kerry J. Vahala. "Optical Microcavities". In: *Nature* 424.6950 (Aug. 2003), pp. 839–846. DOI: 10.1038/nature01939 (cit. on p. 1).

[24] E. Verhagen, S. Deléglise, S. Weis, A. Schliesser, and T. J. Kippenberg. "Quantum-Coherent Coupling of a Mechanical Oscillator to an Optical Cavity Mode". In: *Nature* 482.7383 (Feb. 2012), pp. 63–67. DOI: 10.1038/nature10787 (cit. on pp. 1, 107).

[25] Martin Maldovan and Edwin L. Thomas. "Simultaneous Localization of Photons and Phonons in Two-Dimensional Periodic Structures". In: *Applied Physics Letters* 88.25 (June 2006), p. 251907. DOI: 10.1063/1.2216885 (cit. on p. 1).

[26] Matt Eichenfield, Jasper Chan, Ryan M. Camacho, Kerry J. Vahala, and Oskar Painter. "Optomechanical Crystals". In: *Nature* 462.7269 (Nov. 2009), pp. 78–82. DOI: 10.1038/nature08524 (cit. on p. 1).

[27] Amir H. Safavi-Naeini, Thiago P. Mayer Alegre, Martin Winger, and Oskar Painter. "Optomechanics in an Ultrahigh-Q Two-Dimensional Photonic Crystal Cavity". In: *Applied Physics Letters* 97.18 (Nov. 2010), p. 181106. DOI: 10.1063/1.3507288 (cit. on pp. 1, 107).

[28] E. Gavartin, R. Braive, I. Sagnes, O. Arcizet, A. Beveratos, T. J. Kippenberg, and I. Robert-Philip. "Optomechanical Coupling in a Two-Dimensional Photonic Crystal Defect Cavity". In: *Physical Review Letters* 106.20 (May 2011), p. 203902. DOI: 10.1103/PhysRevLett.106.203902 (cit. on pp. 1, 107).

[29] J. Moser, J. Güttinger, A. Eichler, M. J. Esplandiu, D. E. Liu, M. I. Dykman, and A. Bachtold. "Ultrasensitive Force Detection with a Nanotube Mechanical Resonator". In: *Nature Nanotechnology* 8.7 (July 2013), pp. 493–496. DOI: 10.1038/nnano.2013.97 (cit. on p. 1).

[30] J. Moser, A. Eichler, J. Güttinger, M. I. Dykman, and A. Bachtold. "Nanotube Mechanical Resonators with Quality Factors of up to 5 Million". In: *Nature Nanotechnology* 9.12 (Dec. 2014), pp. 1007–1011. DOI: 10.1038/nnano.2014.234 (cit. on p. 1).

[31] F. R. Braakman and M. Poggio. "Force Sensing with Nanowire Cantilevers". In: *Nanotechnology* 30.33 (May 2019), p. 332001. DOI: 10.1088/1361-6528/ab19cf (cit. on pp. 1, 2).

[32] Y. T. Yang, C. Callegari, X. L. Feng, K. L. Ekinci, and M. L. Roukes. "Zeptogram-Scale Nanomechanical Mass Sensing". In: *Nano Letters* 6.4 (Apr. 2006), pp. 583–586. DOI: 10.1021/nl052134m (cit. on p. 1).

[33] J. Chaste, A. Eichler, J. Moser, G. Ceballos, R. Rurali, and A. Bachtold. "A Nanomechanical Mass Sensor with Yoctogram Resolution". In: *Nature Nanotechnology* 7.5 (May 2012), pp. 301–304. DOI: 10.1038/nnano.2012.42 (cit. on p. 1).

[34] Gershon Kurizki, Patrice Bertet, Yuimaru Kubo, Klaus Mølmer, David Petrosyan, Peter Rabl, and Jörg Schmiedmayer. "Quantum Technologies with Hybrid Systems". In: *Proceedings of the National Academy of Sciences* 112.13 (Mar. 2015), pp. 3866–3873. DOI: 10.1073/pnas.1419326112 (cit. on p. 1).

[35] Yiwen Chu and Simon Gröblacher. "A Perspective on Hybrid Quantum Opto- and Electromechanical Systems". In: *Applied Physics Letters* 117.15 (Oct. 2020), p. 150503. DOI: 10.1063/5.0021088 (cit. on p. 1).

[36] Menno Poot and Herre S. J. van der Zant. "Mechanical Systems in the Quantum Regime". In: *Physics Reports*. Mechanical Systems in the Quantum Regime 511.5 (Feb. 2012), pp. 273–335. DOI: 10.1016/j.physrep.2011.12.004 (cit. on p. 1).

[37] J. D. Teufel, T. Donner, Dale Li, J. W. Harlow, M. S. Allman, K. Cicak, A. J. Sirois, J. D. Whittaker, K. W. Lehnert, and R. W. Simmonds. "Sideband Cooling of Micromechanical Motion to the Quantum Ground State". In: *Nature* 475.7356 (July 2011), pp. 359–363. DOI: 10.1038/nature10261 (cit. on p. 1).

[38] A. D. O'Connell et al. "Quantum Ground State and Single-Phonon Control of a Mechanical Resonator". In: *Nature* 464.7289 (Apr. 2010), pp. 697–703. DOI: 10.1038/nature08967 (cit. on p. 1).

[39] William Marshall, Christoph Simon, Roger Penrose, and Dik Bouwmeester. "Towards Quantum Superpositions of a Mirror". In: *Physical Review Letters* 91.13 (Sept. 2003), p. 130401. DOI: 10.1103/PhysRevLett.91.130401 (cit. on p. 1).

[40] Adrian Bachtold, Joel Moser, and M. I. Dykman. "Mesoscopic Physics of Nanomechanical Systems". In: *Reviews of Modern Physics* 94.4 (Dec. 2022), p. 045005. DOI: 10.1103/RevModPhys.94.045005 (cit. on pp. 2, 5).

[41] X. L. Feng, Rongrui He, Peidong Yang, and M. L. Roukes. "Very High Frequency Silicon Nanowire Electromechanical Resonators". In: *Nano Letters* 7.7 (July 2007), pp. 1953–1959. DOI: 10.1021/nl0706695 (cit. on p. 2).

[42] Vera Sazonova, Yuval Yaish, Hande Üstünel, David Roundy, Tomás A. Arias, and Paul L. McEuen. "A Tunable Carbon Nanotube Electromechanical Oscillator". In: *Nature* 431.7006 (Sept. 2004), pp. 284–287. DOI: 10.1038/nature02905 (cit. on p. 2).

[43] J. Scott Bunch, Arend M. van der Zande, Scott S. Verbridge, Ian W. Frank, David M. Tanenbaum, Jeevak M. Parpia, Harold G. Craighead, and Paul L. McEuen. "Electromechanical Resonators from Graphene Sheets". In: *Science* 315.5811 (Jan. 2007), pp. 490–493. DOI: 10.1126/science.1136836 (cit. on pp. 2, 3, 63, 105).

[44] Xu-Qian Zheng, Jaesung Lee, and Philip X.-L. Feng. "Hexagonal Boron Nitride Nanomechanical Resonators with Spatially Visualized Motion". In: *Microsystems & Nanoengineering* 3.1 (July 2017). DOI: 10.1038/micronano.2017.38 (cit. on pp. 2, 3, 7, 65, 66, 78, 81, 82, 86, 105).

[45] Santiago J. Cartamil-Bueno, Matteo Cavalieri, Ruizhi Wang, Samer Houri, Stephan Hofmann, and Herre S. J. van der Zant. "Mechanical Characterization and Cleaning of CVD Single-Layer h-BN Resonators". In: *npj 2D Materials and Applications* 1.1 (June 2017), p. 16. DOI: 10.1038/s41699-017-0020-8 (cit. on pp. 2, 3, 63, 65, 72, 75, 86, 87, 105).

[46] Castellanos-Gomez Andres, van Leeuwen Ronald, Buscema Michele, van der Zant Herre S. J., Steele Gary A., and Venstra Warner J. "Single-Layer MoS2 Mechanical Resonators". In: *Advanced Materials* 25.46 (Dec. 2013), pp. 6719–6723. DOI: 10.1002/adma.201303569 (cit. on pp. 2, 3, 105).

[47] Peter G. Steeneken, Robin J. Dolleman, Dejan Davidovikj, Farbod Alijani, and Herre S. J. van der Zant. "Dynamics of 2D Material Membranes". In: *2D Materials* 8.4 (Oct. 2021), p. 042001. DOI: 10.1088/2053-1583/ac152c (cit. on pp. 2, 3, 61, 107).

[48] Bo Xu et al. "Nanomechanical Resonators: Toward Atomic Scale". In: *ACS Nano* 16.10 (Oct. 2022), pp. 15545–15585. DOI: 10.1021/acsnano.2c01673 (cit. on p. 2).

[49] Y. Tsaturyan, A. Barg, E. S. Polzik, and A. Schliesser. "Ultracoherent Nanomechanical Resonators via Soft Clamping and Dissipation Dilution". In: *Nature Nanotechnology* 12.8 (Aug. 2017), pp. 776–783. DOI: 10.1038/nnano.2017.101 (cit. on pp. 2, 90, 106).

[50] A. H. Ghadimi, S. A. Fedorov, N. J. Engelsen, M. J. Bereyhi, R. Schilling, D. J. Wilson, and T. J. Kippenberg. "Elastic Strain Engineering for Ultralow Mechanical Dissipation". In: *Science* 360.6390 (May 2018), pp. 764–768. DOI: 10.1126/science.aar6939 (cit. on p. 2).

[51] B. M. Zwickl, W. E. Shanks, A. M. Jayich, C. Yang, A. C. Bleszynski Jayich, J. D. Thompson, and J. G. E. Harris. "High Quality Mechanical and Optical Properties of Commercial Silicon Nitride Membranes". In: *Applied Physics Letters* 92.10 (Mar. 2008), p. 103125. DOI: 10.1063/1.2884191 (cit. on pp. 2, 95).

[52] T. P. Purdy, R. W. Peterson, and C. A. Regal. "Observation of Radiation Pressure Shot Noise on a Macroscopic Object". In: *Science* 339.6121 (Feb. 2013), pp. 801–804. DOI: 10.1126/science.1231282 (cit. on p. 2).

[53] M. Underwood, D. Mason, D. Lee, H. Xu, L. Jiang, A. B. Shkarin, K. Børkje, S. M. Girvin, and J. G. E. Harris. "Measurement of the Motional Sidebands of a Nanogram-Scale Oscillator in the Quantum Regime". In: *Physical Review A* 92.6 (Dec. 2015), p. 061801. DOI: 10.1103/PhysRevA.92.061801 (cit. on p. 2).

[54] R. W. Peterson, T. P. Purdy, N. S. Kampel, R. W. Andrews, P.-L. Yu, K. W. Lehnert, and C. A. Regal. "Laser Cooling of a Micromechanical Membrane to the Quantum Backaction Limit". In: *Physical Review Letters* 116.6 (Feb. 2016), p. 063601. DOI: 10.1103/PhysRevLett.116.063601 (cit. on p. 2).

[55] William Hvidtfelt Padkær Nielsen, Yeghishe Tsaturyan, Christoffer Bo Møller, Eugene S. Polzik, and Albert Schliesser. "Multimode Optomechanical System in the Quantum Regime". In: *Proceedings of the National Academy of Sciences* 114.1 (Jan. 2017), pp. 62–66. DOI: 10.1073/pnas.1608412114 (cit. on p. 2).

[56] Massimiliano Rossi, David Mason, Junxin Chen, Yeghishe Tsaturyan, and Albert Schliesser. "Measurement-Based Quantum Control of Mechanical Motion". In: *Nature* 563.7729 (Nov. 2018), pp. 53–58. DOI: 10.1038/s41586-018-0643-8 (cit. on p. 2).

[57] David Mason, Junxin Chen, Massimiliano Rossi, Yeghishe Tsaturyan, and Albert Schliesser. "Continuous Force and Displacement Measurement below the Standard Quantum Limit". In: *Nature Physics* 15.8 (Aug. 2019), pp. 745–749. DOI: 10.1038/s41567-019-0533-5 (cit. on p. 2).

[58] S. Stapfner, L. Ost, D. Hunger, J. Reichel, I. Favero, and E. M. Weig. "Cavity-Enhanced Optical Detection of Carbon Nanotube Brownian Motion". In: *Applied Physics Letters* 102.15 (Apr. 2013), p. 151910. DOI: 10.1063/1.4802746 (cit. on pp. 2, 3, 61, 107).

[59] Francesco Fogliano, Benjamin Besga, Antoine Reigue, Philip Heringlake, Laure Mercier de Lépinay, Cyril Vaneph, Jakob Reichel, Benjamin Pigeau, and Olivier Arcizet. "Mapping the Cavity Optomechanical Interaction with Subwavelength-Sized Ultrasensitive Nanomechanical Force Sensors". In: *Physical Review X* 11.2 (Apr. 2021), p. 021009. DOI: 10.1103/PhysRevX.11.021009 (cit. on pp. 2, 3, 24, 107).

[60] Prasoon K. Shandilya, Johannes E. Fröch, Matthew Mitchell, David P. Lake, Sejeong Kim, Milos Toth, Bishnupada Behera, Chris Healey, Igor Aharonovich, and Paul E. Barclay. "Hexagonal Boron Nitride Cavity Optomechanics". In: *Nano Letters* 19.2 (Feb. 2019), pp. 1343–1350. DOI: 10.1021/acs.nanolett.8b04956 (cit. on pp. 2, 105).

[61] X. Song, M. Oksanen, J. Li, P. J. Hakonen, and M. A. Sillanpää. "Graphene Optomechanics Realized at Microwave Frequencies". In: *Physical Review Letters* 113.2 (July 2014), p. 027404. DOI: 10.1103/PhysRevLett.113.027404 (cit. on pp. 2, 106).

[62] V. Singh, S. J. Bosman, B. H. Schneider, Y. M. Blanter, A. Castellanos-Gomez, and G. A. Steele. "Optomechanical Coupling between a Multilayer Graphene Mechanical Resonator and a Superconducting Microwave Cavity". In: *Nature Nanotechnology* 9.10 (Oct. 2014), pp. 820–824. DOI: 10.1038/nnano.2014.168 (cit. on pp. 2, 106).

[63] Robert A. Barton et al. "Photothermal Self-Oscillation and Laser Cooling of Graphene Optomechanical Systems". In: *Nano Letters* 12.9 (Sept. 2012), pp. 4681–4686. DOI: 10.1021/nl302036x (cit. on p. 2).

[64] Hendrik M. Meyer, Moritz Breyer, and Michael Köhl. "Monolayer Graphene as Dissipative Membrane in an Optical Resonator". In: *Applied Physics B* 122.12 (Nov. 2016), p. 290. DOI: 10.1007/s00340-016-6564-z (cit. on p. 2).

[65] Arthur W. Barnard, Mian Zhang, Gustavo S. Wiederhecker, Michal Lipson, and Paul L. McEuen. "Real-Time Vibrations of a Carbon Nanotube". In: *Nature* 566.7742 (Feb. 2019), pp. 89–93. DOI: 10.1038/s41586-018-0861-0 (cit. on p. 2).

[66] Antoine Reigue, Francesco Fogliano, Philip Heringlake, Laure Mercier de Lépinay, Benjamin Besga, Jakob Reichel, Benjamin Pigeau, and Olivier Arcizet. "Cavity Nano-Optomechanics with Suspended Subwavelength-Sized Nanowires". In: *Physical Review Applied* 20.1 (July 2023), p. 014025. DOI: 10.1103/PhysRevApplied.20.014025 (cit. on pp. 2, 9, 18).

[67] Ian A. D. Williamson, S. Hossein Mousavi, and Zheng Wang. "Large Cavity-Optomechanical Coupling with Graphene at Infrared and Terahertz Frequencies". In: *ACS Photonics* 3.12 (Dec. 2016), pp. 2353–2361. DOI: 10.1021/acsphotonics.6b00553 (cit. on p. 2).

[68] Kenji Watanabe, Takashi Taniguchi, and Hisao Kanda. "Direct-Bandgap Properties and Evidence for Ultraviolet Lasing of Hexagonal Boron Nitride Single Crystal". In: *Nature Materials* 3.6 (June 2004), pp. 404–409. DOI: 10.1038/nmat1134 (cit. on p. 2).

[69] Seong-Yeon Lee, Tae-Young Jeong, Suyong Jung, and Ki-Ju Yee. "Refractive Index Dispersion of Hexagonal Boron Nitride in the Visible and Near-Infrared". In: *physica status solidi (b)* 256.6 (2019), p. 1800417. DOI: 10.1002/pssb.201800417 (cit. on pp. 2, 94).

[70] Irene Sánchez Arribas, Takashi Taniguchi, Kenji Watanabe, and Eva M. Weig. "Radiation Pressure Backaction on a Hexagonal Boron Nitride Nanomechanical Resonator". In: *Nano Letters* 23.14 (July 2023), pp. 6301–6307. DOI: 10.1021/acs.nanolett.3c00544 (cit. on pp. 2, 94, 106).

[71] Aleksey Falin et al. "Mechanical Properties of Atomically Thin Boron Nitride and the Role of Interlayer Interactions". In: *Nature Communications* 8.1 (June 2017), p. 15815. DOI: 10.1038/ncomms15815 (cit. on p. 2).

[72] Jiangtao Wu, Baolin Wang, Yujie Wei, Ronggui Yang, and Mildred Dresselhaus. "Mechanics and Mechanically Tunable Band Gap in Single-Layer Hexagonal Boron-Nitride". In: *Materials Research Letters* 1.4 (Dec. 2013), pp. 200–206. DOI: 10.1080/21663831.2013.824516 (cit. on pp. 2, 65, 83).

[73] Changgu Lee, Xiaoding Wei, Jeffrey W. Kysar, and James Hone. "Measurement of the Elastic Properties and Intrinsic Strength of Monolayer Graphene". In: *Science* 321.5887 (July 2008), pp. 385–388. DOI: 10.1126/science.1157996 (cit. on p. 2).

[74] L. Wang et al. "One-Dimensional Electrical Contact to a Two-Dimensional Material". In: *Science* 342.6158 (Nov. 2013), pp. 614–617. DOI: 10.1126/science.1244358 (cit. on p. 2).

[75] Xu Cui et al. "Multi-Terminal Transport Measurements of MoS2 Using a van Der Waals Heterostructure Device Platform". In: *Nature Nanotechnology* 10.6 (June 2015), pp. 534–540. DOI: 10.1038/nnano.2015.70 (cit. on p. 2).

[76] K. S. Novoselov, A. Mishchenko, A. Carvalho, and A. H. Castro Neto. "2D Materials and van Der Waals Heterostructures". In: *Science* 353.6298 (July 2016), aac9439. DOI: 10.1126/science.aac9439 (cit. on p. 2).

[77] Mohammad Jafar Molaei, Mohammad Younas, and Mashallah Rezakazemi. "A Comprehensive Review on Recent Advances in Two-Dimensional (2D) Hexagonal Boron Nitride". In: *ACS Applied Electronic Materials* 3.12 (Dec. 2021), pp. 5165–5187. DOI: 10.1021/acsaelm.1c00720 (cit. on pp. 2, 63).

[78] Cheng Gong et al. "Discovery of Intrinsic Ferromagnetism in Two-Dimensional van Der Waals Crystals". In: *Nature* 546.7657 (June 2017), pp. 265–269. DOI: 10.1038/nature22060 (cit. on p. 2).

[79] Bevin Huang et al. "Layer-Dependent Ferromagnetism in a van Der Waals Crystal down to the Monolayer Limit". In: *Nature* 546.7657 (June 2017), pp. 270–273. DOI: 10.1038/nature22391 (cit. on p. 2).

[80] Changyao Chen, Sami Rosenblatt, Kirill I. Bolotin, William Kalb, Philip Kim, Ioannis Kymissis, Horst L. Stormer, Tony F. Heinz, and James Hone. "Performance of Monolayer Graphene Nanomechanical Resonators with Electrical Readout". In: *Nature Nanotechnology* 4.12 (Dec. 2009), pp. 861–867. DOI: 10.1038/nnano.2009.267 (cit. on pp. 2, 72, 87, 105).

[81] Changyao Chen, Sunwoo Lee, Vikram V. Deshpande, Gwan-Hyoung Lee, Michael Lekas, Kenneth Shepard, and James Hone. "Graphene Mechanical Oscillators with Tunable Frequency". In: *Nature Nanotechnology* 8.12 (Dec. 2013), pp. 923–927. DOI: 10.1038/nnano.2013.232 (cit. on p. 2).

[82] Alexander S. Mayorov, Daniel C. Elias, Ivan S. Mukhin, Sergey V. Morozov, Leonid A. Ponomarenko, Kostya S. Novoselov, A. K. Geim, and Roman V. Gorbachev. "How Close Can One Approach the Dirac Point in Graphene Experimentally?" In: *Nano Letters* 12.9 (Sept. 2012), pp. 4629–4634. DOI: 10.1021/nl301922d (cit. on p. 2).

[83] Andrea Splendiani, Liang Sun, Yuanbo Zhang, Tianshu Li, Jonghwan Kim, Chi-Yung Chim, Giulia Galli, and Feng Wang. "Emerging Photoluminescence in Monolayer MoS2". In: *Nano Letters* 10.4 (Apr. 2010), pp. 1271–1275. DOI: 10.1021/nl903868w (cit. on p. 2).

[84] Ajit Srivastava, Meinrad Sidler, Adrien V. Allain, Dominik S. Lembke, Andras Kis, and A. Imamoğlu. "Optically Active Quantum Dots in Monolayer WSe2". In: *Nature Nanotechnology* 10.6 (June 2015), pp. 491–496. DOI: 10.1038/nnano.2015.60 (cit. on p. 2).

[85] Toan Trong Tran, Kerem Bray, Michael J. Ford, Milos Toth, and Igor Aharonovich. "Quantum Emission from Hexagonal Boron Nitride Monolayers". In: *Nature Nanotechnology* 11.1 (Jan. 2016), pp. 37–41. DOI: 10.1038/nnano.2015.242 (cit. on pp. 2, 72).

[86] Noah Mendelson, Marcus Doherty, Milos Toth, Igor Aharonovich, and Toan Trong Tran. "Strain-Induced Modification of the Optical Characteristics of Quantum Emitters in Hexagonal Boron Nitride". In: *Advanced Materials* 32.21 (2020), p. 1908316. DOI: 10.1002/adma.201908316 (cit. on p. 3).

[87] Snežana Lazić et al. "Dynamically Tuned Non-Classical Light Emission from Atomic Defects in Hexagonal Boron Nitride". In: *Communications Physics* 2.1 (Sept. 2019), pp. 1–8. DOI: 10.1038/s42005-019-0217-6 (cit. on p. 3).

[88] Juan Restrepo, Ivan Favero, and Cristiano Ciuti. "Fully Coupled Hybrid Cavity Optomechanics: Quantum Interferences and Correlations". In: *Physical Review A* 95.2 (Feb. 2017), p. 023832. DOI: 10.1103/PhysRevA.95.023832 (cit. on p. 3).

[89] Ondřej Černotík, Claudiu Genes, and Aurélien Dantan. "Interference Effects in Hybrid Cavity Optomechanics". In: *Quantum Science and Technology* 4.2 (Jan. 2019), p. 024002. DOI: 10.1088/2058-9565/aaf5a6 (cit. on p. 3).

[90] Stephan Camerer, Maria Korppi, Andreas Jöckel, David Hunger, Theodor W. Hänsch, and Philipp Treutlein. "Realization of an Optomechanical Interface Between Ultracold Atoms and a Membrane". In: *Physical Review Letters* 107.22 (Nov. 2011), p. 223001. DOI: 10.1103/PhysRevLett.107.223001 (cit. on p. 3).

[91] Stefan Blien, Patrick Steger, Niklas Hüttner, Richard Graaf, and Andreas K. Hüttel. "Quantum Capacitance Mediated Carbon Nanotube Optomechanics". In: *Nature Communications* 11.1 (Apr. 2020), p. 1636. DOI: 10.1038/s41467-020-15433-3 (cit. on p. 3).

[92] N. Carlon Zambon, Z. Denis, R. De Oliveira, S. Ravets, C. Ciuti, I. Favero, and J. Bloch. "Enhanced Cavity Optomechanics with Quantum-Well Exciton Polaritons". In: *Physical Review Letters* 129.9 (Aug. 2022), p. 093603. DOI: 10.1103/PhysRevLett.129.093603 (cit. on p. 3).

[93] Jaesung Lee, Zenghui Wang, Keliang He, Jie Shan, and Philip X.-L. Feng. "High Frequency MoS2 Nanomechanical Resonators". In: *ACS Nano* 7.7 (July 2013), pp. 6086–6091. DOI: 10.1021/nn4018872 (cit. on pp. 3, 63, 105).

[94] R. van Leeuwen, A. Castellanos-Gomez, G. A. Steele, H. S. J. van der Zant, and W. J. Venstra. "Time-Domain Response of Atomically Thin MoS2 Nanomechanical Resonators". In: *Applied Physics Letters* 105.4 (July 2014), p. 041911. DOI: 10.1063/1.4892072 (cit. on p. 3).

[95] E. Kramer, J. van Dorp, R. van Leeuwen, and W. J. Venstra. "Strain-Dependent Damping in Nanomechanical Resonators from Thin MoS2 Crystals". In: *Applied Physics Letters* 107.9 (Aug. 2015), p. 091903. DOI: 10.1063/1.4929507 (cit. on p. 3).

[96] Dejan Davidovikj, Jesse J. Slim, Santiago J. Cartamil Bueno, Herre S. J. van der Zant, Peter G. Steeneken, and Warner J. Venstra. "Visualizing the Motion of Graphene Nanodrums". In: *Nano Letters* 16.4 (Apr. 2016), pp. 2768–2773. DOI: 10.1021/acs.nanolett.6b00477 (cit. on pp. 3, 81).

[97] D. Garcia-Sanchez, A. M. van der Zande, A. San Paulo, B. Lassagne, P. L. McEuen, and A. Bachtold. "Imaging Mechanical Vibrations in Suspended Graphene Sheets". In: *Nano Letters* 8.5 (May 2008), pp. 1399–1403. DOI: 10.1021/nl080201h (cit. on pp. 3, 81).

[98] D. Hunger, T. Steinmetz, Y. Colombe, C. Deutsch, T. W. Hänsch, and J. Reichel. "A Fiber Fabry–Perot Cavity with High Finesse". In: *New Journal of Physics* 12.6 (June 2010), p. 065038. DOI: 10.1088/1367-2630/12/6/065038 (cit. on pp. 3, 29).

[99] Thibaud Ruelle, Martino Poggio, and Floris Braakman. "Optimized Single-Shot Laser Ablation of Concave Mirror Templates on Optical Fibers". In: *Applied Optics* 58.14 (May 2019), pp. 3784–3789. DOI: 10.1364/AO.58.003784 (cit. on pp. 3, 29, 31).

[100] D. Hunger, C. Deutsch, R. J. Barbour, R. J. Warburton, and J. Reichel. "Laser Micro-Fabrication of Concave, Low-Roughness Features in Silica". In: *AIP Advances* 2.1 (Jan. 2012), p. 012119. DOI: 10.1063/1.3679721 (cit. on pp. 3, 31).

[101] Andreas Muller, Edward B. Flagg, John R. Lawall, and Glenn S. Solomon. "Ultrahigh-Finesse, Low-Mode-Volume Fabry–Perot Microcavity". In: *Optics Letters* 35.13 (July 2010), pp. 2293–2295. DOI: 10.1364/OL.35.002293 (cit. on p. 3).

[102] H. J. Kimble. "Strong Interactions of Single Atoms and Photons in Cavity QED". In: *Physica Scripta* 1998.T76 (Jan. 1998), p. 127. DOI: 10.1238/Physica.Topical.076a00127 (cit. on p. 3).

[103] Yves Colombe, Tilo Steinmetz, Guilhem Dubois, Felix Linke, David Hunger, and Jakob Reichel. "Strong Atom–Field Coupling for Bose–Einstein Condensates in an Optical Cavity on a Chip". In: *Nature* 450.7167 (Nov. 2007), pp. 272–276. DOI: 10.1038/nature06331 (cit. on p. 3).

[104] Andreas Muller, Edward B. Flagg, Michael Metcalfe, John Lawall, and Glenn S. Solomon. "Coupling an Epitaxial Quantum Dot to a Fiber-Based External-Mirror Microcavity". In: *Applied Physics Letters* 95.17 (Oct. 2009), p. 173101. DOI: 10.1063/1.3245311 (cit. on pp. 3, 107).

[105] C. Toninelli, Y. Delley, T. Stöferle, A. Renn, S. Götzinger, and V. Sandoghdar. "A Scanning Microcavity for in Situ Control of Single-Molecule Emission". In: *Applied Physics Letters* 97.2 (July 2010), p. 021107. DOI: 10.1063/1.3456559 (cit. on p. 3).

[106] Matthias Steiner, Hendrik M. Meyer, Christian Deutsch, Jakob Reichel, and Michael Köhl. "Single Ion Coupled to an Optical Fiber Cavity". In: *Physical Review Letters* 110.4 (Jan. 2013), p. 043003. DOI: 10.1103/PhysRevLett.110.043003 (cit. on p. 3).

[107] Javier Miguel-Sánchez, Andreas Reinhard, Emre Togan, Thomas Volz, Atac Imamoglu, Benjamin Besga, Jakob Reichel, and Jérôme Estève. "Cavity Quantum Electrodynamics with Charge-Controlled Quantum Dots Coupled to a Fiber Fabry–Perot Cavity". In: *New Journal of Physics* 15.4 (Apr. 2013), p. 045002. DOI: 10.1088/1367-2630/15/4/045002 (cit. on p. 3).

[108] Roland Albrecht, Alexander Bommer, Christian Deutsch, Jakob Reichel, and Christoph Becher. "Coupling of a Single Nitrogen-Vacancy Center in Diamond to a Fiber-Based Microcavity". In: *Physical Review Letters* 110.24 (June 2013), p. 243602. DOI: 10.1103/PhysRevLett.110.243602 (cit. on p. 3).

[109] B. Brandstätter et al. “Integrated Fiber-Mirror Ion Trap for Strong Ion-Cavity Coupling”. In: *Review of Scientific Instruments* 84.12 (Dec. 2013), p. 123104. DOI: 10.1063/1.4838696 (cit. on pp. 3, 55).

[110] Benjamin Besga, Cyril Vaneph, Jakob Reichel, Jérôme Estève, Andreas Reinhard, Javier Miguel-Sánchez, Ataç Imamoğlu, and Thomas Volz. “Polariton Boxes in a Tunable Fiber Cavity”. In: *Physical Review Applied* 3.1 (Jan. 2015), p. 014008. DOI: 10.1103/PhysRevApplied.3.014008 (cit. on p. 3).

[111] Julia Benedikter, Hanno Kaupp, Thomas Hümmer, Yuejiang Liang, Alexander Bommer, Christoph Becher, Anke Krueger, Jason M. Smith, Theodor W. Hänsch, and David Hunger. “Cavity-Enhanced Single-Photon Source Based on the Silicon-Vacancy Center in Diamond”. In: *Physical Review Applied* 7.2 (Feb. 2017), p. 024031. DOI: 10.1103/PhysRevApplied.7.024031 (cit. on p. 3).

[112] J. Gallego, W. Alt, T. Macha, M. Martinez-Dorantes, D. Pandey, and D. Meschede. “Strong Purcell Effect on a Neutral Atom Trapped in an Open Fiber Cavity”. In: *Physical Review Letters* 121.17 (Oct. 2018), p. 173603. DOI: 10.1103/PhysRevLett.121.173603 (cit. on p. 3).

[113] Hiroki Takahashi, Ezra Kassa, Costas Christoforou, and Matthias Keller. “Strong Coupling of a Single Ion to an Optical Cavity”. In: *Physical Review Letters* 124.1 (Jan. 2020), p. 013602. DOI: 10.1103/PhysRevLett.124.013602 (cit. on p. 3).

[114] Ivan Favero, Sebastian Stapfner, David Hunger, Philipp Paulitschke, Jakob Reichel, Heribert Lorenz, Eva M. Weig, and Khaled Karrai. “Fluctuating Nanomechanical System in a High Finesse Optical Microcavity”. In: *Optics Express* 17.15 (July 2009), pp. 12813–12820. DOI: 10.1364/OE.17.012813 (cit. on p. 3).

[115] N. E. Flowers-Jacobs, S. W. Hoch, J. C. Sankey, A. Kashkanova, A. M. Jayich, C. Deutsch, J. Reichel, and J. G. E. Harris. “Fiber-Cavity-Based Optomechanical Device”. In: *Applied Physics Letters* 101.22 (Nov. 2012), p. 221109. DOI: 10.1063/1.4768779 (cit. on p. 3).

[116] H. Zhong et al. “A Millikelvin All-Fiber Cavity Optomechanical Apparatus for Merging with Ultra-Cold Atoms in a Hybrid Quantum System”. In: *Review of Scientific Instruments* 88.2 (Feb. 2017), p. 023115. DOI: 10.1063/1.4976497 (cit. on pp. 3, 55).

[117] A. B. Shkarin, A. D. Kashkanova, C. D. Brown, S. Garcia, K. Ott, J. Reichel, and J. G. E. Harris. “Quantum Optomechanics in a Liquid”. In: *Physical Review Letters* 122.15 (Apr. 2019), p. 153601. DOI: 10.1103/PhysRevLett.122.153601 (cit. on p. 3).

[118] Felix Rochau, Irene Sánchez Arribas, Alexandre Brieussel, Sebastian Stapfner, David Hunger, and Eva M. Weig. “Dynamical Backaction in an Ultrahigh-Finesse Fiber-Based Microcavity”. In: *Physical Review Applied* 16.1 (July 2021), p. 014013. DOI: 10.1103/PhysRevApplied.16.014013 (cit. on pp. 3, 29, 55).

[119] M. Salz, Y. Herrmann, A. Nadarajah, A. Stahl, M. Hettrich, A. Stacey, S. Prawer, D. Hunger, and F. Schmidt-Kaler. “Cryogenic Platform for Coupling Color Centers in Diamond Membranes to a Fiber-Based Microcavity”. In: *Applied Physics B* 126.8 (July 2020), p. 131. DOI: 10.1007/s00340-020-07478-5 (cit. on pp. 3, 55).

[120] Erika Janitz, Maximilian Ruf, Yannik Fontana, Jack Sankey, and Lilian Childress. “High Mechanical Bandwidth Fiber-Coupled Fabry-Perot Cavity”. In: *Optics Express* 25.17 (Aug. 2017), pp. 20932–20943. DOI: 10.1364/OE.25.020932 (cit. on pp. 3, 55).

[121] Y. Fontana, R. Zifkin, E. Janitz, C. D. Rodríguez Rosenblueth, and L. Childress. "A Mechanically Stable and Tunable Cryogenic Fabry–Pérot Microcavity". In: *Review of Scientific Instruments* 92.5 (May 2021), p. 053906. DOI: 10.1063/5.0049520 (cit. on pp. 3, 55).

[122] Samarth Vadia, Johannes Scherzer, Holger Thierschmann, Clemens Schäfermeier, Claudio Dal Savio, Takashi Taniguchi, Kenji Watanabe, David Hunger, Khaled Karraï, and Alexander Högele. "Open-Cavity in Closed-Cycle Cryostat as a Quantum Optics Platform". In: *PRX Quantum* 2.4 (Oct. 2021), p. 040318. DOI: 10.1103/PRXQuantum.2.040318 (cit. on pp. 3, 55).

[123] Maximilian Pallmann, Timon Eichhorn, Julia Benedikter, Bernardo Casabone, Thomas Hümmer, and David Hunger. "A Highly Stable and Fully Tunable Open Microcavity Platform at Cryogenic Temperatures". In: *APL Photonics* 8.4 (Apr. 2023), p. 046107. DOI: 10.1063/5.0139003 (cit. on pp. 3, 55).

[124] Lukas Greuter, Sebastian Starosielec, Daniel Najer, Arne Ludwig, Luc Duempelmann, Dominik Rohner, and Richard J. Warburton. "A Small Mode Volume Tunable Microcavity: Development and Characterization". In: *Applied Physics Letters* 105.12 (Sept. 2014), p. 121105. DOI: 10.1063/1.4896415 (cit. on p. 3).

[125] Daniel Riedel, Sigurd Flågan, Patrick Maletinsky, and Richard J. Warburton. "Cavity-Enhanced Raman Scattering for In Situ Alignment and Characterization of Solid-State Microcavities". In: *Physical Review Applied* 13.1 (Jan. 2020), p. 014036. DOI: 10.1103/PhysRevApplied.13.014036 (cit. on p. 3).

[126] A. A. Clerk, M. H. Devoret, S. M. Girvin, Florian Marquardt, and R. J. Schoelkopf. "Introduction to Quantum Noise, Measurement, and Amplification". In: *Reviews of Modern Physics* 82.2 (Apr. 2010), pp. 1155–1208. DOI: 10.1103/RevModPhys.82.1155 (cit. on p. 5).

[127] R. Kubo. "The Fluctuation-Dissipation Theorem". In: *Reports on Progress in Physics* 29.1 (Jan. 1966), p. 255. DOI: 10.1088/0034-4885/29/1/306 (cit. on p. 6).

[128] Hideo Suzuki, Naoki Yamaguchi, and Hideaki Izumi. "Theoretical and Experimental Studies on the Resonance Frequencies of a Stretched Circular Plate: Application to Japanese Drum Diaphragms". In: *Acoustical Science and Technology* 30.5 (2009), pp. 348–354. DOI: 10.1250/ast.30.348 (cit. on pp. 7, 109).

[129] Thein Wah. "Vibration of Circular Plates". In: *The Journal of the Acoustical Society of America* 34.3 (July 2005), pp. 275–281. DOI: 10.1121/1.1928110 (cit. on p. 7).

[130] B. D. Hauer, C. Doolin, K. S. D. Beach, and J. P. Davis. "A General Procedure for Thermomechanical Calibration of Nano/Micro-Mechanical Resonators". In: *Annals of Physics* 339 (Dec. 2013), pp. 181–207. DOI: 10.1016/j.aop.2013.08.003 (cit. on pp. 9, 85).

[131] Charlotte Bond, Daniel Brown, Andreas Freise, and Kenneth A. Strain. "Interferometer Techniques for Gravitational-Wave Detection". In: *Living Reviews in Relativity* 19.1 (Feb. 2017), p. 3. DOI: 10.1007/s41114-016-0002-8 (cit. on pp. 9, 12, 16).

[132] R. W. P. Drever, J. L. Hall, F. V. Kowalski, J. Hough, G. M. Ford, A. J. Munley, and H. Ward. "Laser Phase and Frequency Stabilization Using an Optical Resonator". In: *Applied Physics B* 31.2 (June 1983), pp. 97–105. DOI: 10.1007/BF00702605 (cit. on p. 16).

[133] Eric D. Black. "An Introduction to Pound–Drever–Hall Laser Frequency Stabilization". In: *American Journal of Physics* 69.1 (Jan. 2001), pp. 79–87. DOI: 10.1119/1.1286663 (cit. on pp. 16, 60).

[134] Vincent Dumont, Simon Bernard, Christoph Reinhardt, Alex Kato, Maximilian Ruf, and Jack C. Sankey. "Flexure-Tuned Membrane-at-the-Edge Optomechanical System". In: *Optics Express* 27.18 (Sept. 2019), pp. 25731–25748. DOI: 10.1364/OE.27.025731 (cit. on pp. 18, 19).

[135] A. M. Jayich, J. C. Sankey, B. M. Zwickl, C. Yang, J. D. Thompson, S. M. Girvin, A. A. Clerk, F. Marquardt, and J. G. E. Harris. "Dispersive Optomechanics: A Membrane inside a Cavity". In: *New Journal of Physics* 10.9 (Sept. 2008), p. 095008. DOI: 10.1088/1367-2630/10/9/095008 (cit. on p. 18).

[136] J. Gallego, S. Ghosh, S. K. Alavi, W. Alt, M. Martinez-Dorantes, D. Meschede, and L. Ratschbacher. "High-Finesse Fiber Fabry–Perot Cavities: Stabilization and Mode Matching Analysis". In: *Applied Physics B* 122.3 (Mar. 2016), p. 47. DOI: 10.1007/s00340-015-6281-z (cit. on p. 20).

[137] Maryse Ernzer, Manel Bosch Aguilera, Matteo Brunelli, Gian-Luca Schmid, Thomas M. Karg, Christoph Bruder, Patrick P. Potts, and Philipp Treutlein. "Optical Coherent Feedback Control of a Mechanical Oscillator". In: *Physical Review X* 13.2 (May 2023), p. 021023. DOI: 10.1103/PhysRevX.13.021023 (cit. on pp. 24, 107).

[138] Hoi-Kwan Lau and Aashish A. Clerk. "Ground-State Cooling and High-Fidelity Quantum Transduction via Parametrically Driven Bad-Cavity Optomechanics". In: *Physical Review Letters* 124.10 (Mar. 2020), p. 103602. DOI: 10.1103/PhysRevLett.124.103602 (cit. on pp. 24, 107).

[139] Alexander K. Tagantsev and Sergey A. Fedorov. "Quantum-Limited Measurements Using an Optical Cavity with Modulated Intrinsic Loss". In: *Physical Review Letters* 123.4 (July 2019), p. 043602. DOI: 10.1103/PhysRevLett.123.043602 (cit. on pp. 24, 107).

[140] Jingkun Guo and Simon Gröblacher. "Coherent Feedback in Optomechanical Systems in the Sideband-Unresolved Regime". In: *Quantum* 6 (Nov. 2022), p. 848. DOI: 10.22331/q-2022-11-03-848 (cit. on pp. 24, 107).

[141] T. Bodiya, V. Sudhir, C. Wipf, N. Smith, A. Buikema, A. Kontos, H. Yu, and N. Mavalvala. "Sub-Hertz Optomechanically Induced Transparency with a Kilogram-Scale Mechanical Oscillator". In: *Physical Review A* 100.1 (July 2019), p. 013853. DOI: 10.1103/PhysRevA.100.013853 (cit. on pp. 24, 25, 101, 104, 107).

[142] Stefan Weis, Rémi Rivière, Samuel Deléglise, Emanuel Gavartin, Olivier Arcizet, Albert Schliesser, and Tobias J. Kippenberg. "Optomechanically Induced Transparency". In: *Science* 330.6010 (Dec. 2010), pp. 1520–1523. DOI: 10.1126/science.1195596 (cit. on p. 24).

[143] Hao Xiong and Ying Wu. "Fundamentals and Applications of Optomechanically Induced Transparency". In: *Applied Physics Reviews* 5.3 (Aug. 2018), p. 031305. DOI: 10.1063/1.5027122 (cit. on pp. 24, 104).

[144] P. L. Knight, E. A. Hinds, M. B. Plenio, Romain Long, Tilo Steinmetz, Peter Hommelhoff, Wolfgang Hänsel, Theodor W. Hänsch, and Jakob Reichel. "Magnetic Microchip Traps and Single–Atom Detection". In: *Philosophical Transactions of the Royal Society of London. Series A: Mathematical, Physical and Engineering Sciences* 361.1808 (July 2003), pp. 1375–1389. DOI: 10.1098/rsta.2003.1207 (cit. on p. 29).

[145] T. Steinmetz, Y. Colombe, D. Hunger, T. W. Hänsch, A. Balocchi, R. J. Warburton, and J. Reichel. "Stable Fiber-Based Fabry-Pérot Cavity". In: *Applied Physics Letters* 89.11 (Sept. 2006), p. 111110. DOI: 10.1063/1.2347892 (cit. on p. 29).

[146] Alexander Högele, Stefan Seidl, Martin Kroner, Khaled Karrai, Christian Schulhauser, Omar Sqalli, Jan Scrimgeour, and Richard J. Warburton. "Fiber-Based Confocal Microscope for Cryogenic Spectroscopy". In: *Review of Scientific Instruments* 79.2 (Feb. 2008), p. 023709. DOI: 10.1063/1.2885681 (cit. on p. 34).

[147] E. A. Donley, T. P. Heavner, F. Levi, M. O. Tataw, and S. R. Jefferts. "Double-Pass Acousto-Optic Modulator System". In: *Review of Scientific Instruments* 76.6 (June 2005), p. 063112. DOI: 10.1063/1.1930095 (cit. on p. 36).

[148] Yi Jiang. "High-Resolution Interrogation Technique for Fiber Optic Extrinsic Fabry-Perot Interferometric Sensors by the Peak-to-Peak Method". In: *Applied Optics* 47.7 (Mar. 2008), pp. 925–932. DOI: 10.1364/AO.47.000925 (cit. on p. 41).

[149] Andreas Barg, Yeghishe Tsaturyan, Erik Belhage, William H. P. Nielsen, Christoffer B. Møller, and Albert Schliesser. "Measuring and Imaging Nanomechanical Motion with Laser Light". In: *Applied Physics B* 123.1 (Jan. 2017), p. 8. DOI: 10.1007/s00340-016-6585-7 (cit. on pp. 44, 45).

[150] James W. Wagner and James B. Spicer. "Theoretical Noise-Limited Sensitivity of Classical Interferometry". In: *JOSA B* 4.8 (Aug. 1987), pp. 1316–1326. DOI: 10.1364/JOSAB.4.001316 (cit. on p. 45).

[151] Thibaud Ruelle, David Jaeger, Francesco Fogliano, Floris Braakman, and Martino Poggio. "A Tunable Fiber Fabry–Perot Cavity for Hybrid Optomechanics Stabilized at 4 K". In: *Review of Scientific Instruments* 93.9 (Sept. 2022), p. 095003. DOI: 10.1063/5.0098140 (cit. on p. 47).

[152] C. Koks and M. P. van Exter. "Microcavity Resonance Condition, Quality Factor, and Mode Volume Are Determined by Different Penetration Depths". In: *Optics Express* 29.5 (Mar. 2021), pp. 6879–6889. DOI: 10.1364/OE.412346 (cit. on p. 50).

[153] Julia Benedikter, Thomas Hümmer, Matthias Mader, Benedikt Schlederer, Jakob Reichel, Theodor W. Hänsch, and David Hunger. "Transverse-Mode Coupling and Diffraction Loss in Tunable Fabry–Pérot Microcavities". In: *New Journal of Physics* 17.5 (May 2015), p. 053051. DOI: 10.1088/1367-2630/17/5/053051 (cit. on p. 54).

[154] Carlos Saavedra, Deepak Pandey, Wolfgang Alt, Hannes Pfeifer, and Dieter Meschede. "Tunable Fiber Fabry-Perot Cavities with High Passive Stability". In: *Optics Express* 29.2 (Jan. 2021), pp. 974–982. DOI: 10.1364/OE.412273 (cit. on p. 55).

[155] John Bechhoefer. "Feedback for Physicists: A Tutorial Essay on Control". In: *Reviews of Modern Physics* 77.3 (Aug. 2005), pp. 783–836. DOI: 10.1103/RevModPhys.77.783 (cit. on p. 60).

[156] A. Gloppe, P. Verlot, E. Dupont-Ferrier, A. Siria, P. Poncharal, G. Bachelier, P. Vincent, and O. Arcizet. "Bidimensional Nano-Optomechanics and Topological Backaction in a Non-Conservative Radiation Force Field". In: *Nature Nanotechnology* 9.11 (Nov. 2014), pp. 920–926. DOI: 10.1038/nnano.2014.189 (cit. on p. 61).

[157] Camille Maestre, Bérangère Toury, Philippe Steyer, Vincent Garnier, and Catherine Journet. "Hexagonal Boron Nitride: A Review on Selfstanding Crystals Synthesis towards 2D Nanosheets". In: *Journal of Physics: Materials* 4.4 (Oct. 2021), p. 044018. DOI: 10.1088/2515-7639/ac2b87 (cit. on p. 63).

[158] Kyung Yeol Ma, Minsu Kim, and Hyeon Suk Shin. "Large-Area Hexagonal Boron Nitride Layers by Chemical Vapor Deposition: Growth and Applications for Substrates, Encapsulation, and Membranes". In: *Accounts of Materials Research* 3.7 (July 2022), pp. 748–760. DOI: 10.1021/accountsmr.2c00061 (cit. on p. 63).

[159] Erik Pollmann, Lukas Madauß, Simon Schumacher, Uttam Kumar, Flemming Heuvel, Christina vom Ende, Sümeyra Yilmaz, Sümeyra Güngörmüs, and Marika Schleberger. "Apparent Differences between Single Layer Molybdenum Disulphide Fabricated via Chemical Vapour Deposition and Exfoliation". In: *Nanotechnology* 31.50 (Oct. 2020), p. 505604. DOI: 10.1088/1361-6528/abb5d2 (cit. on p. 63).

[160] Roman V. Gorbachev et al. "Hunting for Monolayer Boron Nitride: Optical and Raman Signatures". In: *Small* 7.4 (2011), pp. 465–468. DOI: 10.1002/smll.201001628 (cit. on p. 63).

[161] Andres Castellanos-Gomez, Michele Buscema, Rianda Molenaar, Vibhor Singh, Laurens Janssen, Herre S. J. van der Zant, and Gary A. Steele. "Deterministic Transfer of Two-Dimensional Materials by All-Dry Viscoelastic Stamping". In: *2D Materials* 1.1 (2014), p. 011002. DOI: 10.1088/2053-1583/1/1/011002 (cit. on pp. 63, 67).

[162] Yanan Wang, Vivian Zhou, Yong Xie, Xu-Qian Zheng, and Philip X.-L. Feng. "Optical Contrast Signatures of Hexagonal Boron Nitride on a Device Platform". In: *Optical Materials Express* 9.3 (Mar. 2019), pp. 1223–1232. DOI: 10.1364/OME.9.001223 (cit. on p. 68).

[163] Andrei G. F. Garcia, Michael Neumann, François Amet, James R. Williams, Kenji Watanabe, Takashi Taniguchi, and David Goldhaber-Gordon. "Effective Cleaning of Hexagonal Boron Nitride for Graphene Devices". In: *Nano Letters* 12.9 (Sept. 2012), pp. 4449–4454. DOI: 10.1021/nl3011726 (cit. on p. 72).

[164] Arend M. van der Zande, Robert A. Barton, Jonathan S. Alden, Carlos S. Ruiz-Vargas, William S. Whitney, Phi H. Q. Pham, Jiwoong Park, Jeevak M. Parpia, Harold G. Craighead, and Paul L. McEuen. "Large-Scale Arrays of Single-Layer Graphene Resonators". In: *Nano Letters* 10.12 (Dec. 2010), pp. 4869–4873. DOI: 10.1021/nl102713c (cit. on pp. 72, 87, 105).

[165] Shriram Shivaraman et al. "Free-Standing Epitaxial Graphene". In: *Nano Letters* 9.9 (Sept. 2009), pp. 3100–3105. DOI: 10.1021/nl900479g (cit. on p. 72).

[166] Gabriele Grosso, Hyowon Moon, Benjamin Lienhard, Sajid Ali, Dmitri K. Efetov, Marco M. Furchi, Pablo Jarillo-Herrero, Michael J. Ford, Igor Aharonovich,

and Dirk Englund. "Tunable and High-Purity Room Temperature Single-Photon Emission from Atomic Defects in Hexagonal Boron Nitride". In: *Nature Communications* 8.1 (Sept. 2017), p. 705. DOI: 10.1038/s41467-017-00810-2 (cit. on p. 73).

[167] Toan Trong Tran, Christopher Elbadawi, Daniel Totonjian, Charlene J. Lobo, Gabriele Grosso, Hyowon Moon, Dirk R. Englund, Michael J. Ford, Igor Aharonovich, and Milos Toth. "Robust Multicolor Single Photon Emission from Point Defects in Hexagonal Boron Nitride". In: *ACS Nano* 10.8 (Aug. 2016), pp. 7331–7338. DOI: 10.1021/acsnano.6b03602 (cit. on pp. 73, 107).

[168] A. C. Ferrari and J. Robertson. "Interpretation of Raman Spectra of Disordered and Amorphous Carbon". In: *Physical Review B* 61.20 (May 2000), pp. 14095–14107. DOI: 10.1103/PhysRevB.61.14095 (cit. on p. 73).

[169] Gaurav Nanda, Srijit Goswami, Kenji Watanabe, Takashi Taniguchi, and Paul F. A. Alkemade. "Defect Control and N-Doping of Encapsulated Graphene by Helium-Ion-Beam Irradiation". In: *Nano Letters* 15.6 (June 2015), pp. 4006–4012. DOI: 10.1021/acs.nanolett.5b00939 (cit. on p. 73).

[170] David Jaeger, Francesco Fogliano, Thibaud Ruelle, Aris Lafranca, Floris Braakman, and Martino Poggio. "Mechanical Mode Imaging of a High-Q Hybrid hBN/Si3N4 Resonator". In: *Nano Letters* 23.5 (Mar. 2023), pp. 2016–2022. DOI: 10.1021/acs.nanolett.3c00233 (cit. on pp. 75, 77).

[171] Cornelia Schwarz, Benjamin Pigeau, Laure Mercier de Lépinay, Aurélien G. Kuhn, Dipankar Kalita, Nedjma Bendiab, Laëtitia Marty, Vincent Bouchiat, and Olivier Arcizet. "Deviation from the Normal Mode Expansion in a Coupled Graphene-Nanomechanical System". In: *Physical Review Applied* 6.6 (Dec. 2016), p. 064021. DOI: 10.1103/PhysRevApplied.6.064021 (cit. on pp. 77, 90, 105, 107).

[172] Rajan Singh, Arnab Sarkar, Chitres Guria, Ryan J.T. Nicholl, Sagar Chakraborty, Kirill I. Bolotin, and Saikat Ghosh. "Giant Tunable Mechanical Nonlinearity in Graphene–Silicon Nitride Hybrid Resonator". In: *Nano Letters* 20.6 (June 2020), pp. 4659–4666. DOI: 10.1021/acs.nanolett.0c01586 (cit. on pp. 77, 105, 107).

[173] Christopher F. Reiche, Julia Körner, Bernd Büchner, and Thomas Mühl. "Introduction of a Co-Resonant Detection Concept for Mechanical Oscillation-Based Sensors". In: *Nanotechnology* 26.33 (2015), p. 335501. DOI: 10.1088/0957-4484/26/33/335501 (cit. on p. 77).

[174] Rajan Singh, Ryan J.T. Nicholl, Kirill I. Bolotin, and Saikat Ghosh. "Motion Transduction with Thermo-mechanically Squeezed Graphene Resonator Modes". In: *Nano Letters* 18.11 (Nov. 2018), pp. 6719–6724. DOI: 10.1021/acs.nanolett.8b02293 (cit. on pp. 77, 83, 107).

[175] W. Paszkowicz, J.B. Pelka, M. Knapp, T. Szyszko, and S. Podsiadlo. "Lattice Parameters and Anisotropic Thermal Expansion of Hexagonal Boron Nitride in the 10–297.5 K Temperature Range". In: *Applied Physics A* 75.3 (Sept. 2002), pp. 431–435. DOI: 10.1007/s003390100999 (cit. on p. 86).

[176] Duhee Yoon, Young-Woo Son, and Hyeonsik Cheong. "Negative Thermal Expansion Coefficient of Graphene Measured by Raman Spectroscopy". In: *Nano Letters* 11.8 (Aug. 2011), pp. 3227–3231. DOI: 10.1021/nl201488g (cit. on p. 86).

[177] Nicolas Morell, Antoine Reserbat-Plantey, Ioannis Tsioutsios, Kevin G. Schädler, François Dubin, Frank H. L. Koppens, and Adrian Bachtold. "High Quality Factor Mechanical Resonators Based on WSe2 Monolayers". In: *Nano Letters* 16.8 (Aug. 2016), pp. 5102–5108. DOI: 10.1021/acs.nanolett.6b02038 (cit. on p. 87).

[178] C. Reetz, R. Fischer, G.G.T. Assumpção, D.P. McNally, P.S. Burns, J.C. Sankey, and C.A. Regal. "Analysis of Membrane Phononic Crystals with Wide Band Gaps and Low-Mass Defects". In: *Physical Review Applied* 12.4 (Oct. 2019), p. 044027. DOI: 10.1103/PhysRevApplied.12.044027 (cit. on pp. 90, 106).

[179] Xiao-Bo Yan. "Optomechanically Induced Optical Responses with Non-Rotating Wave Approximation". In: *Journal of Physics B: Atomic, Molecular and Optical Physics* 54.3 (Jan. 2021), p. 035401. DOI: 10.1088/1361-6455/abd645 (cit. on p. 102).

[180] Xiao-Bo Yan. "Optomechanically Induced Transparency and Gain". In: *Physical Review A* 101.4 (Apr. 2020), p. 043820. DOI: 10.1103/PhysRevA.101.043820 (cit. on p. 102).

[181] Robert A. Barton, B. Ilic, Arend M. van der Zande, William S. Whitney, Paul L. McEuen, Jeevak M. Parpia, and Harold G. Craighead. "High, Size-Dependent Quality Factor in an Array of Graphene Mechanical Resonators". In: *Nano Letters* 11.3 (Mar. 2011), pp. 1232–1236. DOI: 10.1021/nl1042227 (cit. on p. 105).

[182] L. Ding, C. Baker, P. Senellart, A. Lemaitre, S. Ducci, G. Leo, and I. Favero. "Wavelength-Sized GaAs Optomechanical Resonators with Gigahertz Frequency". In: *Applied Physics Letters* 98.11 (Mar. 2011), p. 113108. DOI: 10.1063/1.3563711 (cit. on p. 107).

[183] Rick Leijssen, Giada R. La Gala, Lars Freisem, Juha T. Muhonen, and Ewold Verhagen. "Nonlinear Cavity Optomechanics with Nanomechanical Thermal Fluctuations". In: *Nature Communications* 8.1 (July 2017), ncomms16024. DOI: 10.1038/ncomms16024 (cit. on p. 107).

[184] Sampo A. Saarinen, Nenad Kralj, Eric C. Langman, Yeghishe Tsaturyan, and Albert Schliesser. "Laser Cooling a Membrane-in-the-Middle System Close to the Quantum Ground State from Room Temperature". In: *Optica* 10.3 (Mar. 2023), pp. 364–372. DOI: 10.1364/OPTICA.468590 (cit. on p. 107).

[185] David Hälg et al. "Membrane-Based Scanning Force Microscopy". In: *Physical Review Applied* 15.2 (Feb. 2021), p. L021001. DOI: 10.1103/PhysRevApplied.15.L021001 (cit. on p. 107).

Bibliography - Books

[186] Ivan Favero, Jack Sankey, and Eva M. Weig. *Mechanical Resonators in the Middle of an Optical Cavity*. Ed. by Markus Aspelmeyer, Tobias J. Kippenberg, and Florian Marquardt. Quantum Science and Technology. Berlin, Heidelberg: Springer, 2014. DOI: 10.1007/978-3-642-55312-7_5 (cit. on p. 1).

[187] Philipp Treutlein, Claudiu Genes, Klemens Hammerer, Martino Poggio, and Peter Rabl. *Hybrid Mechanical Systems*. Ed. by Markus Aspelmeyer, Tobias J. Kippenberg, and Florian Marquardt. Quantum Science and Technology. Berlin, Heidelberg: Springer, 2014. DOI: 10.1007/978-3-642-55312-7_14 (cit. on p. 1).

[188] Warwick P. Bowen and Gerard J. Milburn. *Quantum Optomechanics*. Boca Raton: CRC Press, Dec. 2015. DOI: 10.1201/b19379 (cit. on p. 1).

[189] Singiresu S. Rao. *Vibration of Continuous Systems*. John Wiley & Sons, Feb. 2007 (cit. on p. 7).

[190] Morse Philip M. *Vibration and Sound*. Mcgraw-hill Book Company, Inc. New York, 1948 (cit. on pp. 8, 109).

[191] Silvan Schmid, Luis Guillermo Villanueva, and Michael Lee Roukes. *Fundamentals of Nanomechanical Resonators*. Cham: Springer International Publishing, 2016. DOI: 10.1007/978-3-319-28691-4 (cit. on p. 9).

[192] Andrew N. Cleland. *Foundations of Nanomechanics*. Advanced Texts in Physics. Berlin, Heidelberg: Springer, 2003. DOI: 10.1007/978-3-662-05287-7 (cit. on p. 9).

[193] A. E. Siegman. *Lasers*. University Science Books, 1986 (cit. on pp. 9, 12, 21).

[194] Max Born, Emil Wolf, and A. B. Bhatia. *Principles of Optics: Electromagnetic Theory of Propagation, Interference and Diffraction of Light*. Cambridge University Press, Oct. 1999 (cit. on pp. 9, 38).

[195] Pochi Yeh. *Optical Waves in Layered Media*. Wiley, Mar. 2005 (cit. on p. 9).

[196] Vladimir B. Braginsky, Farid Ya Khalili, and Kip S. Thorne. *Quantum Measurement*. Cambridge: Cambridge University Press, 1992. DOI: 10.1017/CBO9780511622748 (cit. on p. 45).

Bibliography - Theses

[197] Francesco Fogliano. "Ultrasensitive Nanowire Force Sensors in Extreme Conditions: From Dilution Temperature to Ultra-Strong Coupling in Cavity Nano-Optomechanics". PhD thesis. Université Grenoble Alpes, 2019 (cit. on pp. 2, 18, 23).

[198] Alexey Shkarin. "Quantum Optomechanics with Superfluid Helium". PhD thesis. Yale University, May 2018 (cit. on pp. 17, 37, 100, 102).

[199] Yeghishe Tsaturyan. "Ultracoherent Soft-Clamped Mechanical Resonators for Quantum Cavity Optomechanics". PhD thesis. Danish Center for Quantum Optics: University of Copenhagen, Oct. 2019 (cit. on p. 24).

[200] Thibaud Ruelle. "Towards Hybrid Optomechanics in a Fiber-Based Fabry-Perot Cavity". PhD thesis. University of Basel, 2021 (cit. on pp. 31, 47, 48, 50, 53, 54).

[201] Dalziel Joseph Wilson. "Cavity Optomechanics with High-Stress Silicon Nitride Films". PhD thesis (cit. on pp. 34, 95).

[202] Anna Dmitriyevna Kashkanova. “Optomechanics with Superfluid Helium”. PhD thesis. Yale University, Dec. 2017 (cit. on p. 100).

Bibliography - Miscellaneous

[203] Antoine Reigue. “Modelling a nanowire in an optical cavity”. unpublished. Sept. 2020 (cit. on pp. 9, 18, 19, 21, 23).

[204] Marki Microwave and Doug Jorgesen. *IQ, IMAGE REJECT & Single Sideband Mixer Primer*. 2018 (cit. on p. 39).

Acknowledgements

Writing the manuscript at the end of a PhD is not only a good way to remember all the work that went into producing these results and the many struggles one had to overcome along the way, but also all the help and support that one received over the years.

While doing a PhD is never a trivial task, for me, it will be a section of my life that I will remember fondly. The fact that I can look back on this journey with such positivity is not something I take for granted, and it is something that fills me with gratitude towards the entire Poggio Lab.

I believe that creating a work environment in which outstanding research results can be produced, but all the individuals that make up the group can also feel at home and enjoy their time, is something that starts with the head of the group. So I want to thank Martino not only for giving me the opportunity to pursue a PhD but also for creating a research group that many of us happily identify with.

In a similar way, I would like to thank Floris. I was not only a member of the Poggio Lab but also of the optomechanics sub-group, which was brought to life by his efforts.

Speaking of this little sub-group, the two people that I feel most indebted to at the end of this journey are without a doubt Thibaud and Francesco. It was not only a pleasure working and bantering with both of these gentlemen, but I am also very well aware of the staggering amount of work both of them have poured into this project to make it succeed. The early struggles I lived through with Thibaud and overcoming these challenges are experiences that I wouldn't want to miss. The addition of Francesco and his drive in the lab is a big reason for the success we achieved after many years of work. In addition, his eagerness to support me while writing this manuscript and during the preparation for my defense, something with little benefit to himself, is something that I will always appreciate.

We also had several master students join us over the years. The one that I worked together with the most was Aris, and knowing that he will begin a PhD of his own in our group, I want to wish him the best of luck and endurance.

Finally, to progress to the point where one has the opportunity to do a PhD, many years are spent studying at a university. This is a path that would have been exceedingly difficult without the encouragement and support of my family. This, too, is something that I do not take for granted. For that, thank you.